Final Report to

Gas Well Pressure Drop Prediction under Foam Flow Conditions

09122-01.FINAL

November 30, 2015

Principal Investigator:

Mohan Kelkar, Ph.D.
Williams Endowed Chair Professor
McDougall School of Petroleum Engineering
The University of Tulsa
800 South Tucker Drive (Stephenson Hall)
Tulsa, Oklahoma 74104-3189
Phone: (918) 631-3036
Fax: (918) 631-2059
Email: mohan@utulsa.edu

Co-Principal Investigator:

Cem Sarica, Ph.D.
F. H. "Mick" Merelli/Cimarex Energy Professor
McDougall School of Petroleum Engineering
The University of Tulsa
800 South Tucker Drive (North Campus)
Tulsa, Oklahoma 74104-3189
Phone: (918) 631-5154
Fax: (918) 631-5112
Email: cem-sarica@utulsa.edu

LEGAL NOTICE

This report was prepared by Mohan Kelkar as an account of work sponsored by the Research Partnership to Secure Energy for America, RPSEA. Neither RPSEA members of RPSEA, the National Energy Technology Laboratory, the U.S. Department of Energy, nor any person acting on behalf of any of the entities:

a. MAKES ANY WARRANTY OR REPRESENTATION, EXPRESS OR IMPLIED WITH RESPECT TO ACCURACY, COMPLETENESS, OR USEFULNESS OF THE INFORMATION CONTAINED IN THIS DOCUMENT, OR THAT THE USE OF ANY INFORMATION, APPARATUS, METHOD, OR PROCESS DISCLOSED IN THIS DOCUMENT MAY NOT INFRINGE PRIVATELY OWNED RIGHTS, OR

b. ASSUMES ANY LIABILITY WITH RESPECT TO THE USE OF, OR FOR ANY AND ALL DAMAGES RESULTING FROM THE USE OF, ANY INFORMATION, APPARATUS, METHOD, OR PROCESS DISCLOSED IN THIS DOCUMENT.

THIS IS A FINAL REPORT. THE DATA, CALCULATIONS, INFORMATION, CONCLUSIONS, AND/OR RECOMMENDATIONS REPORTED HEREIN ARE THE PROPERTY OF THE U.S. DEPARTMENT OF ENERGY.

REFERENCE TO TRADE NAMES OR SPECIFIC COMMERCIAL PRODUCTS, COMMODITIES, OR SERVICES IN THIS REPORT DOES NOT REPRESENT OR CONSTIITUTE AND ENDORSEMENT, RECOMMENDATION, OR FAVORING BY RPSEA OR ITS CONTRACTORS OF THE SPECIFIC COMMERCIAL PRODUCT, COMMODITY, OR SERVICE.

Principal Investigator: Mohan Kelkar, Ph.D.

Signed: Mohan Kelkar

Date: December 1, 2015

ABSTRACT

The present study addresses several important questions which are critical for operators who operate gas wells. As the gas rate starts declining, the gas wells will eventually start liquid loading because of gas' inability to carry the liquid to the surface. The present work develops a new correlation to predict the inception of liquid loading for gas wells. Compared to the existing correlations, the new correlation is (i) a function of tubing diameter; (ii) is able to predict liquid loading for inclined wells; (iii) is a function liquid to gas ratio. The correlation has been validated by comparing the results with field data.

In addition to predicting the liquid loading, we also provide improved correlations to predict the use of surfactant (or foam) to eliminate the liquid loading. To accomplish this task, we considered five different surfactants and studied their behavior in both small scale and large scale facilities. The data were collected over a wide range of experimental conditions and based on the data collected, we developed a new correlation to predict the liquid loading under foam flow conditions as well as the pressure drop calculations for foam flow. Currently, the correlation developed is the only correlation available to predict the pressure drop for foam flow. This correlation can help operator to understand and quantify pressure drop behavior under foam flow conditions.

TABLE OF CONTENTS

LEGAL NOTICE i
SIGNATURE AND DATE iii
ABSTRACT iv
TABLE OF CONTENTS v
EXECUTIVE SUMMARY xii
REPORT DETAILS 1
Literature Review 1
Liquid Loading 1
Foam Flow and Liquid Loading 9
Objectives 13
Results and Discussion 14
Liquid Loading 14
Data Available 15
Proposed Model 19
Field Validation 34
Foam Flow 52
Experimental Methods 52
Small Scale Facilities 53
Large Scale Facilities 60
Test Matrix 63
Experimental Data Collection and Observations 66
Small Scale Facilities – Experimental Results 66
Large Scale Facilities – Experimental Results 92
Modeling of Foam Data 122
Liquid Loading Under Foam Flow Conditions 122
Foam Flow Modeling 129
Impact to Producers 159
Technology Transfer Efforts 160
Conclusions 161
Liquid Loading 161
Foam Flow 161
Recommendations 163
BIBLIOGRAPHY 163
LIST OF ACRONYMS AND ABBREVIATIONS 166
APPENDIX A 168

List of Figures

Figure 1.1: Flow Patterns of Two Phase Flow in Vertical Pipe 1
Figure 1.2: Liquid Loading Example 2
Figure 1.3: In-situ Gas Velocity vs. Turner Critical Velocity 5
Figure 1.4: Control Volume in the Zhang et al. Model 6
Figure 1.5: Schematic of Liquid-Gas Two Phase Annular Flow in Wellbore 7
Figure 1.6: Transition Boundary of Different Models 8

Figure 1.7: Gas Dispersion within Lamella of Surfactant 10
Figure 1.8: Surfactant Classification According to the Composition of Their Head: Non-ionic, Anionic, Cationic and Amphoteric (Van Nimwegasn et al., 2013) 10
Figure 2.1: Liquid Loading Example by Veekan et al. (2007) 17
Figure 2.2: Gas Production History 18
Figure 2.3: Gas Well Without Liquid Loading at Early Time 19
Figure 2.4: Gas Well Under Liquid Loading at Later Time 19
Figure 2.5: Gravitational and Frictional Gradient with Respect to Gas Velocity 20
Figure 2.6: Total Pressure Gradient and Pressure Drops in 2-inch pipe 22
Figure 2.7: Film Reversal Observation in 2-inch pipe 22
Figure 2.8: Gravitational and Frictional Pressure Gradient in 2-inch pipe 23
Figure 2.9: Total Pressure Gradient and Pressure Drops in 4-inch pipe 23
Figure 2.10: Film Reversal Observation in 4-inch pipe 24
Figure 2.11: Gravitational and Frictional Pressure Gradient in 4-inch pipe 24
Figure 2.12: Liquid Film Thickness Comparison between Vertical and Inclined Wells 25
Figure 2.13: Barnea's Model Boundaries at Different Inclination Angles 26
Figure 2.14: Critical Gas Velocity Changing with Different Inclination Angle 27
Figure 2.15: Schematic Uniform Thickness Liquid Film 28
Figure 2.16: Schematic Non-uniform Thickness Liquid Film 28
Figure 2.17: Non-uniform Film Thickness at 30 Degree Inclination Angle 29
Figure 2.18: Liquid Film Thickness Distribution around Pipe 30
Figure 2.19: Transition Boundaries of New Model Using Non-Uniform Film Thickness (0 - 30 Degree Inclination Angle) 31
Figure 2.20: Transition Boundaries of New Model Using Non-Uniform Film Thickness (30 - 90 Degree Inclination Angle) 31
Figure 2.21: Critical Gas Velocity of New Model (0 - 90 Degree Inclination Angle) ... 32
Figure 2.22: Comparison of Transition Boundary of Barnea's Model and New Model 33
Figure 2.23 Turner's Data versus Turner's Equation (w/c) Predictions 35
Figure 2.24: Turner's Data versus Turner's Equation (w) Predictions 35
Figure 2.25: Turner's Data versus Zhang et al. Model Predictions 36
Figure 2.26: Turner's Data versus Barnea's Model Predictions 37
Figure 2.27: Turner's Data versus New Model Predictions 37
Figure 2.28: Coleman et al. Data versus Turner's Equation Predictions 39
Figure 2.29: Coleman et al. Data versus Zhang et al. Model Predictions 39
Figure 2.30: Coleman et al. Data versus Barnea's Model Predictions 40
Figure 2.31: Coleman et al. Data versus New Model Predictions 40
Figure 2.32: Veeken et al. Data versus Turner's Equation Predictions 42
Figure 2.33: Veeken et al. Data versus Zhang et al. Model Predictions 42
Figure 2.34: Veeken et al. Data versus Barnea's Model Predictions 43
Figure 2.35: Veeken et al. Data versus New Model Predictions 43
Figure 2.36: Chevron Data versus Turner's Equation Predictions 44
Figure 2.37: Chevron Data versus Zhang et al. Model Predictions 45
Figure 2.38: Chevron Data versus Barnea's Model Predictions 45
Figure 2.39: Chevron Data versus New Model Predictions 46

Figure 2.40: ConocoPhillips Data versus Turner's Equation Predictions 47
Figure 2.41: ConocoPhillips Data versus Zhang et al. Model Predictions 47
Figure 2.42: ConocoPhillips Data versus Barnea's Model Predictions 48
Figure 2.43: ConocoPhillips Data versus New Model Predictions 48
Figure 2.44: Barnea's Results of Veeken's Data at Different Inclination Angle 49
Figure 2.45: New Model's Results of Veeken's Data at Different Inclination Angle ... 50
Figure 2.46: Experimental Data (Yuan, 2011) (Vertical) 51
Figure 2.47: Experimental Data (15 degree) (Yuan, 2011) 51
Figure 2.48: Experimental Data (30 degree) (Yuan, 2011) 52
Figure 3.1: Pendent Drop Apparatus (Arashiro and Demarquette, 1999) 54
Figure 3.2: The Pendent Drop Geometry (Arashiro and Demarquette, 1999) 55
Figure 3.3: Unloading Test Facility 57
Figure 3.4: Stability Test Facility 59
Figure 3.5: Foam Flow Loop Schematic 60
Figure 3.6: Foam Structure as a Function of Time in the Middle Section 63
Figure 3.7: Surface Tension as a Function of Time 66
Figure 3.8: Surface Tension Result of All Surfactants Tested 67
Figure 3.9: Least Gas Rate and Least Concentration for Sparging 100 mL of Test Solution 68
Figure 3.10: Repeatability Tests for Anionic Surfactant at 600 ppm 69
Figure 3.11: Repeatability Tests for Anionic Surfactant at 2,400 ppm 70
Figure 3.12: Drained Volume with Time for Anionic Surfactant at 0.35 LPM 71
Figure 3.13: Drained Volume with Time for Amphoteric I Surfactant at 0.75 LPM ... 71
Figure 3.14: Drained Volume with Time for Amphoteric II Surfactant at 0.75 LPM . 72
Figure 3.15: Drained Volume with Time for Sulphonate Surfactant at 0.35 LPM 72
Figure 3.16: Drained Volume with Time for Cationic Surfactant at 0.75 LPM 73
Figure 3.17: Volumetric Rate of Liquid Drainage at 0.35 LPM 74
Figure 3.18: Volumetric Rate of Liquid Drainage at 0.75 LPM 74
Figure 3.19: Half-Life of Surfactants Tested at 0.35 LPM 75
Figure 3.20: Half-Life of Surfactants Tested at 0.75 LPM 75
Figure 3.21: Half-life of Anionic, Amphoteric I, Amphoteric II and Cationic Surfactants at 0.75 LPM 76
Figure 3.22: Unloading Repeatability Test Results for Anionic Surfactant at 0.50 LPM 77
Figure 3.23: Unloading Repeatability Test Results for Anionic Surfactant at 0.75 LPM 78
Figure 3.24: Unloading Test Results for Anionic at 0.75 LPM 79
Figure 3.25: Unloading Test Result for Amphoteric I at 0.75 LPM 79
Figure 3.26: Unloading Test Results for Amphoteric II at 0.75 LPM 80
Figure 3.27: Unloading Test Results for Sulphonate at 0.75 LPM 80
Figure 3.28: Unloading Test Results for Cationic at 0.75 LPM 81
Figure 3.29: Mass Unloaded at 10 minutes for Unloading Test at 0.50 LPM 82
Figure 3.30: Mass Unloaded at 10 Minutes for Unloading Test Conducted at 0.75 LPM 82
Figure 3.31: Unloaded Mass at 0.50 LPM with Concentrations at Highest Half-life Value 83

Figure 3.32: Unloaded Mass at 0.75 LPM with Concentrations at Highest Half-life Value 84
Figure 3.33: Unloaded Mass (%) at End of Unloading Test at 0.50 LPM 85
Figure 3.34: Unloaded Mass (%) at End of Unloading Test at 0.75 LPM 85
Figure 3.35: Comparison of Half-life at 0.40 LPM in different Media and at different Temperatures 87
Figure 3.36: Comparison of Volumetric Rate of Liquid Drainage at 0.40 LPM in Different Media and at Different Temperatures 87
Figure 3.37: Comparison of Half-life at 0.80 LPM in different Media and at different Temperatures: Sulphonate Included 88
Figure 3.38: Comparison of Volumetric Rate of Liquid Drainage at 0.80 LPM in different Media and at different Temperatures: Sulphonate Included 89
Figure 3.39: Comparison of Half-life at 0.40 LPM in different Media and at different Temperatures: Cationic Included 90
Figure 3.40: Comparison of Volumetric Rate of Liquid Drainage at 0.40 LPM in different Media and at different Temperatures: Cationic Included 90
Figure 3.41: Percent Mass of Liquid Unloaded at 10 Minutes in Different Mediums at 0.50 LPM 91
Figure 3.42: Percent Mass of Liquid Unloaded at 10 minutes in Different Mediums at 0.75 LPM 92
Figure 3.43: Single Phase Pressure Gradient: 2-inch Pipe, Theory and Experiment. 93
Figure 3.44: Single Phase Pressure Gradient: 4-inch Pipe, Theory and Experiment. 94
Figure 3.45: Experimental Pressure Drop in 2 and 4-inch Pipes 95
Figure 3.46: Theoretical Pressure Drop in 2 and 4-inch Pipes 95
Figure 3.47(a): Still Frame of Air-Water Flow in 2-inch ID at $v_{Sg} = 15.4\ m/s$ and $v_{SL} = 0.01\ m/s$ (Skopich, 2012) 96
Figure 3.47(b): Still Frame of Air-Water Flow in 2-inch ID at $v_{Sg} = 15.4\ m/s$ and $v_{SL} = 0.01\ m/s$ (Skopich, 2012) 97
Figure 3.48(a): Still Frame of Air-Water Flow in 2-inch ID at $v_{Sg} = 20.6\ m/s$ and $v_{SL} = 0.01\ m/s$ (Skopich, 2012) 98
Figure 3.48(b): Still Frame of Air-Water Flow in 2-inch ID at $v_{Sg} = 20.6\ m/s$ and $v_{SL} = 0.01\ m/s$ (Skopich, 2012) 98
Figure 3.49: Pressure Gradient in Anionic Foamer at 1600 ppm in 2-inch Pipe at $v_{SL} = 0.01\ m/s$ 99
Figure 3.50: Foam Film Structure: Anionic Foamer in 2-inch Pipe at 1600 ppm, $v_{Sl} = 0.01\ m/s$, $v_{Sg} = 4.72\ m/s$ 100
Figure 3.51: Foam Film Structure: Anionic Foamer in 2-inch Pipe at 1600 ppm, $v_{Sl} = 0.01\ m/s$, $v_{Sg} = 9.35\ m/s$ 100
Figure 3.52: Foam Film Structure: Anionic Foamer in 2-inch Pipe at 1600 ppm, $v_{Sl} = 0.01\ m/s$, $v_{Sg} = 23.54\ m/s$ 101
Figure 3.53: Pressure Gradient in Anionic Foamer at 1600 ppm in 4-inch Pipe at $v_{SL} = 0.01\ m/s$ 102
Figure 3.54(a): Still Frame of Foam Flow in 4-inch ID at $v_{Sg} = 10.85\ m/s$ and $v_{SL} = 0.01\ m/s$ 103

Figure 3.54(b): Still Frame of Foam Flow in 4-inch ID at $v_{Sg} = 10.85\ m/s$ and $v_{SL} = 0.01\ m/s$ 104
Figure 3.55: Foam Film Structure: Anionic Foamer in 4-inch Pipe at 1600 ppm, $v_{Sl} = 0.01\ m/s$, $v_{Sg} = 17.59\ m/s$ 104
Figure 3.56: Foam Film Structure: Anionic Foamer in 4-inch Pipe at 1,600 ppm, $v_{Sl} = 0.01\ m/s$, $v_{Sg} = 21.25\ m/s$ 105
Figure 3.57: Foam Film Structure: Anionic Foamer in 4-inch Pipe at 1,600 ppm, $v_{Sl} = 0.01\ m/s$, $v_{Sg} = 24.98\ m/s$ 105
Figure 3.58: Pressure Gradient for Anionic Foamer [v_{SL}= 0.01 m/s, 2-in pipe] 106
Figure 3.59: Liquid Holdup for Anionic Foamer [v_{SL}= 0.01 m/s, 2-in pipe] 106
Figure 3.60: Pressure Gradient for Anionic Foamer [v_{SL}= 0.01 m/s, 4-in pipe] 107
Figure 3.61: Liquid Holdup for Anionic Foamer [v_{SL}= 0.01 m/s, 4-in pipe] 108
Figure 3.62: Pressure Gradients at Half-life Concentrations: 2-inch Pipe, $v_{SL} = 0.01\ m/s$ 109
Figure 3.63: Pressure Gradients at Half-life Concentrations: 2-inch Pipe, $v_{SL} = 0.03\ m/s$ 110
Figure 3.64: Pressure Gradients at Half-life Concentrations: 4-inch Pipe, $v_{SL} = 0.01\ m/s$ 111
Figure 3.65: Pressure Gradients at Half-life Concentrations: 4-inch Pipe, $v_{SL} = 0.03\ m/s$ 111
Figure 3.66: Liquid Holdup for Anionic Surfactant [800 ppm, $v_{SL} = 0.01\ m/s$] vs. Liquid Holdup in Air-Water Flow 112
Figure 3.67: Liquid Holdup for Anionic Surfactant [1200 ppm, $v_{SL} = 0.01\ m/s$] vs. Holdup in Air-water Flow 113
Figure 3.68: Liquid Holdup with Time for Anionic (1000 ppm), Amphoteric I (600 ppm) and Sulphonate (800 ppm) Foamers at $v_{SG} = 4.50\ m/s$ and $v_{SL} = 0.01\ m/s$ 114
Figure 3.69: Liquid Holdup with Time for Anionic (1,000 ppm), Amphoteric I (600 ppm) and Sulphonate (800 ppm) Foamers at $v_{SG} = 4.50\ m/s$ and $v_{SL} = 0.03\ m/s$ 114
Figure 3.70: Fraction of Gas Trapped in Foam: Anionic Surfactant at 1,000 ppm 115
Figure 3.71: Fraction of Gas Trapped in Foam: Amphoteric I Surfactant at 600 ppm 116
Figure 3.72: Fraction of Gas Trapped in Foam: Sulphonate Foamer at 800 ppm 116
Figure 3.73: Fraction of Gas Trapped in Foam: Cationic Surfactant at 1200 ppm 117
Figure 3.74: Fraction of Gas Trapped in Foam: Sulphonate Foamer at 400 and 800 ppm 117
Figure 3.75: Fraction of Gas Trapped in Foam: Cationic Surfactant at 1,200 and 2,400 ppm 118
Figure 3.76: Fraction of Gas Trapped in Foam for Anionic, Amphoteric I, Sulphonate and Cationic Surfactants at Optimum Concentration in 2 and 4-inch Pipes 119
Figure 3.77: Foam Holdup: Anionic Surfactant at 1000 ppm ($v_{SL} = 0.01\ and\ 0.03\ m/s$) 120
Figure 3.78: Foam Holdup: Amphoteric I at 800 ppm ($v_{SL} = 0.01\ and\ 0.03\ m/s$) 120

Figure 3.79: Foam Holdup: Sulphonate Foamer at 800 ppm ($v_{SL} = 0.01\ and\ 0.03\ m/s$) 121
Figure 3.80: Foam Holdup in Anionic, Amphoteric I and Sulphonate Foamers in 2 and 4-inch Pipes ($v_{SL} = 0.01\ and\ 0.03\ m/s$) 122
Figure 3.81: Pressure Gradient and Residual Pressure Gradient: Anionic Surfactant, 1600 ppm, 2-inch Pipe, $v_{SL} = 0.01\ m/s$ 123
Figure 3.82: Pressure Gradient and Residual Pressure Gradient: Anionic Surfactant, 1600 ppm, 2-inch Pipe, $v_{SL} = 0.03\ m/s$ 124
Figure 3.83: Pressure Gradient and Residual Pressure Gradient: Anionic Surfactant, 1600 ppm, 4-inch Pipe, $v_{SL} = 0.01\ m/s$ 124
Figure 3.84: Pressure Gradient and Residual Pressure Gradient: Anionic Surfactant, 1600 ppm, 4-inch Pipe, $v_{SL} = 0.03\ m/s$ 125
Figure 3.85: Average Critical Velocity Anionic Surfactant in 2 and 4-inch Pipes 126
Figure 3.86: Average Critical Velocity Amphoteric I Surfactant in 2 and 4-inch Pipes 126
Figure 3.87: Average Critical Velocity Amphoteric II Surfactant in 2 and 4-inch Pipes 127
Figure 3.88: Average Critical Velocity Sulphonate Foamer in 2 and 4-inch Pipes 127
Figure 3.89: Average Critical Velocity Cationic Surfactant in 2 and 4-inch Pipes 128
Figure 3.90: Schematic of Air-Water-Foam Flow Structure in Annular Flow 129
Figure 3.91: Percent Mass of Liquid Unloaded with Time (Anionic Surfactant) 136
Figure 3.92: Percent Mass of Liquid Unloaded with Time (Amphoteric I Surfactant) 137
Figure 3.93: Anionic Surfactant, 2-inch pipe, $v_{Sl} = 0.01\ m/s$: Decrease in Liquid Holdup with Increase in Surfactant Concentration 138
Figure 3.94: Volumetric Rate of Liquid Removal (Amphoteric I at 600 ppm) 139
Figure 3.95: Unloading Potential at 4.1 mm/s 140
Figure 3.96: Unloading Potential at 6.2 mm/s 140
Figure 3.97: Predicted Versus Measured Liquid Holdup for Four Surfactants at Unloading Test at 4.1 mm/s (No Cationic) 142
Figure 3.98: Predicted versus Measured Liquid Holdup for Four Surfactants at Unloading Test at 6.2 mm/s (No Cationic) 143
Figure 3.99: Foam Holdup versus Superficial Gas Velocity (No Cationic) 144
Figure 3.100: Foam Holdup versus Liquid Holdup (No Cationic) 145
Figure 3.101: Predicted Foam Holdup versus Experimental Foam Holdup 146
Figure 3.102: Fraction of Gas Trapped in Foam 147
Figure 3.103: Predicted versus Measured Fraction of Gas Trapped in Foam 148
Figure 3.104: Interfacial Friction Factor versus Superficial Gas Reynolds Number 149
Figure 3.105: Predicted Interfacial Friction Factor (Equation 3.36) versus Interfacial Friction Factor Calculated from Experiment 150
Figure 3.106: Predicted Interfacial Friction Factor (Equation 3.32) versus Interfacial Friction Factor Calculated from Experiment 150
Figure 3.107: Transition Boundary Plot: Anionic Surfactant, 800 ppm, 2-inch Pipe, $v_{Sl} = 0.01\ m/s$ and $v_{Sg} = 4.39\ m/s$ 151

Figure 3.108: Transition Boundary Plot: Anionic Surfactant, 800 ppm, 4-inch Pipe, $v_{Sl} = 0.01\ m/s$ and $v_{Sg} = 23.65\ m/s$ 152
Figure 3.109: Predicted versus Observed Critical Velocity Obtained using the Interfacial Friction Factor Given by Equation (3.36) 154
Figure 3.110: Predicted versus Observed Critical Velocity Obtained using the Interfacial Friction Factor Given by Equation (3.32) 154
Figure 3.111: Predicted versus Observed Pressure Gradient Obtained using the Interfacial Friction Factor Given by Equation (3.36) 155
Figure 3.112: Predicted versus Observed Pressure Gradient Obtained using the Interfacial Friction Factor Given by Equation (3.37) 156
Figure 3.113: Pressure Gradient for Sulphonate Foamer [v_{SL}= 0.01 m/s, 2-in pipe] 157
Figure 3.114: Liquid Holdup for Sulphonate Foamer [v_{SL}= 0.01 m/s, 2-in pipe] 157
Figure 3.115: Rate of Liquid Transport (For Unloading Tests Conducted at 4.1 mm/s) 158
Figure 3.116: Predicted Pressure Gradient (Gray Correlation (1978)) versus Observed Pressure Gradient 159

List of Tables

Table 2.1: Prediction Results of Turner's Data 38
Table 2.2: Prediction Results of Coleman's Data 41
Table 2.3: Prediction Results of Veeken's Data 44
Table 2.4: Prediction Results of Chevron Data 46
Table 2.5: Prediction Results of ConocoPhillips Data 49
Table 3.1: Surfactants Studied in this Investigation 53
Table 3.2: Test Matrix for Stability Test at Room Temperature in Deionized Water 64
Table 3.3: Test Matrix for Stability Tests at Room and High Temperatures in Brine I and II 64
Table 3.4: Test Matrix for Unloading Test at Room Temperature in Deionized Water 65
Table 3.5: Test Matrix for Unloading Test at Room Temperature in Brine Solution. 65
Table 3.6: Test Matrix for Large Scale Test 65
Table 3.7: Optimum Concentration from Parameters used in Bench Top Tests 86
Table 3.8: Constants in Gas Void Fraction (Equation 3.38) 141
Table 3.9: Constants in Correlations for Predicting Interfacial Friction Factor 149
Table A.1: Turner's Field Data and Calculation Results 169
Table A.2: Coleman's Field Data and Calculation Results 171
Table A.3: Veeken's Field Data and Calculation Results 173
Table A.4: Chevron Data and Calculation Results 175
Table A.5: ConocoPhillips Data and Calculation Results 177

EXECUTIVE SUMMARY

When natural gas is produced from gas wells, it always is accompanied by liquid. At the later stages of a well's life, the gas is unable to carry liquid to the surface, resulting in liquid accumulation at the bottom of the well; this is called "Liquid Loading". Knowing when the liquid loading will occur is important for developing appropriate solutions to prevent it. The most popular method in the literature for determining the onset of liquid loading is the equation developed by Turner et al. This equation is a droplet model and is based on terminal velocity of liquid droplet in single phase gas column. Recently, Veeken et al. have shown that, in many inclined, as well as in some of the vertical wells, Turner's equation under-predicts the true critical flow rate (the flow rate at which liquid loading starts). This may be due to the angle of inclination as well as the fact that inception of liquid loading is more likely due to liquid film reversal in annular flow rather than droplet fall back.

In this work, we propose a new liquid loading model that is based on liquid film reversal. We improve Barnea's model for better prediction of liquid loading. The improvements include: (i) development of a variable film thickness model to account for inclination of the well; (ii) development of equation to account for annular flow; and (iii) improvement in friction factor equation at the interface between the liquid film and the gas core. We validated our model against all of the available literature data, as well as additional data collected from various operators. The results show significant improvement over original Turner's method as well as various ad hoc modifications made to that equation.

Foam lift is one of the most cost effective methodologies for unloading gas wells. The surfactants are either injected intermittently or continuously to lift the liquid to the surface. By reducing the gravitational gradient and increasing the frictional gradient, the critical gas velocity at which liquid loading occurs is shifted to the left. Although foam lift is a popular technique, currently we do not have a methodology to predict the pressure drop under foam flow conditions. When foam lift is installed, the operator is interested in correctly predicting the critical velocity at the transition boundary of annular and intermittent flow. Furthermore, the operator also needs to predict the pressure drop for foam flow as a function of the type of surfactant as well as the surfactant concentration.

To address the calculation of critical velocity and pressure drop under foam flow conditions, we measured several foam flow characteristics in both small scale and large scale facilities. The small-scale facility involved measurement of foam carryover capacity as a function of time and surfactant concentration. The large-scale facility involved measurement of liquid holdup, pressure drop, fraction of gas trapped in foam, and foam holdup in 40-foot 2-inch and 4-inch tubing. The small-scale data are easy to collect and follow standard procedures used by service companies in the oil industry. By using the data collected in the small-scale facility, we are able to develop pressure drop correlations in the large-scale facility.

Specifically, we developed correlations for liquid holdup, foam holdup, fraction of gas trapped in the foam, and interfacial friction factor by combining the small-scale data with the large-scale experiments. These correlations are applicable to four different surfactants tested. A new transition criterion was developed and successfully used to predict onset of liquid loading under foam flow. We observed mostly annular flow for foam flow in vertical pipe with liquid film replaced by foam film.

Using a force balance over the gas core in annular flow, we developed a new procedure to calculate the pressure drop under foam flow conditions. We compared our model results with actual measurements in the large-scale facility. Our model was reasonably able to predict the pressure drop within ±30%. The reason for such a large variance is that the small-scale facility was not able to capture all the characteristics of the foam that were observed in the large-scale facility. It is very difficult to reproduce the foam characteristics exactly in two different experiments. The developed correlation is the only correlation that is currently available to calculate the pressure drop under the foam flow conditions using the small-scale data. It is superior to conventional annular flow pressure drop prediction models that are currently available in the literature.

REPORT DETAILS

This report is divided into several sections. In the first section, we provide broad literature review of what has been done in the past regarding both liquid loading in gas wells as well as the mitigation strategies used to prevent liquid loading.

Literature Review

Liquid Loading

To understand liquid loading in a gas well, we can first look at the flow behavior of liquid and gas two-phase flow. Throughout the production life of a gas well, several flow patterns will present in the wellbore, as shown in Figure 1.1. At the beginning of production with a high gas rate, liquid and gas produce together under annular flow, where liquid is transported as entrained liquid droplets and as the liquid film flowing around the pipe, and gas is moving in the center core. As more water and condensate accumulates in the system and the gas rate is reduced, annular flow configuration will become unstable and the flow pattern in the wellbore will change to slug flow or churn flow. Slug flow consists of successive Taylor bubbles and liquid slugs and churn flow can be treated as the transition region between annular flow and slug flow. As the gas rate decreases further, the gas phase is dispersed into small bubbles in continuous liquid phase, which is called bubble flow. Bubble flow is not normally seen in gas wells but is observed in foam flow. To predict the inception of liquid loading is basically to predict the critical gas rate when the annular flow structure becomes unstable.

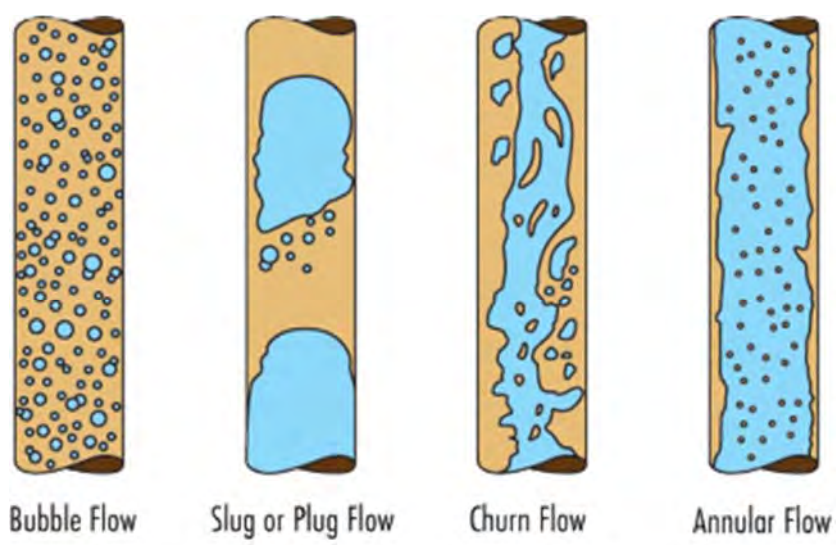

Figure 1.1: Flow Patterns of Two-Phase Flow in Vertical Pipe

When liquid loading starts, the gas production rate drops very quickly, then the gas well will present the repeated transition between stable and unstable flow.

Figure 1.2 shows an example of a gas well after onset of liquid loading (Van't Westende et al., 2007), where gas rate is plotted in green, wellhead pressure in blue, wellhead temperature in red, and critical gas rate, Q_{min}, is noted in a purple horizontal line. Notice that the gas rate quickly decreases at inception of liquid loading and drops to zero for a certain period of time, then the gas well produces again with accelerated decline gas rate. The length of the production cycle can vary from hours to weeks. Wellhead pressure and temperature also respond to liquid loading. When liquid loading occurs, wellhead pressure increases and wellhead temperature decreases. Thus, we can use this method to identify inception of liquid loading, if sufficient data is available for gas wells.

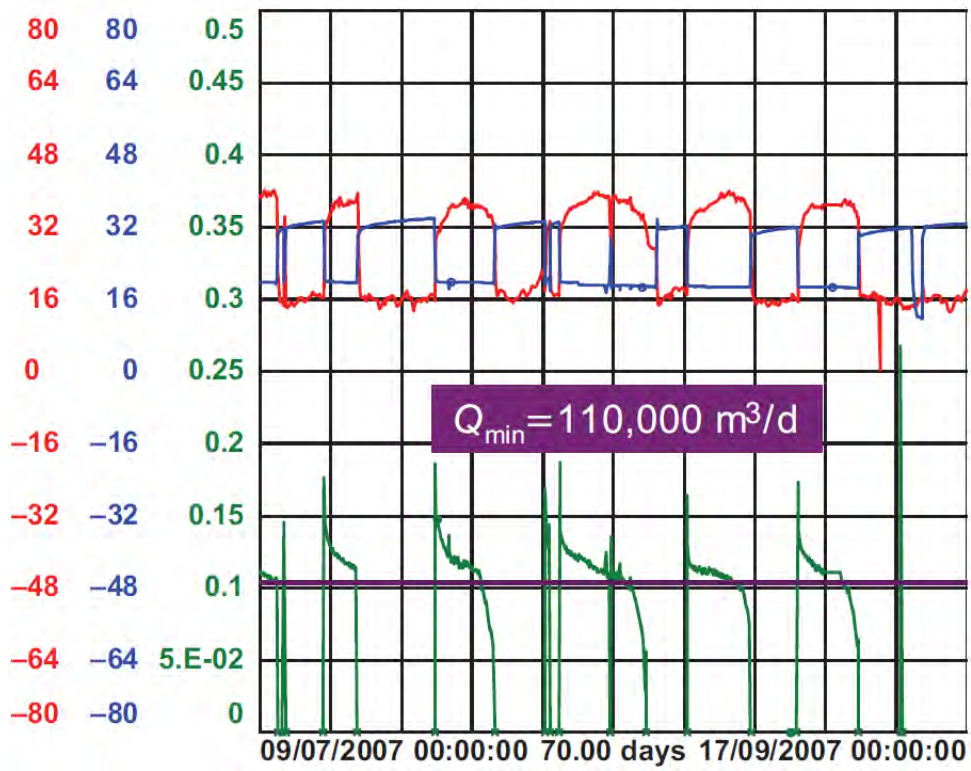

Figure 1.2: Liquid Loading Example

Liquid loading occurs due to decreasing gas velocity, which leads to instability of annular flow. Thus, transition between annular flow and slug flow can be considered as the inception liquid loading. Many papers are published to predict the inception of liquid loading (Chupin et al., 2007; Dousi et al., 2006; Duggan, 1961; Guo et al., 2000). In this section, several models that predict liquid loading will be reviewed. In general, there are two mechanisms describing the cause of liquid loading, liquid droplet reversal, and liquid film reversal. The droplet reversal model suggests that liquid loading is caused by liquid droplet fall back in the gas column. Turner's equation (Turner et al., 1969) is a droplet model. This model is based on the analysis of droplet transportation by gas flow. The inception of liquid loading is related to the minimum gas velocity to lift the largest liquid droplet in the gas core. Other modifications have been proposed to this equation to improve the prediction

using this equation. Coleman et al. (1991a; 1991b) tested Turner's equation with their low pressure well data and claimed that the 20% upward adjustment recommended by Turner is unnecessary. Recently, Veeken et al. (2010) and Waltrich et al. (2011) have shown that in many inclined, as well as some of the vertical wells, Turner's equation is too optimistic. Belfroid et al. (2008) have proposed a model that accounts for the influence of inclination. They observed that maximum critical gas velocity (the velocity at which liquid loading starts) occurs at medium range of inclination angle (around 30 degrees from vertical direction). Unlike Turner et al. and Coleman et al., film reversal models predict the inception of liquid loading by analyzing liquid film instability. The Zhang et al. model (2003a, 2003b) and Barnea's model (1986a, 1986b), which are both film models, will be discussed in this section. In general, film models predict more conservative (or higher) critical gas velocity than droplet models. In this report, we will demonstrate that the film model is more accurate in predicting liquid loading than the droplet model.

In annular flow, some of the liquid is transported as droplets. In order to lift liquid in a gas well, gas is required to provide sufficient energy to sustain all liquid droplets to travel upwards or in suspension. The droplet is treated as a free-falling particle with only two forces acting on it - drag force (F_D) in flowing direction and gravitational force (F_G). These two forces can be calculated with Equations (1.1) and (1.2).

$$F_D = C_D \frac{\pi d^2}{4} \frac{\rho_G v_G^2}{2}, \tag{1.1}$$

$$F_G = (\rho_L - \rho_G) \frac{4}{3} \pi \left(\frac{d}{2}\right)^3 g, \tag{1.2}$$

where C_D is the drag coefficient and d is the droplet diameter.

When the gas rate is sufficiently high, F_D is bigger than F_G and liquid droplet will move upward. As gas rate drops to the point that F_D equals F_G, the droplet reaches terminal velocity and suspends in the gas stream. We can calculate this terminal velocity with this equation:

$$v_{G,T} = 3.617 \left[\frac{d\,(\rho_L - \rho_G)}{C_D\,\rho_G}\right]^{0.5}. \tag{1.3}$$

According to Equation (1.3), terminal velocity is a function of droplet diameter d. The size of the droplet is controlled by force trying to shatter the droplet and force trying to hold the drop together. This force balance can be described by the Weber number, which is the ratio of kinetic energy to surface tension. The Weber number is defined as

$$W_e = \frac{\rho_G v_G^2 d}{\sigma}. \tag{1.4}$$

Tuner suggested that the Weber number ranges from 20 to 30 at critical condition and the largest droplet diameter can be found when the Weber number equals 30. It is known that drag coefficient C_D for a sphere object is 0.44. With these conditions, the terminal velocity can be calculated as

$$v_{G,T} = 5.465 \left[\frac{\sigma\,(\rho_L - \rho_G)}{\rho_G^2}\right]^{0.25}. \tag{1.5}$$

In order to match the field data, Turner adjusted this model by increasing the terminal velocity by 20 %. He claimed the reason for this adjustment is critical. The Weber number used here is established in an air-water experiment and not for gas well conditions. Thus, Turner uses Equation (1.6) to calculate the critical gas velocity:

$$v_{G,T} = 6.558 \left[\frac{\sigma\,(\rho_L - \rho_G)}{\rho_G^2}\right]^{0.25}. \tag{1.6}$$

It should be noted that, in addition to examining the liquid droplet theory, Turner also examined the liquid film reversal theory. However, he found that the calculated gas flow rates are too high to match the field data and results depend on GLR (gas/liquid ratio), which is contradictory to field observation; hence, he rejected the liquid film reversal approach (Turner et al., 1969).

Later, Coleman et al. (1991a, 1991b) examined Turner's equation with low wellhead pressure data. They concluded that the original Turner's derivation (without 20% upward adjustment) matches better with Coleman's data. Coleman et al. suggested, instead, using Equation (1.5) to predict critical gas velocity. Veeken et al. (2010) compared prediction results from Turner's equation to their offshore data. He proposed a Turner ratio, which is the ratio of observed critical rate to Turner's critical rate, to examine the validity of the model. This ratio is always between 1.0 and 2.0, which suggests Turner's method underestimates the critical velocity. He also believed liquid loading occurs due to liquid film reversal instead of droplet reversal.

When using the Turner et al. equation, we need to know the correct gas density for the calculation. The gas density can vary significantly from surface to the bottom hole conditions. Turner et al. recommend using only surface conditions to predict critical velocity. However, this assumption can cause some errors in unloading calculations (Sutton et al., 2010). If data is available at bottom hole, it is reasonable to use Turner's method by plotting the critical velocity profile along the wellbore and comparing with actual gas velocity. Figure is an illustration of the plot. It is possible that the gas velocity is sufficiently high near surface area, but lower than critical velocity at the bottom hole, especially for low surface pressure wells. In this case, gas well is liquid loading at bottom but cannot be predicted by Turner's

method with surface condition, as shown in Figure 1.3. In addition, it should be remembered that, even though the well may be producing both condensate and water, only water properties should be used to calculate the critical velocity (Chupin et al., 2007). This is because all gas wells produce water vapor from the reservoir that will condense in tubing as pressure and temperature decrease from the bottom hole to the surface. Also, water is heavier than condensate.

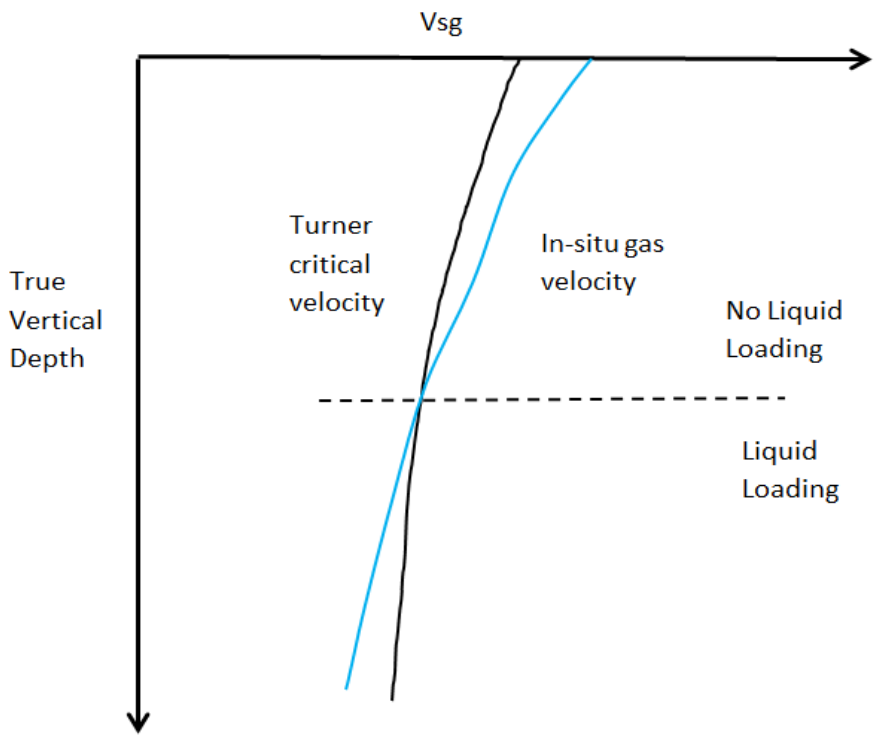

Figure 1.3: In-situ Gas Velocity vs. Turner Critical Velocity

Several subsequent papers have shown that the droplet model may be inappropriate to predict liquid loading. Westende et al. (2007) carried out upward annular air-water experiments to study the droplet behavior. Their data showed the droplet size used in Turner's paper is too large and it is unrealistic under gas well conditions. The Weber number used in Turner's equation should be much smaller than 30. They also found only 0.4% of droplets have an axial velocity close to zero when transition of churn-annular flow occurs (Westende, 2008). This data suggests that droplet reversal may not be the reason of liquid loading.

Turner's equation is developed from an individual droplet, thus inclination angle will not affect the critical gas velocity. Belfroid et al. (2008) showed the experimental results that indicate inclination angle have big impact on liquid loading. For inclined wells, a maximum critical velocity is observed and is around a 30 degree deviation from the vertical position. An inclination angle corrected model based on Turner's equation was also proposed to match the experimental data. Recently, Yuan (2011) carried out the experiments on liquid loading at 0, 15, 30 inclination angles. His results also show significant influence of inclination angle on

the liquid loading. This influence of inclination angle can be obtained by a film model if a non-uniform thickness film is considered, which is included in our modified Barnea's model.

In addition, the critical velocity calculated by the Turner equation does not depend on pipe diameter. Subsequent experimental observations showed that the inception of liquid loading could be influenced by the diameter of the pipe (Chupin et al., 2007). Due to these limitations of Turner's equation, film models are much better equipped to predict liquid loading.

Slug flow can be related to all other flow patterns and is always surrounded by all other flow patterns in the flow pattern map. The Zhang et al. (2003a, 2003b) unified model is developed based on slug dynamics and uses slug flow as the starting point. They constructed the momentum and continuity equations for slug flow by considering the entire liquid film region as the control volume, as in Figure 1.4.

$$\frac{\rho_L(v_T-v_F)(v_S-v_F)-\rho_C(v_T-v_C)(v_S-v_C)}{l_F} - \frac{\tau_F S_F}{H_{LF}A} + \frac{\tau_C S_C}{(1-H_{LF})A} + \tau_I S_I\left(\frac{1}{H_{LF}A} + \frac{1}{(1-H_{LF})A}\right) - (\rho_L - \rho_C) g \sin\theta = 0\,. \tag{1.7}$$

The first term on *LHS* in Equation (1.7) is momentum exchange between slug body and film zone. The next three terms are shear stresses corresponding to the forces acting on film and pipe wall interface, gas and pipe wall interface, and film and gas interface. When transition from slug to annular flow happens, liquid film length (l_F) becomes infinitely long and, thus, the momentum exchange terms are removed. In addition, the shear stress term between the pipe wall and gas pocket will be eliminated in the momentum equation. With continuity equations and proper closure relationships, like interfacial friction factor and liquid entrainment in the gas core, the critical velocity from slug flow to annular flow can be calculated.

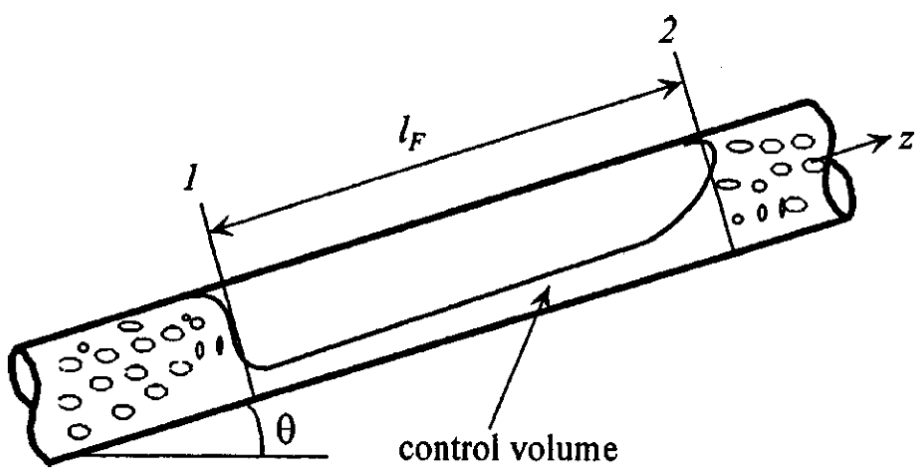

Figure 1.4: Control Volume in the Zhang et al. Model

Barnea's (1986a, 1986b) model is the other film model we investigated in this study. There are two mechanisms that trigger the transition from annular to slug flow. The first mechanism is the instability of the liquid film causing reverse flow near the pipe wall. The second mechanism is the gas core spontaneous blockage due to a large amount of liquid supply. However, the liquid rate in the gas well is relatively low and most of gas wells' liquid accumulation occurs due to liquid film instability, so we only need to use the first mechanism to predict liquid loading. Different from the Zhang et al. model, Barnea constructs force balance for annular flow and predicts the transition from annular to slug flow by analyzing interfacial shear stress change in the liquid film. In annular flow, gas flows in the center core and liquid flows as liquid film along the inner pipe wall, as shown in Figure 1.5. The velocity profile in liquid film has a parabola shape and is directed upwards. Two assumptions are made by Barnea to simplify the model: 1) no liquid droplet exists in the gas core and 2) liquid film thickness is always constant regardless of the inclination angle. Uniform film thickness is not reasonable for inclined wells, which will be improved in the new model to be discussed later. Results show that film thickness makes a big difference in liquid loading for inclined wells.

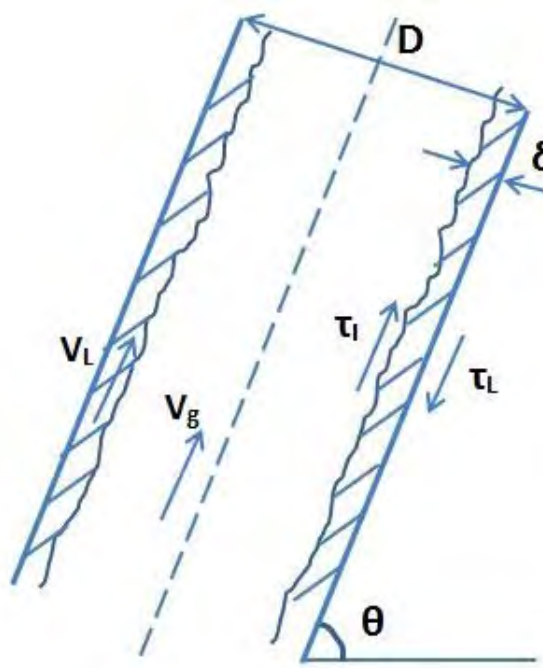

Figure 1.5: Schematic of Liquid-Gas Two Phase Annular Flow in Wellbore

The combined momentum balance equation for annular flow is shown as

$$\tau_I S_I \left(\frac{1}{A_L} + \frac{1}{A_G}\right) - \tau_L \frac{S_L}{A_L} - (\rho_L - \rho_G) g \sin\theta = 0 \,. \tag{1.8}$$

As gas velocity decreases, interfacial shear stress between gas and liquid film also decreases. When the direction of the velocity profile in the liquid film changes, liquid starts to fall back and accumulates at the bottom of the well. The film thickness at the transition point can be obtained when the interfacial shear stress

reaches minimum value. Then, the critical velocity can be calculated by solving the momentum equation and Wallis (1969) interfacial friction factor correlation, which can be seen in Equations (1.9) and (1.10)

$$\tau_I = \frac{1}{2} f_I \rho_G \frac{v_{SG}^2}{(1-2\tilde{\delta})^4}, \tag{1.9}$$

where

$$f_I = f_G \left(1 + 300\frac{\delta}{D}\right). \tag{1.10}$$

Transition boundaries from different models are plotted in a flow patter map, as shown in Figure 1.6. The boundaries are generated for liquid-gas flow in a vertical well with 0.762 m tubing size. Generally speaking, Turner's boundary has the smallest critical velocity and Barnea's model has the most conservative results, while the Zhang et al. boundary is somewhere in between. The difference in the predicted critical velocity is large between droplet and film models. Barnea's critical velocity can be twice that of Turner's results.

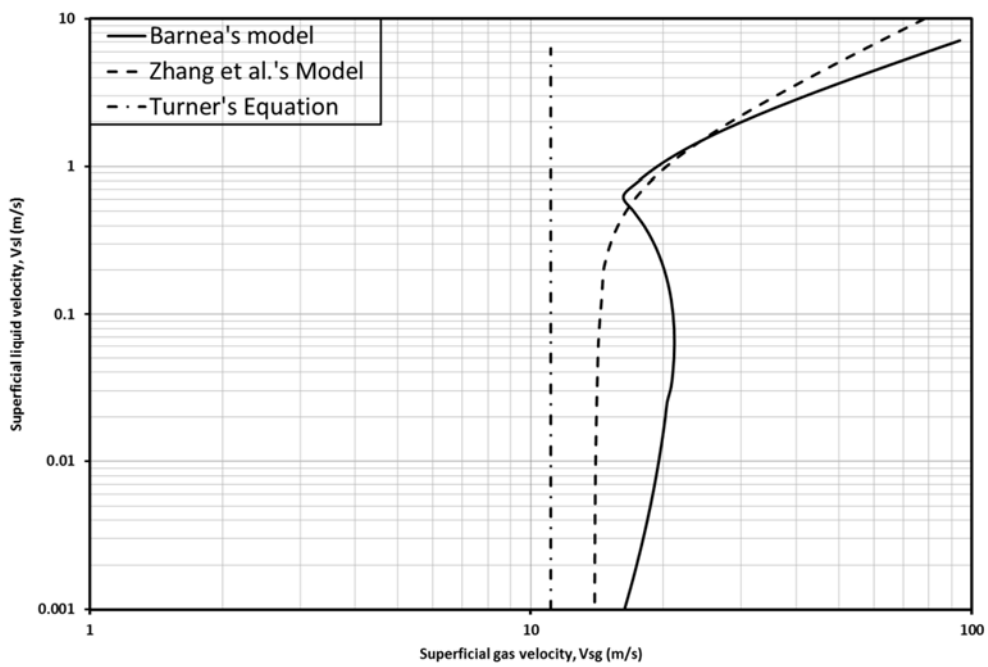

Figure 1.6: Transition Boundary of Different Models

In our work, we have reconciled the difference between the various models by understanding the field data and comparing the results of the field data with model predictions. Using the field data as guidance, we have proposed a new approach for predicting the liquid loading.

Foam Flow and Liquid Loading

One of the most successful strategies to remove liquid (unloading) is to introduce surfactant in the well. Surfactants are usually organic compounds that are amphiphilic, meaning they contain both hydrophobic groups (their tails) and hydrophilic groups (their heads). Therefore, a surfactant molecule contains a water insoluble (or oil soluble component) and a water soluble component. Surfactant molecules will migrate to the water surface, where the insoluble hydrophobic group may extend out of the bulk water phase, either into the air or, if water is mixed with oil, into the oil phase, while the water soluble head group remains in the water phase. This alignment and aggregation of surfactant molecules at the surface, acts to alter the surface properties of water at the water/air or water/oil interface (Wikipedia, 2014).

The advantages of using surfactants are as follows:

- Cost effectiveness (low set-up and operating cost)
- Versatility for different completions and environments
- Can be used to boost mechanical artificial lift methods
- Tolerance of particulates, pressure and high temperature
- Rapid response from wells
- Automated continuous programs
- Customized surfactant combination products can control downhole corrosion, scale or paraffin problems (Heuvei and Adelizzi, 2013).

When surfactants are applied to gas wells, they act as surface active agents that reduce the surface tension of liquid by adsorbing at the liquid-gas interface. They also reduce the interfacial tension between oil and water by adsorbing at the liquid-liquid interface. Many surfactants can also assemble in the bulk solution into aggregates. Examples of such aggregates are vesicles and micelles. Surface tension falls with surfactants addition until the surfactant molecules begin to form micelles in bulk solution. The concentration at which surfactants begin to form micelles is known as the critical micelle concentration (CMC).

The reduction in surface or interfacial tension allows for gas dispersion rate to increase, hence forming a foam structure. Foam assisted lift can be accomplished by dropping soap sticks or by injecting surfactant in the well through capillary strings. Surfactants migrate to the interface where their hydrophilic and hydrophobic portions change the surface characteristics. The foam created consists of small gas bubbles surrounded by thin lamella within which water and condensate are held as shown in Figure 1.7.

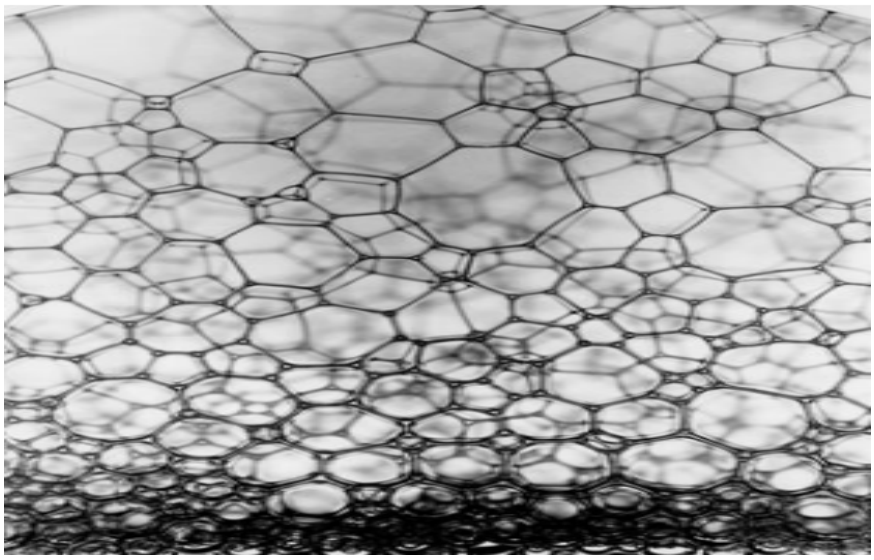

Figure 1.7: Gas Dispersion within Lamella of Surfactant

The swarm of gas bubbles increases gas holdup, and the gravitational gradient is reduced. The gas slippage under air-water foam flow is lower compared to air-water flow, which causes the gas to be produced with the liquid in the lamella; hence foam postpones the transition from annular to slug flow.

Surfactants are classified according to their polar head group. These are as shown in Figure 1.8.

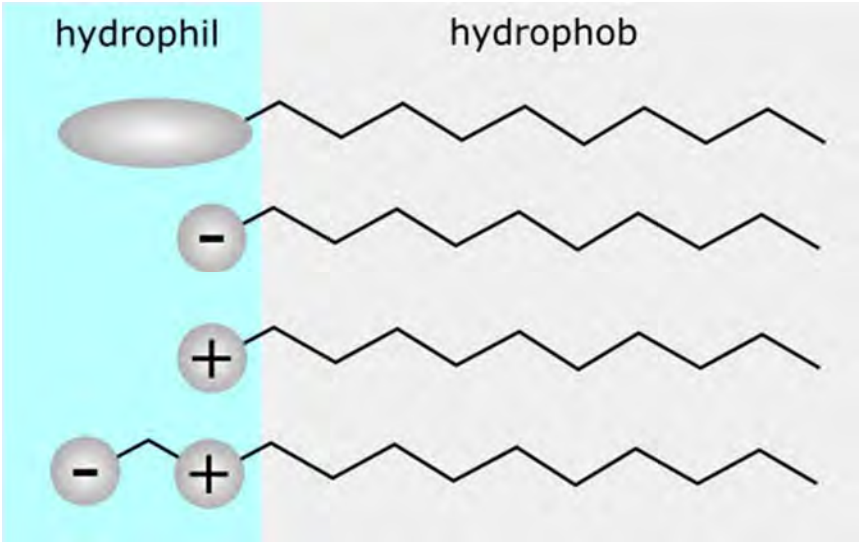

Figure 1.8: Surfactant classification according to the composition of their head: non-ionic, anionic, cationic and amphoteric (Van Nimwegasn et al., 2013)

As shown in Figure 1.8, a non-ionic surfactant has no charge in its head. The head of ionic surfactants carries a net charge: if the charge is negative, the surfactant is called anionic and if the charge is positive, it is called cationic. If a surfactant

contains a head with two oppositely charged groups, it is termed amphoteric/zwitterionic (Van Nimwegasn et al., 2013).

For proper selection of products, different laboratory tests are often conducted on surfactants to determine their foaming characteristics and unloading potential at different surfactant concentrations, temperatures, water composition and water/hydrocarbon ratios (Heuvei and Adelizzi, 2013; Schinagl et al., 2007; Solesa and Sevic, 2006; Willis et al., 2008; Xu and Yang, 1995; Yang et al., 2007). These laboratory tests include surface tension tests (static or dynamic), stability test and unloading rig test. Parameters determined from these tests include reduced surface tension due to surfactant in solution, maximum foam height/foam volume, half-life, drainage of liquid, and volume of liquid unloaded with time. The best surfactant for a particular application is selected based on a combination of aforementioned parameters from the laboratory tests.

Several papers have been published in the literature to evaluate the performance of foam flow. The focus of these papers is on the usage of foam to unload liquid (water or condensates) from vertical gas wells suffering from liquid loading problems. A review of previous publications shows that foam lift requires a trial-and-error procedure. Uncertainties exist in terms of what type of surfactant is appropriate, what is the right concentration of surfactant, how the surfactant performs in vertical pipes of different diameters and how to sustain stable flow under foam flow. Few works on theoretical understanding of foam flow and the pressure drop under foam flow conditions is reported in the literature. Efforts will be made to summarize these works in the following section.

Siddiqui and Yang (1999) conducted experiments using a non-ionic surfactant at 0.25 to 1 percent by weight in 1-inch inner diameter and 40-foot vertical tubing in a 4-inch casing with and without packers. Their experimental gas rate ranges from 3.10 to 12.41 m/s while liquid flow rate ranges from 0.0035 to 0.01 m/s. Water, air and surfactant solutions are injected at the bottom of the tubing through a foam generator (gravel pack). Two parameters are used to quantify liquid lifting efficiency: 1) liquid holdup and 2) liquid lifting rate for experimental runs with and without packers respectively. These parameters are as expressed as follows:

$$Liquid\ Holdup = \frac{H_{L(Final\ Volume)}}{H_{L(Total\ Pipe\ Volume)}}, \tag{1.11}$$

$$Liquid\ Lifting\ Rate = \frac{(H_1 - H_2)A}{t}, \tag{1.12}$$

where $H_1 and\ H_2$ are the initial and final heights of liquid in the casing respectively. t is the time required for the system to reach steady state and A is the area of the pipe. The authors observed that the liquid lifting efficiency (decrease in liquid holdup and increase in liquid lifting rate) increases as the surfactant concentration

increases up to a certain optimum concentration. Beyond the optimum concentration, the authors did not observe any gain in adding more surfactant. They also reported that liquid lifting efficiency in air-water flow was adversely affected by large diameter pipe.

Liu et al. (2014) investigated liquid holdup reduction and pressure drop reduction caused by application of an anionic surfactant at a 1,000 ppm concentration to air-water flow in a 1.57 m inner diameter by 5.6 m vertical Plexiglas pipe. Their experimental gas-liquid ratio ranges from 100 to 10,000. Using high-speed video, they observed the following flow regimes: bubbly, slug, churn and annular flows. The authors reported that the maximum liquid holdup reduction caused by surfactant was as high as 88.6% in churn flow regime. Slug flow exhibited a maximum pressure drop reduction of 96.5% when compared with the air-water base case. They concluded that the addition of surfactant does not have a significant effect on transition of two-phase flow pattern. This is in contrast with conclusions and observations of every other author in the literature.

Zhou (2013) conducted an experiment using 100 ppm of an anionic surfactant (Sodium Dodecyl Sulfate (SDS)) in a 2-inch by 10.36 m vertical pipe. The author's experimental gas rate ranges from 0.15 to 10.3 m/s while liquid flowrate ranges from 0.15 to 0.91 m/s. Zhou (2013) characterized the flow pattern behavior of two phase vertical flow to determine the flow pattern transition boundaries with the addition of surfactant. Observed flow patterns did not exhibit annular flow because of the low concentration of surfactant as well as low gas and low liquid velocities in the test range. Hence no drastic change was observed in flow pattern map under air-water two phase flow and air-water-foam flow. In the range tested, the author observed that slug to churn transition boundary in SDS solution was significantly different from those observed in air-water mixture due to the presence of foam.

Bariogu and Davidson (1996) conducted experiments using 0.2 g/l of anionic, cationic and non-ionic surfactants respectively in a 1.7-inch inner diameter by 40-foot vertical pipe. Foam velocity was measured by visually tracking a bubble and timing its travel. The author's experimental gas and foam velocities range from 0.001 to 0.025 m/s. The authors investigated pressure drop and liquid entrainment characteristics of foam. A slip and turbulent flow regimes were observed for low and high gas rates respectively. They reported that the transition between these flow regimes is marked by a step rise in pressure drop and holdup values. This transition was also reported to be surfactant dependent and the authors cautioned that it cannot be simply defined in terms of a Reynolds number.

Christiansen (2006) conducted experiment using 0.05% by weight of a surfactant (Champion Foamatron VDF-127) in a 2-inch inner diameter by 40-foot vertical pipe. The author's experimental gas rate ranges from 58 to 79 m/s while liquid flowrate ranges from 0.013 to 0.036 m/s. The authors observed that

surfactant increased and decreased critical velocity for low and high liquid flowrates respectively.

Saleh and Al-Jamae'y (1997) conducted an experiment using one surfactant with a 1-inch diameter, 40-foot long vertical pipe. They investigated the effect of the surfactant on critical velocity and found that the critical velocity under foam flow decreases by a factor of four when compared to the air-water case. They observed that foam acts as a pressure dampener in the two-phase flow conditions associated with the slug flow regime. Nimwegan et al. (2012; 2013; 2014) investigated the hydrodynamics of air-water foam flow using a 2-inch inner diameter by 40-foot vertical pipe. The authors' experimental gas velocity ranges from 6.4 to 45 m/s, liquid velocity ranges from 0.02 to 0.05 m/s and surfactant concentration ranges from 0 (air-water base case) to 3,000 ppm. These ranges are relevant to liquid loading conditions. Using high speed camera videos, the authors observed that film reversal occurs around a superficial gas velocity of 14.3 m/s for air water flow. In the presence of foam, the transition velocity to churn flow was observed to decrease to less than half of the transition velocity for air-water flow (approximately 7m/s). We observed the film reversal at even lower superficial gas velocities in our foam flow experiments. These authors have not observed this because their lowest gas velocity is 6.4 m/s. They observed that surfactants increase the pressure drop at high gas flow rates and decrease the pressure drop at low gas flowrates. They reported that adding foamers to water will lead to a lower pressure drop at gas velocities below critical velocity. Their results also revealed that both the critical micelle concentration and the equilibrium surface tension are poor predictors of the type and concentration of surfactant required to decrease the pressure drop.

Although widely used in gas fields, as evident from the discussion above, the effect of surfactants on multiphase flow regimes is still a subject of significant uncertainty. In this study, experimental data are collected in a large scale facility (2-inch and 4-inch 40-foot transparent acrylic vertical pipes) for anionic, amphoteric I, amphoteric II, sulphonate and cationic surfactants at superficial liquid velocities of 0.01 and 0.03 m/s and at superficial gas velocities in the range of slug to annular flow regime (1.85 to 25 m/s). The concentrations of surfactants tested in the large scale facility are those adjudged to be at and around the optimum concentration from bench top tests conducted on the five surfactants investigated.

Objectives

As discussed in the previous section, significant research has been done to understand the liquid loading and how to prevent it using foam or surfactants. The proposed research fills some of the gaps discussed in the literature. Specifically, the proposed research addresses the following questions that have yet to be addressed in the literature:

1. The most popular equation for predicting liquid loading is Turner's equation. However, it is based on a liquid droplet model and does not account for either pipe diameter or inclination angle. Is it possible that a better correlation for prediction for liquid loading can be developed based on liquid film reversal model?
2. To test a newly developed model using existing field data in the literature as well as additional data collected from various operators.
3. To conduct a detailed experimental study for foams using both small-scale and large-scale facilities. Small-scale facilities will replicate what is traditionally done for foam flow studies in various labs. The large-scale facilities will replicate what happens in the field. The goal is to relate what we observe in the small-scale facility with what is observed in the large-scale facility.
4. To develop a better understanding of liquid loading under foam flow conditions. To build a model that can predict the liquid loading under foam flow conditions.
5. To evaluate the effect of pipeline diameter on the ability to postpone liquid loading using foam.
6. To collect comprehensive data on foam flow for various types of surfactants as well as wide range of operating conditions.
7. To develop a correlation to predict the pressure drop under foam flow conditions.
8. To test and validate the developed correlations using the field data.

Results and Discussion

This section is divided into several subsections. We discuss the liquid loading and the new proposed model. Following that section, we provide the details of the experimental data collection and the modeling of foam flow.

Liquid Loading

In this section, we will discuss the new correlation we have developed for liquid loading. The newly developed correlation has been widely tested against both the laboratory and the field data and has proven to be superior to the existing correlations. There are several important improvements in the proposed correlation compared to other available correlations. These are:

- The proposed correlation is based on liquid film model rather than droplet model
- The proposed correlation can account for the effect of tubing diameter on the inception of liquid loading
- The proposed correlation uses improved correlation for interfacial friction factor compared to what has been used in the literature.

- The proposed correlation can be applied to both vertical and inclined pipes.

Data Available

In this section, we briefly discuss the data that was available for testing our model. Some of the data were available from the literature; other data were collected from our industrial partners.

Turner reported field data from gas wells producing liquid in his paper and used this data to determine the critical gas velocity (Turner et al., 1969). Some of the data was designed specifically to determine the critical flow rate and other data comes from conventional well test data. The data matrix consists of a total 106 gas wells that are treated as vertical wells since no inclination angle is reported. The method Turner used to examine liquid loading of the gas wells is by looking at the current gas flow rate and liquid loading status. The calculated critical rates from Turner's equation are compared with the observed rates. If the observed rate is higher than the critical rate, liquid should be produced under stable conditions. If the observed rate is inadequate, liquid should accumulate in this well. He then used this prediction and compared with the observed liquid loading status. Among all the gas wells, 37 wells are loaded up, 53 wells are unloaded, and the rest of the wells were reported as questionable.

In Turner's paper, producing depth and wellhead pressure are reported. Wellhead pressures for these wells range from several hundred to several thousand psi. All the wells are flowing either through standard production tubing or the annular area between casing and tubing. The pipe sizes included in the paper range from 1.750 inches for tubing to 8 inches for casing. Tubing ID is reported for tubing producing wells and tubing OD and casing ID are reported for annular flowing wells. For wells producing from the annular region, hydraulic diameter should be used to calculate the critical gas velocity. However, Turner's equation does not depend on pipe diameter, as seen in Equation (1.6), and pipe size will not change the prediction results of Turner's equation.

Liquid produced from these wells contains both water and condensate. In Turner's paper, different equations for water and condensate are provided, and we will evaluate gas wells producing water and condensate separately. When both water and condensate exist in the well, only the water equation will be used. The condensate density varies between 43.8 lb/ft^3 and 51.5 lb/ft^3. Therefore, a constant condensate density is used for calculation. Also, for water density, he used a constant value of 67 lb/ft^3. Surface tension is not determined from a lab test for an individual well. Constant values of 20 dynes/cm for condensate and 60 dynes/cm for water were used in his calculation. Turner also used constant gas gravity (0.6) and gas temperature (120 F) since these parameters showed less impact in calculation than other parameters, like pressure. Average value of z factor (0.9) is used to simplify the calculation.

Turner included his calculation results in the table. The results of both the droplet model and the film model are compared with test flow rate. The droplet model matched better with field data and the film model was discarded. Although a 20% adjustment is recommended in his paper, Turner reported the critical rate without the adjustment for the droplet model. Turner's data and calculation results can be found in Table A.1, Appendix A.

Turner's published data had wellhead pressure above 500 psi. Coleman et al. (1991a; 1991b) focused on the wells experiencing liquid loading with lower reservoir pressure that will have more loading problem with low reservoir energy. All of Coleman's wells have well head flowing pressure below 500 psi, which is much smaller than Turner's data. Fifty-six vertical gas wells are analyzed and all the wells produce through tubing. The tubing size is all the same with a 2.441-inch ID.

For Coleman's data, both water and condensate are produced in gas wells. After comparison, condensed water is the primary source of loading liquid and only water property should be used to evaluate critical gas velocity. Coleman also found that liquid amount (LGR below 22.5 bbl/MMscf) in the gas well has little impact on determine critical rate.

Instead of reporting current gas flow rate like Turner's data, Coleman reported gas flow rate when liquid loading is observed in gas wells. They increased well head pressure stepwise to force the gas well into loading condition. When a typical exponential rate decline is observed, they reported this rate and compared with the prediction results. Coleman suggested not using 20% correction to calculate critical gas velocity instead of Turner's equation for his low pressure wells. This equation is Turner's equation without the empirical adjustment. However, he reported the calculated critical velocity with Turner's adjustment. Coleman's data and calculation results can be found in Table A.2, Appendix A.

Veeken et al. (2010) extracted liquid loading data to improve the prediction of onset of liquid loading. Their field data is from offshore gas wells with larger tubing sizes and their data include some inclined wells. Based on their observations, critical rate exceeds Turner's prediction by an average of 40%.

They reported data from a total of 67 wells that include both vertical and inclined wells. Tubing size ranges from 2 to 6 inches. Gas specific gravity, well head temperature and pressure are also included in the paper. The liquid produced are water and condensate and most of the liquid comes from condensation of water. However, WGR or CGR were not reported in the paper and we assume a constant water rate of 5 STB/MMSCF. We also tried other liquid rates and results show insignificant influence on determining critical gas velocity that is consistent with Turner and Coleman's observations.

Veeken determined the critical gas rate by observing the gas production rate. They reported gas rate when they observed an accelerated decline of gas rate and

constant or decreasing wellhead pressure. An example of choosing the minimum rate is shown in Figure 2.1. Q_{min} (purple line) is critical gas rate, where gas rate starts to decline drastically, and Q_{meta} (red line) is the measured metastable gas rate. Veeken used the Turner ratio ($TR = \frac{Q_{min}}{Q_{Turner}}$) to examine the model and proposed a modified Turner expression to predict liquid loading. Veeken's data and calculation results can be found in Table A.3, Appendix A.

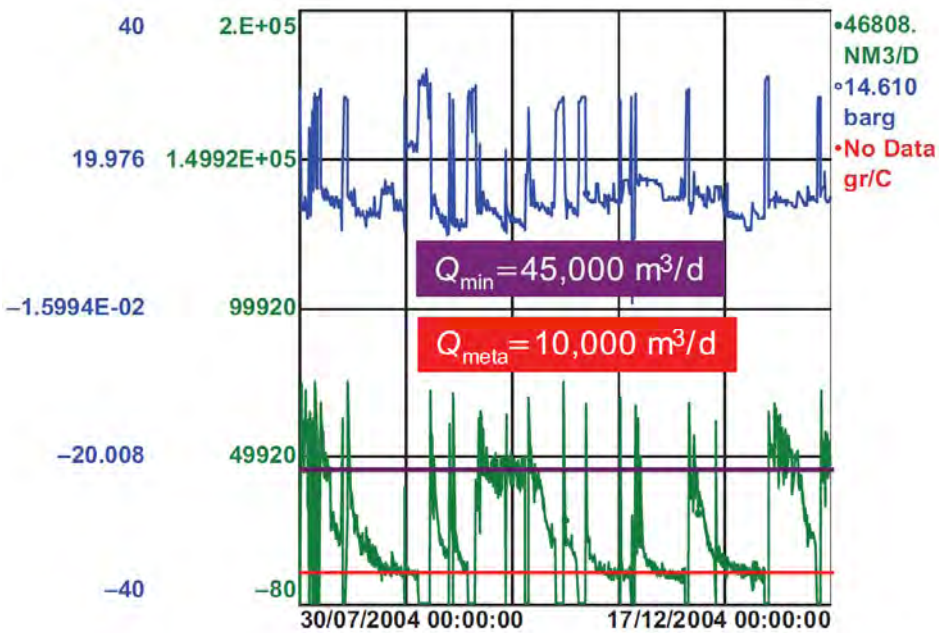

Figure 2.1: Liquid Loading Example by Veekan et al. (2007)

In addition to the field data collected from published papers, we have investigated the field data from other operators with more production details. We gathered gas well data from a Chevron gas field with monthly gas and liquid production rates, wellbore profile, tubing pressure and service history (remarks on when cap string installed). Most of Chevron's wells produce with a small tubing size of 1.995 or 2.441 inches and all data are from vertical wells. Data from a total 308 wells were collected but only 82 wells are used to compare with the models' prediction due to incomplete pressure data. We attempted to determine the inception of liquid loading by observing accelerating decline in gas production and LGR data. However, this decline is hard to detect due to the quality of monthly data. We know that capillary string is installed to solve the liquid loading problem by injecting soap for these wells. Thus we can assume the capillary string is used after liquid loading is detected. Then we find the capillary string installation date in service history and consider this well is loaded up at this time. For example, in Figure 2., the capillary string is installed for this well at the time denoted by the red line. By calculating the average gas and liquid rate at this point, we can compare the observed average gas rates to the prediction results. More details of Chevron data can be seen in Table A.4, Appendix A.

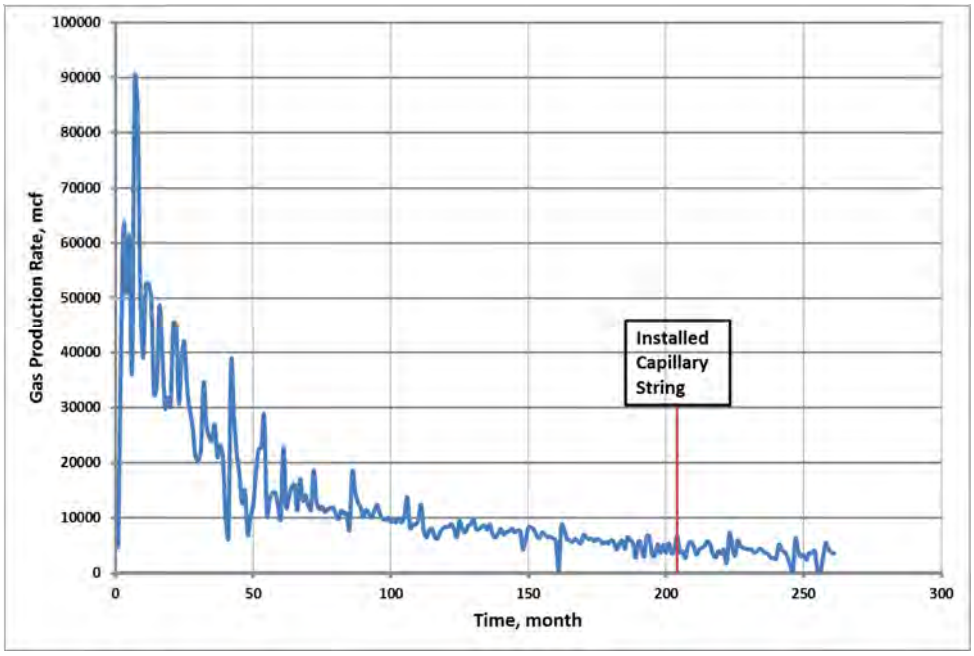

Figure 2.2: Gas Production History

We also collected additional data from ConocoPhillips. We collected data from a total of 62 wells including 7 off-shore Gulf of Mexico wells. Tubing size is 1.995 or 2.441 inch for most of the wells. For these data, minute-by-minute data are available for gas production rate, tubing and casing pressures and temperature, so that we can determine the inception of liquid loading with better accuracy. If liquid loading occurs in a gas well, gas rate has a fast decline and then goes to zero. As pressure builds up, the gas well produces again with a high gas rate spike and follows another accelerating rate decline. This cycle repeats continuously with time span ranging from hours to days. It is known that tubing and casing pressures diverge when liquid loading starts. The rise of liquid level in the tubing causes additional back pressure, which will result in an increase in the casing pressure.

Figure 2. is an example of gas well daily production data, where the blue line is the gas rate, the red line is the casing pressure and the green line is the tubing pressure. This well is producing without liquid accumulation at this point, because the rate is not decreasing and the tubing and casing pressures do not diverge. At a later time, signs of liquid loading have presented in this well, as seen in Figure 2.. We can see that the gas rate has more fluctuations and decline much faster. More importantly, tubing and casing pressures show a clear divergence, which is denoted by a vertical line. We pick the gas rate at this time as observed gas rate with liquid loading, which is around 400 MCFD, and compare it with model predictions. For ConocoPhillips data, we identify some gas wells under stable flow, with production data similar to Figure 2.. Out of all the wells, 49 wells are operating under loading conditions and 13 wells are producing under stable conditions. A complete list of ConocoPhillips data can be found in Table A.5, Appendix A.

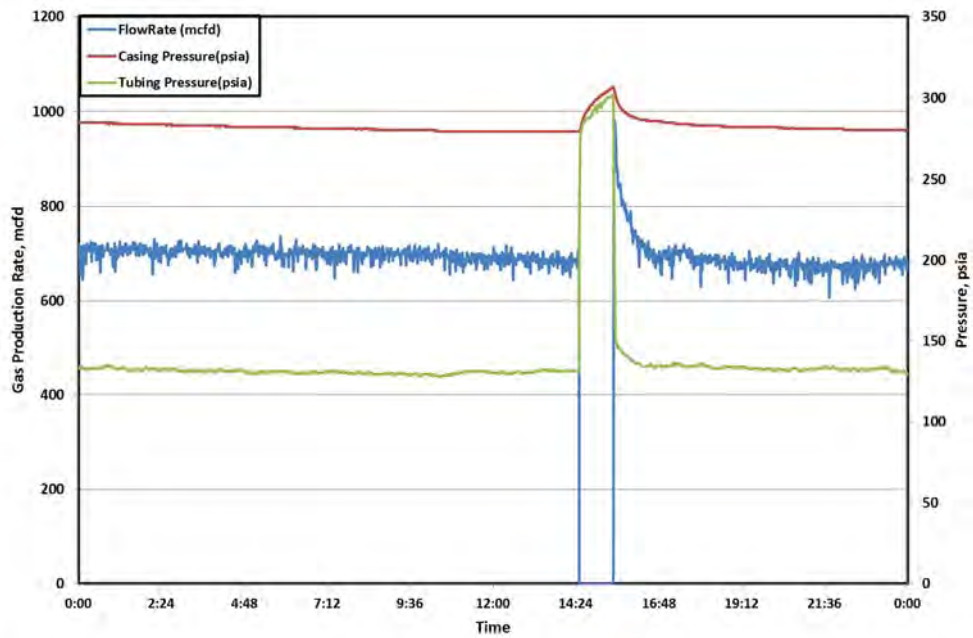

Figure 2.3: Gas Well Without Liquid Loading at Early Time

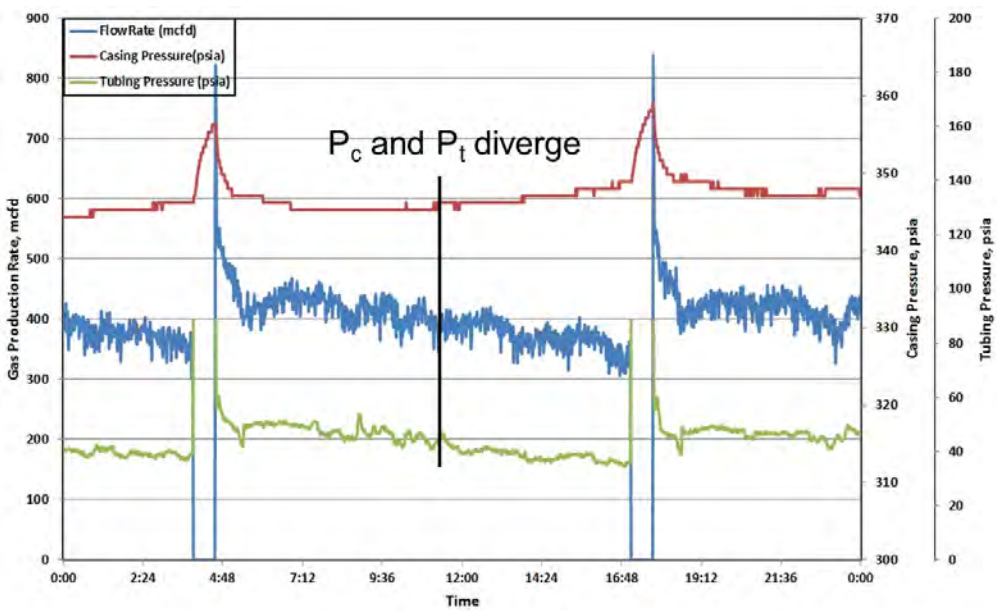

Figure 2.4: Gas Well Under Liquid Loading At Later Time

Proposed Model

As already mentioned, we used the film reversal model for predicting liquid loading. Before we go into details about our model, it is important to understand the rationale for selecting the liquid film model for predicting liquid loading.

There are a few ways to define the liquid loading. The traditional definition is that the liquid loading starts when the minimum pressure drop in the tubing is

reached. As the gas flow rate increases, the gravitational pressure gradient with respect to gas velocity decreases and the frictional pressure gradient with respect to gas velocity increases. At low gas velocity, the gravitational pressure gradient decreases faster than the increase of the frictional pressure gradient, which makes the total pressure gradient decrease. When the decrease in gravitational gradient and the increase in frictional pressure gradient are equal, the minimum total pressure gradient occurs, and the minimum point occurs on the pressure drop in the tubing. Figure shows an example of changes in gravitational and frictional pressure gradients with respect to gas velocity for 2-inch pipe air-water flow. The change in gravitational pressure gradient (plotted by the blue line) is negative and the change in frictional pressure gradient (plotted by the green line) is positive. When the absolute values of the two are equal to each other (at about 20 m/s), the overall pressure drop will reach a minimum.

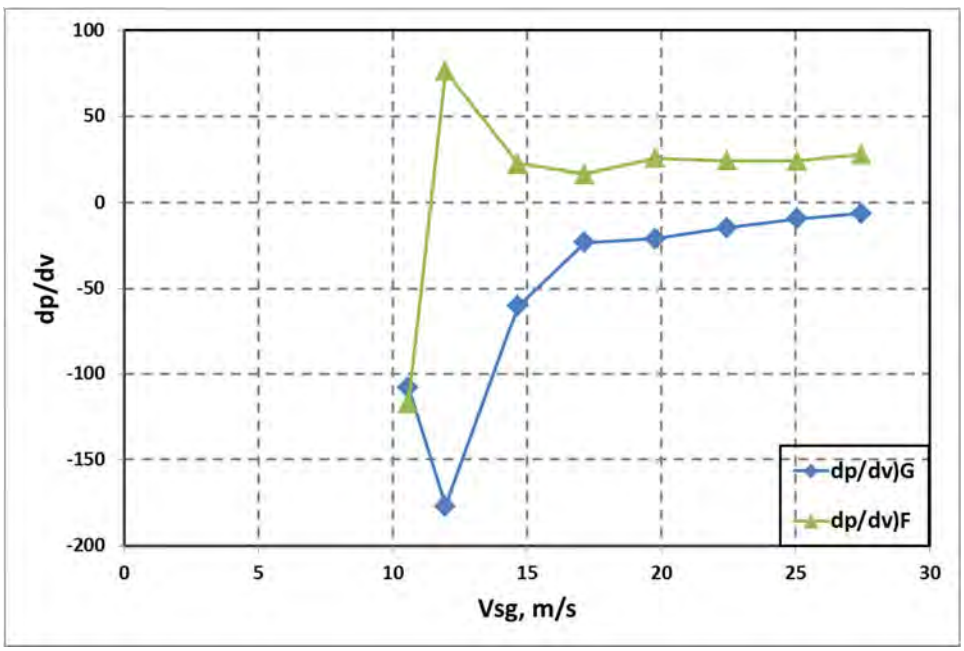

Figure 2.5: Gravitational and Frictional Gradient with Respect to Gas Velocity

The second definition of liquid loading is the liquid droplet cannot be entrained by gas phase, which is the droplet model (Turner et al; 1969). Also, liquid loading can be caused by the liquid film reversal model (Zhang et al., 2003a; 2003b) and Barnea's model (1986a). The results from these definitions are different. From the literature review, we believe that film model is more appropriate to predict the liquid loading than droplet model. Thus, we will compare the film model with the traditional definition.

We collected the air-water experimental data in 2 and 4-inch pipes (Skopich, 2012). The pressure drop is measured at different gas velocities by pressure transducers. The calculation of pressure gradient follows this procedure:

- Total pressure drop is measured and the gradient is calculated by dividing the length between the pressure transducers.
- Holdup is measured in the trap section and the gravitational gradient is calculated by

$$\left(\frac{dp}{dz}\right)_G = \rho_m g \,. \tag{2.11}$$

- Frictional pressure gradient can be calculated by subtracting gravitational pressure gradient from total pressure gradient,

$$\left(\frac{dp}{dz}\right)_F = \left(\frac{dp}{dz}\right)_T - \left(\frac{dp}{dz}\right)_G \,. \tag{2.12}$$

A high speed camera is used to observe the liquid film flowing direction in the pipe. Liquid loading inception is determined when we observe the liquid film flowing downwards. The results based on film reversal and based on minimum pressure drop are different.

In Figure 2.6, we plot the total pressure gradient, and changes in gravitational and frictional pressure drop with respect to gas velocity. From this plot, we observe that the minimum pressure drop occurs around 20 m/s. Figure 2.7 shows the liquid film flowing direction at different gas velocities. We notice that film reversal occurs around 15 m/s, which is different from minimum pressure drop definition. In Figure 2.8, we plot gravitational pressure gradient in the blue line calculated from Equation (2.1), and frictional pressure gradient in the green line calculated from Equation (2.2). The frictional pressure gradient is negative at lower gas velocity and increases with gas velocity. The reason of negative frictional gradient is that liquid film is flowing in the opposite direction of the flowing direction of gas at low gas velocity. Also, the frictional pressure gradient changes from negative to positive around 15 m/s, which is consistent with the film reversal definition, and the traditional definition (instability occurs at 20 m/s) over-predicts the critical gas velocity.

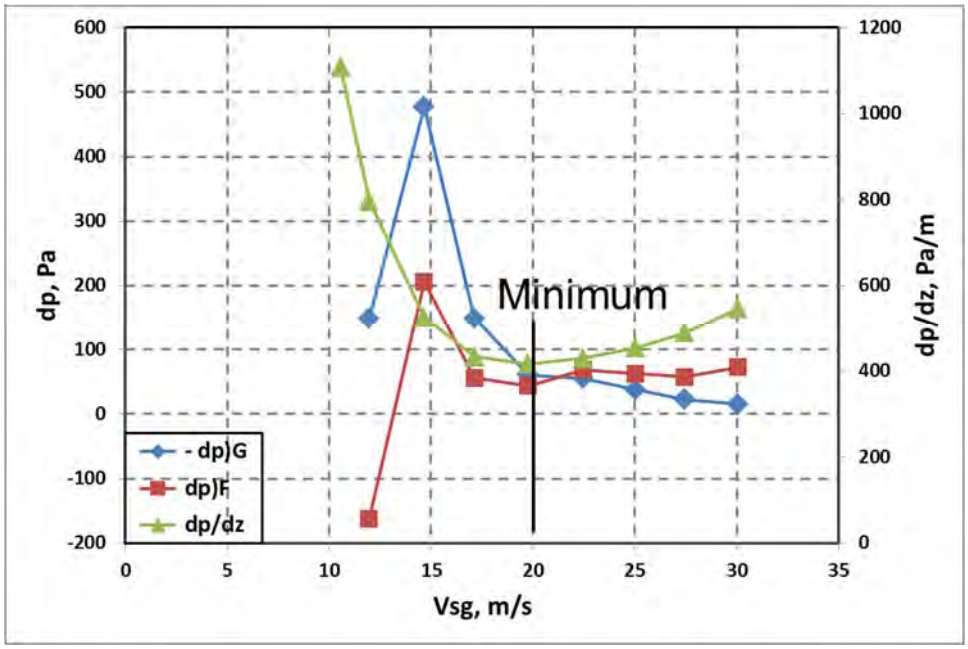

Figure 2.6: Total Pressure Gradient and Pressure Drops in 2-inch pipe

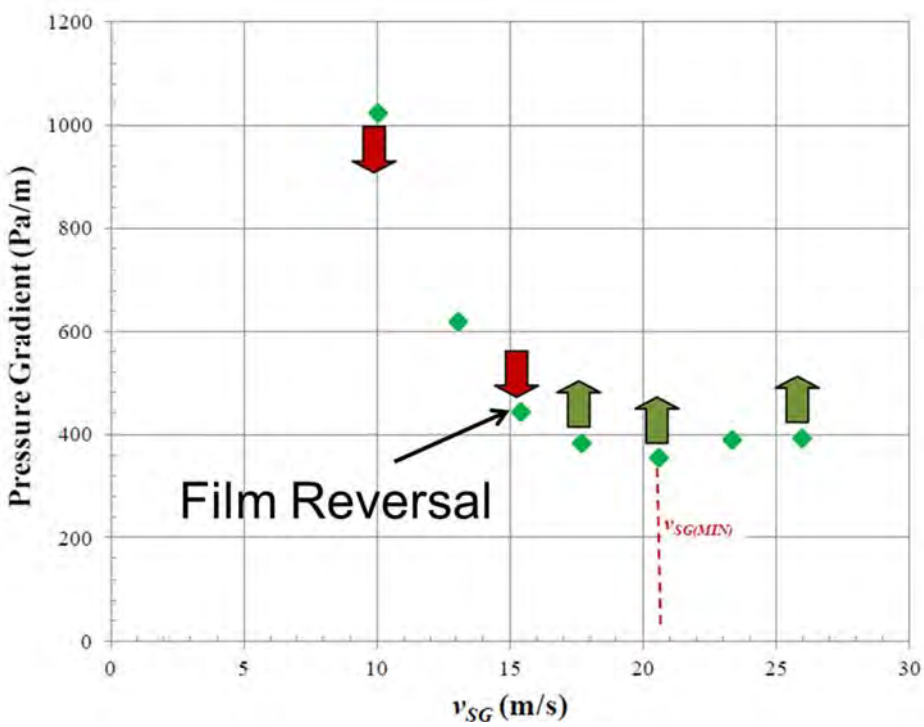

Figure 2.7: Film Reversal Observation in 2-inch pipe

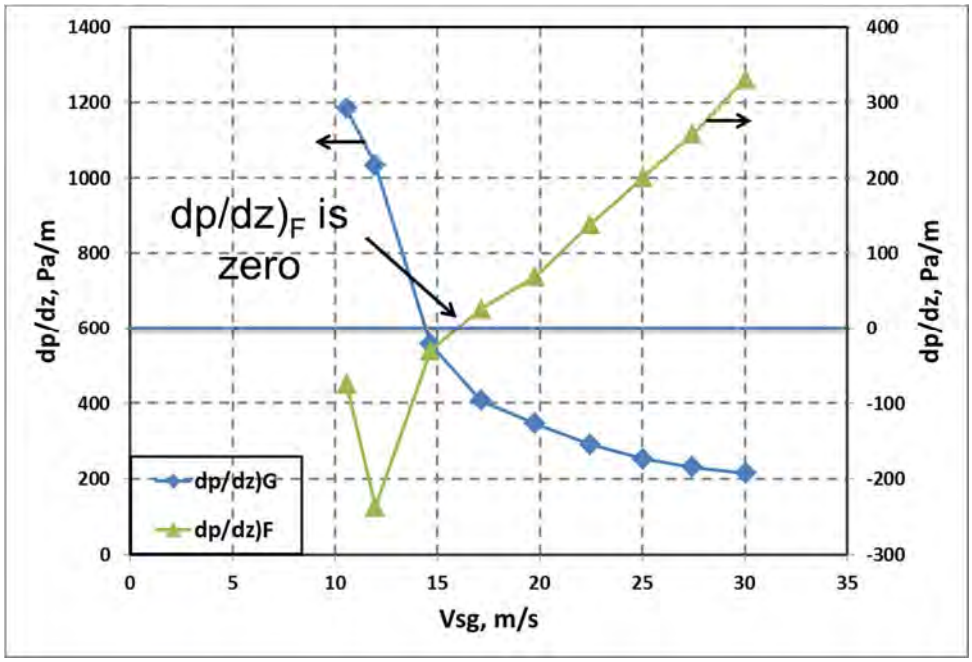

Figure 2.8: Gravitational and Frictional Pressure Gradient in 2-inch pipe

For the 4-inch data, we can observe a similar situation. The pressure drop and pressure gradients are plotted in Figure 2.9. We observe that the minimum pressure drop occurs around 15 m/s. While from the liquid film flow direction in Figure 2.10, we find that the liquid reversal occurs around 20 m/s, which is different from minimum pressure drop definition. In Figure 2.11, the frictional pressure gradient equals to zero around 20 m/s, which is also the same as the film reversal definition.

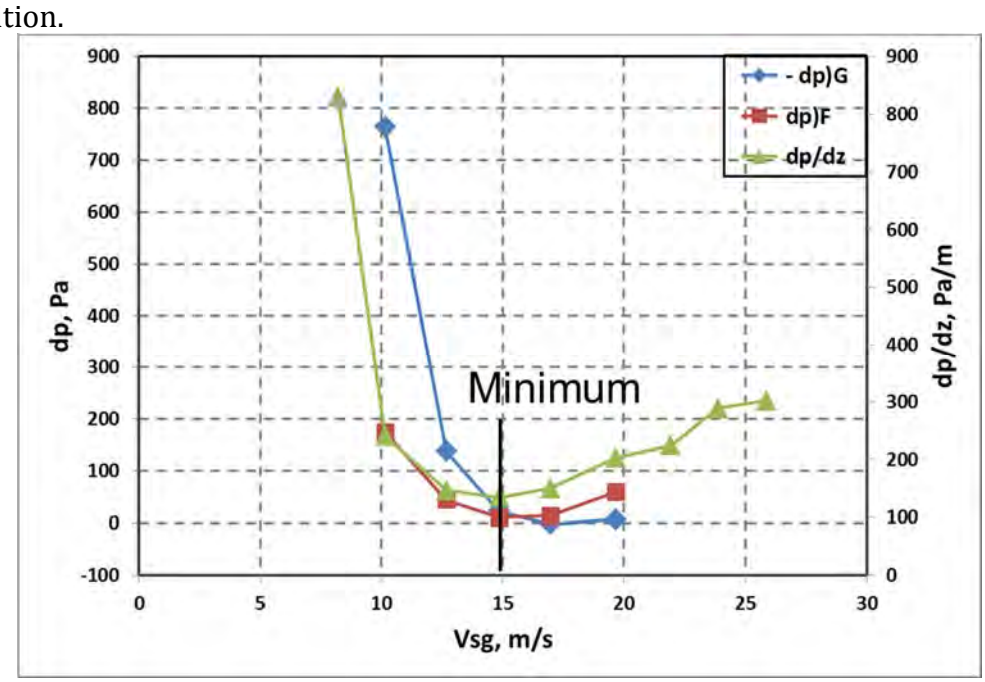

Figure 2.9: Total Pressure Gradient and Pressure Drops in 4-inch pipe

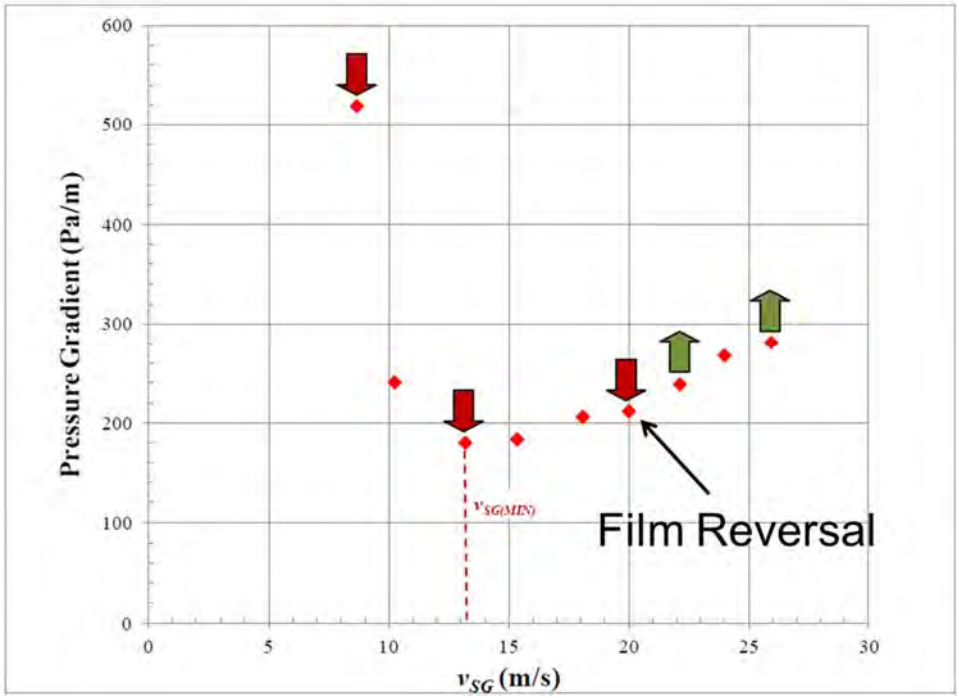

Figure 2.10: Film Reversal Observation in 4-inch pipe

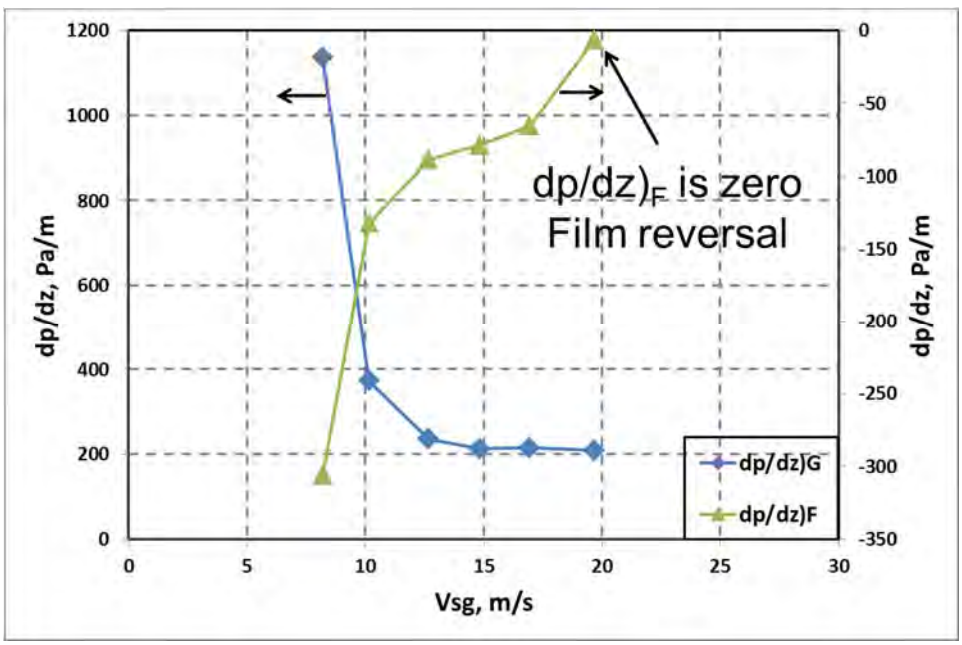

Figure 2.11: Gravitational and Frictional Pressure Gradient in 4-inch pipe

These observations are important to understand why we reach different conclusions about liquid loading depending on the definition. The film reversal model indicates that the liquid loading will start earlier in larger diameter pipe; whereas, the minimum pressure drop model indicates that the liquid loading will start earlier in a smaller diameter pipe. The data from Veekan et al. (2010), which is

mostly collected in larger diameter pipe, indicates that liquid loading starts earlier in larger diameter pipe. To summarize, what we physically observe (liquid film falling down in the pipe) is consistent with when the residual pressure gradient (difference between total and gravitational gradient) becomes zero. This is an indication of liquid falling down and the direction of frictional gradient has changed. Because of physical as well as field observations, we used liquid film model to predict the inception of liquid loading.

Out of the two models available, we concentrated on Barnea's model. In this section, we illustrate the modifications we made to the model and the reasons for those changes.

Barnea's model cannot correctly predict liquid loading for inclined wells. This is due to the assumption made in the model that film thickness is uniform at every inclination angle. In reality, liquid film thickness is not constant in inclined well and tend to be thicker on one side of the pipe due to gravity, as in Figure 2.12. Also in inclined well, the liquid loading problem is more severe than in vertical well. It is desirable to improve the model for predicting liquid loading in inclined well.

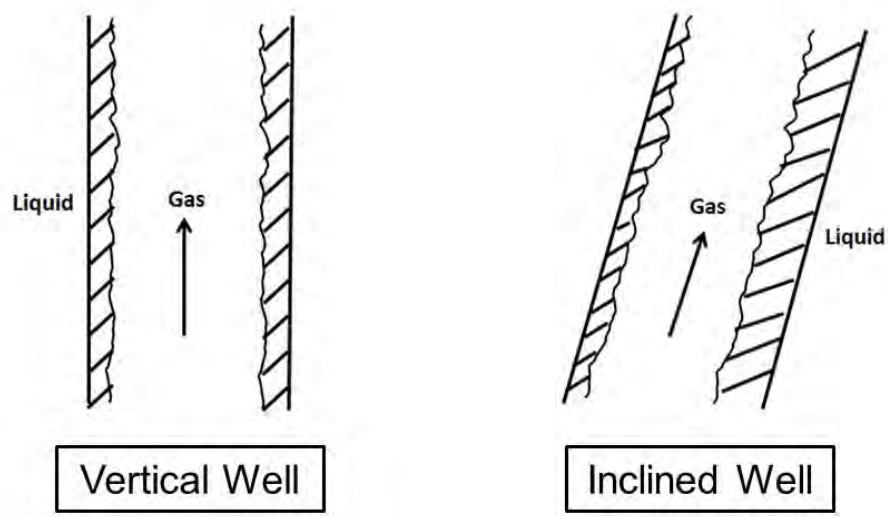

Figure 2.12: Liquid Film Thickness Comparison between Vertical and Inclined Wells

Among all the current models reviewed, we found that none of them includes inclination angle effect on film thickness distribution around the pipe. Although Barnea's model is able to predict the flow pattern transition in horizontal and inclined pipe (1986a), the film thickness is assumed to be uniform at all inclination angles.

This assumption of constant film thickness is not true due to the fact that liquid film at the bottom of the pipe is much thicker than the film at the top, which is caused by gravitational force acting on the liquid film. Since thicker film requires

more energy to be carried to the surface, it tends to fall back earlier when gas velocity is insufficient, which means higher critical velocity should be observed for inclined wells. However, in Barnea's original model, the boundary shifts slightly to the left as the angle decreases from 90 (assuming vertical flow is represented by 90), which is shown in Figure 2.13. This is contradictory to what is observed from the experimental data. Experimental studies from Belfroid et al. (2008) observed earlier transition from annular to slug by increasing the inclination angle. This effect should be included in the model so that liquid loading in inclined wells can be correctly predicted.

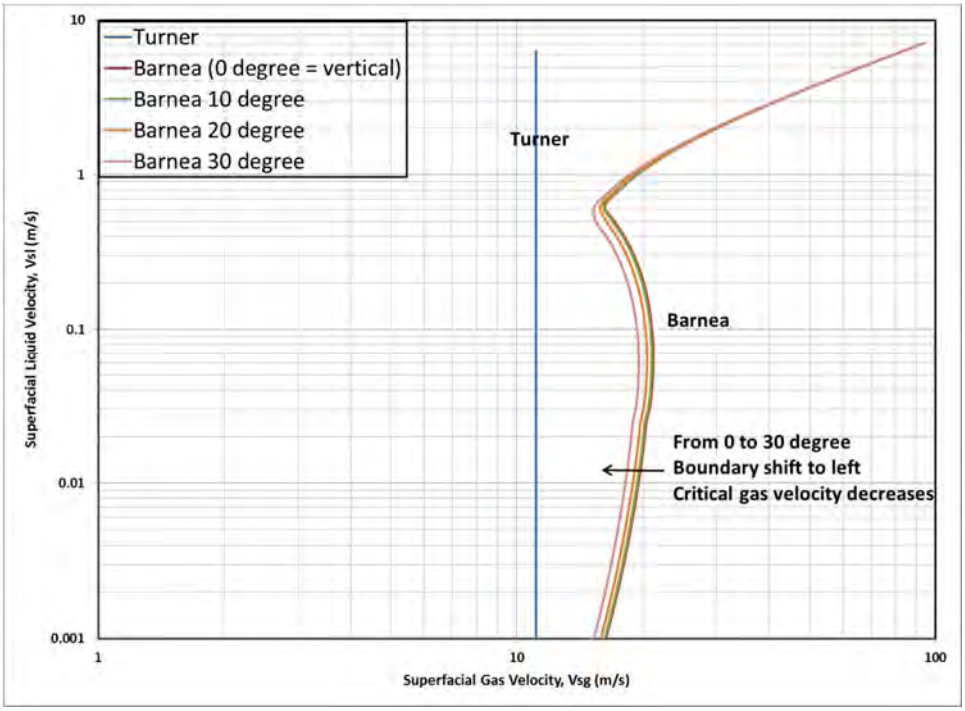

Figure 2.13: Barnea's Model Boundaries at Different Inclination Angles

The Belfroid et al. experiment (2008) shows that critical gas velocity reaches maximum value around 30 degree of inclination angle. The critical gas velocity at different inclination angle is plotted in Figure 2.13. As inclination angle increases from 0 to 30 degrees, critical gas velocity increases, which means liquid loading occurs earlier. The increasing critical velocity results from more and more liquid flow to the lower side of the pipe and much higher gas velocity is needed to lift this thicker film. On the other hand, gravitational force in flow direction is decreasing as the pipe inclined, which reduces critical gas velocity. The combined effect of thicker film and less gravitational gradient determines the change of critical velocity at different inclination angles. When the inclination angle is less than 30 degree, influence of thicker film is larger than gravitational gradient change and thus critical gas velocity increases. At larger inclination angle above 30 degrees, critical gas velocity decreases as inclination angle increases. In this range, decreasing gravitational gradient in the flow direction exceeds the influence of thicker film on

liquid loading. Based on this experimental result, we can thus make the assumption that film thickness reaches the maximum value at a 30 degree inclination angle.

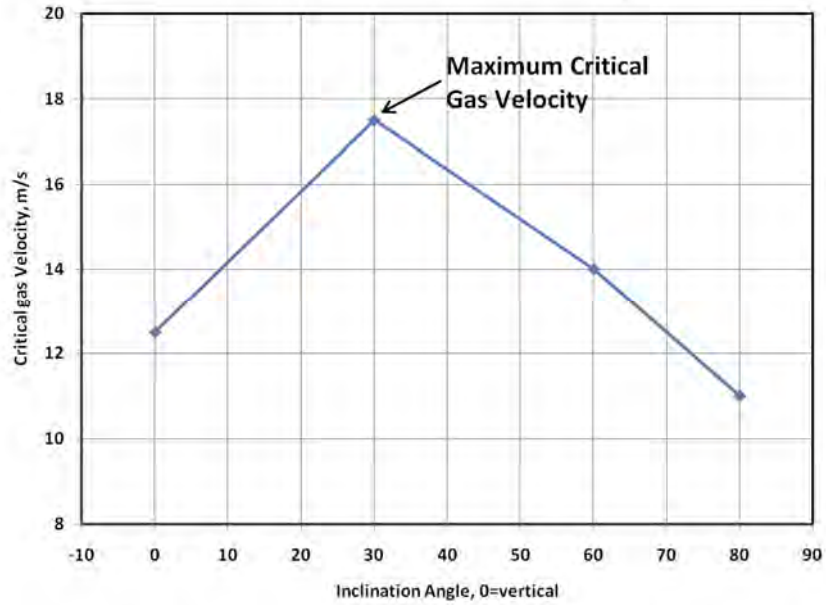

Figure 2.14: Critical Gas Velocity Changing with Different Inclination Angle

To incorporate this behavior in Barnea's model, we developed a non-uniform film thickness model. To build a model that accounts for variable thickness as the inclination angle changes, we compared uniform thickness model with non-uniform thickness model as shown in Figures 2.15 and 2.16. We used material balance to ensure that, in both cases, the amount of liquid carried would not change. For a constant film thickness, the area of the film approximately equals to the area of an expanded rectangle, which can be calculated with Equation (2.3). For the non-uniform case, film thickness is the function of both circular pipe position (φ) and inclination angle of the pipe (θ). If we assume the film thickness changes linearly with circular pipe position at any inclination angle, area of the film can be approximated with a trapezoid and can be calculated with Equation (2.4).

$$A_1 = \pi D \delta_c \,, \tag{2.3}$$

$$A_2 = \frac{1}{2}[\delta(0,\theta) + \delta(\pi,\theta)]\pi D \,, \tag{2.4}$$

where D is pipe diameter, δ_c is constant film thickness, $\delta(0,\theta)$ is film thickness at the top of the pipe and $\delta(\pi,\theta)$ is film thickness at the bottom of the pipe. Two variables that determine film thickness δ are pipe circumferential position and inclination angle.

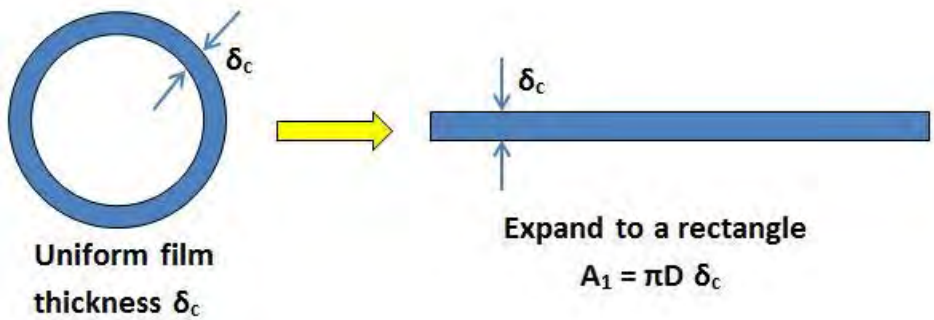

Figure 2.15: Schematic Uniform Thickness Liquid Film

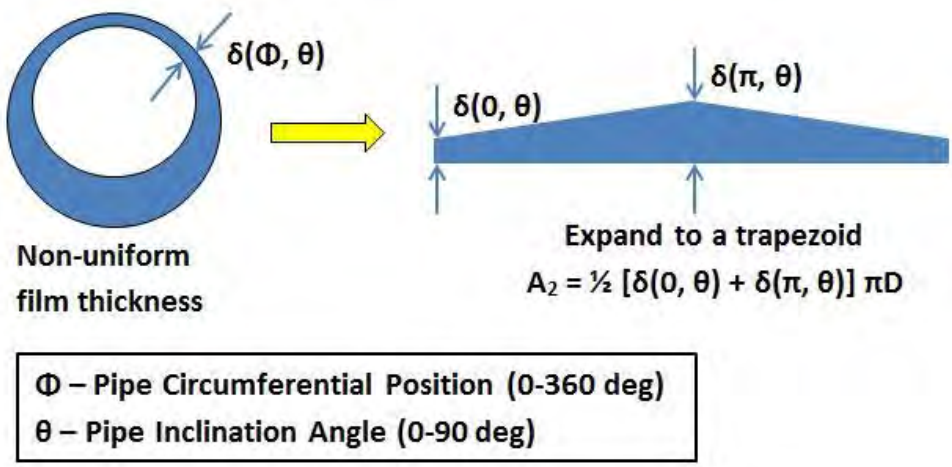

Figure 2.16: Schematic Non-uniform Thickness Liquid Film

For both cases, liquid mass flow rate in the pipe is the same, so the area of the liquid film should also be equivalent. When A_1 equals A_2, we can find the relationship between non-uniform film thickness and constant film thickness, which can be seen in Equation (2.5).

$$\delta_c = \frac{1}{2}[\delta(0,\theta) + \delta(\pi,\theta)]\,, \tag{2.5}$$

We know that maximum film thickness will be reached at an inclination angle equals to 30 degree based on earlier experimental data. At this inclination angle, we assume the top film thickness almost equals to zero, which corresponds to $\delta(0, 30)$ in Figure 2.17, and bottom film thickness, $\delta(\pi, 30)$, is the maximum thickness it could reach, which equals $2\delta_c$, the shape of the liquid film is shown in Figure 2.17.

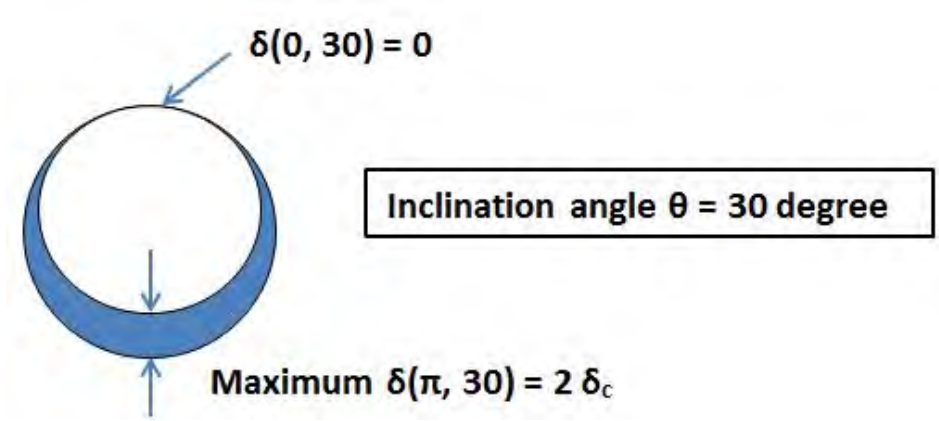

Figure 2.17: Non-uniform Film Thickness at 30 Degree Inclination Angle

For film distribution around the pipe, we use the following film thickness equation in the new model:

$$\delta(\Phi,\theta) = \left[\frac{\theta}{30} sin(\Phi - 90) + 1\right] \delta_c \quad for\ 0 \le \theta \le 30\ degree\ , \tag{2.6}$$

$$\delta(\Phi,\theta) = [sin(\Phi - 90) + 1]\ \delta_c \qquad for\ \theta > 30\ degree\ , \tag{2.7}$$

where Φ is pipe circumferential position (range from 0 to 360 degree) and θ is pipe inclination angle (range from 0 to 90 degree).

Note that Equation (2.6) is equal to Equation (2.7) when $\theta = 30$ degree, this means that the film structure remain the same as inclination angle exceeds 30 degree, as shown in Figure 2.17. We assume the film thickness will not increase after 30 degree and there is a very thin film at top to ensure that annular flow structure still exists. Plotting Equation (2.6) as function of circular position of pipe, we can see the film distribution at different inclination angles in Figure 2.18. The film distribution at inclination angle larger than 30 degrees is the same as for 30 degree.

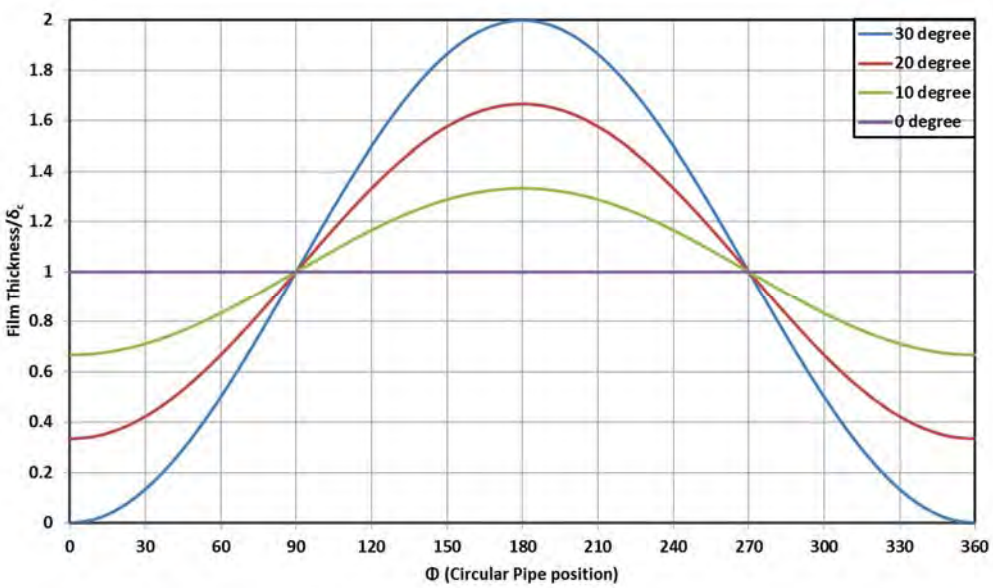

Figure 2.18: Liquid Film Thickness Distribution around Pipe

Knowing the biggest film thickness at different inclination angles, we can incorporate this into Barnea's (1986a) model. First, we can calculate the critical film thickness δ_T by differentiating combined momentum equation. This critical film thickness δ_T should equal to the maximum film thickness because a maximum liquid film will initiate liquid fall back and will lead to liquid loading. To calculate critical velocity for inclined wells, we need to convert δ_T to constant film thickness δ_c. As an example, let us examine this relationship when the inclination angle equals to 30 degree, critical film thickness δ_T is calculated from Equation (2.8) and δ_T equals to the bottom film thickness. In order to conserve the mass of liquid, Equation (2.5) can be used to calculate δ_c. Then, δ_c will be calculated from Equation (2.8) and is used to calculate the critical gas velocity.

$$\delta_c = \frac{1}{2}[0 + \delta(\pi, 30)\,] = \frac{1}{2}\delta_T\,, \tag{2.8}$$

Using a similar procedure, we calculated the transition boundary at different inclination angles. In Figures 2.19 and 2.20, transition boundary of 0 - 30 degree and 30 - 90 degree inclination angle are plotted based on the new model.

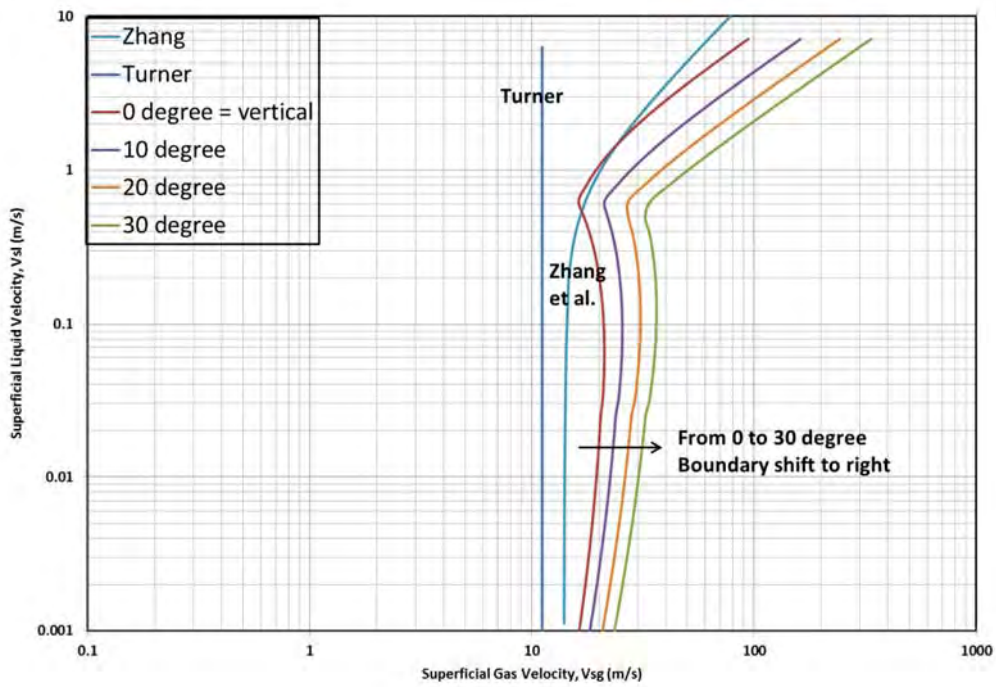

Figure 2.19: Transition Boundaries of New Model Using Non-Uniform Film Thickness (0 - 30 Degree Inclination Angle)

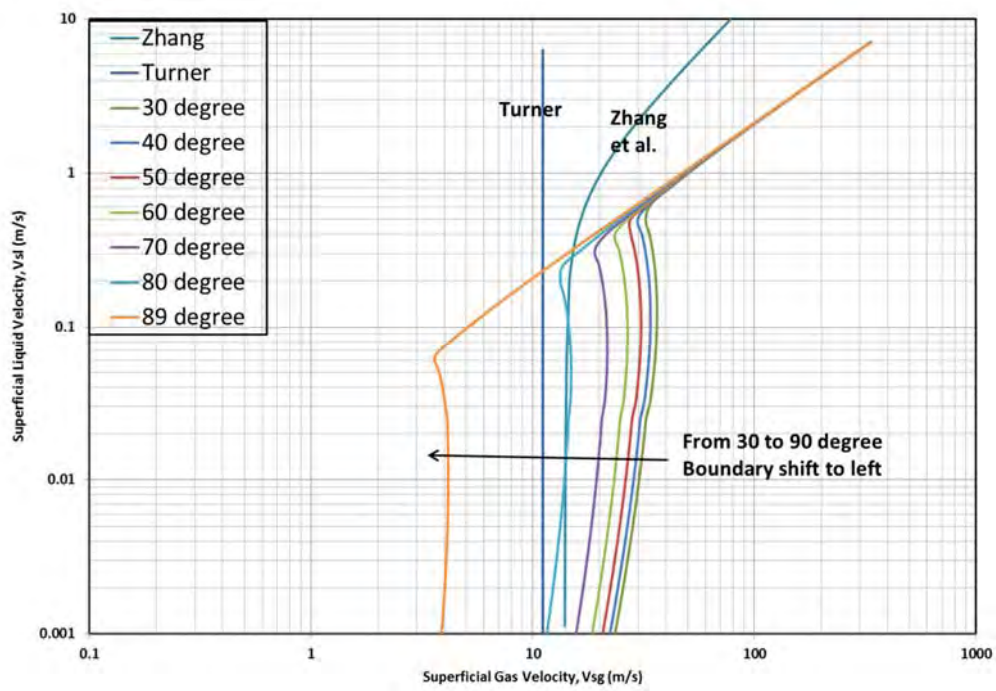

Figure 2.20: Transition Boundaries of New Model Using Non-Uniform Film Thickness (30 - 90 Degree Inclination Angle)

Comparing to Barnea's original model, transition boundary shifts to the right at 0 to 30 degrees in Figure 2.19, which means liquid loading starts earlier in this range. From 30 to 90 degrees, the boundary shifts to the left, and critical velocity

decreases due to less gravitational force in flow direction, as can be seen in Figure 2.20. We also plot critical gas velocity at different inclination angles, which is shown in Figure 2.21. This plot shows a similar trend as Belfroid et al. (2008) data as shown in Figure 2.14.

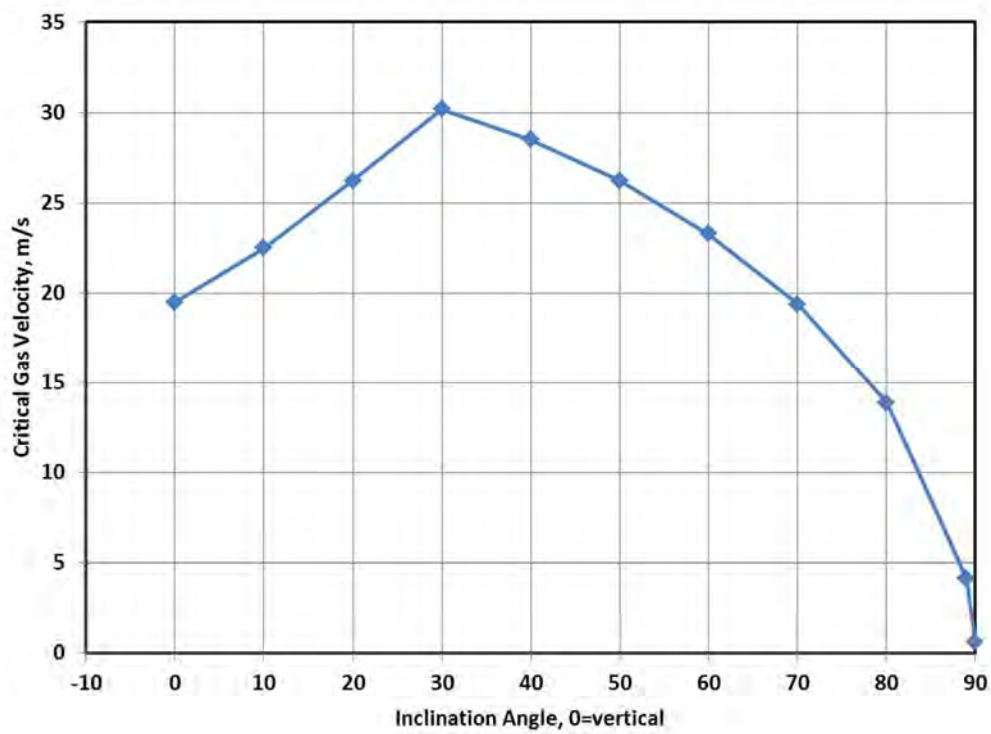

Figure 2.21: Critical Gas Velocity of New Model (0 - 90 Degree Inclination Angle)

In addition to defining a model for an inclined well, we also examined the friction factor equation used by Barnea. In Barnea's model, the Wallis correlation is used and the results are too conservative when predicting inception of liquid loading. It is possible that interfacial shear stress calculated by using the Wallis correlation is too small for annular to slug transition. Many other interfacial friction factor correlations have been proposed to match experimental data. Fore et al. (2000) showed that the Wallis correlation is reasonable for small values of film thickness and is not suitable for a larger liquid film thickness. Since transition to slug flow is due to an increasingly larger thickness of liquid film, the Wallis correlation may be not good for prediction of liquid loading. A new correlation (Fore et al., 2000) is used in this model as shown Equation (2.9).

$$f_I = 0.005\left\{1 + 300\left[\left(1 + \frac{17500}{Re_G}\right)\frac{h}{D} - 0.0015\right]\right\}, \tag{2.9}$$

In addition, entrained liquid droplet was not considered in Barnea's model. This means all the liquid is in film and results in over-prediction of the film thickness as well as critical gas velocity. It is known that Barnea's prediction is conservative which may be due to neglect of the liquid droplet in the gas column. In

our new model, we include the entrainment droplet by calculating entrainment fraction factor, f_E, which is defined as the fraction of liquid flow rate that is entrained in the gas core as droplets. The correlation used is developed by Wallis (1969), as in Equation (2.10).

$$f_E = 1 - e^{[-0.125(\varphi - 1.5)]}, \tag{2.10}$$

where

$$\varphi = 10^4 \frac{v_{SG}\mu_G}{\sigma}\left(\frac{\rho_G}{\rho_L}\right)^{0.5}. \tag{2.11}$$

Then we can use Equation (2.12) to calculate the liquid flow rate in film.

$$q_F = q_L(1 - f_E), \tag{2.12}$$

Comparison of the original model and new model with the entrained droplet for vertical wells can be seen in Figure 2.22. Critical gas velocity from the new model is approximately 10% lower than the original model's calculation.

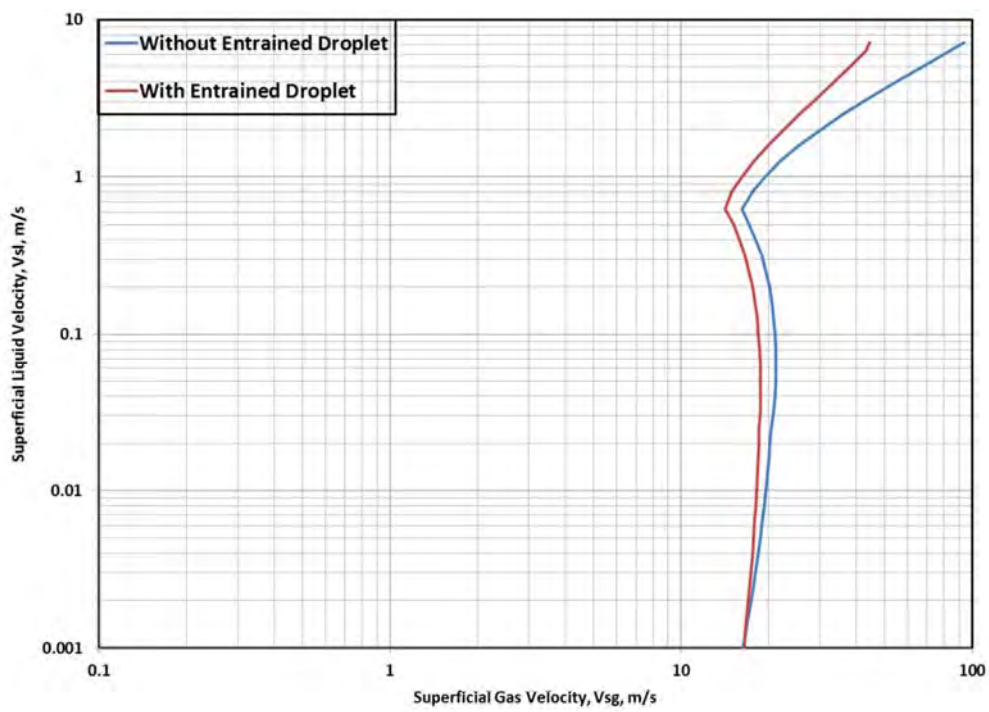

Figure 2.22: Comparison of Transition Boundary of Barnea's Model and New Model

The new model is also validated with the field data in the next section. For vertical wells, the new model is less conservative than Barnea's model. For inclined wells, the new model is validated by experimental data in inclined pipes and wells and shows improvement over other models.

Field Validation

In this section, we will examine and validate the liquid loading prediction model using five sets of data. The models we examined are Turner's model (1969), Coleman's model (1991), Zhang's model (2003), Barnea's model (1986) and our new model. The prediction results from these models will be compared. Also, our model will be validated with data in inclined wells. All the field data and calculation results can be found in Appendix A. Note that all the calculation results are in SI unit, so are the units used in the figures of this section. All the data are presented in the same format, therefore, some explanation of how the data are presented is in order. We always plot calculated gas loading velocity (critical velocity) on y axis against the actual gas velocity based on the surface data. If the loading velocity is greater than actual velocity (i.e., the data are above the 45 degree line), the well will be loading (not enough gas velocity to sustain the liquid). If the loading velocity is smaller than the actual velocity (i.e., the data are below the 45 degree line), the well will be producing under unloading conditions. We use different symbols to indicate the actual observations of whether the well is loading or unloading. If the model is able to correctly predict the loading and unloading conditions, all the loaded wells will be above the 45 degree line and all the unloaded wells will be below the 45 degree line.

We start with Turner et al. (1969) data in Appendix A. Observed gas flow rate is compared with prediction from Turner's equation, which is shown in Figure 2.23. Test flow gas rate reported in the paper is converted to superficial gas velocity and it is compared with Turner's critical gas velocity, which is calculated for every single well. Both water and condensate equations have been used to calculate critical gas velocity according to the Turner et al. (1969) paper. The gas well's loading condition during tests can be used to examine the model. In Figure 2.23, loaded wells are represented by blue squares and stable wells are represented by red triangles. A 45 degree line in the plot is the loading boundary, where which shows the transition between loading and unloading conditions. This boundary divides the plot into two regions, which are loaded up region and unloaded region. If Turner's equation can predict critical gas velocity accurately, loaded wells should fall into the loaded up region and unloaded wells should be below the 45 degree line. In Figure 2.23, we can see that all unloaded wells show a good match with predictions (correct predictions 53/53 with 100% accuracy), but many loaded data are in the unloaded region in the plot (correct predictions 17/37 with 46% accuracy). It is also suggested in some studies that only water property should be used in Turner's equation (1969). In Figure 2.24, critical gas velocity is calculated by using water properties only. Although some data points show higher critical gas velocity, many loading data still fall in the unloaded region (correct predictions 23/37 with 62% accuracy). This indicates that Turner's equation underestimates the critical gas velocity.

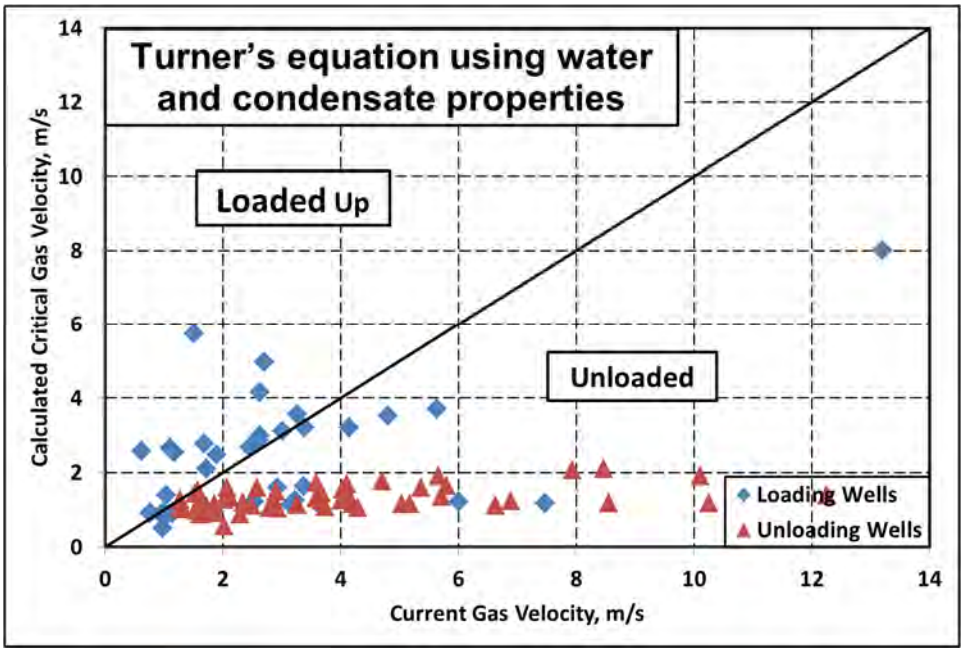

Figure 2.23 Turner's Data versus Turner's Equation (w/c) Predictions

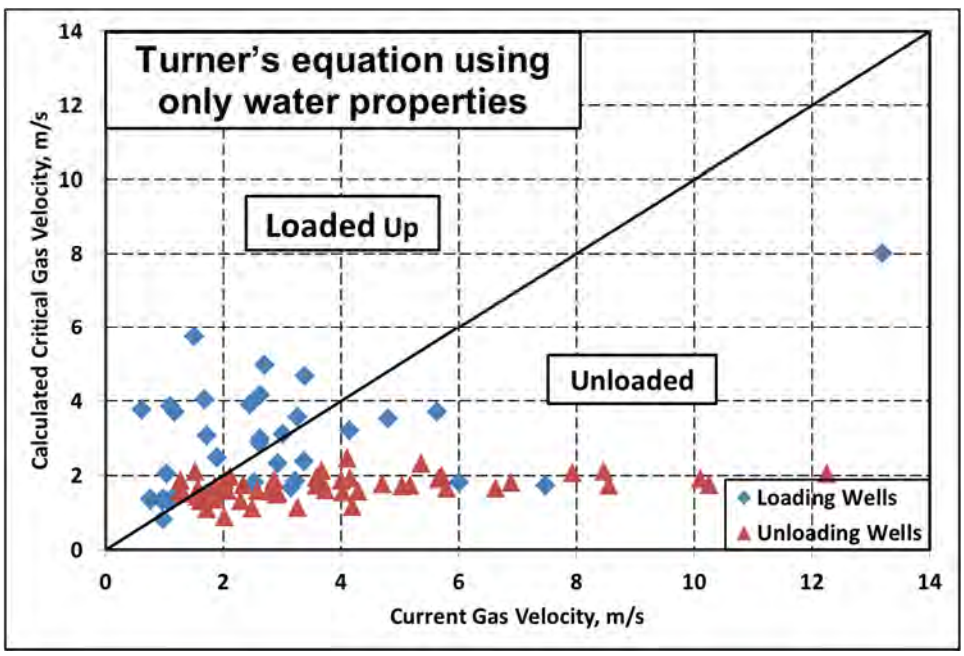

Figure 2.24: Turner's Data versus Turner's Equation (w) Predictions

The prediction result of the Zhang et al. (2003) model can be seen in Figure 2.25. Since critical gas velocity calculated from the film model is affected by pipe diameter, tubing diameter will be used as an input parameter. We used hydraulic diameter for wells producing through annulus, which is defined as the difference of casing ID and tubing OD. We know that Zhang's boundary from annular to slug flow is higher than Turner's boundary in the flow pattern map. Thus, most of the data have higher critical gas velocity than Tuner's prediction. From Figure 2.24, we can

observe better predictions for loaded wells (correct predictions 30/37 with 81% accuracy), and some unloaded wells with low gas velocity fall in the loaded region (correct predictions 36/53 with 68% accuracy). However, the discrepancy between critical velocities is small.

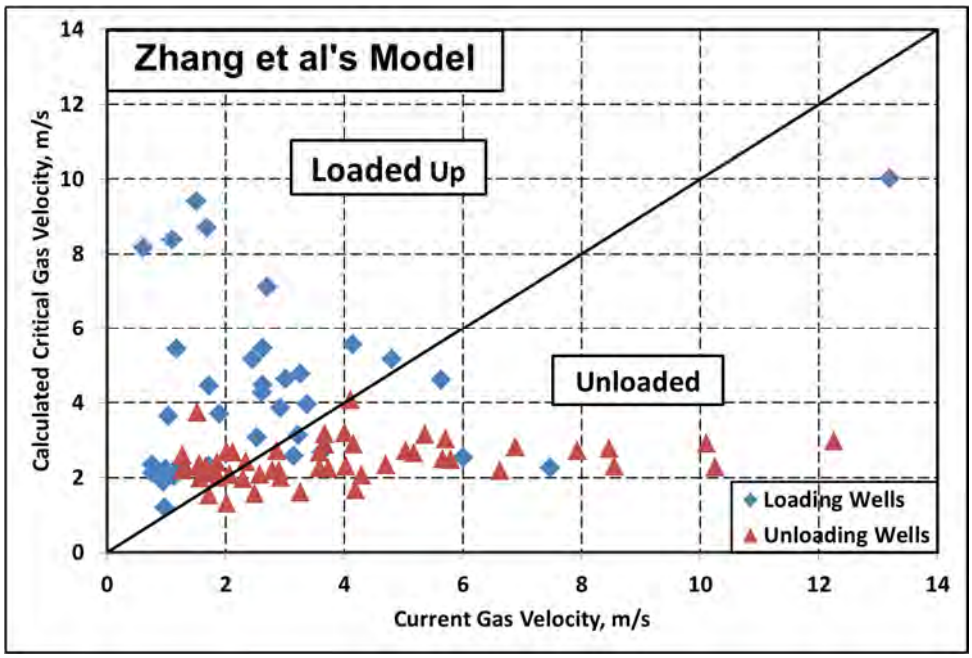

Figure 2.25: Turner's Data versus Zhang et al. Model Predictions

Among all the models, Barnea's model has the highest critical gas velocity. In Figure 2.26, the critical gas velocity predicted by Barnea's model is compared with test flow gas velocity. Hydraulic diameter is also used for annular completion wells and water property is used for all wells. We can see that, although most of loaded wells are in the correct region (correct predictions 35/37 with 95% accuracy), many unloaded wells locate above the 45 degree line (correct predictions 24/53 with 45% accuracy). This result indicates that Barnea's model may over-predict the critical gas velocity for Turner's data.

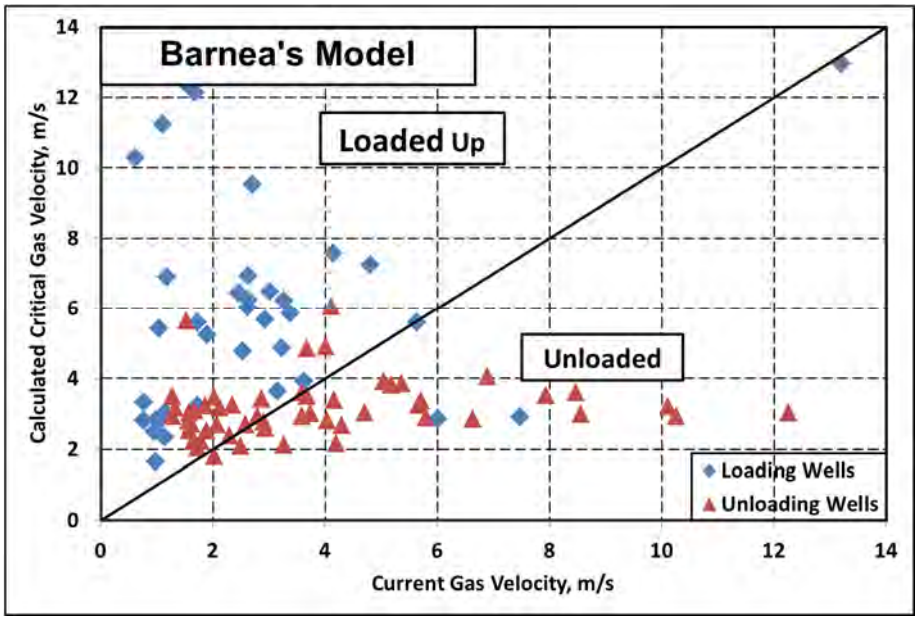

Figure 2.26: Turner's Data versus Barnea's Model Predictions

In Figure 1.1, we can see the prediction results from the new model show improvement compared to Barnea's original model. The loading well predictions are correct in 32 out of 37 wells. Although some unloading wells are still over-predicted (correct predictions 37/53 with 70% accuracy), they are very close to the loading boundary. In Table 2.1, we summarize the prediction results of all the models. Turner's equation shows the best total accuracy, but its prediction for loading and unloading data are biased, which predicts poorly for loading wells. The new model shows good accuracy for both loading and unloading wells and its results are better than other models.

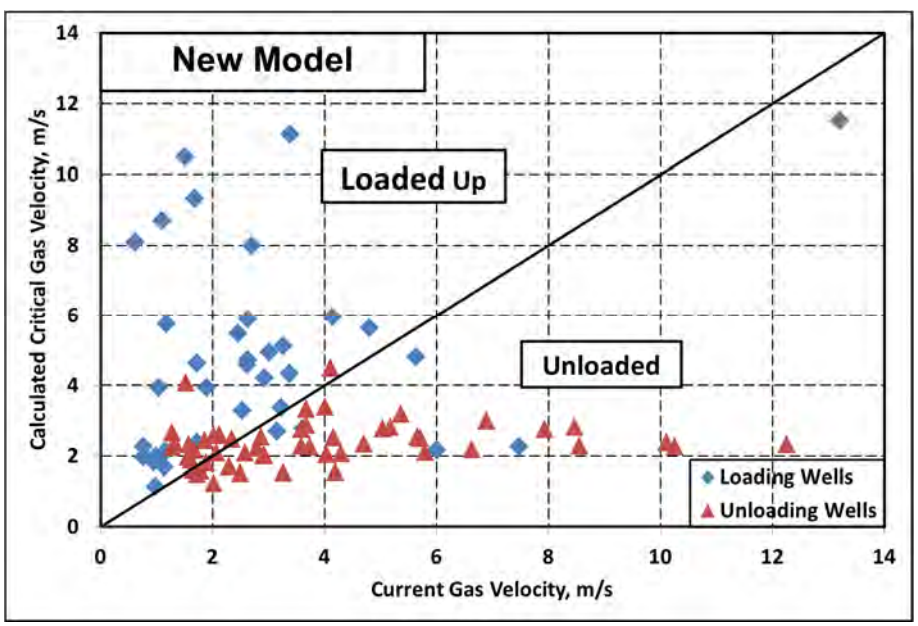

Figure 2.27: Turner's Data versus New Model Predictions

Table 2.1: Prediction Results of Turner's Data

	Correct Loaded Predictions (Total:37)	Correct Unloaded Predictions (Total:53)	Loaded Accuracy (%)	Unloaded Accuracy (%)	Total Accuracy (%)
Turner's Equation (w/c)	17	53	46%	100%	78%
Turner's Equation (w)	23	48	62%	91%	79%
Zhang et al. Model	30	36	81%	68%	73%
Barnea's Model	35	24	95%	45%	66%
New Model	32	37	86%	70%	77%

Now we compare Coleman et al. (1991 a, b) data with all the correlations. In Figure 2.28, we can see the comparison between Turner's critical velocities and Coleman's observed gas velocities. Since Coleman et al. reported critical rate after they observed liquid loading, all data should fall in the loaded region, which is the region above the 45 degree line and data points should also be close to loading boundary. However, nearly half of the data points are plotted in the unloaded region (correct predictions 28/56 with 50% accuracy). Similar to Turner's data, this indicates that Turner's equation underestimates critical gas velocity. In Figures 2.29 and 2.30, results from the Zhang et al. model and Barnea's model are plotted with observed data. Both film models provide better prediction results than Turner's equation for the reason that most of data is in the loaded up region (both correct predictions 53/56 with 95% accuracy). Critical gas velocity calculated from Barnea's model is higher than Zhang's results, but the difference is not significant for the Coleman et al. data. The new model's results are plotted in Figure and are very close to the results from Zhang's and Barnea's model (correct predictions 54/56 with 96% accuracy). For the Coleman et al. data, predictions of the film model are much better than the droplet model, and film models' predictions do not have much difference, as shown in Table 2.2.

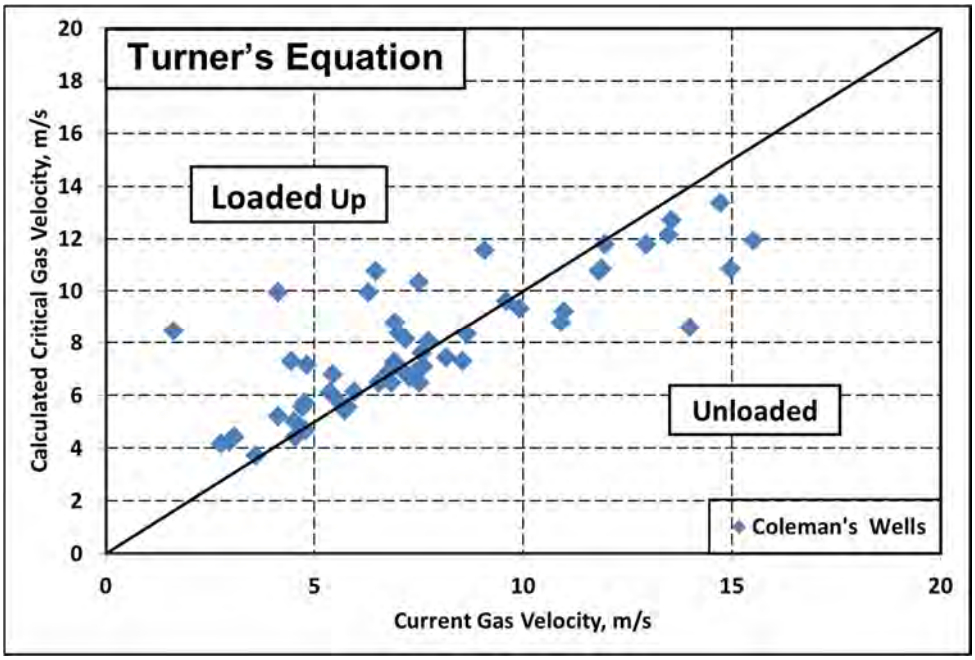

Figure 2.28: Coleman et al. Data versus Turner's Equation Predictions

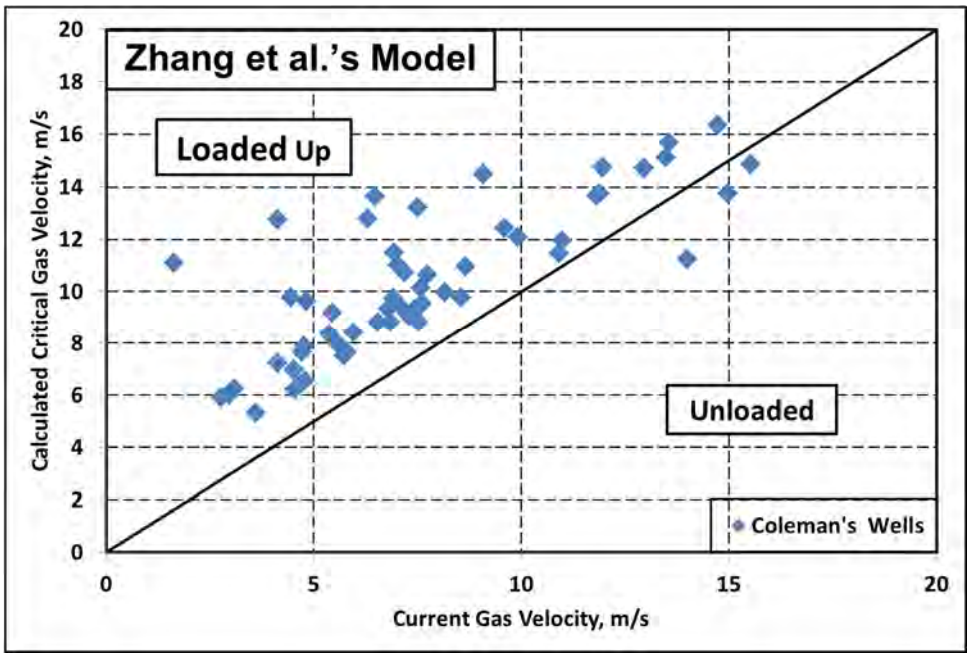

Figure 2.29: Coleman et al. Data versus Zhang et al. Model Predictions

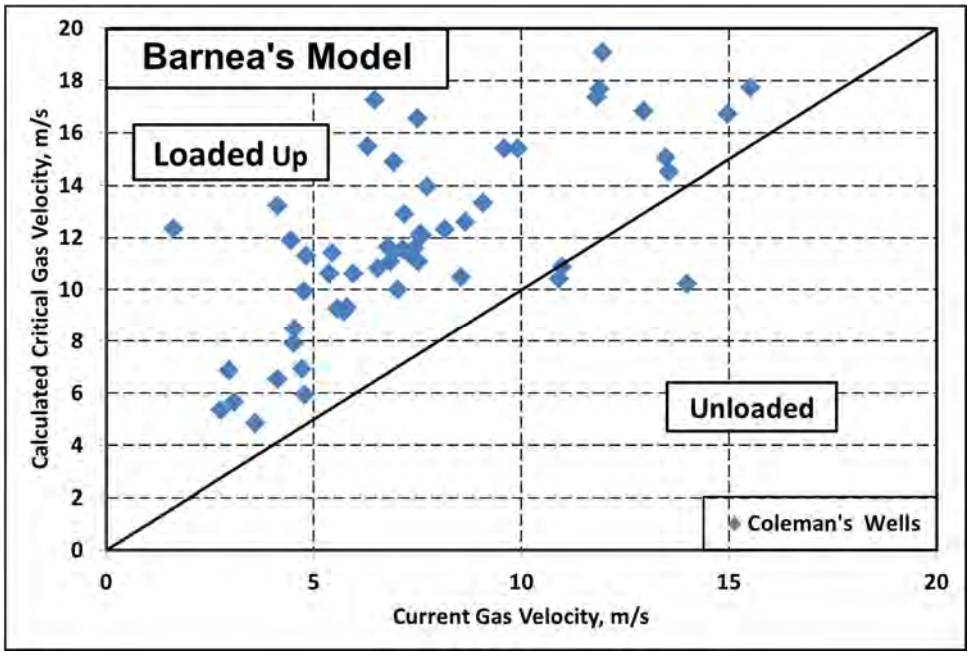

Figure 2.30: Coleman et al. Data versus Barnea's Model Predictions

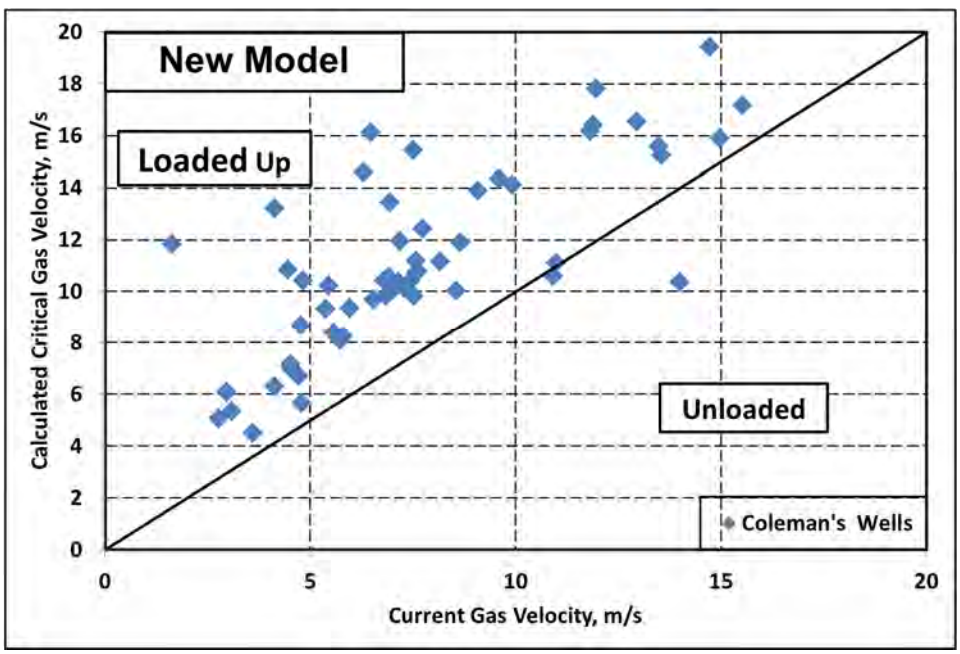

Figure 2.31: Coleman et al. Data versus New Model Predictions

Table 2.2: Prediction Results of Coleman's Data

	Correct Predictions (Total:56)	**Accuracy (%)**
Turner's Equation	28	50%
Zhang et al. Model	53	95%
Barnea's Model	53	95%
New Model	54	96%

Similar to Coleman's data, Veeken et al. (2010) reported gas rate after liquid loading is observed in the gas well. Thus, all the data should locate in the region above the 45 degree line if model predictions are correct. However, Turner's equation failed to predict liquid loading for Veeken's data (0% accuracy), as shown in Figure 2.32. This may be due to the fact that Turner's critical velocity is not affected by pipe diameter. Turner's equation can only be applied to smaller pipe diameter wells, but does not work for Veeken's offshore large tubing wells. Inclination angle might be another reason for this poor prediction from Turner's equation. In Figure 2.33, although having higher critical gas velocity, the Zhang et al. model only correctly predicts about half of the wells and many loaded wells are still in the unloaded region (correct predictions 27/67 with 40% accuracy). Barnea's model's predictions in Figure show a good match with observed data. However, there are still few data points in the unloaded region (correct predictions 59/67 with 88% accuracy). These points can be improved by considering non-uniform film thickness, which is shown in Figure 2.34. The prediction result from the new model is much better than other models (correct predictions 61/67 with 91% accuracy). The new model has the best prediction results for the Veeken et al. data.

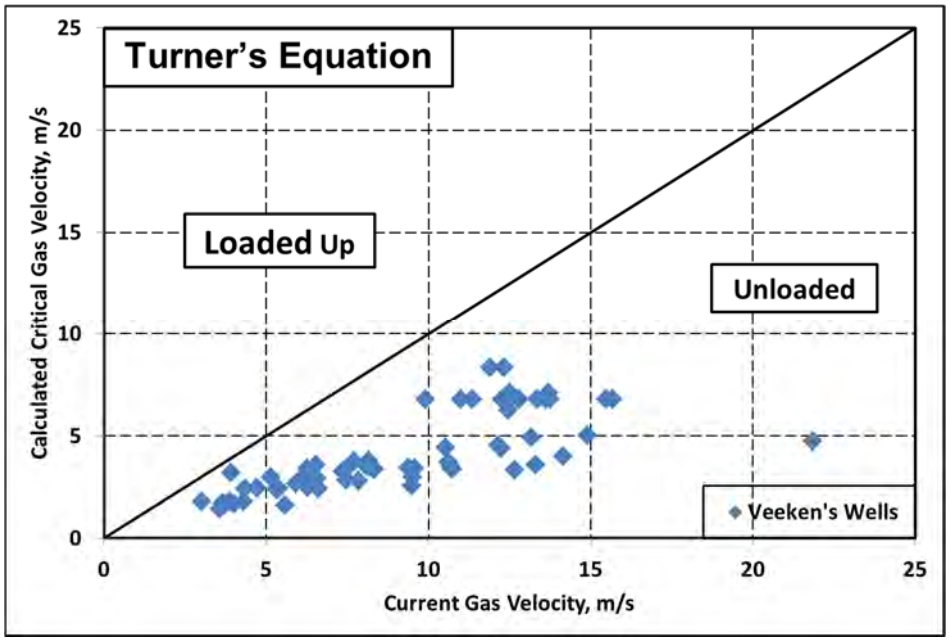

Figure 2.32: Veeken et al. Data versus Turner's Equation Predictions

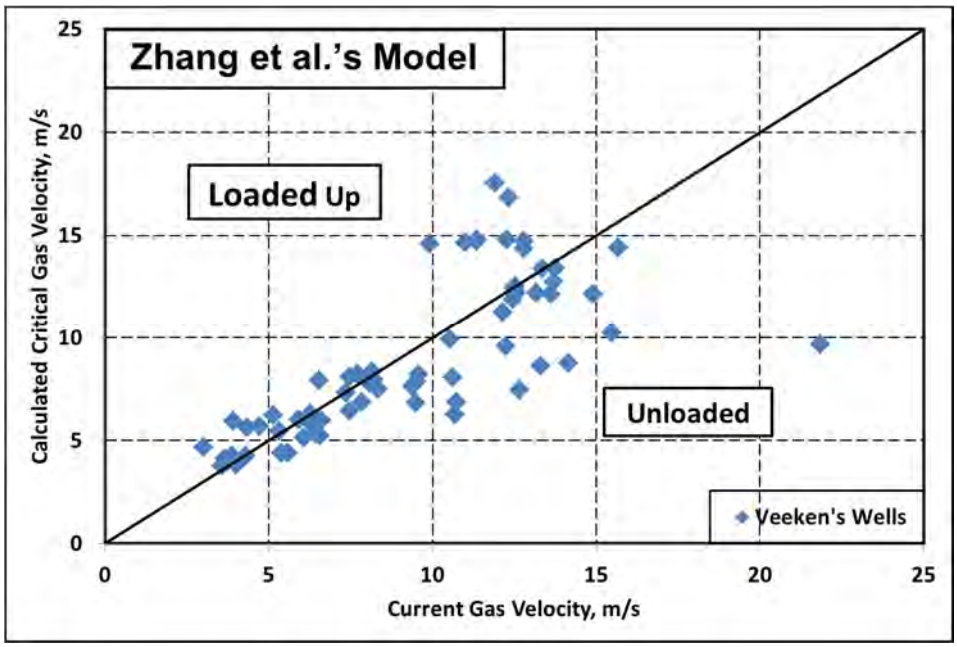

Figure 2.33: Veeken et al. Data versus Zhang et al. Model Predictions

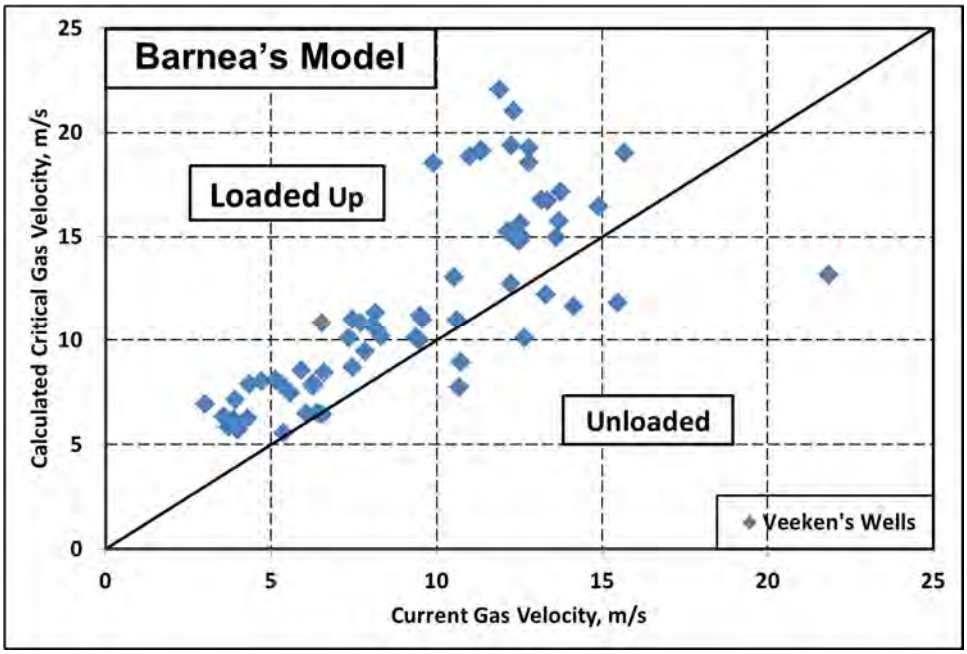

Figure 2.34: Veeken et al. Data versus Barnea's Model Predictions

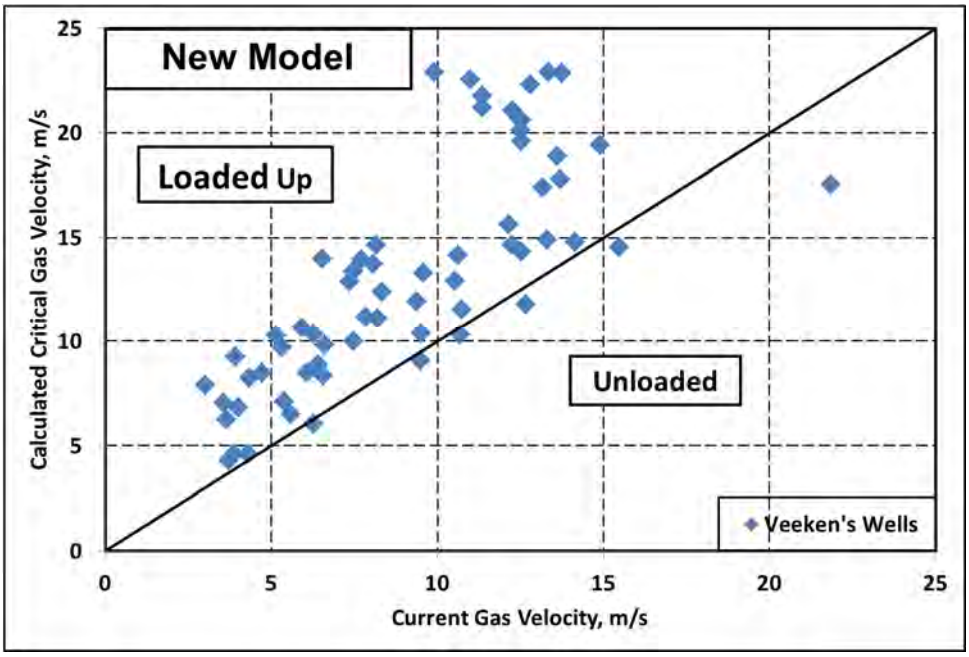

Figure 2.35: Veeken et al. Data versus New Model Predictions

Table 2.3: Prediction Results of Veeken's Data

	Correct Predictions (Total:67)	Accuracy (%)
Turner's Equation	0	0%
Zhang et al. Model	27	40%
Barnea's Model	59	88%
New Model	61	91%

The observed gas velocity of Chevron's data is collected when the capillary string is installed, which means liquid accumulation has started. Thus, we expect to see all the data points in the loaded region. Turner's equation gave reasonable predictions for critical gas velocity (correct predictions 72/82 with 88% accuracy), which are shown in Figure 2.36. For film models, three models have similar prediction results (correct predictions 78/82 with 95% accuracy). For Chevron data, all the models have good accuracy, around 90%, on liquid loading prediction. This may be because the observed gas rate we picked is too conservative, which could be much lower than the actual critical gas velocity.

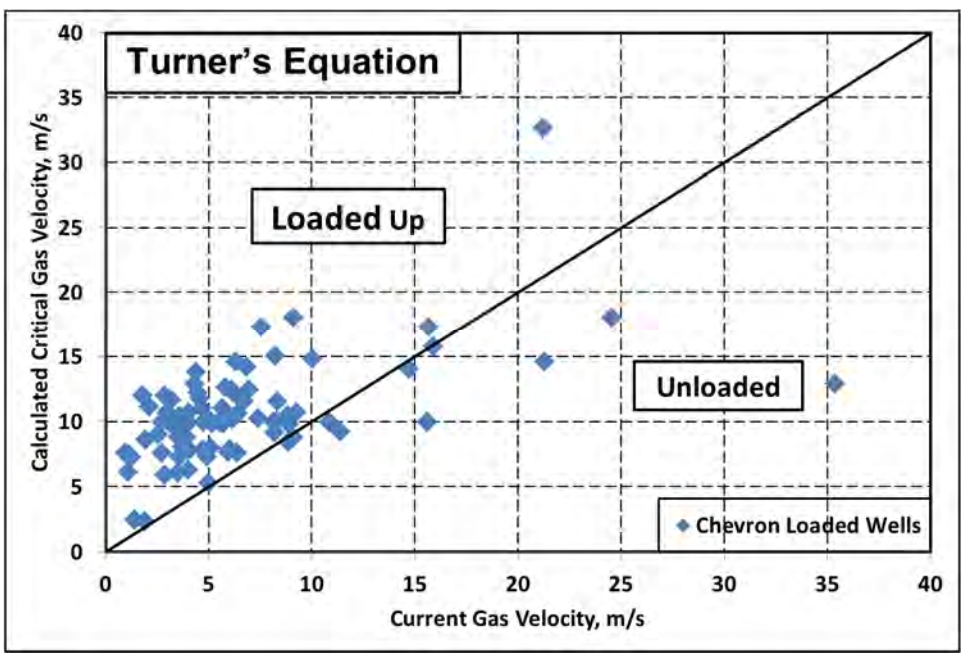

Figure 2.36: Chevron Data versus Turner's Equation Predictions

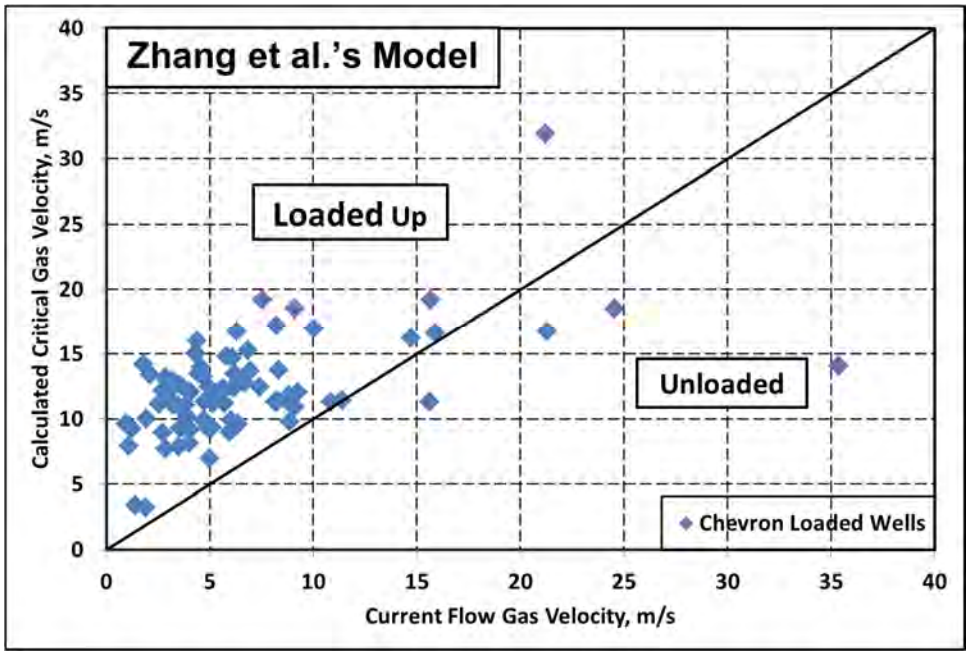

Figure 2.37: Chevron Data versus Zhang et al. Model Predictions

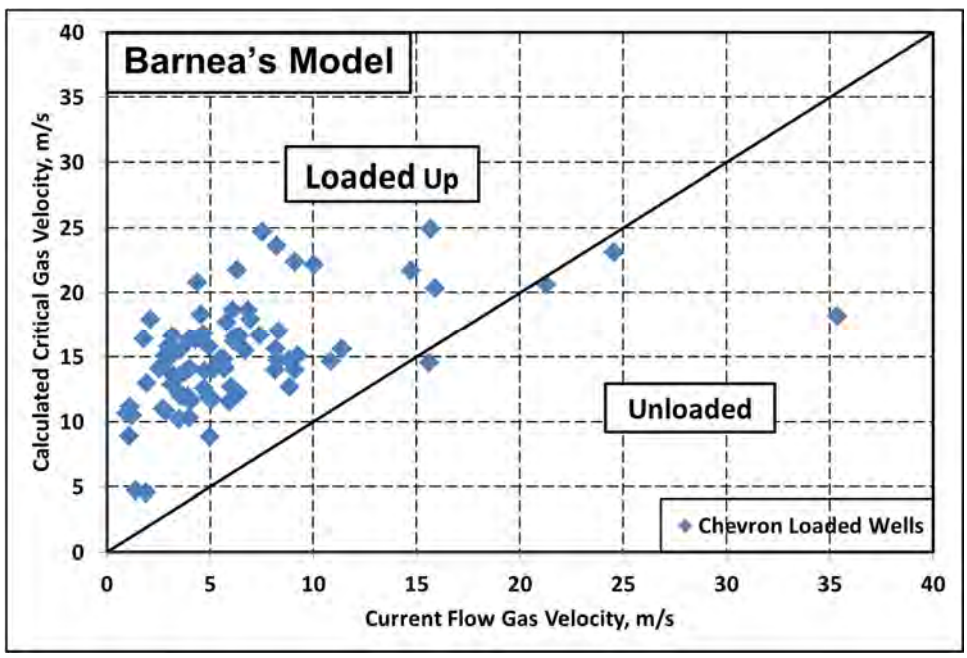

Figure 2.38: Chevron Data versus Barnea's Model Predictions

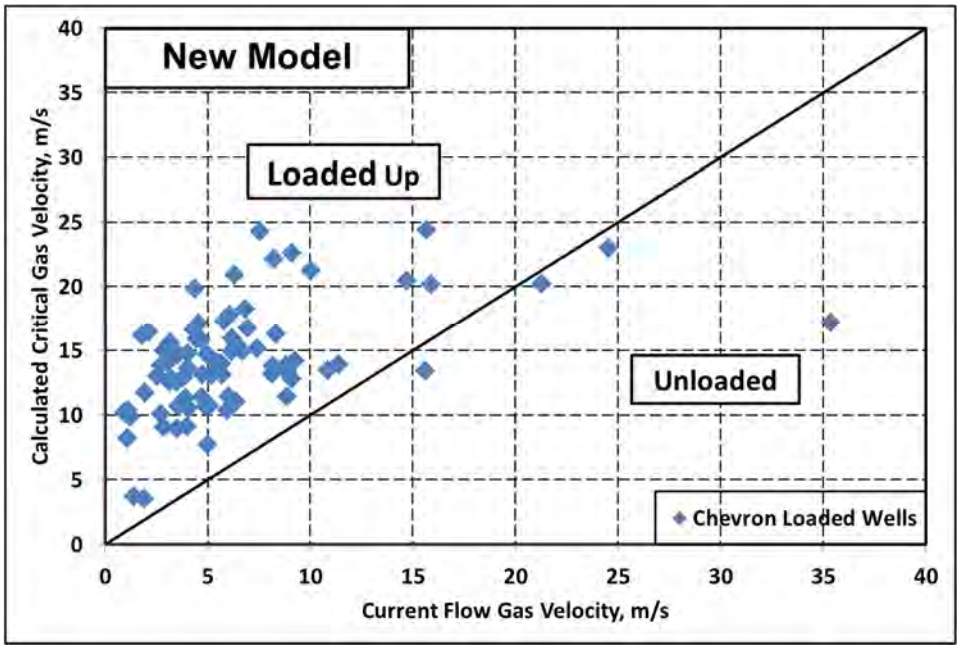

Figure 2.39: Chevron Data versus New Model Predictions

Table 2.4: Prediction Results of Chevron Data

	Correct Predictions (Total:82)	Accuracy (%)
Turner's Equation	72	88%
Zhang et al. Model	78	95%
Barnea's Model	78	95%
New Model	78	95%

For ConocoPhillips gas wells, we have minute-by-minute gas production data, which can be used to identify when the liquid loading starts. The tubing and casing divergence criteria has been used to pinpoint the liquid loading. This data is similar to Turner's data, since we have both loading and unloading wells. If prediction is accurate, we should see blue squares in the upper region and red triangles in the lower region. The result of Turner's equation is plotted in Figure 2.40. Due to underestimation of critical gas velocity, most of the loading wells are located in the unloading region (correct predictions 14/49 with 29% accuracy). In Figure 2.41, we can see that the Zhang et al. model's prediction is better than Turner's results (with total accuracy 65%). There are a lot of points in the wrong region. In Figure 2.42, Barnea's model shows good prediction results (with total accuracy 82%), which is much better than the Zhang et al. results. The new model's

prediction in Figure 2.43 is very similar to Barnea's result (with total accuracy 81%). Comparing statistics in Table 2.5, Barnea's model and new model are better than the other two models.

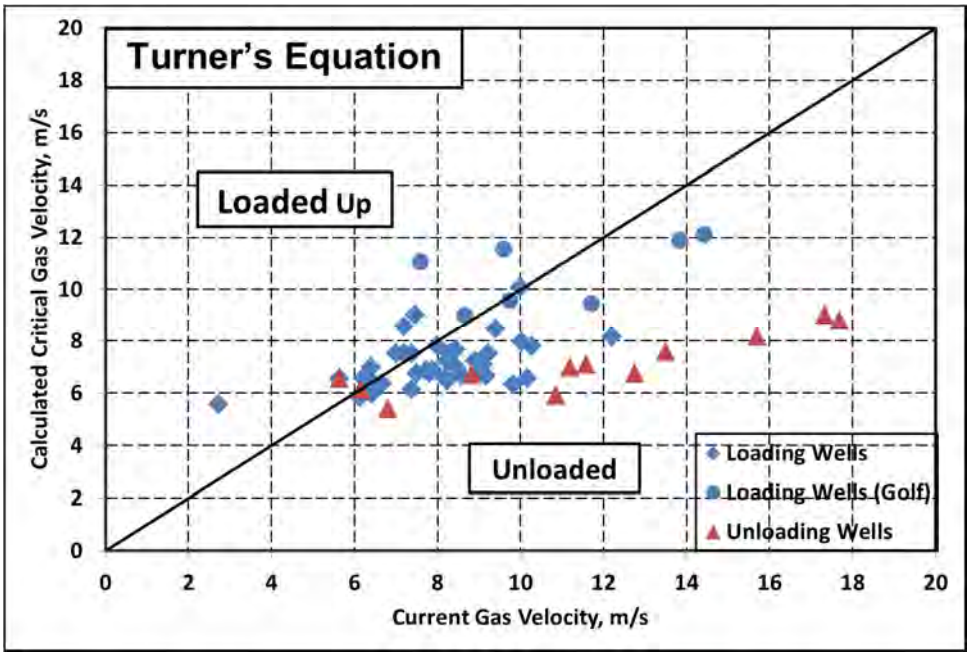

Figure 2.40: ConocoPhillips Data versus Turner's Equation Predictions

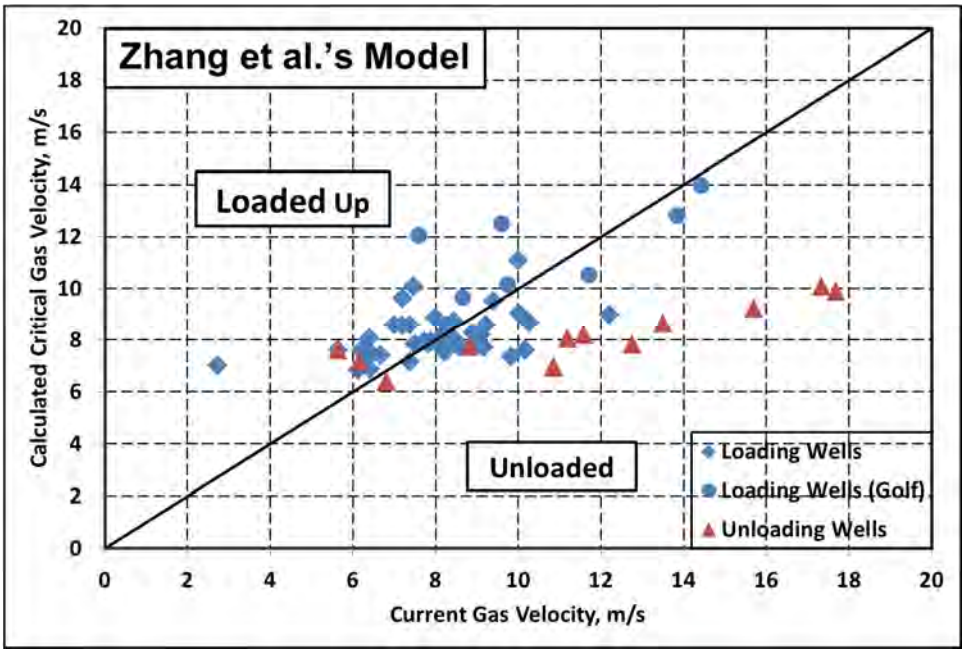

Figure 2.41: ConocoPhillips Data versus Zhang et al. Model Predictions

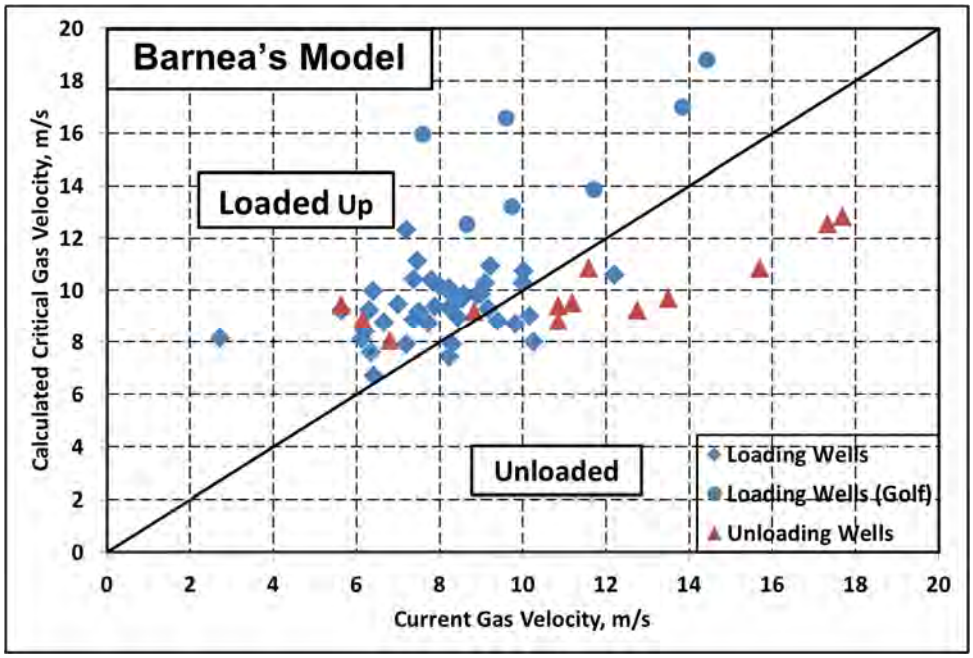

Figure 2.42: ConocoPhillips Data versus Barnea's Model Predictions

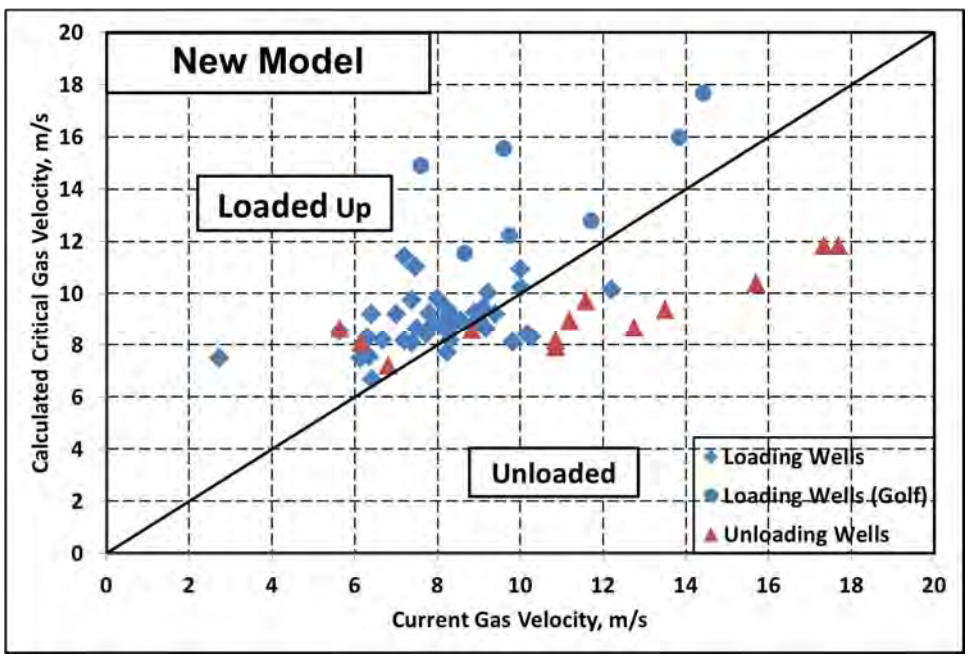

Figure 2.43: ConocoPhillips Data versus New Model Predictions

Table 2.5: Prediction Results of ConocoPhillips Data

	Correct Loaded Predictions (Total:49)	Correct Unloaded Predictions (Total:13)	Loaded Accuracy (%)	Unloaded Accuracy (%)	Total Accuracy (%)
Turner's Equation	14	12	29%	92%	42%
Zhang et al. Model	29	11	59%	85%	65%
Barnea's Model	42	9	86%	69%	82%
New Model	40	10	82%	77%	81%

In order to validate our new model (which can accommodate inclined wells) we will use the Veeken et al. data in inclined wells. In Figure 2.44, gas wells have been divided to four groups based on their inclination angle. According to experimental results, we know that maximum critical velocity is around the 30 degree inclination. For Barnea's prediction results in Figure 2.44, data with a high inclination angle is located in the wrong region, which is due to higher critical gas velocity for the inclined well. After considering non-uniform film thickness in the inclined well, the new model is able to improve the prediction for the Veeken et al. data, as shown in Figure 2.45. Note that those high inclination angle wells in the lower region are moved upward to the loaded region and very close to the loading boundary. This improvement validates the non-uniform film thickness model.

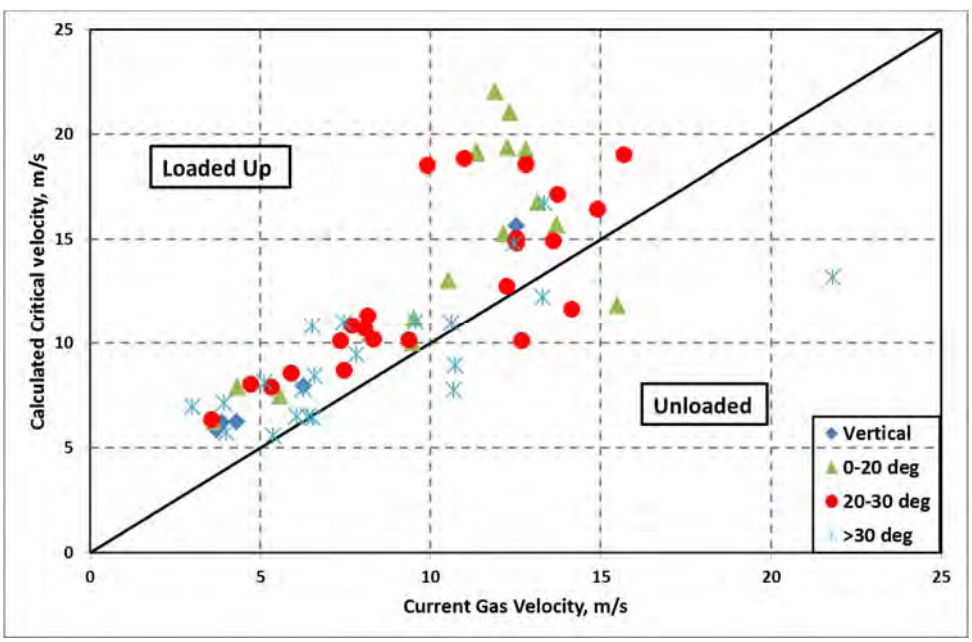

Figure 2.44: Barnea's Results of Veeken's Data at Different Inclination Angle

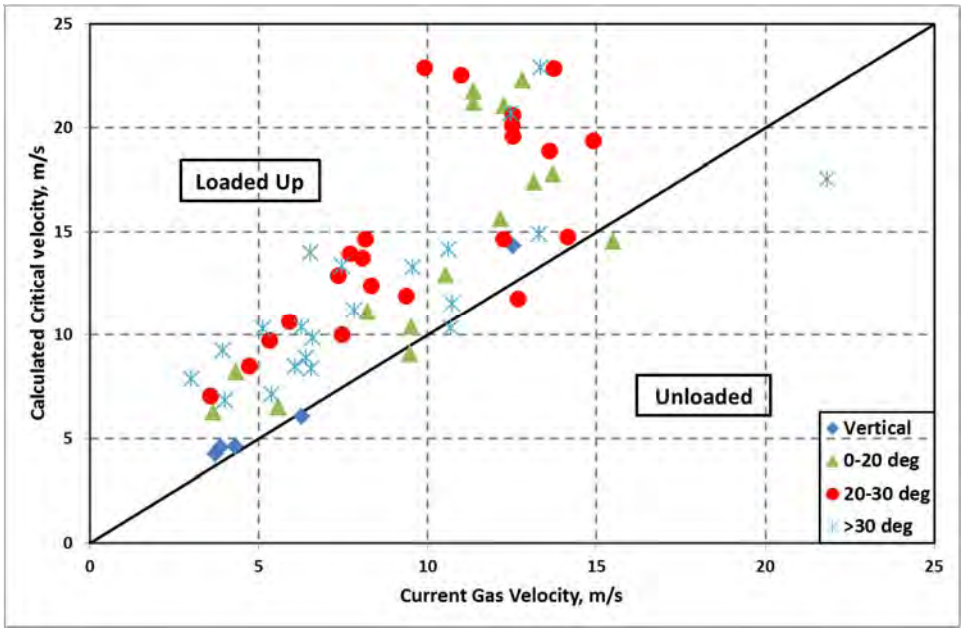

Figure 2.45: New Model's Results of Veeken's Data at Different Inclination Angle

We also compared the new model with experimental data (Yuan, 2011) of two phase flow with different inclination angle. Experimental results with 3 inclination angles (vertical, 15 degree and 30 degree) are plotted and compared with Turner's boundary and the new model's boundary, which is shown in Figures 2.46, 2.47, and 2.48. Loading data are represented by the squares and unloading data are represented by the diamonds. We can clearly see from the data that the boundary is shifted to the right as the inclination angle changes from vertical to 30 degree. The transition boundary predicted by the new model also shifts to the right with increasing inclination angle, whereas Barnea's boundary shifts to the left. Although the data for the vertical position does not match well with the prediction, the trend of increasing critical gas velocity is clear and predictions of the new model match with experimental data at 15 and 30 degrees.

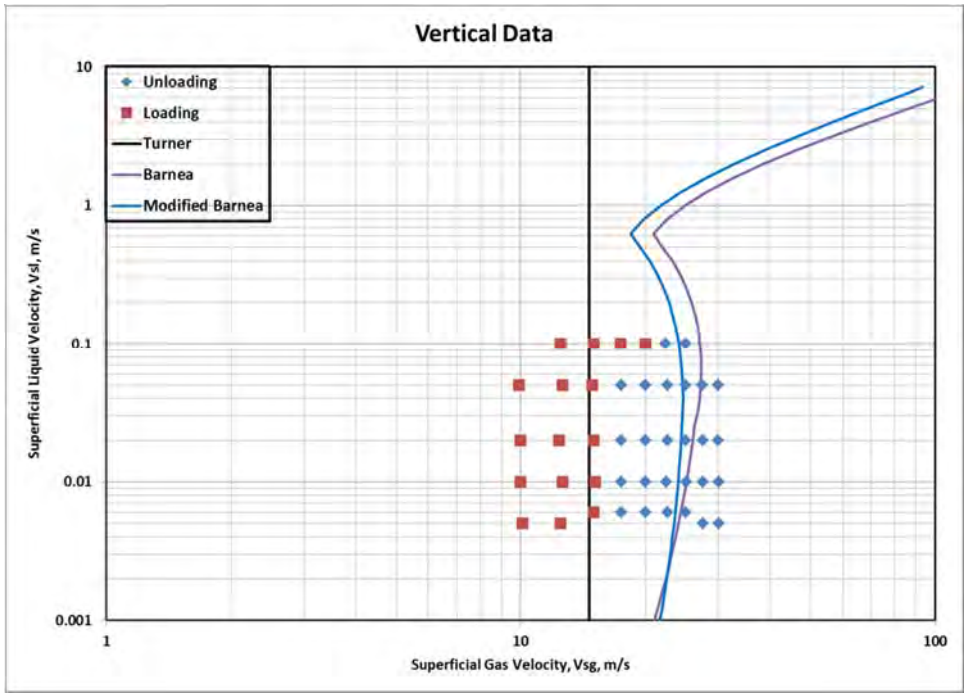

Figure 2.46: Experimental Data (Yuan, 2011) (Vertical)

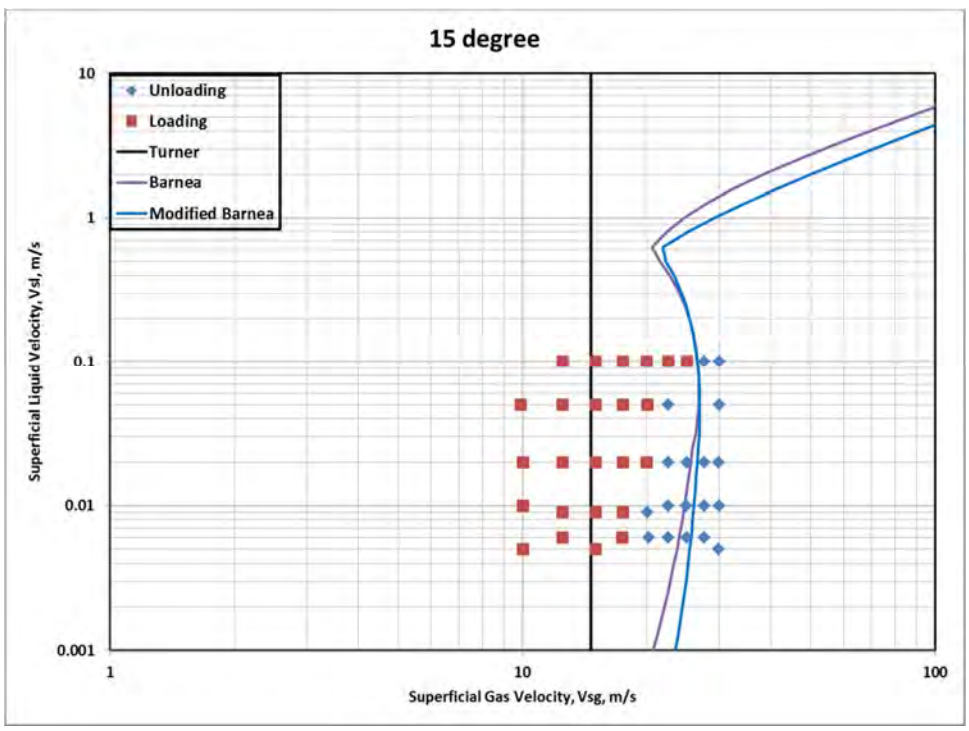

Figure 2.47: Experimental Data (15 degree) (Yuan, 2011)

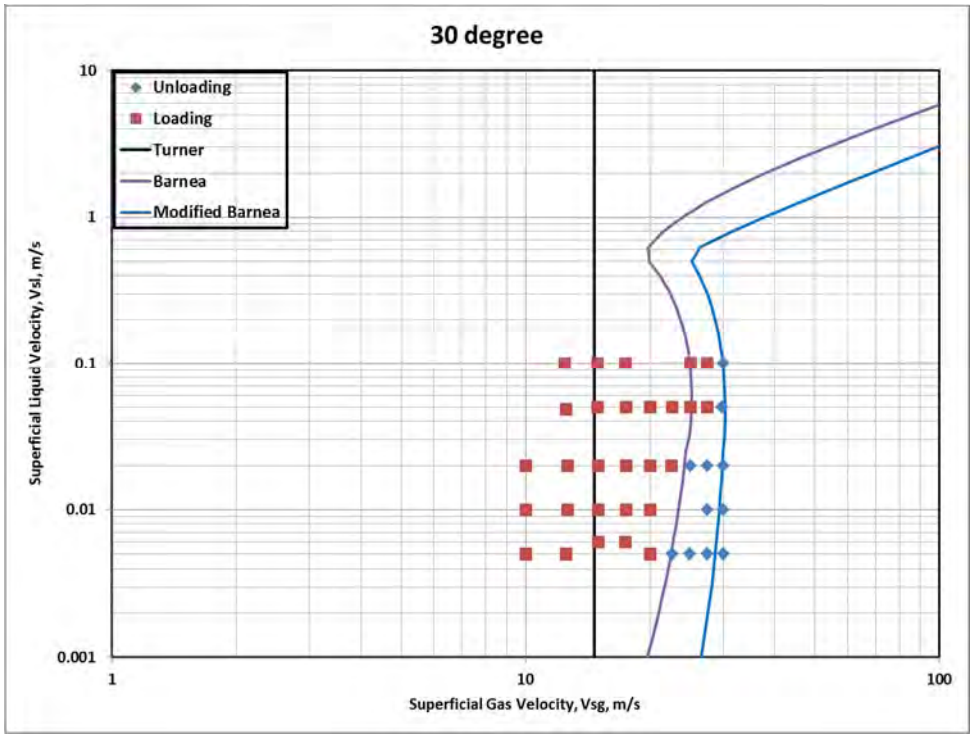

Figure 2.48: Experimental Data (30 degree) (Yuan, 2011)

To summarize the results in this section, we have developed a new model to predict the inception of liquid loading. The new model is based on liquid film reversal. Compared to other literature model, the proposed model is capable of accounting for pipe diameter and pipe inclination angle. The comparison of the model with field as well as laboratory data indicates that the proposed model is superior to other existing models.

Foam Flow

This section discusses the effect of surfactant (foam) on liquid loading. The section is divided into several sub-sections. We first discuss the experimental procedures we used. We have two facilities developed specifically for this purpose: small scale and large scale, and we discuss both of them. We follow that with the results obtained from both the small scale and the large scale facilities. We then discuss the model proposed to predict both the inception of liquid loading under foam flow conditions as well as the pressure drop prediction for foam flow.

Experimental Methods

We have two experimental facilities: small scale and large scale. Both are described in this section. In both these facilities, we tested five different surfactants. We list in Table 3.1 the five surfactants we investigated. The surfactants selected in this investigation represent all the possible types of surfactants typically used in the

industry: anionic, amphoteric, sulphonate, and cationic. We wanted to ensure that the range of experiments we have cover as broad range as possible.

Table 3.1: Surfactants Studied in this Investigation

Product Name	Surfactant Type	Specific Gravity	Chemical Composition	Weight %
MC MXI 4-2158	ANIONIC	1.0375 - 1.0625	Surfactant Isopropyl alcohol	Varies 5-10
MC MXI 4-2557	AMPHOTERIC I	1.0935 – 1.1185	Surfactant	30-60
MC-MX 4-3311	AMPHOTERIC II	1.0413-1.0663	Surfactant NaCl	15-40 5-10
MC-MXI 4-2160	SULPHONATE (ANIONIC)	1.0657 – 1.0907	Dodecane-1-sulfonic acid, Na Salt	10-30
			1-Dodecanesulfonic acid, hydroxyl-, Na salt	10-30
			1-Dodecene	1-5
			Sodium sulfate	1-5
MC-MX 4-3442	FLUOROCHEMICAL CATIONIC SURFACTANT	1.3375-1.3625	Fluorochemical cationic Surfactant	10-30
			Hexylene glycol	7-13

<u>Small Scale Facilities</u>

Four different experiments were conducted on bench top facilities; these are as follows:

- Surface tension tests
- Foam unloading test (at room temperature with de-ionized water)
- Foam stability tests (at room temperature with de-ionized water)
- Foam unloading tests (in two different brine compositions at room temperature) and foam stability tests (in two different brine compositions at room temperature and at 150 degree Fahrenheit).

It is important to measure surface tension so as to determine the theoretical optimum critical concentration at which a given surfactant is most effective in unloading liquid from a vertical gas well. Figure 3.1 displays a schematic of the Tensiometer we used in measuring surface tension. This device works on the principle of the pendant drop method which involves the determination of the profile of a drop of the test solution in air at mechanical equilibrium; from this, the surface tension is determined using a software.

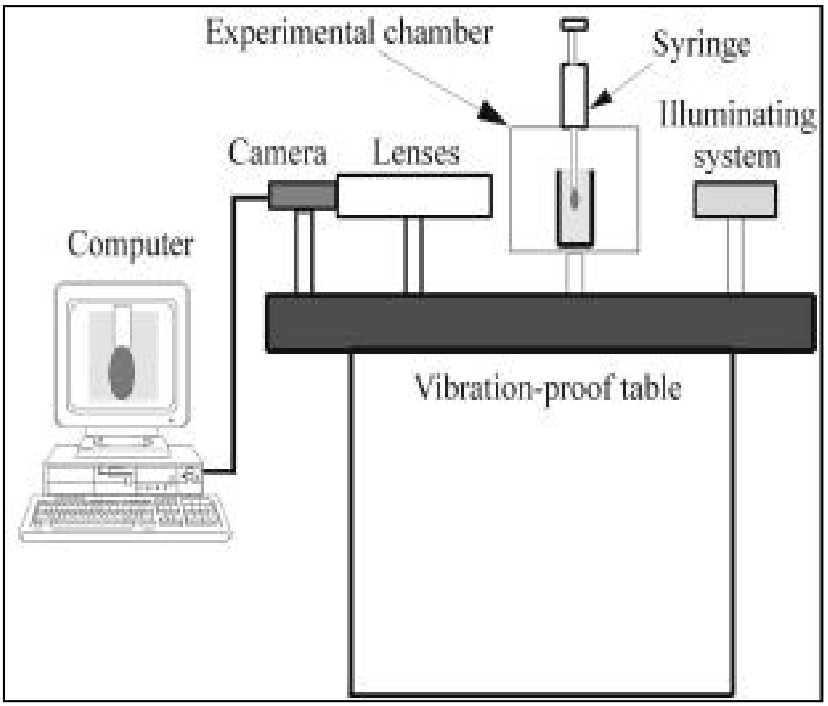

Figure 3.1: Pendent Drop Apparatus (Arashiro and Demarquette, 1999)

The profile of the captured droplet of the test solution in the experimental chamber surrounded by the air (second medium) is as shown in Figure 3.2.

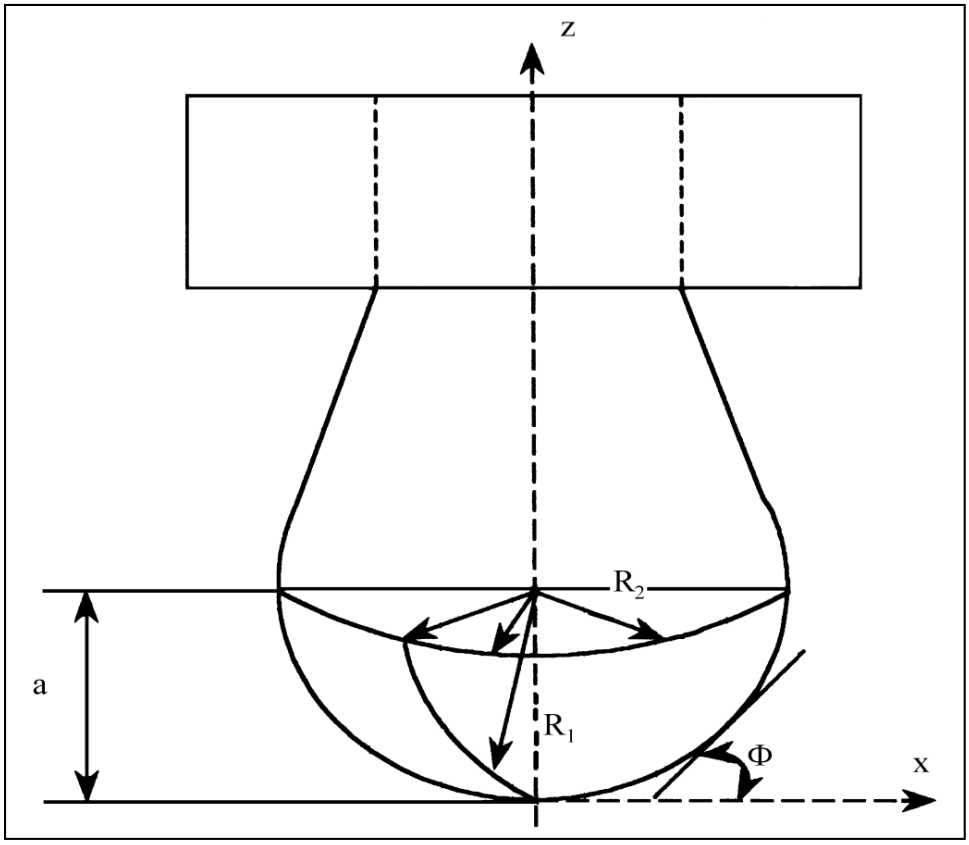

Figure 3.2: The Pendent Drop Geometry (Arashiro and Demarquette, 1999)

Determination of the surface tension starts from the Laplace equation which states the relationship between interfacial pressure ΔP and radii of curvature R_1 and R_2. This relationship is given by

$$\Delta P = \gamma \left(\frac{1}{R_1} + \frac{1}{R_2}\right), \tag{3.1}$$

For a drop or capillary that is symmetric about the central vertical axis, the pressure drop, ΔP, can be written as a function of gravity and densities of the drop and surrounding media (air for our case). If $\Delta\rho$ is the difference in densities, g the acceleration due to gravity and h the height in the drop, then the pressure drop can be written as

$$\Delta P = \Delta\rho g h. \tag{3.2}$$

The combination of Equations 3.1 and 3.2 is called the Laplace-Young equation. This is given by

$$\Delta\rho g h = \gamma \left(\frac{1}{R_1} + \frac{1}{R_2}\right). \tag{3.3}$$

R_1 and R_2 are measured from the drop profile as shown in Figure 3.2 using a software. When these are expressed in X-Y coordinates, a differential equation results with no analytical solution. The equation of Bashforth and Addams (1982) is a numerical solution to the Laplace–Young equation with R_1 and R_2 in X-Y coordinates. It relates the drop profile to the interfacial tension through a nonlinear differential equation. Details of this can be found in the publication of Arashiro and Demarquette. (1999).

The test solution at the desired concentration of the surfactant is placed in a shell and pumped to the experimental chamber where a droplet is formed. A camera captures the droplet image and software installed on the computer digitizes the image of the pendant drop. The software also extracts the drop contours, determines the radius of curvature at the apex of the droplet and smoothens the extracted contours using polynomial regression. Finally, the theoretical and experimental drop contours are compared to infer the surface tension value. The process is repeated at specified time intervals pre-set by the user.

The result obtained is the surface tension value with a preset time. Average of these values is obtained and reported at the surface tension of the test solution. The concentration in each test solution is increased and corresponding surface tension value is recorded until we no longer see changes in the surface tension value. The concentration of the solution at this point is termed the critical micelle's concentration (CMC). This shows that micelles have occupied the liquid interface and further increase in the surfactant concentration will not reduce the surface tension value any further.

Figure 3.3 shows a picture of the unloading rig facility. The facility is divided into four sections; these are the air supply section, the main test cell, the heating section and the weighing section.

Figure 3.3: Unloading Test Facility

The gas source is an air compressor which supplies compressed air at pressures above 80 psi. The air supply line to the facility has a pressure regulator to reduce the pressure to 18 psi and after this we have an air filter to remove dust particles and moisture from the air. The dry air is then passed through a Rosemount flow controller which has a precision +/- 0.0001 LPM. Upon exit from the flow meter, the air is passed through a three way valve which either diverts the incoming gas to the atmosphere (before the test starts) or diverts the air into a check valve at the base of the column (when the test is in progress). The check valve prevents backflow of the test solution into the airline when the test is not in progress.

The main test cell is a 2-inch inner diameter 3-ft tall and 0.25-inch thick transparent acrylic pipe. It is equipped with a 22 micron 2-inch diameter and 0.125-inch thick ceramic sparger at its base. The sparger gives uniformly distributed foam texture hence we have a controlled experiment from one test to the other. This sparger size was selected for the experiment because it gave the most consistent foam structure during the facility preliminary testing stage. An acrylic carryover arm of the same specification as the test cell is fitted to the top of the test column to carryover air-water foam solution from the column to a collector placed on a weighing scale.

The heating section consists of a silicon rubber heater which is controlled using a thermostat and temperature sensors. The heat generated from the heating jacket around the test column is used to sustain the heat of the pre-heated test fluid in the test column to reduce heat lost during high temperature test.

The weighing section consists of a Mettler Toledo M3600 weighing scale with a precision of +/_0.01g. It captures the mass of the unloaded solution and displays the values online real time on the computer for post experiment analysis.

750 mL of the test solution at desired concentration of the surfactant is placed in the test column. The air flow controller is preset to desired gas rate for the test and the scale is equally activated. The test starts by switching the air flow in the three way valve from the atmosphere to the airline below the test column. The air flows through the sparger and makes foam upon passing through the sparger and entering the test column. Unloaded air-water foam solution is collected in the collection pan for 30 minutes and the test is stopped, or the test is stopped if the unloading stops before 30 minutes.

Data gathered is the mass of liquid unloaded in 10 minutes. The unloading rate is reported as the percent of liquid transferred from the column to the collector in ten minutes after the test is started.

$$Mass\ Unloaded, (\%) = \frac{w_{t=0\ minutes}}{w_{initial}} 100, \tag{3.4}$$

Figure 3.4 shows a picture of the stability test facility. It is same as the facility described in section 3.1.2 for the unloading test. However, it does not require a carryover arm and the weighing scale.

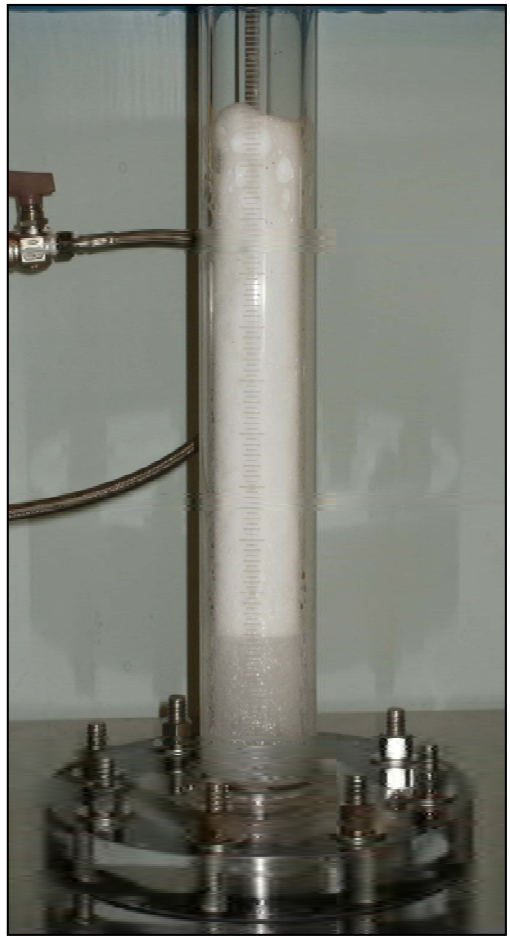

Figure 3.4: Stability Test Facility

We have simply modified the facility from the unloading test for the stability test so as to preserve the foam quality generated in both tests.

To conduct the stability test, we only use 100 mL of the fluid Also, we stop sparging air as soon as all the fluid is converted into foam. At the instant the test is stopped, the draining fluid interface is physically monitored with a hand held camera mounted on a camera stand. As the height of the draining fluid increases, the camera is ramped up so as to record the height of the fluid. Also, at the instant of stopping the test, the height of the foam generated is noted. Data collected are the height of foam, volume of liquid draining from the foam with time and half-life of the foam. The half-life of the foam is the time taken to recover 50% of the initial test solution from the foam structure formed after air sparging stops.

We used the same procedures in conducting stability and unloading tests using two different brine compositions as the base fluid. Furthermore, the stability tests were conducted using brine at 150 degree Fahrenheit. For these tests, the heating jacket is wrapped around the column and turned on for about 5 hours before the experiment starts. The test solution is then pre-heated to 150^{0}F. This is

then poured using a rubber hose into the column. The pre-heated column sustains the temperature of the pre-heated fluid poured into the column. The test is started when temperature probe indicates that the temperature of the test fluid is steady at 150^{0}F. The unloading test was not conducted at high temperature. The parameters collected in the brine at room temperature tests and brine at high temperature tests are same as those collected when de-ionized water was used as the base fluid.

The composition of the brines used for these tests are discussed next. Brine I is 150g of Morton rock salt dissolved in one liter of de-ionized water. This has been recommended because the rock salt is representative of the composition of sea water. The density of the resulting solution is 1.0957 g/cm^3. Brine II was formulated in the Laboratory based on common composition of the water found in the Gulf of Mexico. This consists of 8743.6 g of de-ionized water, 1140 g of sodium chloride and 111g of calcium chloride.

<u>Large Scale Facilities</u>

The facility used for conducting the large scale test is same as that used by Skopich (2012). Figure 3.4 shows a schematic of this facility.

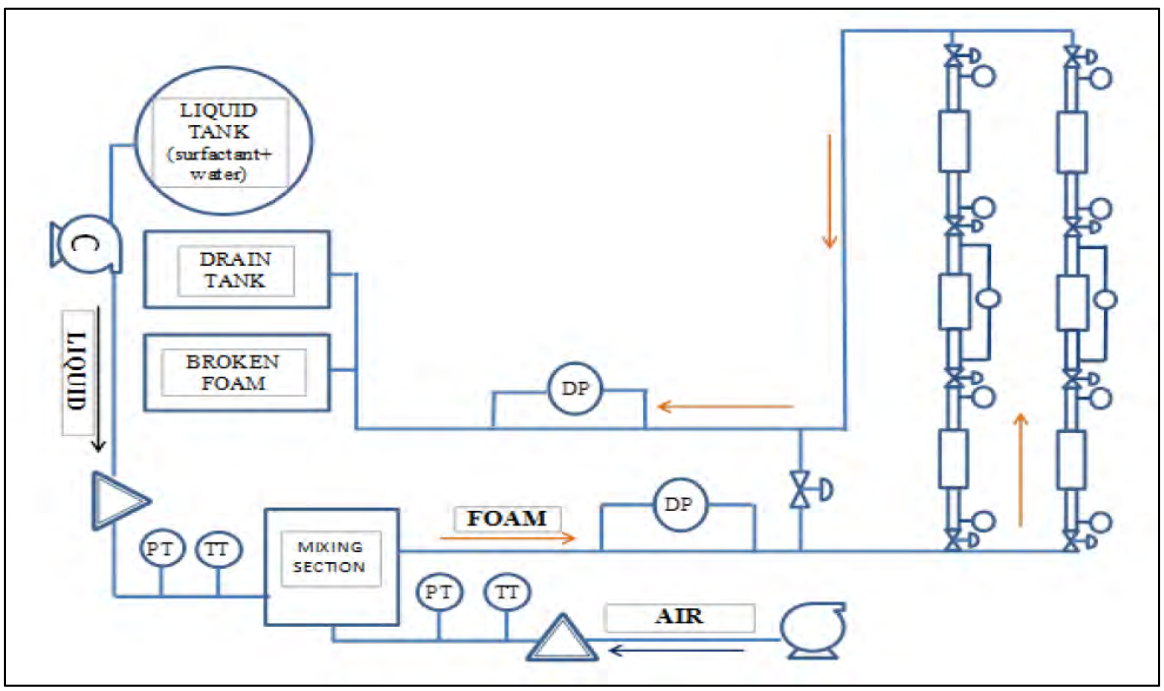

Figure 3.5: Foam Flow Loop Schematic

Detailed description of the pressure and temperature measuring devices, trapping sections with quick closing valves, air-water foam mixing section and the video observation section of the facility can be found in Skopich (2012). We have a liquid tank in which surfactant and water are mixed. The liquid flows into mixing section where gas is introduced. Both liquid and gas flow rates are measured. The foam flows through either 2” or 4” sections which are 40 feet tall. Pressure

transducers are installed on the pipes to measure the pressure values. In addition, a differential pressure is used to measure pressure drop in the middle section of the pipe. The pipes are also equipped with quick closing valves so that the in-situ liquid hold up can be measured accurately. The foam is circulated back into another tank where the residence time is long enough to break the foam. Both the pipe sections are equipped with high speed cameras so that videos as well as pictures can be taken of the foam flow in the pipe as well as how the liquid hold up changes as a function of time.

The facility has three 2000 gallons storage tanks made of plastic: one is vertical while the other two are horizontal. 1600 gallons of test fluid at desired concentration is prepared for every test; this is placed in the first tank. The solution is pumped through a galvanized steel horizontal line to a liquid Micro motion flow meter. A manual needle valve is used after the liquid flow meter to regulate it to the desired flowrate. The liquid is then flown to the mixing section. Air from the air compressor is flown through a back pressure regulator to isolate the air output from the disturbances at the upstream (compressor) and this is then passed through an air Micro motion flow meter. A ball valve is used after the air flow meter to regulate it to the desired flowrate. The air is passed through a wire mesh to simulate air flow from porous media and then mixed with the test fluid to produce foam.

Produced foam is then flown through a horizontal section to either a 2-inch or 4-inch vertical riser. The risers are each equipped with one three way valve and four quick closing valves in that order from the base. When the facility is in operation, the three way valve in either riser is maintained in the closed position so flow is only upward through the riser. The four quick closing valves in each riser make up three trap sections when all are closed. Each section is approximately 3.44 m long. The quick closing valves in either the 2-inch or 4-inch riser are set to open mode when foam is flowing through the selected riser. The middle section has a pressure drop transducer while the first and last sections have absolute pressure transducers. Produced foam is allowed to flow through the facility until steady state is achieved; this is decided by allowing the foam to flow through the facility for five minutes after the foam has started dropping from the top of the return line.

After the flow has attained steady state, the LabVIEW software is switched on to record data. Data recorded are differential pressure in the second section, absolute pressure values in the first and third sections, absolute pressure values and absolute temperature values in the mixing section. The high speed camera is placed on the middle platform of the tower adjacent to the second section of each of 2-in and 4-inch pipes. Images of foam flow are recorded at the same time as when data is being recorded by the LabVIEW software. However, the high speed recording ends after about 10 seconds. At the end of 3 minutes, we stop collecting data by switching off the LabVIEW software. At this instant, the four quick closing valves in the riser under operation are simultaneously shut and a bypass quick closing valve is opened to allow flowing foam to bypass the two risers and flow from the horizontal pipe

section after the mixing section to another horizontal pipe section at the base of the return line/riser.

We have collected two sets of data. For the first set of data collected, the following procedures are undertaken after shutting the quick closing valves. The needle valve after the micro motion flowmeter for liquid is closed to stop the flow of liquid. Compressed air rate is increased so as to flush the foam in the horizontal flow lines to the spent fluid tanks. The ball valve after the air micro motion flowmeter is then closed so as to stop the flow of air. The last quick closing valve at the base of the first section is then selectively opened. Further, selected riser is opened at the base after the quick closing valve. This permits the foam trapped in this section to flow to the surrounding as a waste. A hose with water flowing at a jet speed is inserted into the first section to clean the foam in it. The base of the tower is then closed and we wait for the water used in cleaning the first section to drain off. After this, a liquid collector is placed at the exit of the pipe extending from the three way valve. The three-way valve is then opened. The second quick closing valve is then opened and the foam trapped in the second section will flow into the liquid collector after the three-way valve. The foam collected breaks down into liquid and its volume is measured using a graduated plastic cylinder. Liquid holdup for this test is obtained from Equation (3.5).

$$Liquid\ Holdup = \frac{Volume\ of\ liquid\ collected}{Volume\ of\ pipe\ in\ the\ middle\ section}, \tag{3.5}$$

The three way valve is then closed to permit upward flow, the bypass valve isolating the horizontal section from the riser is then closed, the first two quick closing valves that were selectively opened are then closed and all four quick closing valves on the riser are opened at once. This signifies the end of a test and another test can be performed.

For the second set of data collected, the following procedures are undertaken after shutting the quick closing valves. An operator on the middle platform of the tower adjacent to the second section of the riser manually records the height of the foam formed. This operator also notes the volume of the liquid draining from the foam and the corresponding height of foam at every minute afterwards. The final liquid volume is recorded when there is no change in the volume of the liquid draining from the foam with time. The dissipation in foam height and corresponding rise in liquid drained from the foam structure are illustrated in Figure 3.6.

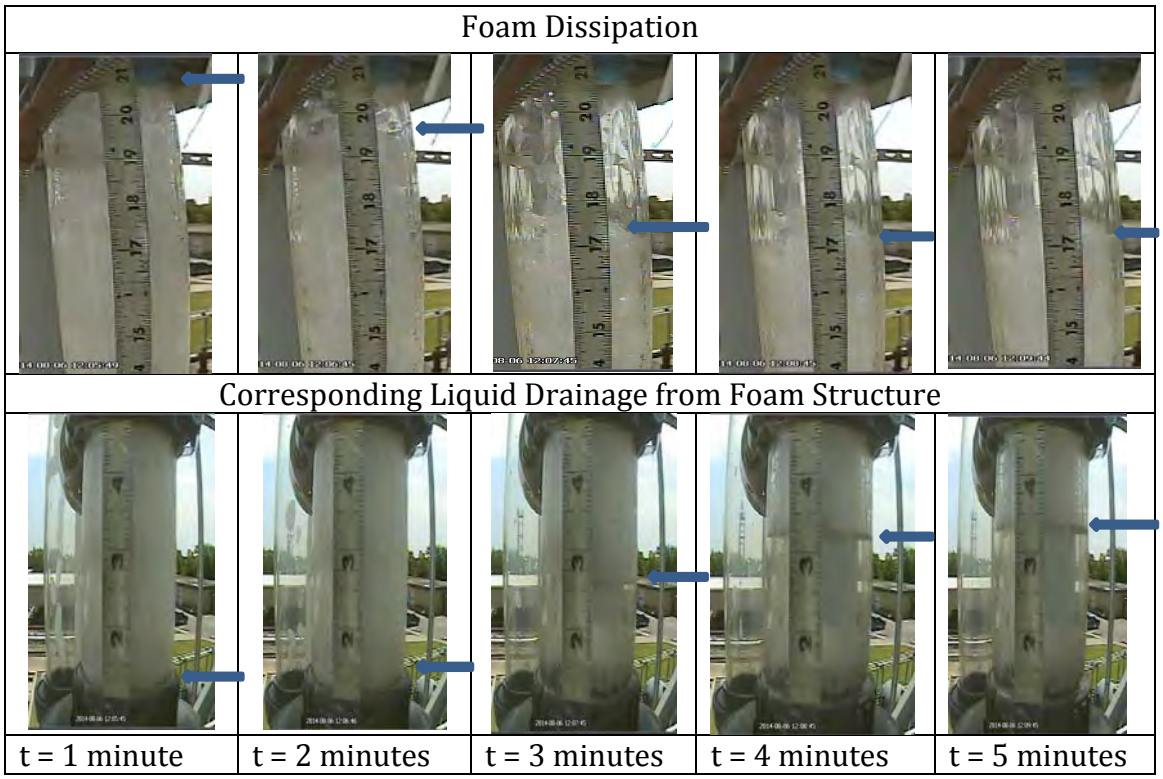

Figure 3.6: Foam Structure as a Function of Time in the Middle Section

From the information gathered, foam holdup and fraction of the gas in foam are calculated as follows:

$$Foam\ Holdup, (h_f) = \frac{Vol_{initial\ foam}}{Vol_{Pipe\ in\ second\ section}}, \tag{3.6}$$

$$Fraction\ of\ gas\ in\ foam, (f_g) = \frac{Vol_{initial\ foam} - Vol_{final\ liquid}}{Vol_{initial\ foam}}, \tag{3.7}$$

The four quick closing valves on the riser in use are then opened, the system is flushed with compressed air and this signifies the end of a test and another test can be conducted.

Test Matrix

The surfactant concentrations used for the bench top experiments are those before and after the critical micelles concentration are obtained for each surfactant from the surface tension test. The concentrations used for the brine and high temperature tests are those at half-life of each surfactant except or the Sulphonate surfactant where two different concentrations are used. For the large scale test, two types of experiments were conducted; the base case where tap water is used as liquid and foam flow experiment where tap water is dosed with surfactant of desired concentration. Two superficial liquid velocities were selected and the superficial gas velocities were selected to cover the entire range of annular to

intermittent flow as is indicated on two phase vertical flow pattern map. Details of the test matrix are as shown in the following tables.

Table 3.2: Test Matrix for Stability Test at Room Temperature in Deionized Water

Test Variables	Anionic	Amphoteric I	Amphoteric II	Sulphonate	Cationic
Sparger Size, (micron)	22	22	22	22	22
Initial Test Volume, (mL)	100	100	100	100	100
Gas Flowrate, (LPM)	0.35, 0.40	0.75, 0.80	0.75, 0.80	0.35, 0.40	0.75, 0.80
Concentrations, (ppm)	400, 600, 800, 1000, 1600, 2000, 2400, 3000	100, 200, 300, 400, 600, 800, 1000	600, 800, 1000, 1400, 2000, 3000	400, 600, 800, 1000, 1200, 1600, 2000	800, 1000, 1200, 1600, 2000, 2400, 3000, 4000, 5000

Table 3.3: Test Matrix for Stability Tests at Room and High Temperatures in Brine I and II

Test Variables	Anionic	Amphoteric I	Amphoteric II	Sulphonate	Cationic
Sparger Size, (micron)	22	22	22	22	22
Initial Test Volume, (mL)	100	100	100	100	100
Gas Flowrate, (LPM)	0.40	0.80	0.80	0.40	0.80
Concentrations, (ppm)	1600	600	1000	400, 1000	3000
Test Medium	Brine I at 74°F Brine I at 150°F Brine II at 74°F Brine II at 150°F				

Table 3.4: Test Matrix for Unloading Test at Room Temperature in Deionized Water

Test Variables	Anionic	Amphoteric I	Amphoteric II	Sulphonate	Cationic
Sparger Size, (micron)	22	22	22	22	22
Initial Test Volume, (mL)	750	750	750	750	750
Gas Flowrate, (LPM)	0.50, 0.75	0.50, 0.75	0.50, 0.75	0.50, 0.75	0.50, 0.75
Concentrations, (ppm)	400, 600, 800, 1000, 1600, 2000, 2400, 3000	100, 200, 300, 400, 600, 1000	100, 200, 300, 400, 600, 800, 1000, 1400, 2000, 3000	400, 600, 800, 1000, 1200, 1600, 2000	800, 1000, 1200, 1600, 2000, 2400, 3000, 4000, 5000

Table 3.5: Test Matrix for Unloading Test at Room Temperature in Brine Solution

Test Variables	Anionic	Amphoteric I	Amphoteric II	Sulphonate	Cationic
Sparger Size, (micron)	22	22	22	22	22
Initial Test Volume, (mL)	750	750	750	750	750
Gas Flowrate, (LPM)	0.50, 0.75				
Concentrations, (ppm)	1600	600	1000	400, 1000	3000

Table 3.6: Test Matrix for Large Scale Test

	Anionic	Amphoteric I	Amphoteric II	Sulphonate	Cationic
Pipe Diameter, (in)	2, 4				
Vsg, (m/s)	1.85 – 25 (based on pipe diameter)				
Vsl, (m/s)	0.01 , 0.03				
Concentrations, (ppm)	400, 800, 1200, 1600, 3000	200, 400, 600, 1000	400, 600, 800, 1000	400, 800, 1200	800, 1200, 2400

Experimental Data Collection and Observations

In this section, we present the results of the experiments conducted on Bench Top Facilities and Large Scale Facility as explained in previous section. We provide plausible explanations for the trends seen in all the plots. The results are divided into broad groups: results from experiments conducted on Bench Top Facilities (small scale) and results from experiments conducted on Large Scale Facility.

Small Scale Facilities – Experimental Results

We cover the results first for de-ionized water and then we discuss what we observed when we used brine solution.

Figure 3.7 shows the results of the surface tension tests conducted on de-ionized water; our base fluid for the bench top test.

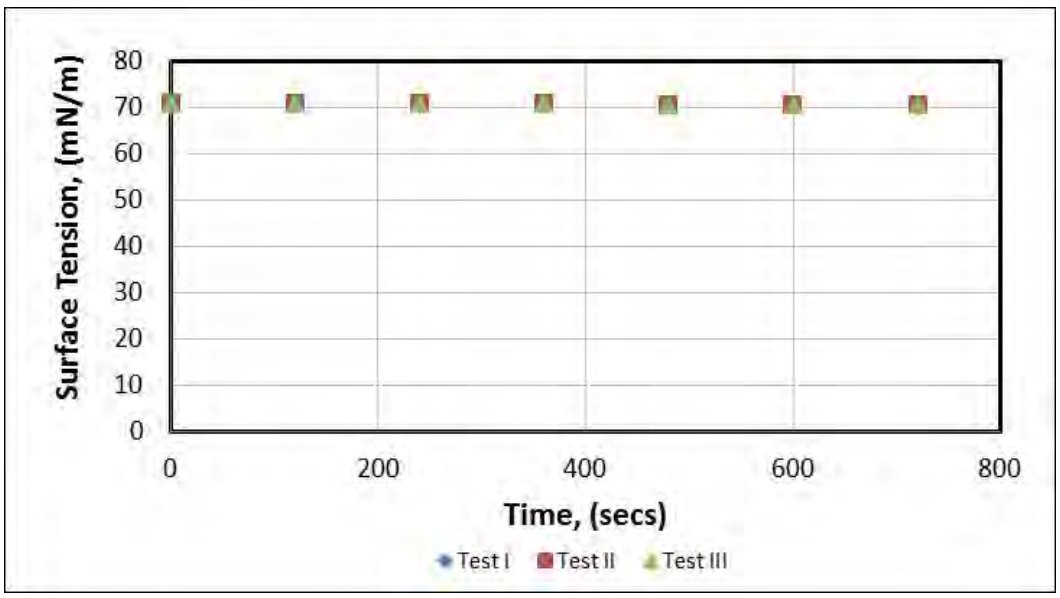

Figure 3.7: Surface Tension as a Function of Time

For each test, the surface tension value is noted at two minutes interval; this is recorded for at least 12 minutes. The software gives the mean surface tension value of each test run. The test is then repeated three times so as to ensure we have good repeatability. The average of the mean from the three tests is reported as the surface tension of the solution being tested.

Figure 3.8 shows the surface tension results from the Tensiometer for the five chemicals tested.

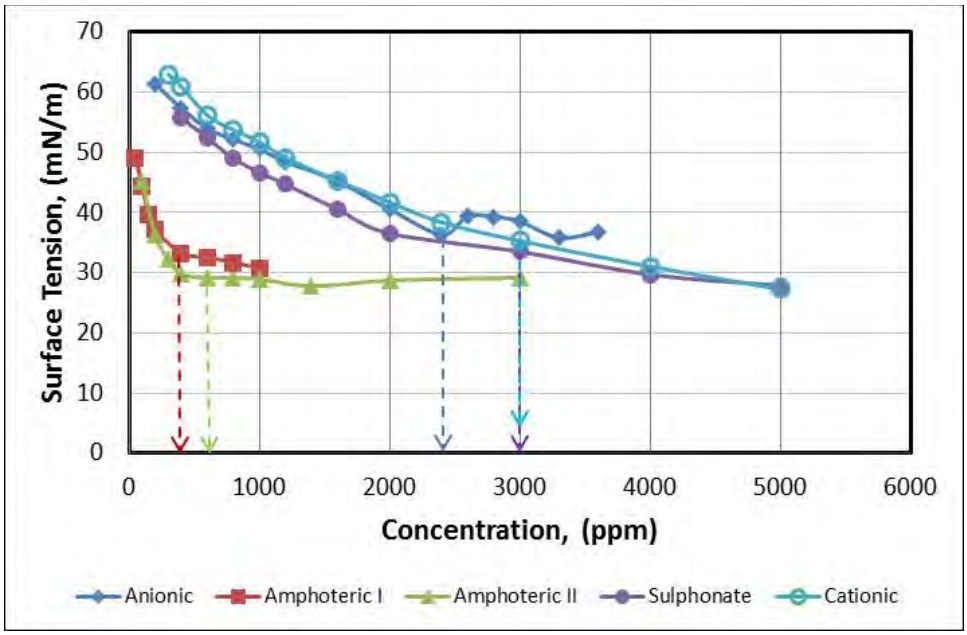

Figure 3.8: Surface Tension Result of All Surfactants Tested

By comparing Figures 3.7 and 3.8, it can be seen that a slight addition of surfactant will always reduce the surface tension value from 71 mN/m to lower values at any concentration of each of the surfactants.

From Figure 3.8, theoretically, the critical micelle's concentration (CMC) for the Anionic, Amphoteric I, Amphoteric II, Sulphonate and Cationic surfactants are 2400 ppm, 400 ppm, 600 ppm, 3000 ppm and 3000 ppm respectively. The CMC is defined as the concentration of surfactants at which micelles form and all additional surfactants added to the solution go to micelles. Before reaching the CMC, the surface tension changes strongly with the concentration of the surfactant. After reaching the CMC, the surface tension remains relatively constant or changes with a lower slope. The CMC provides an optimum concentration for each surfactant which will be used in our subsequent experiments.

Foaming Capacity in De-ionized Water at Room Temperature: To enhance variability and in order not to lose important trends, there is a need to determine what minimum gas rate and what minimum concentration is appropriate to sparge 100 mL of a given surfactant solution. The stability test is started with a trial and error procedure which involves increasing the gas rate and concentration gradually until we find the least combination of these variables that can cause 100 mL of the test solution to sparge completely. Figure 3.9 shows the least gas rate and least concentration that will completely sparge 100 mL of test solution for the five surfactants tested.

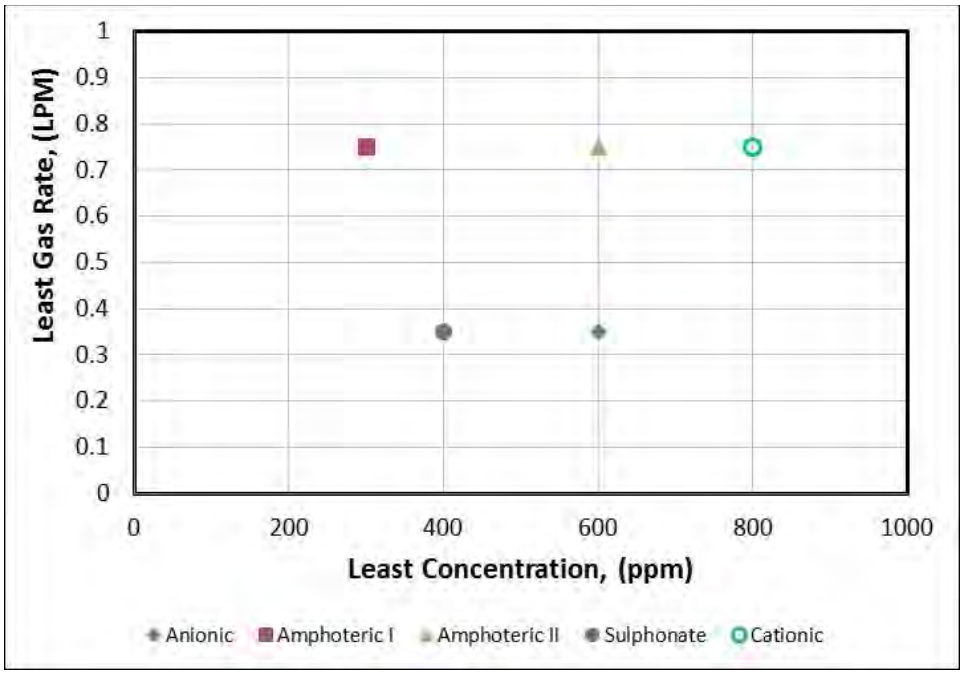

Figure 3.9: Least Gas Rate and Least Concentration for Sparging 100 mL of Test Solution

On the basis of our test conditions, Figure 3.9 reveals that 100 mL test solution of Sulphonate surfactant cannot be completely sparged at a gas rate below 0.35 LPM and at a concentration below 400 ppm. Likewise, 100 mL of Amphoteric I surfactant cannot be completely sparged at a gas rate below 0.75 LPM and at a concentration below 300 ppm. Accordingly, the anionic and sulphonate surfactants exhibited a higher foaming capacity than the other formers at room temperature in de-ionized water. The anionic and sulphonate surfactants require less agitation to initiate foaming while Amphoteric I, Amphoteric II and Cationic surfactants require more agitation to initiate foaming in de-ionized water at room temperature.

Repeatability of Experiments: For Anionic surfactant, to confirm that there is repeatability in the experimental procedure, the stability test is conducted three times using the same solution. Figures 3.10 and 3.11 show the drained volume of liquid with time for Anionic surfactant at 0.35 LPM and 0.40 LPM for 600 and 2400 ppm respectively.

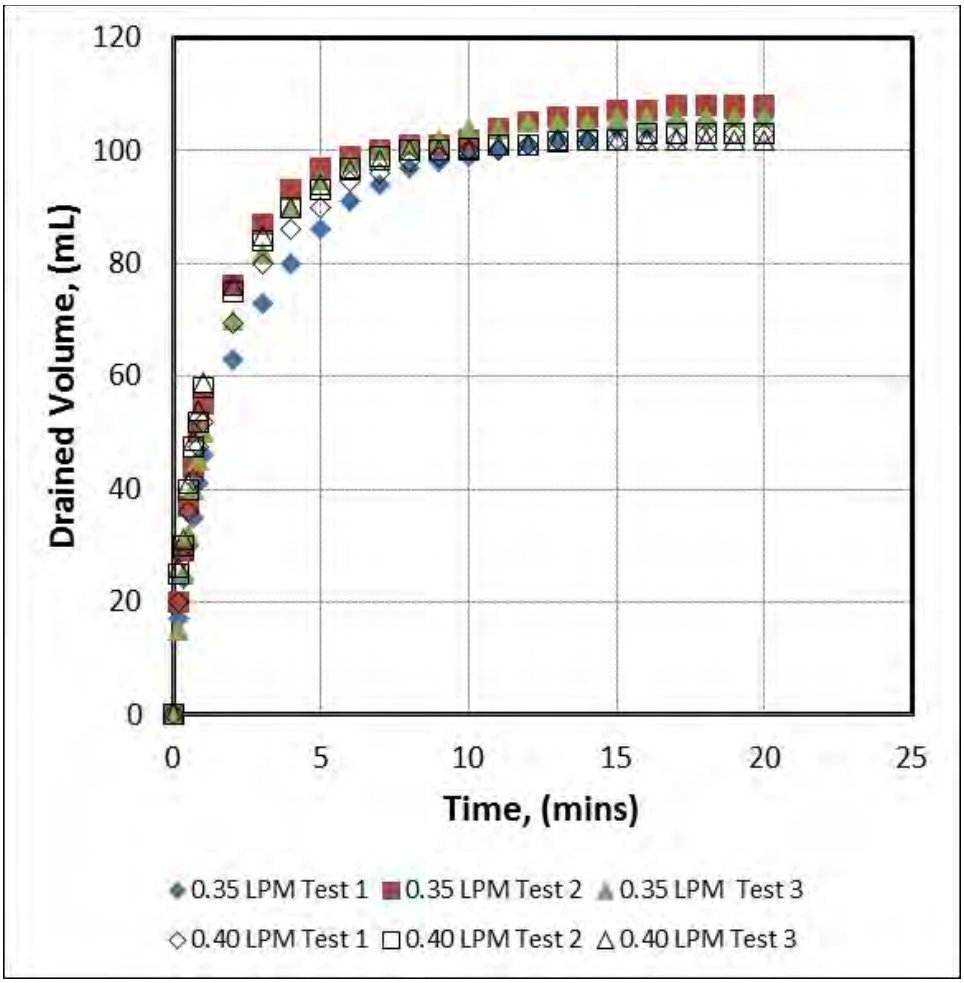

Figure 3.10: Repeatability Tests for Anionic Surfactant at 600 ppm

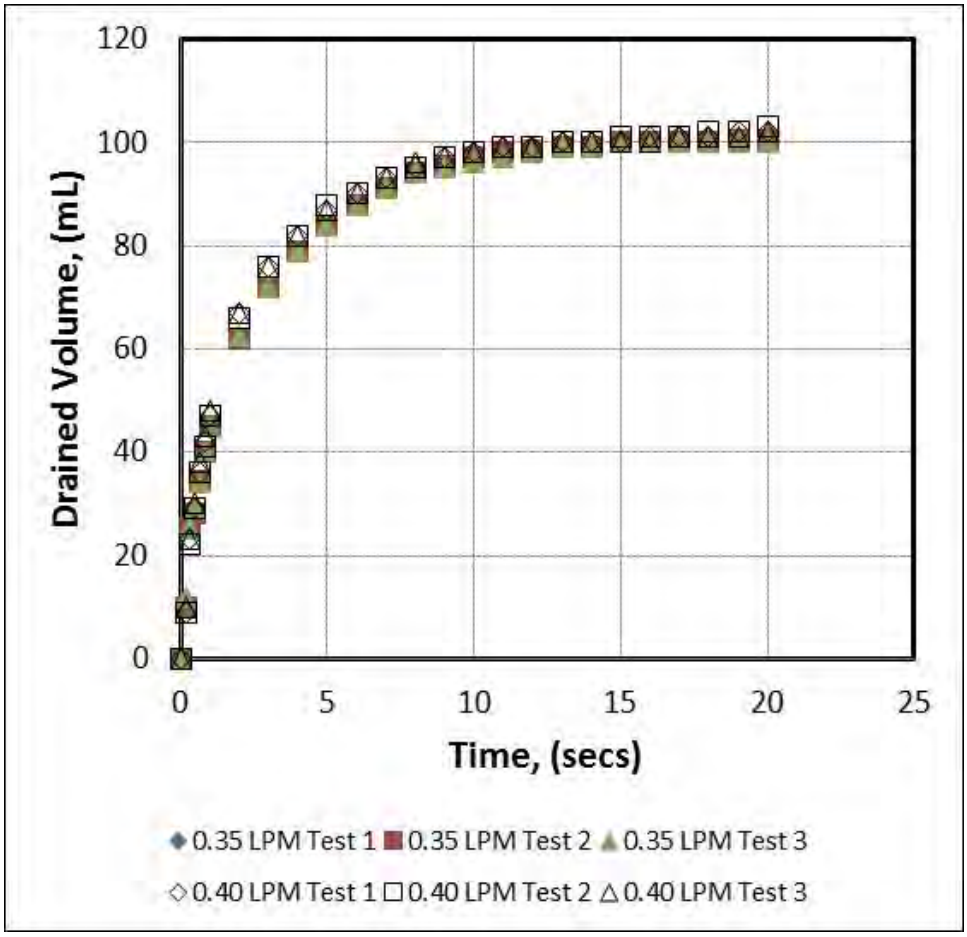

Figure 3.11: Repeatability Tests for Anionic Surfactant at 2,400 ppm

Figure 3.10 shows that there is a little variability from one test to the next at low concentration (600 ppm) and low gas rate (0.35 LPM). However, we have little or no variation among the three tests conducted at low concentration and at higher gas rate (0.40LPM). Figures 3.11 shows that the test results show good reproducibility with higher concentration at low and high gas rates respectively. Repeatability was ascertained by conducting three tests for Anionic surfactant. Average values of test two and three are reported for this surfactant. Other surfactants have been tested only once.

Figures 3.12 to 3.16 show the volume of liquid drained with time for the five surfactants tested at lower rates (0.35 LPM for Anionic and Sulphonate surfactants and 0.75 LPM for Amphoteric I, Amphoteric II and Cationic surfactants respectively). The volume of liquid drained with time at higher rates (0.40 LPM for Anionic and Sulphonate surfactants and 0.80 LPM for Amphoteric I, Amphoteric II and Cationic surfactants respectively) can be found in Ajani (2014).

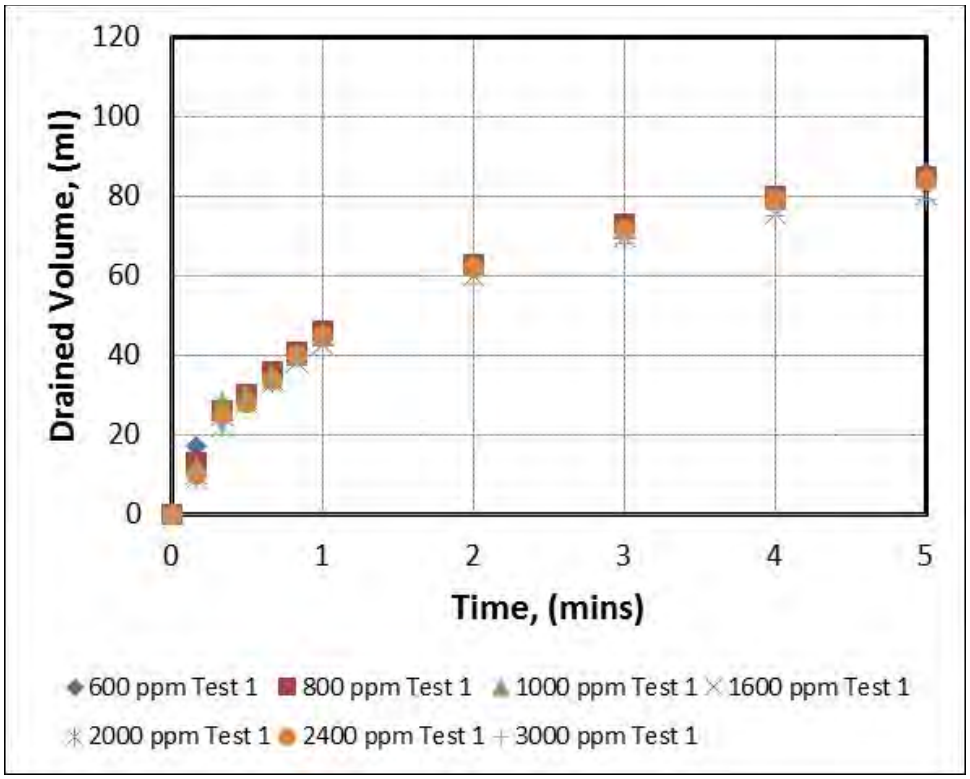

Figure 3.12: Drained Volume with Time for Anionic Surfactant at 0.35 LPM

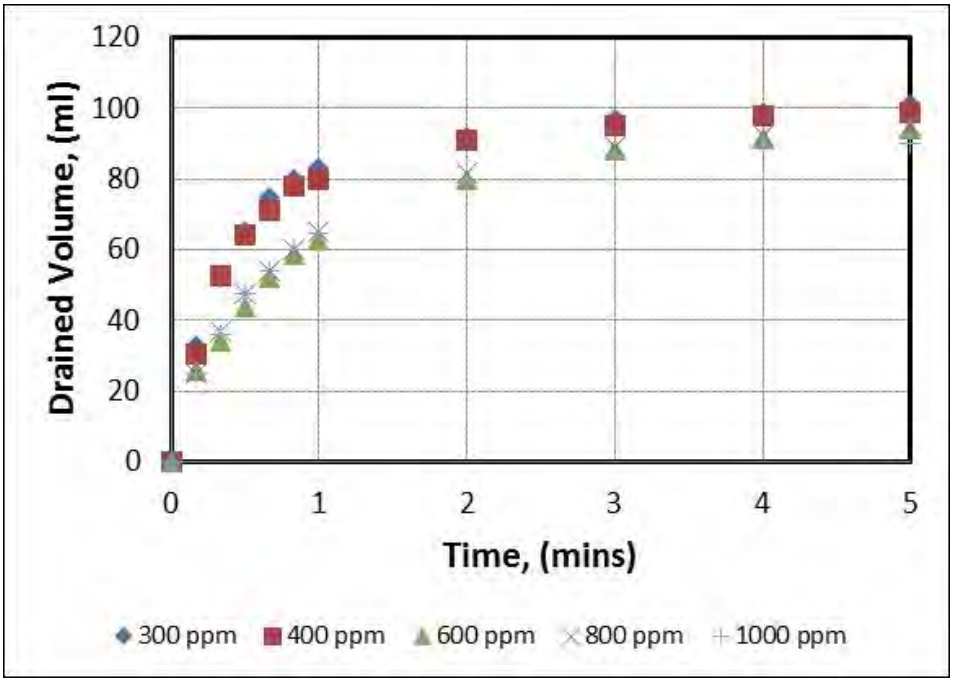

Figure 3.13: Drained Volume with Time for Amphoteric I Surfactant at 0.75 LPM

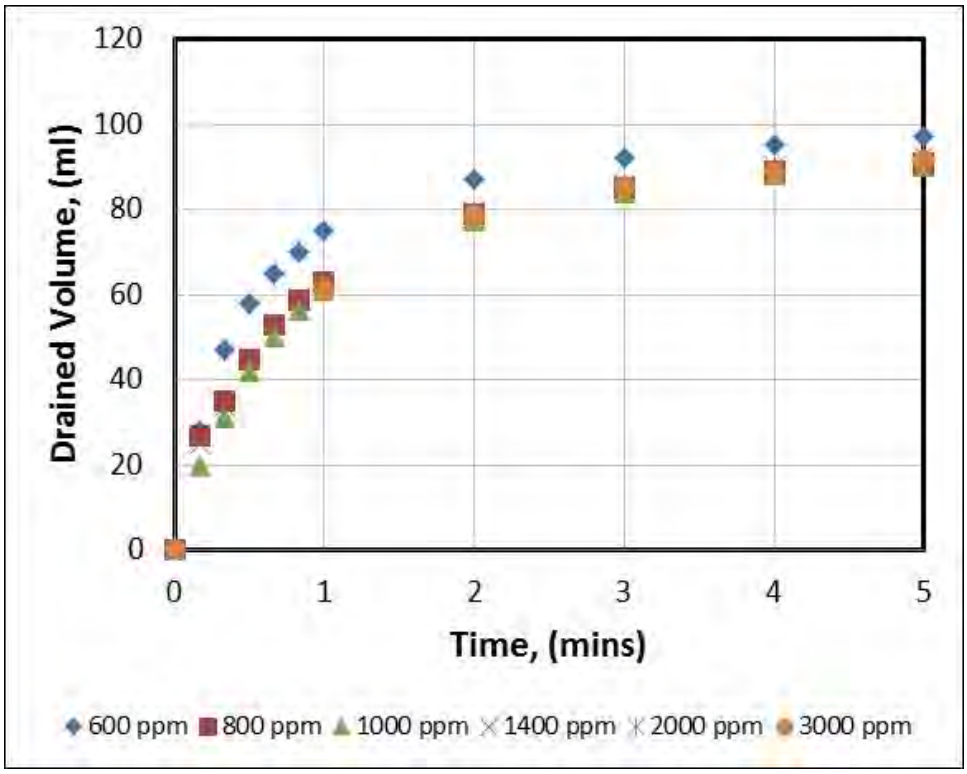

Figure 3.14: Drained Volume with Time for Amphoteric II Surfactant at 0.75 LPM

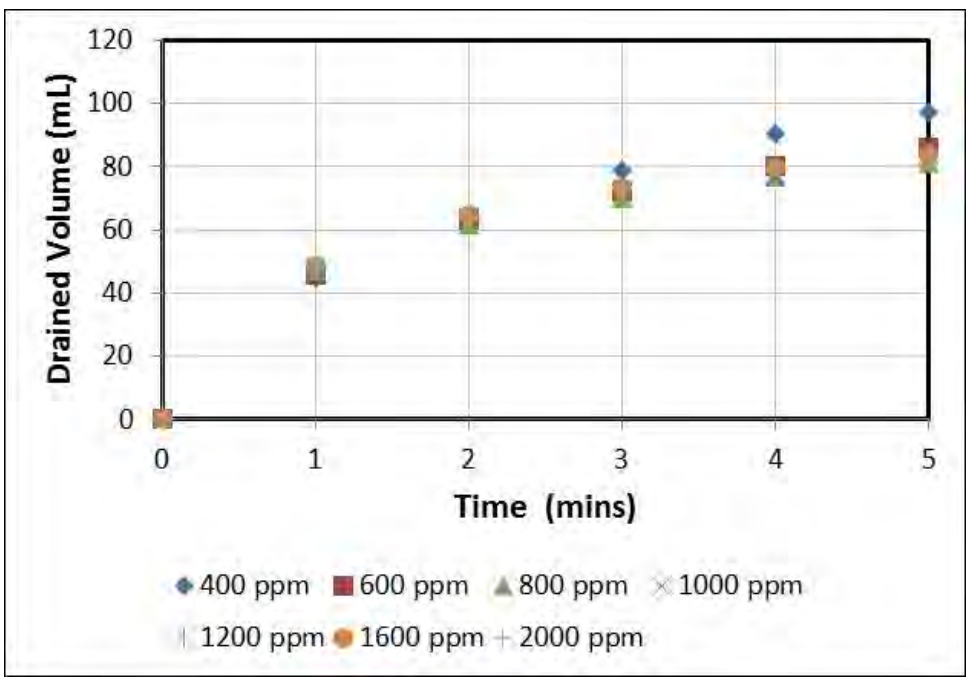

Figure 3.15: Drained Volume with Time for Sulphonate Surfactant at 0.35 LPM

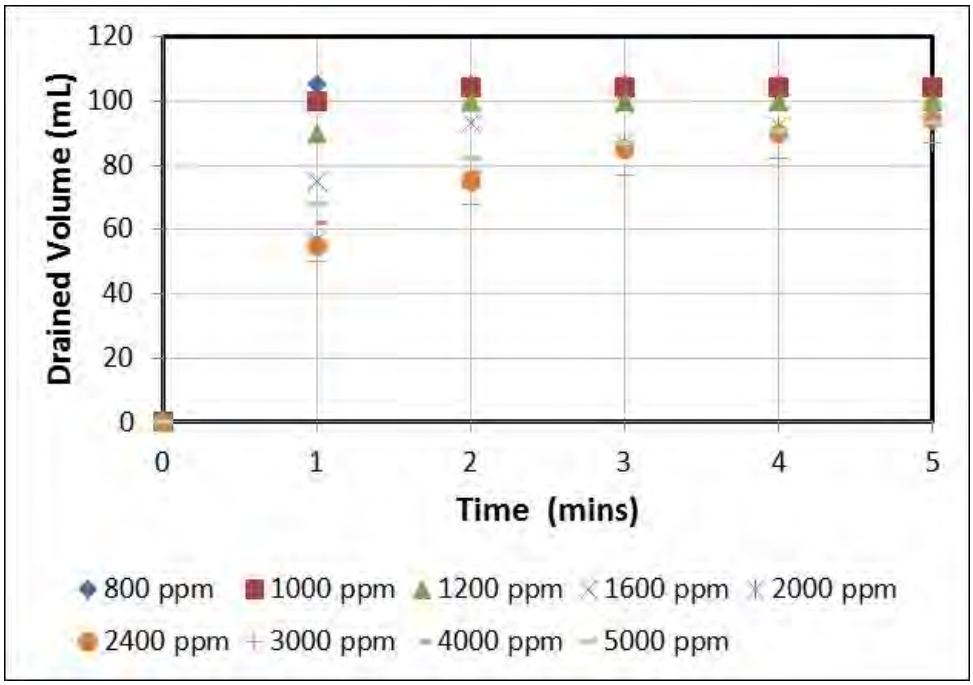

Figure 3.16: Drained Volume with Time for Cationic Surfactant at 0.75 LPM

The Anionic (Figure 3.12) and Sulphonate surfactants (Figure 3.15) are able to retain the test solution longer than other surfactants. At the end of five minutes, they have given up approximately eighty percent of their initial volume while the other three surfactants (Figures 3.13, 3.14 and 3.16) have already given up eighty percent of their initial volume at two minutes. Coincidentally, the anionic and sulphonate surfactants are the surfactants that require little agitation to make foam. The trends above are the same as those observed for experiments conducted at higher rates as shown by Ajani (2014). Next we examine the volumetric rate of liquid drainage at one minute. This is defined as

$$Volumetric\ Rate\ of\ Liquid\ Drainage = \frac{Volume\ of\ liquid\ drained_{1\ minute}}{Time_{1\ minute}} \tag{3.8}$$

Figures 3.17 and 3.18 shows the volumetric rate of liquid drainage for the experiments conducted at 0.35 LPM (Anionic and Sulphonate surfactants) and at 0.75 LPM (Amphoteric I, Amphoteric II and Cationic surfactants). The volumetric rate of liquid drainage with time at 0.40 LPM (for Anionic and Sulphonate surfactants) and at 0.80 LPM (for Amphoteric I, Amphoteric II and Cationic surfactant) can be found in Ajani (2014).

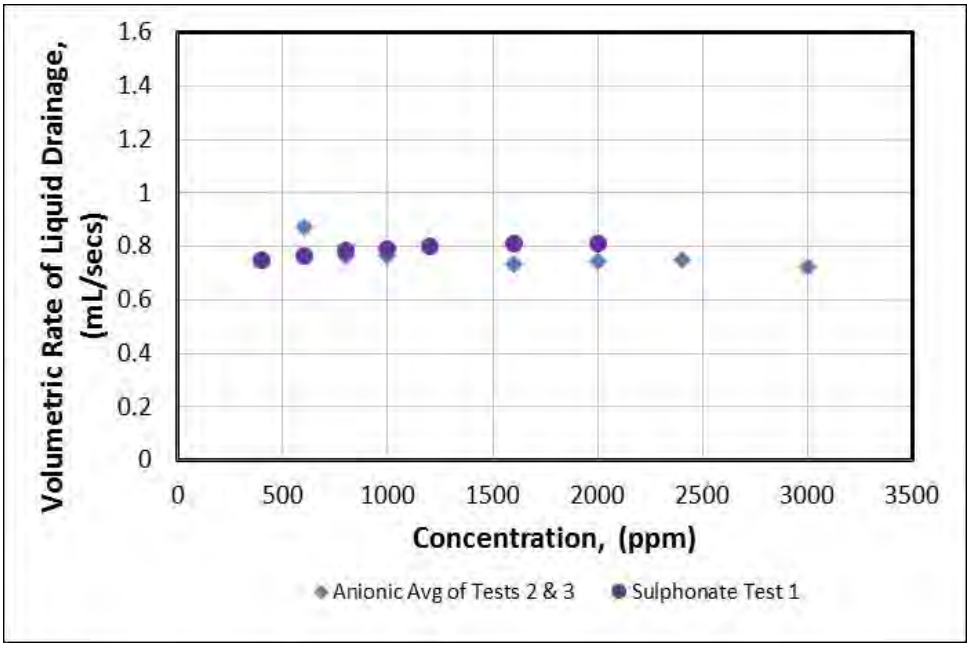

Figure 3.17: Volumetric Rate of Liquid Drainage at 0.35 LPM

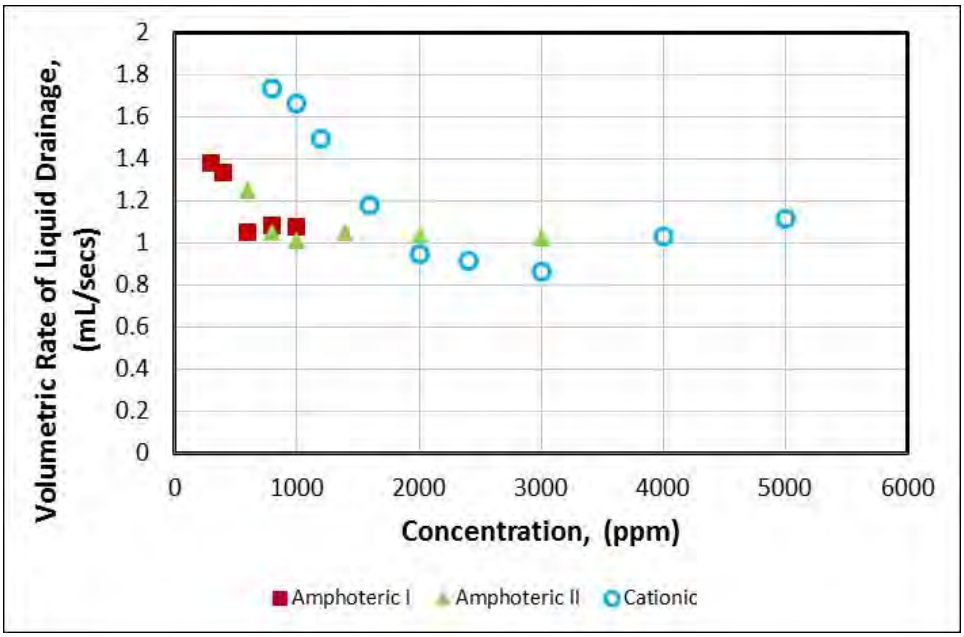

Figure 3.18: Volumetric Rate of Liquid Drainage at 0.75 LPM

In Figure 3.17, liquid drains out of a foam structure of either the Anionic or Sulphonate surfactants at approximately 0.8 mL/sec regardless of the concentration. However, in Figure 3.18, the volumetric rate at which liquid drains out of a foam structure of Amphoteric I, Amphoteric II or cationic surfactant is a strong function of the concentration. It is high at low concentration (> 1.2 mL/sec) then it declines and attains a steady value (around 1 mL/sec) with increase in concentration. These trends are same as those observed in experiments conducted at 0.40 LPM and at 0.80 LPM (See Ajani, 2014).

Next, we examine the time it takes to recover fifty percent of the initial volume of the test solution; the half-life of the liquid draining out of the foam structure formed. Figures 3.19 and 3.20 show the half-life of the surfactants tested at 0.35 LPM (Anionic and Sulphonate surfactants) and 0.75 LPM (Amphoteric I, Amphoteric II and Cationic surfactants). The half-life of surfactants tested at 0.40 LPM (Anionic and Sulphonate surfactants) and at 0.80 LPM (Amphoteric I, Amphoteric II and Cationic surfactants) can be found in Ajani (2014).

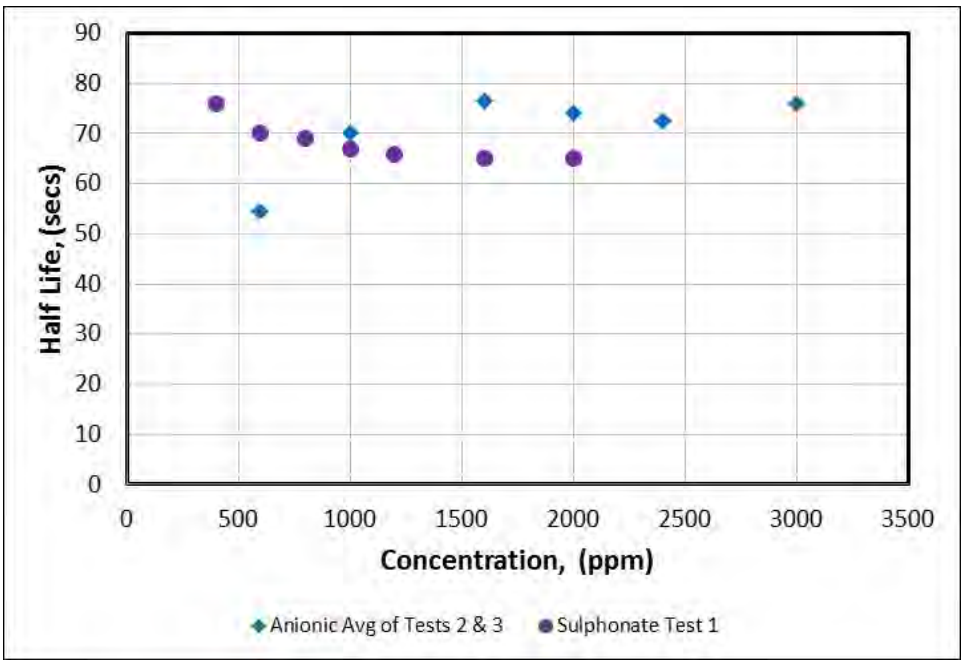

Figure 3.19: Half-Life of Surfactants Tested at 0.35 LPM

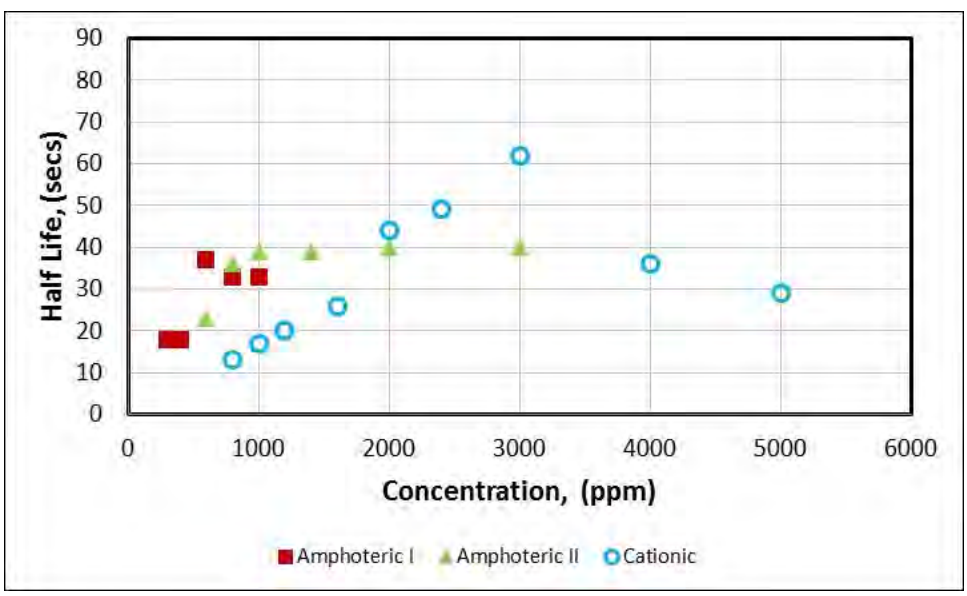

Figure 3.20: Half-Life of Surfactants Tested at 0.75 LPM

In Figure 3.19, the half-life of Anionic surfactant increases slightly with increase in concentration up to approximately 1600 ppm (at 76.5 seconds) after which it becomes insensitive to increase in concentration. On the other hand, in the same Figure, the Sulphonate surfactant exhibited a slight decrease in half-life with increase in concentration up to 1000 ppm (at 67 seconds) after which the decrease becomes insensitive to increase in concentration. Generally, in Figure 3.19, fifty percent of the initial volume of the test fluid for the anionic and sulphonate surfactants was recovered between 65 to 74 seconds.

Whereas in Figure 3.20, the time it takes to recover fifty percent of the initial volume of the test fluid changes remarkably with concentration. The half-life increases up to 600 ppm (at 37 seconds) for Amphoteric I then declines afterwards, it increases up to 1000 ppm (at 39 seconds) for Amphoteric II then remains steady afterwards and it increases up to 3000 ppm (at 62 seconds) for Cationic surfactant and then decreases afterwards. Clearly, the latter surfactants in Figure 3.20 have a lower liquid retention capability when compared with the former surfactants in Figure 3.19. These trends are same as those observed in experiments conducted at other gas flow rates (Ajani, 2014).

Although we had observed that anionic surfactant can be sparged at lower gas rate, we also tested it at high gas rates. Figure 3.21 shows the half-life of Anionic surfactant plotted alongside those of Amphoteric I, Amphoteric II and Cationic surfactants for a stability test conducted at 0.75 LPM.

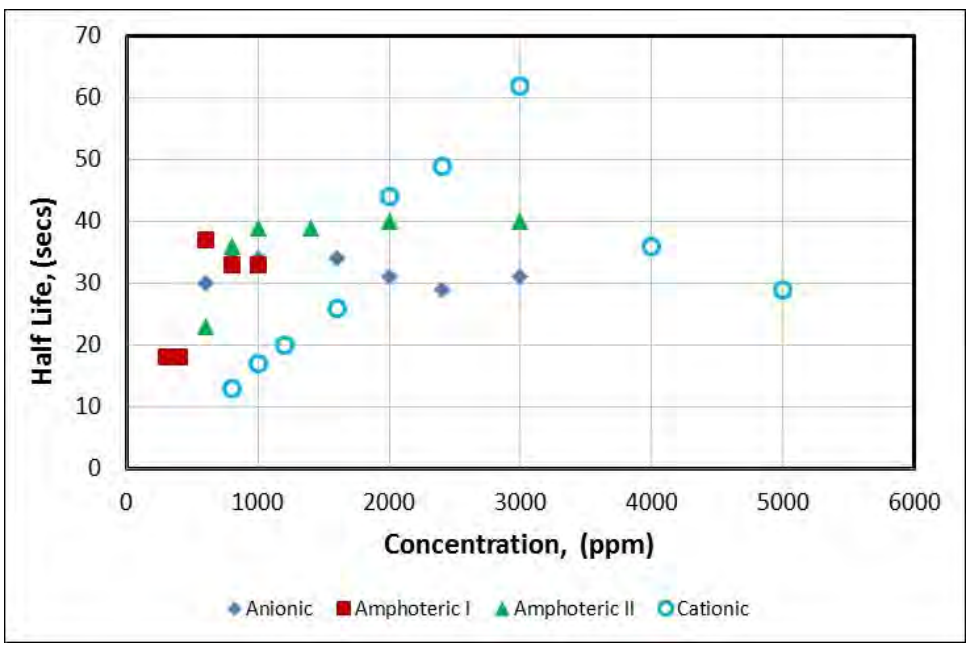

Figure 3.21: Half-life of Anionic, Amphoteric I, Amphoteric II and Cationic Surfactants at 0.75 LPM

In Figure 3.21, the Anionic surfactant exhibited the least half-life with increasing concentration. Judging by the liquid retention ability of this surfactant

earlier when sparged at 0.35 LPM, we observe that its liquid retention capacity has been impacted negatively when it was sparged at a higher rate. Hence, for testing purposes, it is pertinent to investigate and apply the appropriate rate that will show the dynamics of the surfactant being tested. For practical purposes, this surfactant will be a good product for wells operating at very low gas rate.

Now we demonstrate the repeatability in our unloading experiment with Anionic surfactant. We will also show the mass of liquid unloaded at 10 minutes for the different surfactants tested. Lastly, we show the mass of liquid unloaded by all surfactants at the critical concentration. Figures 3.22 and 3.23 show unloading test results for Anionic surfactant at 400 ppm at 0.50 LPM and 1,000 ppm at 0.75 LPM respectively.

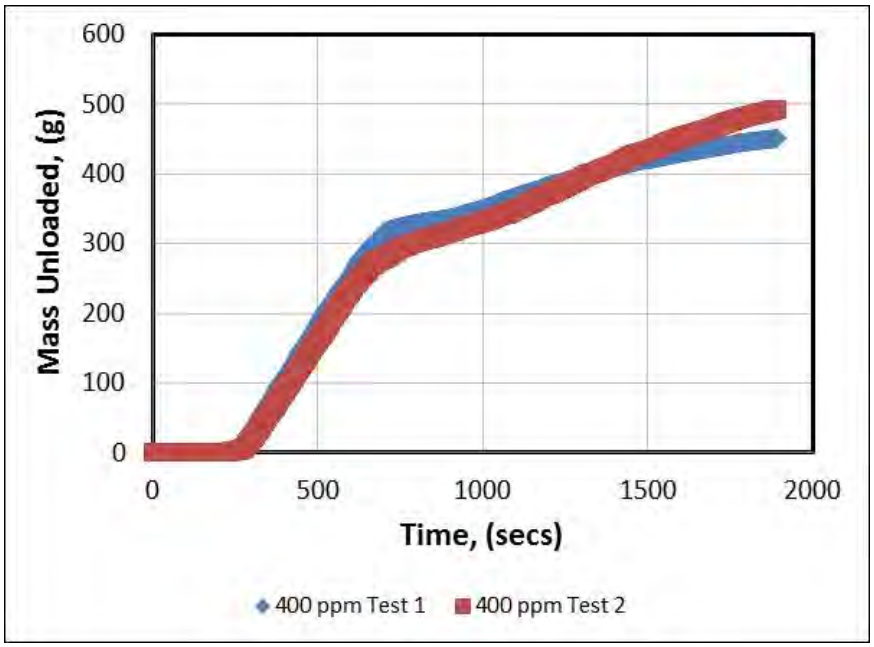

Figure 3.22: Unloading Repeatability Test Results for Anionic Surfactant at 0.50 LPM

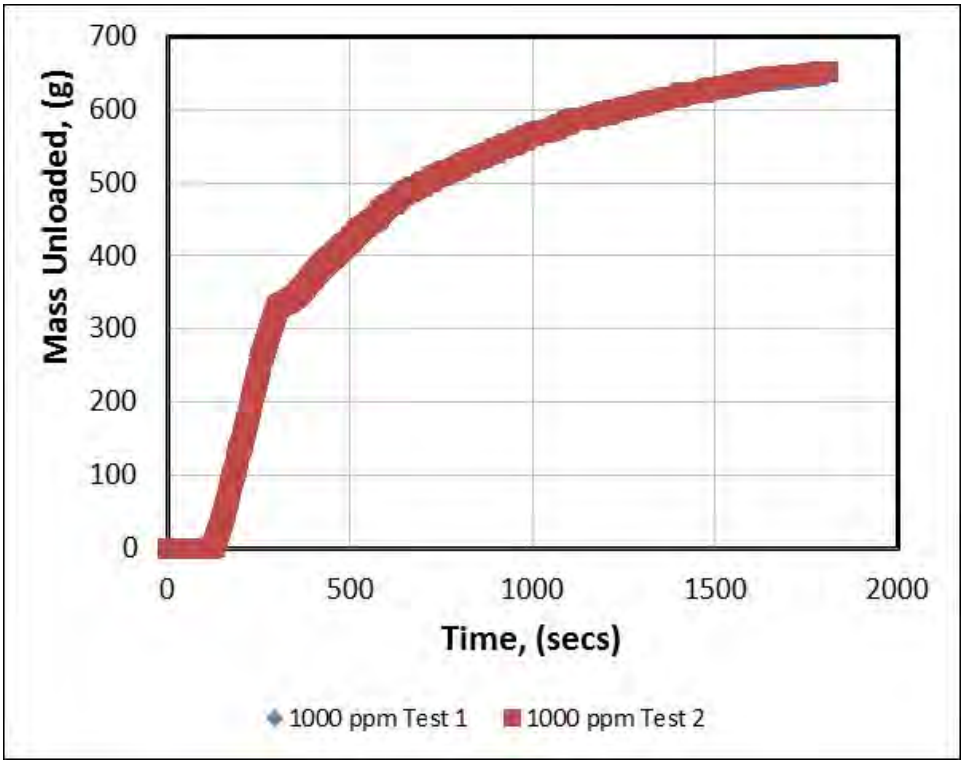

Figure 3.23: Unloading Repeatability Test Results for Anionic Surfactant at 0.75 LPM

In Figures 3.22 and 3.23, a good repeatability is observed between two independent unloading test results at the same concentration. Two gas rates are considered for each concentration. To keep track of how repeatable the test is, either of the gas rates is repeated in going from experiment conducted from one concentration to the other. For cases where we repeated a particular gas rate, an average value of the repeated tests is reported.

Figures 3.24 to 3.28 show the percent mass of liquid unloaded for each of the five surfactants tested at 0.75 LPM. The percent mass of liquid unloaded for all five surfactants at 0.50 LPM is shown in Ajani (2014).

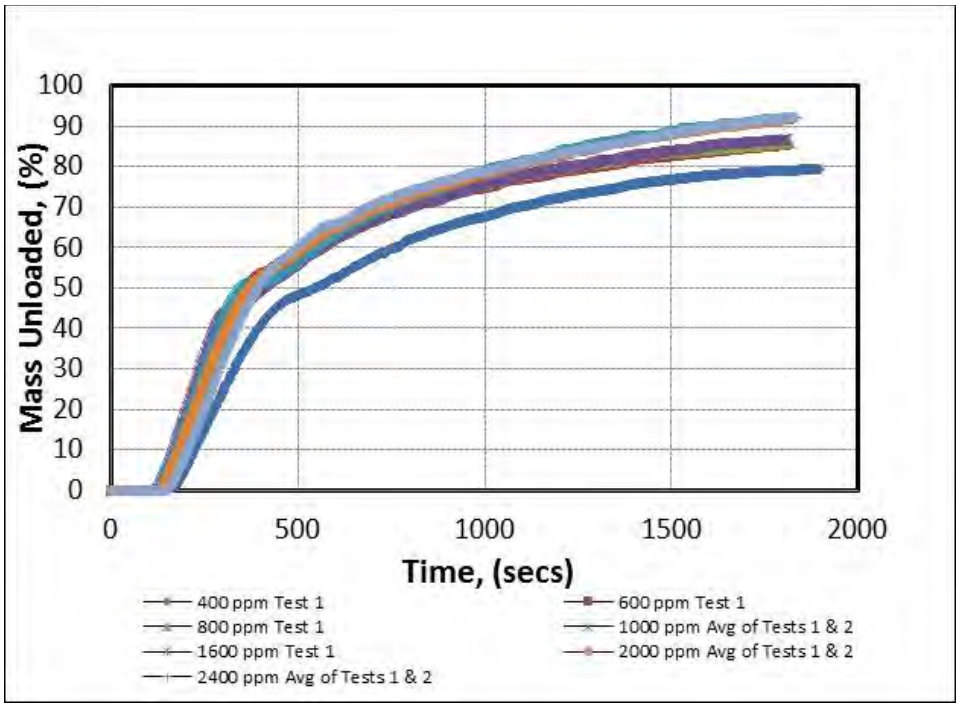

Figure 3.24: Unloading Test Results for Anionic at 0.75 LPM

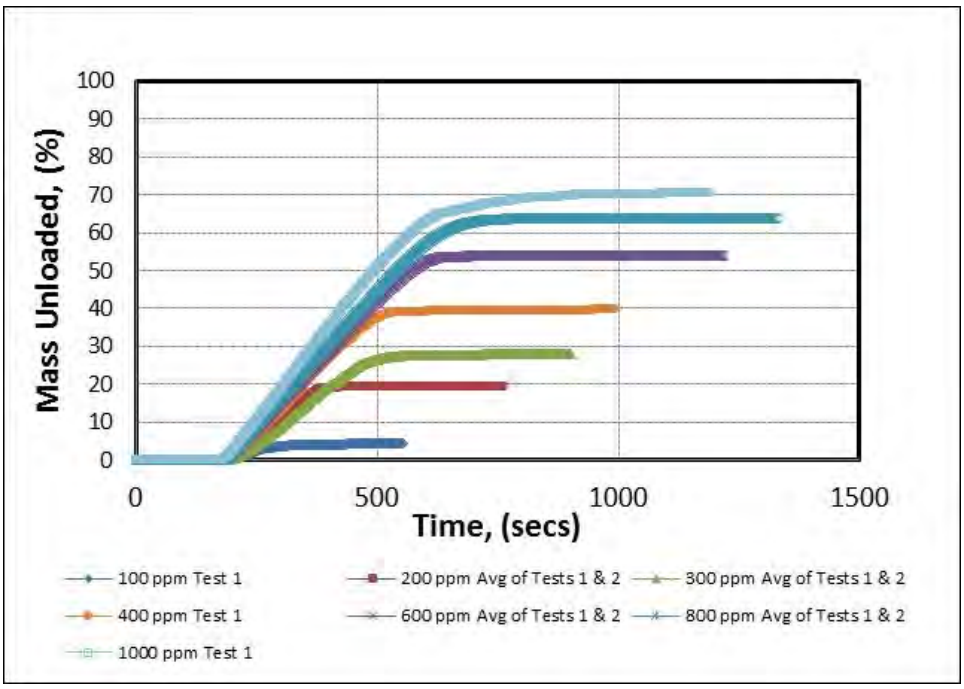

Figure 3.25: Unloading Test Result for Amphoteric I at 0.75 LPM

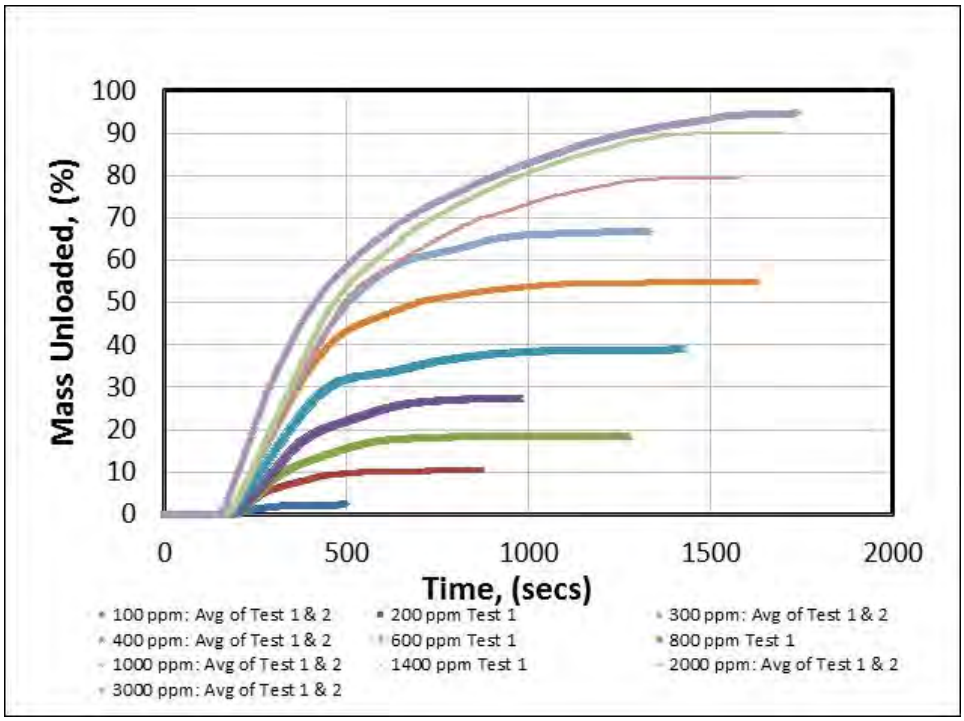

Figure 3.26: Unloading Test Results for Amphoteric II at 0.75 LPM

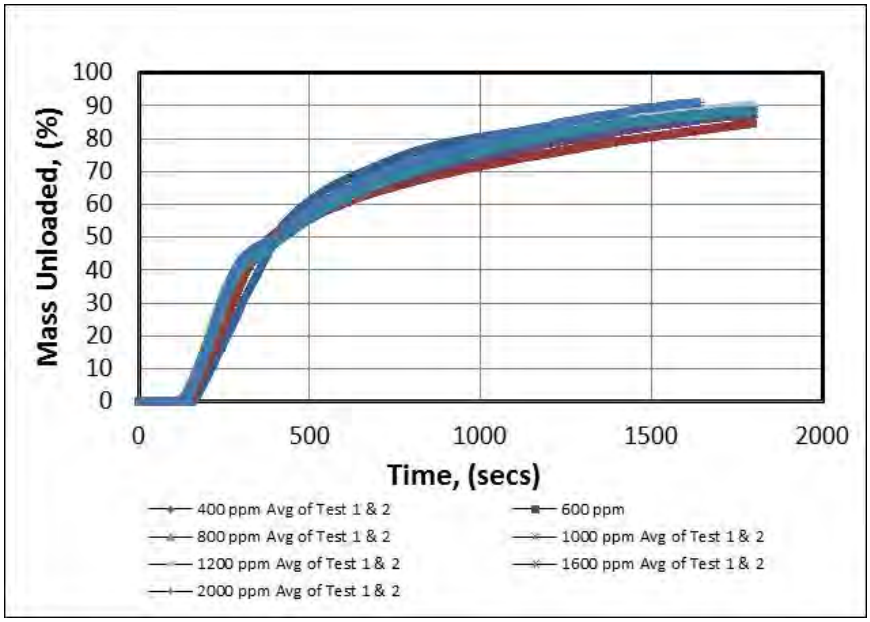

Figure 3.27: Unloading Test Results for Sulphonate at 0.75 LPM

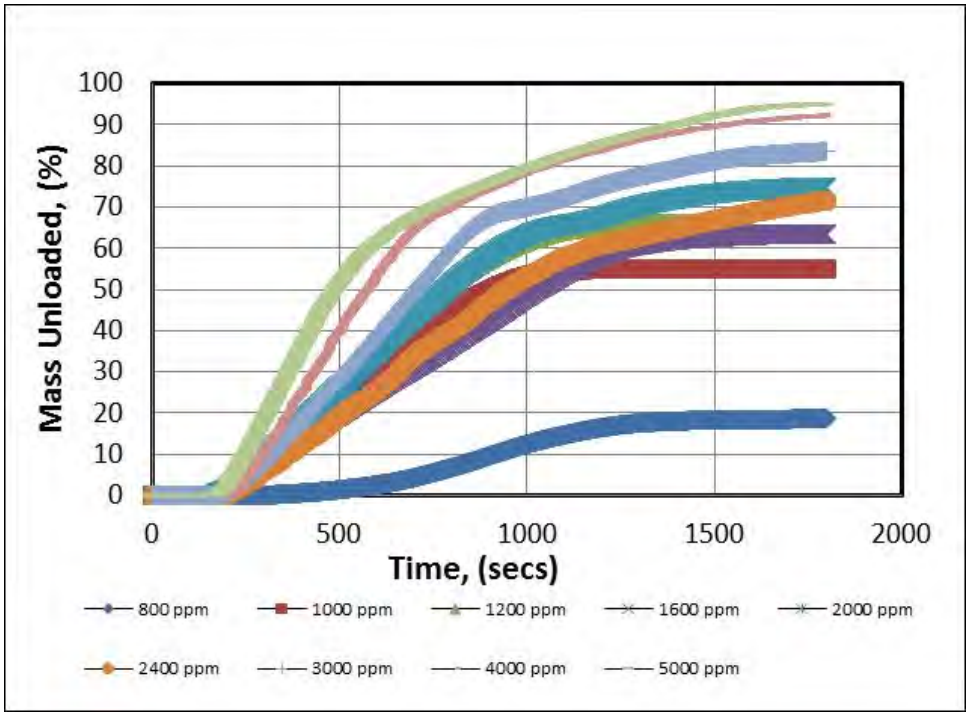

Figure 3.28: Unloading Test Results for Cationic at 0.75 LPM

As shown in Figures 3.24 to 3.28, different surfactants show different capacity to unload liquid as concentration increases. Figures 3.24 and 3.27 show that percent of liquid unloaded by the Anionic and Sulphonate surfactants is not very sensitive to increase in concentration. In contrast, the percent of liquid unloaded by the Amphoteric I and Amphoteric II surfactants increases with increase in concentration. It is also observed that the gain in percent of liquid unloaded becomes smaller at higher concentration. However, in Figure 3.28, the Cationic surfactant does not show a consistent trend in the percent of liquid unloaded with increase in concentration. Aforementioned trend may be due to the fact that the surfactant is not suitable for testing in deionized water at room temperature. Closer attention will be paid to the trend exhibited by this surfactant in other mediums (Brine and Brine at high temperature). These trends are same as those observed in experiments conducted at 0.50 LPM (Ajani, 2014).

Next we collate the percent of liquid unloaded in 10 minutes for unloading tests experiments conducted at 0.50 LPM and 0.75 LPM. These are shown in Figures 3.29 and 3.30 for 0.50 LPM and 0.75 LPM respectively.

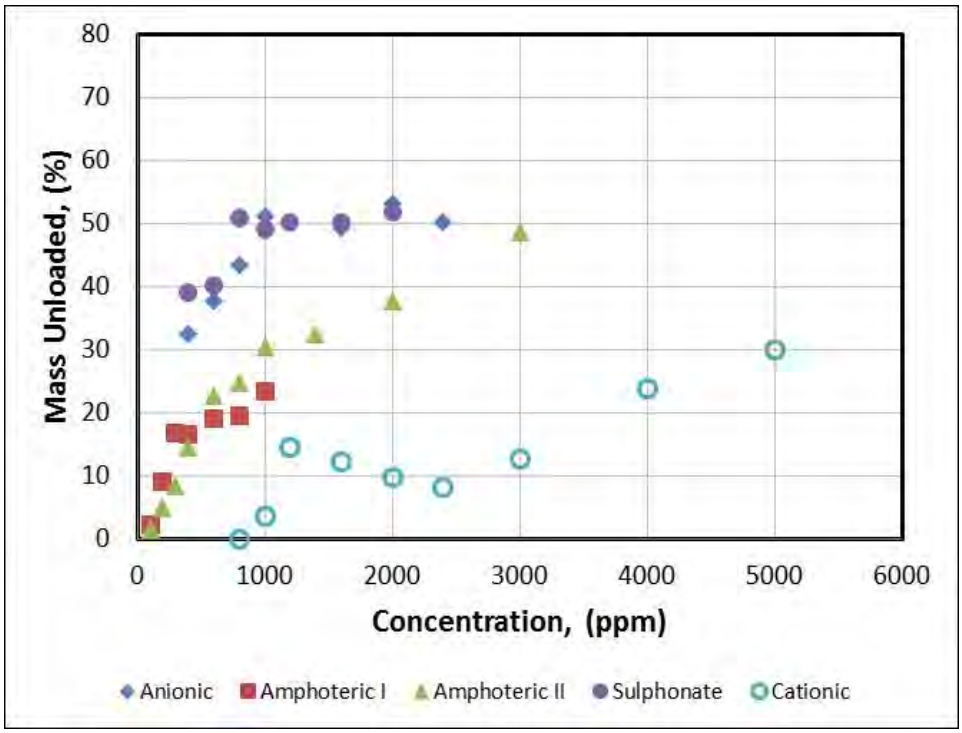

Figure 3.29: Mass Unloaded at 10 minutes for Unloading Test at 0.50 LPM

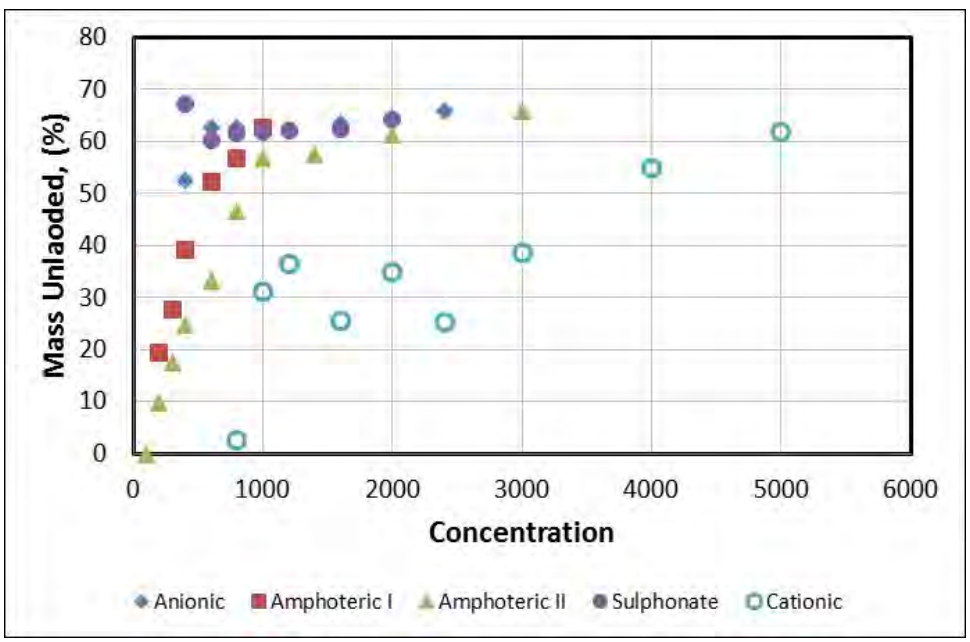

Figure 3.30: Mass Unloaded at 10 Minutes for Unloading Test Conducted at 0.75 LPM

In Figures 3.29 and 3.30, percent of liquid unloaded at 10 minutes by the Anionic and Sulphonate surfactants generally increases until approximately 800 ppm and becomes steady afterwards. Observe that the sulphonate surfactant at 400 ppm in Figure 3.30 is an exception to aforementioned trend. For Amphoteric I and II, the percent of liquid unloaded increases with increase in concentration. Cationic

surfactant shows a haphazard trend with concentration. These are consistent with previous observations.

In a bid to use a common measure to compare all surfactants, using the concentration at which the highest half-life values were obtained, we compared the percent of liquid unloaded by all surfactants at the optimum concentration. These are as shown in Figures 3.31 and 3.32.

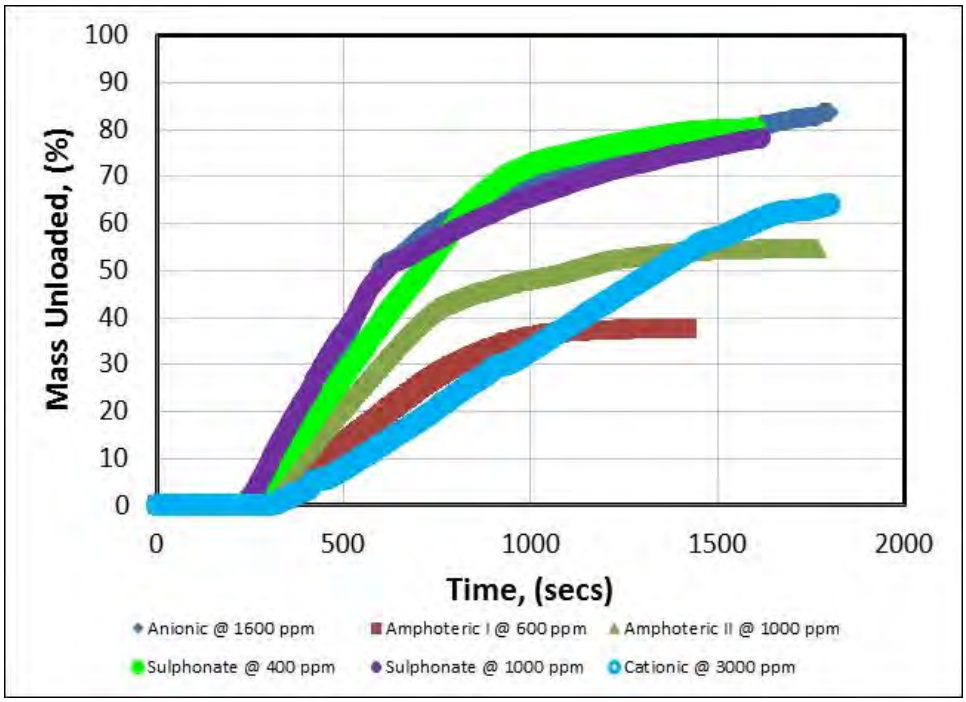

Figure 3.31: Unloaded Mass at 0.50 LPM with Concentrations at Highest Half-life Value

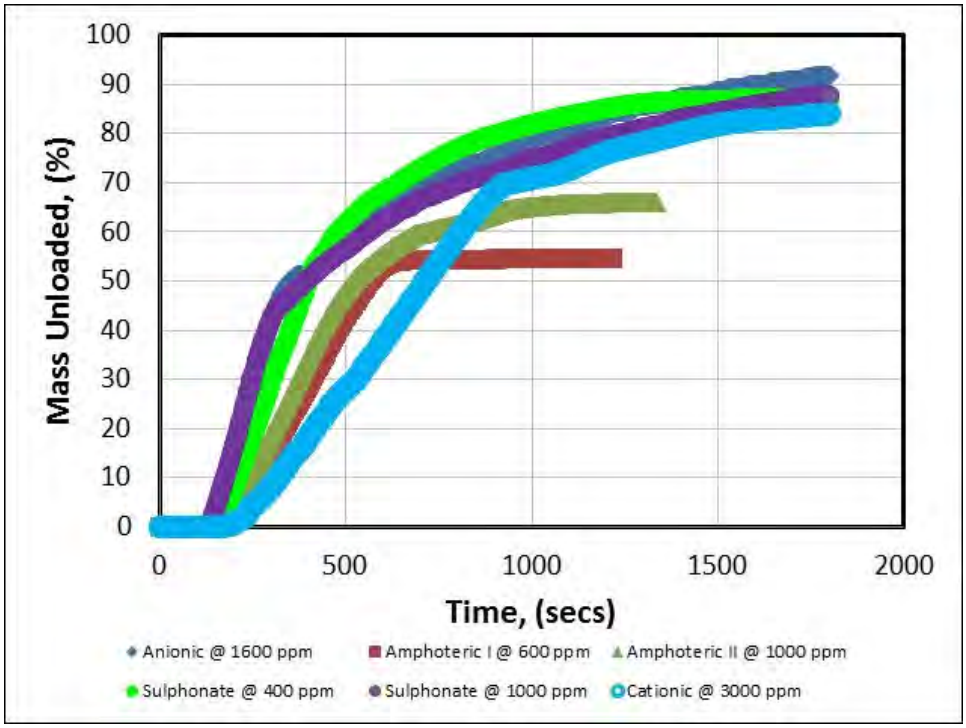

Figure 3.32: Unloaded Mass at 0.75 LPM with Concentrations at Highest Half-life Value

In Figures 3.31 and 3.32, we have included the percent of liquid unloaded by the sulphonate at 400 ppm and 1000 ppm. This is because it gave a higher half-life value at lowest concentration 400 ppm (76 seconds) than at 1000 ppm (67 seconds). The latter concentration is when the half-life becomes steady with increase in concentration. For this chemical, the percent of liquid unloaded at 400 ppm is higher than that unloaded at 1000 ppm. By comparing Figure 3.31 with Figure 3.32, it can be observed that the difference between the unloading capacities of the different chemicals tends to be minimized when the unloading test is conducted at a higher sparge rate. However, there is a difference in unloading capacity in different surfactants.

The observation above is more conspicuous in Figures 3.33 and 3.34 where we have plotted the percent mass of liquid unloaded by all surfactants at different concentrations at the end of the unloading experiment (after at most thirty minutes).

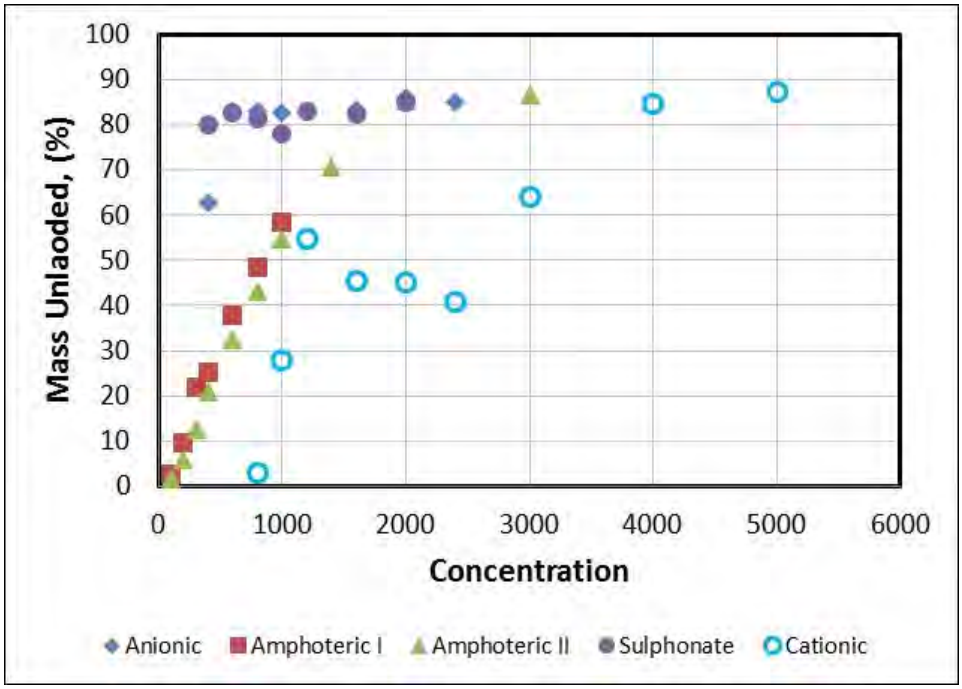

Figure 3.33: Unloaded Mass (%) at End of Unloading Test at 0.50 LPM

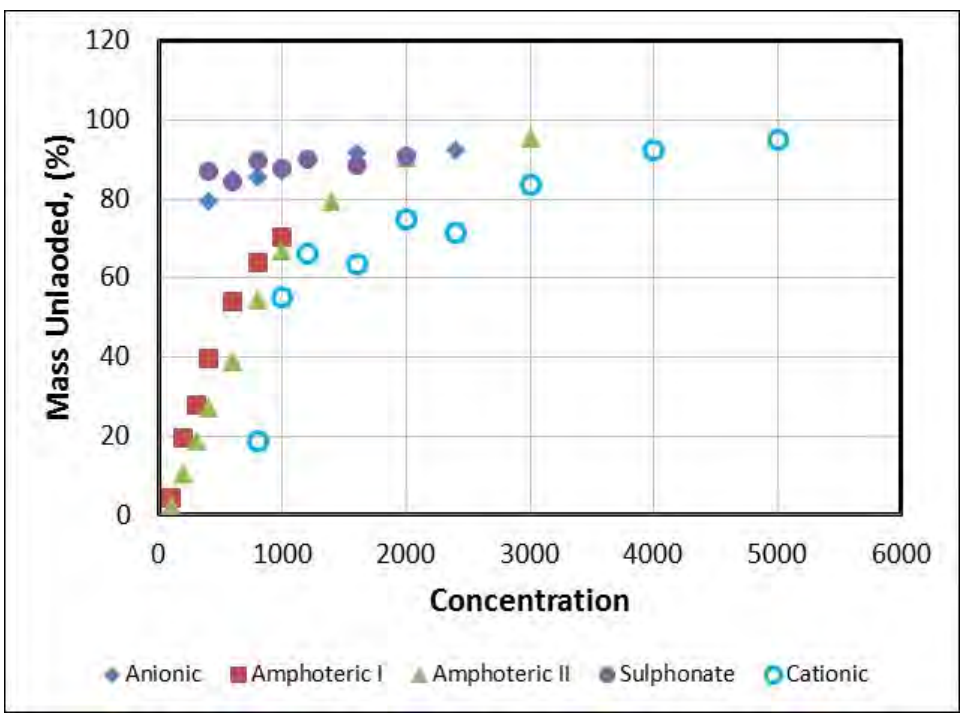

Figure 3.34: Unloaded Mass (%) at End of Unloading Test at 0.75 LPM

In Table 3.7, we compare the optimum concentrations observed from the all the parameters used to quantify foam efficacy in the bench top tests conducted at room temperature with de-ionized water.

Table 3.7: Optimum Concentration from Parameters used in Bench Top Tests

Experiments →	Surface Tension Test	Foam Stability Tests		Liquid Unloading Tests
Samples ↓	Tensiometer	Rate of Liquid Drainage, (mL/secs)	Half-life, (secs)	Mass Unloaded in 10 minutes, (%)
Anionic	2400 ppm	1600 ppm	1600 ppm	Plateau at 1000 ppm
Amphoteric I	400 ppm	600 ppm	600 ppm	Inflection at 600 ppm
Amphoteric II	600 ppm	1000 ppm	1000 ppm	Inflection at 1000 ppm
Sulphonate	3000 ppm	1000 ppm	1000 ppm	Plateau at 800 ppm
Cationic	3000 ppm	3000 ppm	3000 ppm	Unstable

From Table 3.7, we observe that the tensiometer is not a good indicator of efficacy of surfactants based on half-life, rate of liquid drainage and percent mass of liquid unloaded at 10 minutes. Based on proximity of results obtained, the stability parameters (half-life, rate of liquid drainage and percent mass of liquid unloaded in 10 minutes) are better indicators of critical concentration for a given chemical. In addition, the ability of a chemical to foam at low sparging rate is also an indicator of a good surfactant.

In addition to conducting the experiments in de-ionized water, we also conducted some limited number of experiments in the presence of brine. Results are presented in two groups based on the gas rate used in conducting the stability test (0.40 LPM and 0.80 LPM). In Figure 3.35, the half-life of Anionic and Sulphonate surfactants are compared in de-ionized water, Brine I, Brine I at 150°F, Brine II and Brine II at 150°F for experiments conducted at 0.40 LPM. Likewise, in Figure 3.36, the volumetric rate of liquid drainage of Anionic and Sulphonate surfactants are compared in de-ionized water, Brine I, Brine I at 150°F, Brine II and Brine II at 150°F for experiments conducted at 0.40 LPM.

We have presented results from two different concentrations for experiments conducted on Sulphonate. This is because it exhibited a higher half-life at 400 ppm than at 1000 ppm as shown earlier. By investigating the Sulphonate further in brine and at high temperature, we can identify its optimum concentration and clarify the ambiguity from the half-life result.

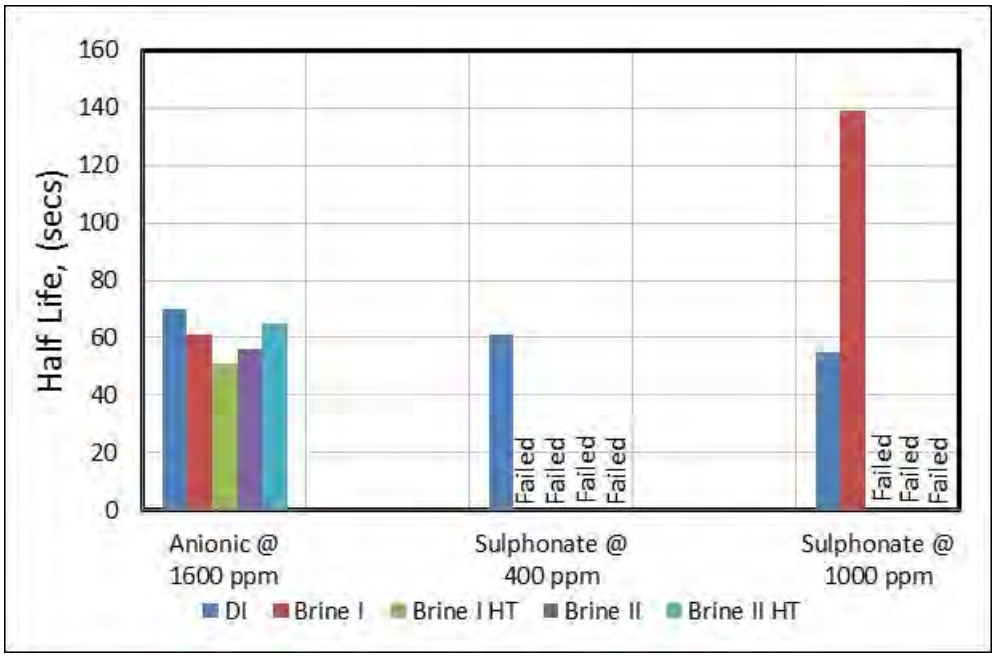

Figure 3.35: Comparison of Half-life at 0.40 LPM in different Media and at different Temperatures

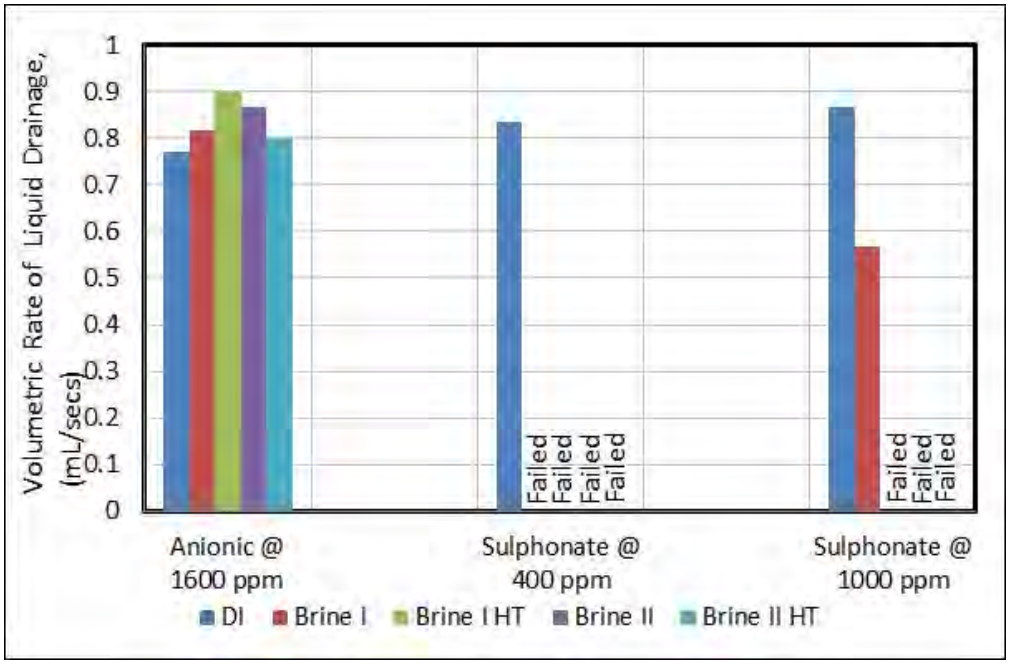

Figure 3.36: Comparison of Volumetric Rate of Liquid Drainage at 0.40 LPM in Different Media and at Different Temperatures

In Figures 3.35 and 3.36, a failed test signifies a test in which it was not possible to completely sparge 100 mL of the test solution at 0.40 LPM. That is, no matter how long we sparge, we could not completely turn 100 mL of the test solution into foam. By inspecting Figures 3.35 and 3.36, we observe that the Anionic surfactant was able to sustain its liquid retention capability in different media.

Except in Brine II at 1000 ppm and at 74°F, the Sulphonate lost its efficacy in Brine I, Brine I at high temperature and in Brine II at high temperature when sparged at 0.40 LPM. It is worthwhile testing the Sulphonate foamer in De-ionized water, Brine I, Brine I at high temperature, Brine II and Brine II at High Temperature.

In Figure 3.37, the half-life of Amphoteric I, Amphoteric II, Cationic and Sulphonate surfactants are compared in de-ionized water, Brine I, Brine I at 150°F, Brine II and Brine II at 150°F for experiments conducted at 0.80 LPM. Likewise, in Figure 3.38, the volumetric rate of liquid drainage of Amphoteric I, Amphoteric II, Cationic and Sulphonate surfactants are compared in de-ionized water, Brine I, Brine I at 150°F, Brine II and Brine II at 150°F for experiments conducted at 0.80 LPM.

Previously, we stated that the Sulphonate Foamer as a foamer suitable for testing at a least gas rate of 0.35 LPM. However, because it was negatively impacted as illustrated in Figures 3.35 and 3.36 at 0.40 LPM, we investigate its efficacy further by testing it at 0.80 LPM. Hence, it has been lined up with foamers in the higher sparge rate category for comparison as shown in Figures 3.37 and 3.38.

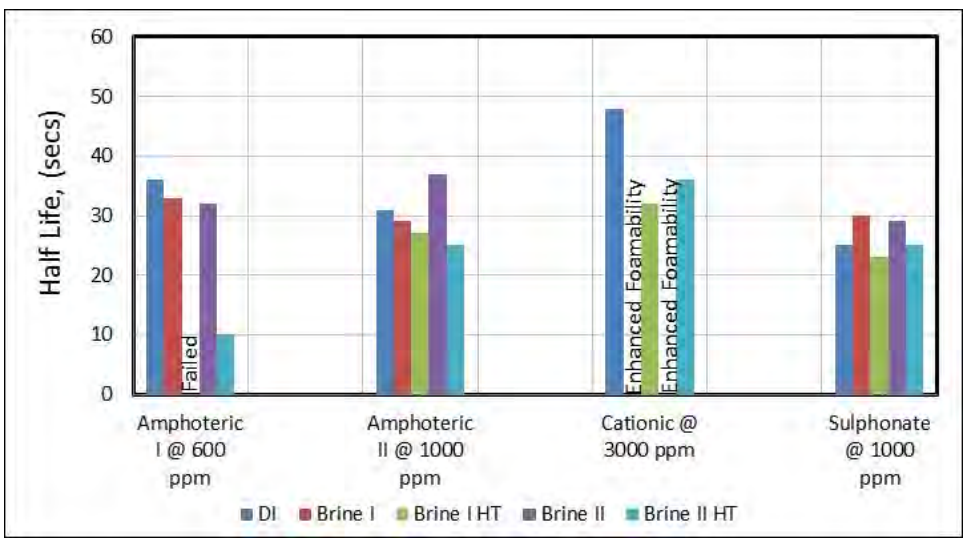

Figure 3.37: Comparison of Half-life at 0.80 LPM in different Media and at different Temperatures: Sulphonate Included

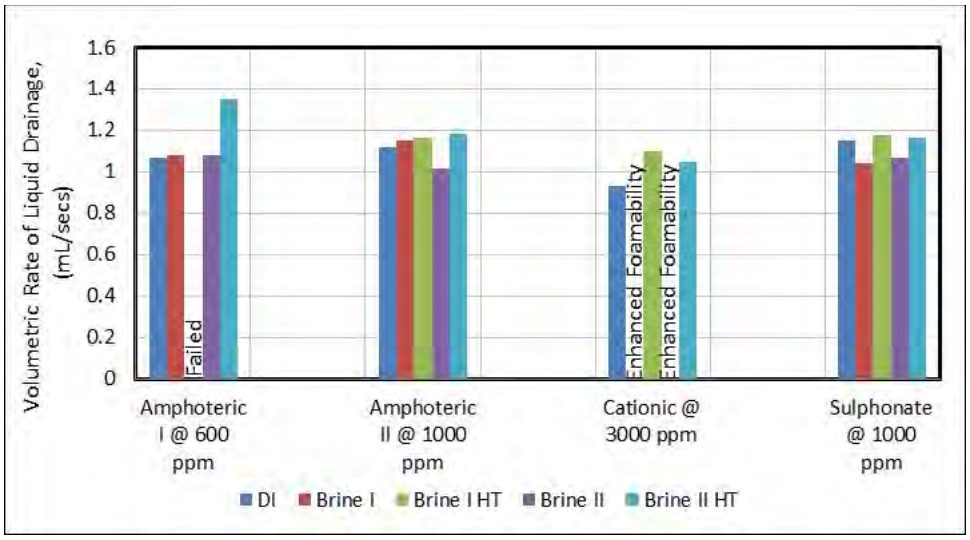

Figure 3.38: Comparison of Volumetric Rate of Liquid Drainage at 0.80 LPM in different Media and at different Temperatures: Sulphonate Included

In Figures 3.37 and 3.38, enhanced foaming ability means the foam structure formed while sparging the mixture was so rich that it was impossible for us to follow the interface of the remaining unfoamed test solution. This causes difficulty in interpretation.

In Figures 3.37 and 3.38, Amphoteric I has a higher resistance in Brine I at room temperature than Amphoteric II. However, at 150^{0}F, Amphoteric I lost its efficacy in Brine I while Amphoteric II was able to resist this medium. Amphoteric II has an enhanced performance in Brine II at room temperature than Amphoteric I. In Brine II at 150^{0}F, the impact of temperature on Amphoteric II is lower than that of Amphoteric I. The Cationic foamer exhibited enhanced foaming ability in Brine I and II. Cationic foamer was also able to resist the effect of temperature in Brine I and II.

The Sulphonate foamer was sparged at a higher rate in Figures 3.37 and 3.38. It shows a better performance in Brine I and II and was slightly impacted in the presence of Brine I and II at 150^{0}F. It shows a better resistance than Amphoteric I but did not show a better performance than Amphoteric II and Cationic surfactants. Previously, we demonstrated that the Anionic surfactant (appropriate for testing at a least rate of 0.35 LPM) had its performance impacted when tested at a higher gas rate (0.75 LPM) in de-ionized water. The sulphonate foamer has the same least sparge rate of 0.35 LPM as the Anionic surfactant. In Brine solution, while the sulphonate foamer could not foam at the lower rate (0.40 LPM), it actually foamed at the higher rate (0.80 LPM).

The Cationic foamer exhibited enhanced foaming ability in Brine I and II at room temperature. Hence, we could not determine an appropriate half-life and volumetric rate of liquid drainage for it. This has been further tested at 0.40 LPM so as to investigate further if the foamer truly has an enhanced foaming capacity in

Brine. Figures 3.39 and 3.40 show the result of half-life and volumetric rate of foam drainage from stability tests conducted on the Cationic foamer at 0.40 LPM. The cationic foamer has been lined up with Anionic and Sulphonate surfactants for comparison. The latter are low rate foamers while the former was originally classified as a high rate foamer.

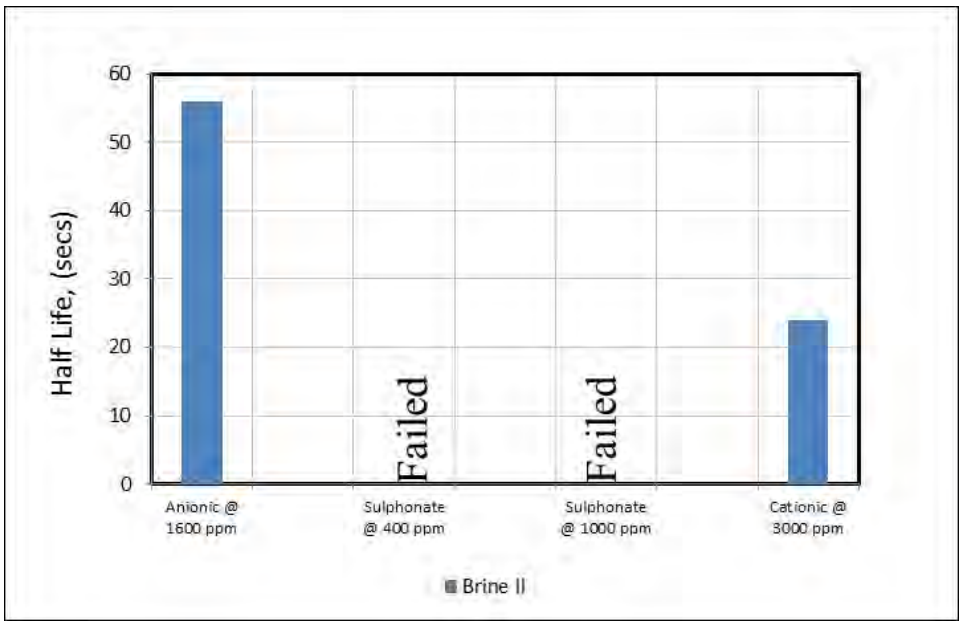

Figure 3.39: Comparison of Half-life at 0.40 LPM in different Media and at different Temperatures: Cationic Included

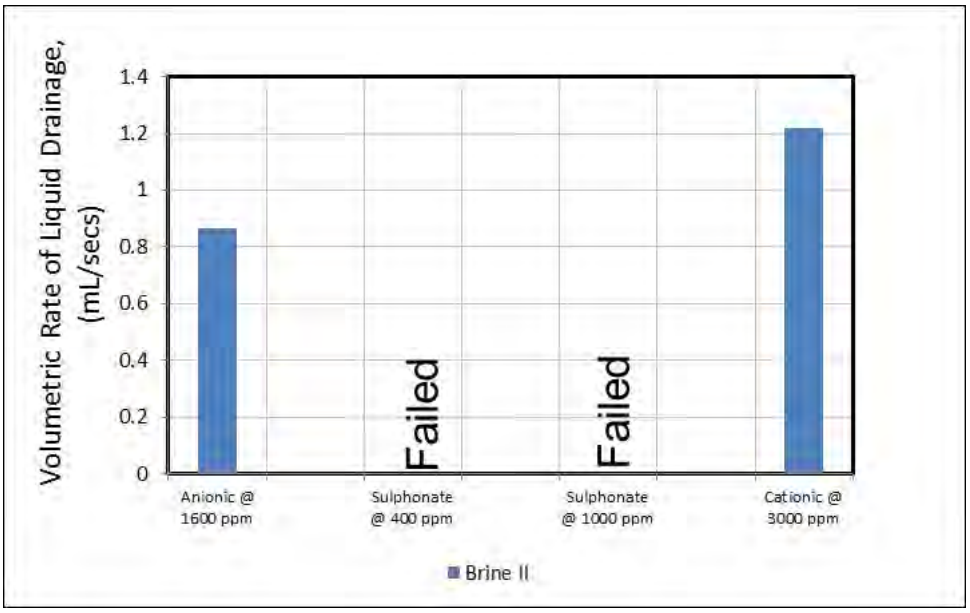

Figure 3.40: Comparison of Volumetric Rate of Liquid Drainage at 0.40 LPM in different Media and at different Temperatures: Cationic Included

From Figures 3.39 and 3.40, Cationic foamer exhibited a lower half-life and a higher volumetric rate of liquid drainage at one minute when compared to Anionic surfactant. The Cationic foamer has an enhanced foaming ability when sparged at 0.80 LPM. It has a shorter half-life when compared to Anionic surfactant for experiment conducted at 0.40 LPM. Based on all the results from the stability tests, the cationic foamer is a better product than the sulphonate in every medium except in de-ionized water.

In Figures 3.41 and 3.42, percent mass of liquid unloaded for all surfactants tested are compared in de-ionized water, Brine I and Brine II at room temperature for experiments conducted at 0.50 LPM and 0.75 LPM respectively.

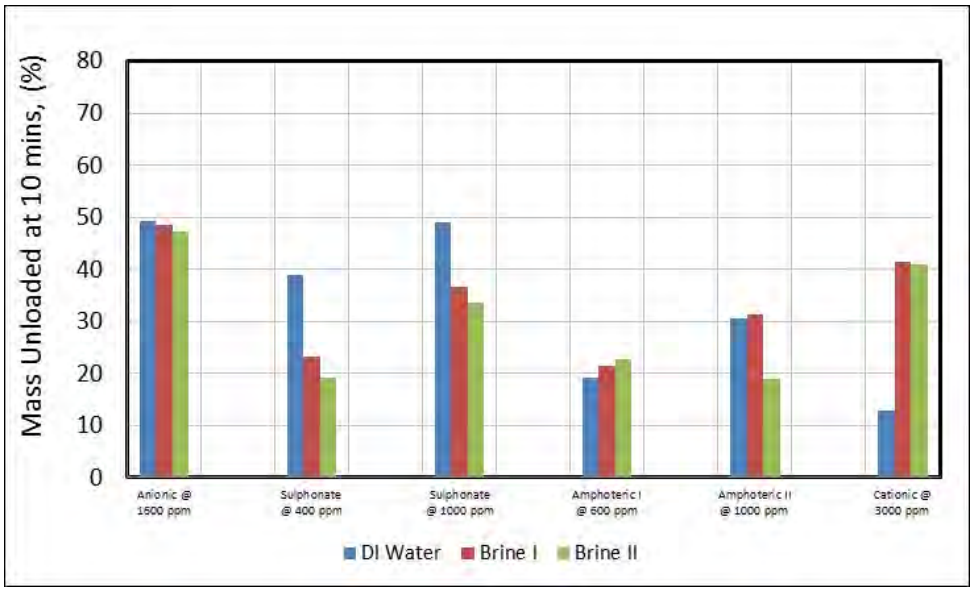

Figure 3.41: Percent Mass of Liquid Unloaded at 10 Minutes in Different Mediums at 0.50 LPM

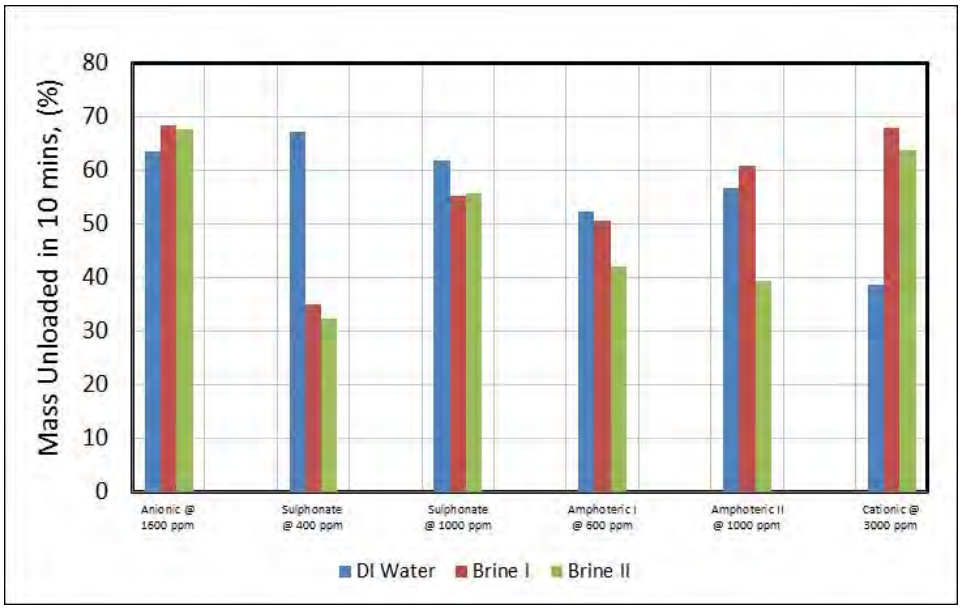

Figure 3.42: Percent Mass of Liquid Unloaded at 10 minutes in Different Mediums at 0.75 LPM

From Figures 3.41 and 3.42, Anionic surfactant was able to resist the influence of Brine I and II. The Sulphonate former is impacted in the presence of Brine; its unloading potential decreases in brine I and II. Amphoteric I is slightly impacted in both Brine solutions. Amphoteric II is not impacted in Brine I but impacted in Brine II. The Cationic surfactant exhibited an enhanced unloading capability in Brine I and II.

<u>Large Scale Facilities – Experimental Results</u>

Results in this section have been divided into nine groups; these are as follows:

- Verification of End Point Result: Single Phase Gas Flow
- Film Reversal in Air-Water Two Phase Flow
- Film Reversal in Air-Water-Foam Flow (Anionic Surfactant at 1600 ppm as a Case Study)
- Pressure Gradient and Liquid Holdup in Air-Water-Foam Flow
- Pressure Gradient in Large Scale and Percent of Liquid Unloaded in Bench Top Test
- Effect of Pipe Diameter on Liquid Holdup in Air-Water Foam Flow
- Liquid Drainage with Time
- Fraction of Gas Trapped in Foam
- Foam Holdup

The rest of this section explains the results from each group.

We conducted single phase gas flow experiments and recorded pressure gradient values in the second section of the 2-in and 4-in pipes. The pressure

gradient values were compared with theoretical pressure gradient values using the Blasius type equation for friction factor in a smooth pipe as

$$\frac{dP}{dZ} = \frac{2}{d} f_F \rho v^2. \tag{3.9}$$

Figures 3.43 and 3.44 show the experimental and theoretical pressure gradient values for 2-in and 4-in pipes respectively.

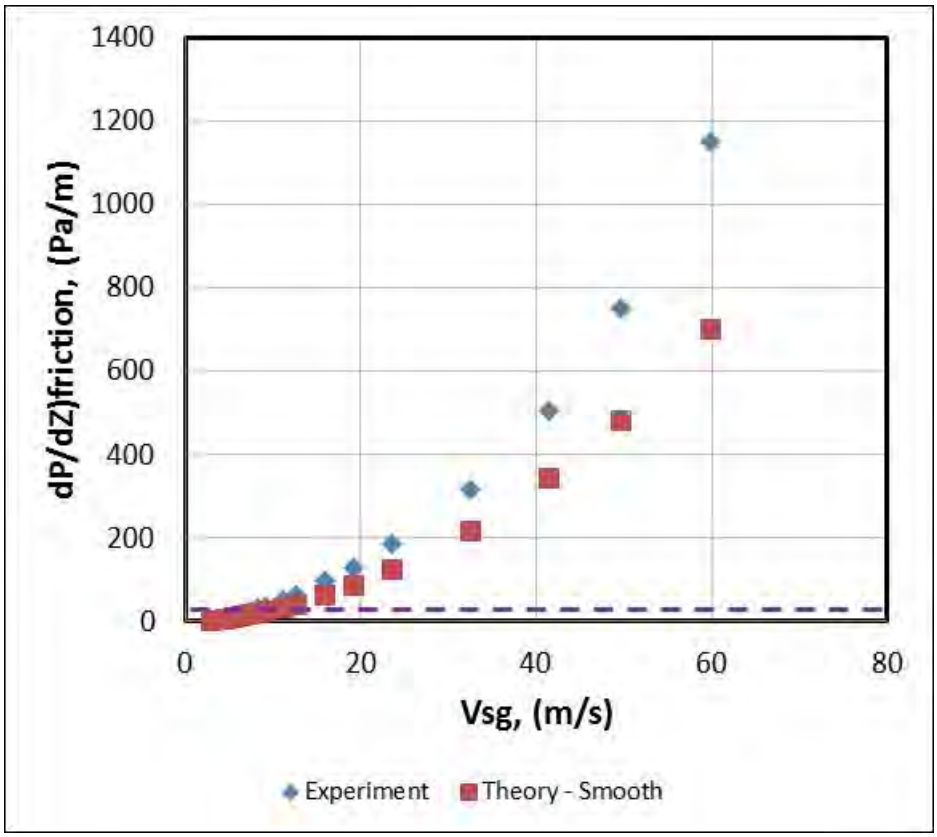

Figure 3.43: Single Phase Pressure Gradient: 2-inch Pipe, Theory and Experiment

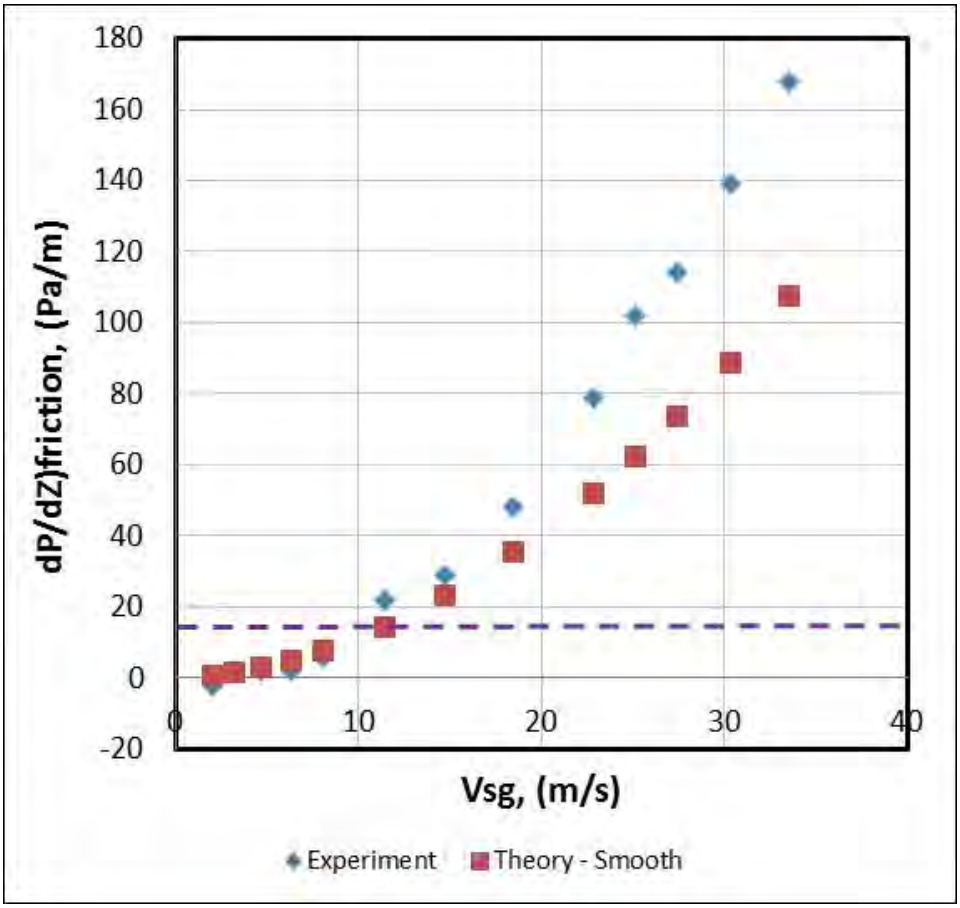

Figure 3.44: Single Phase Pressure Gradient: 4-inch Pipe, Theory and Experiment

In Figures 3.43 and 3.44, after the uncertainty region as indicated by the dashed purple line, the theoretical value under predicts the measured values in the 2-in and 4-in pipes. We do not know the actual friction factor for the tubing. Next, in Figure 3.45, we plot the normalized pressure drop (pressure drop multiplied by diameter) versus the superficial gas velocity for 2-inch and 4-inch pipes from experimental measurements. Figure 3.46 shows the theoretical normalized pressure drop values versus superficial gas velocity for 2-inch and 4-inch pipes. If frictional loses are correctly measured, the 2-inch and 4-inch graphs should overlay each other. Indeed this happens. The discrepancy between theoretical and experimental observations is most likely due to wrong assumption of roughness factor as well as the gas velocity being calculated at atmospheric rather than actual pressure.

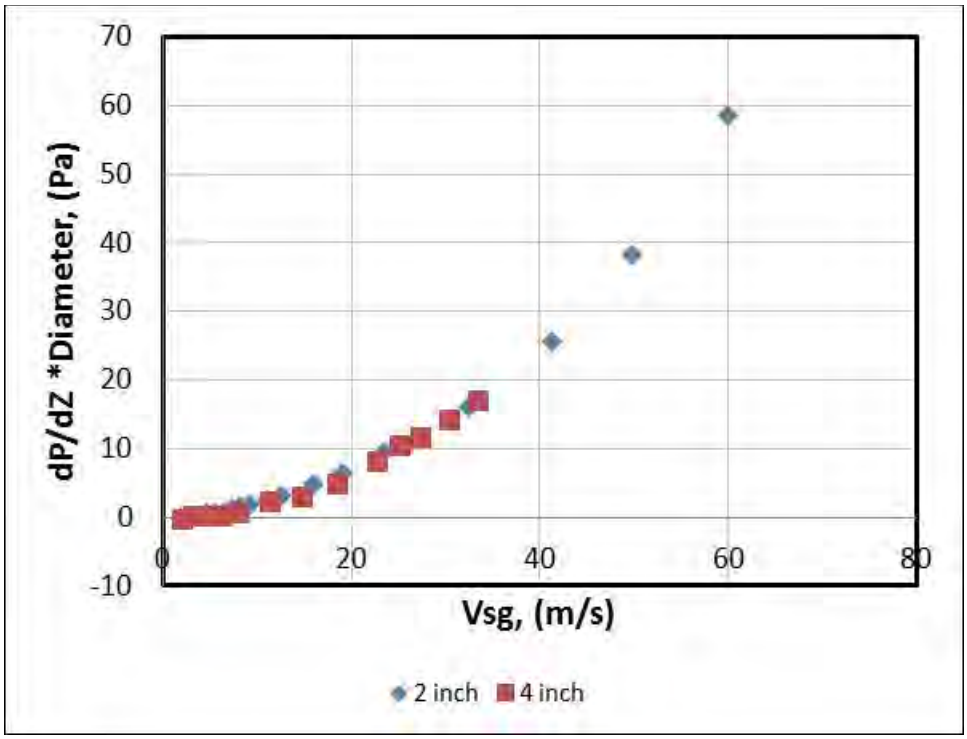

Figure 3.45: Experimental Pressure Drop in 2 and 4-inch Pipes

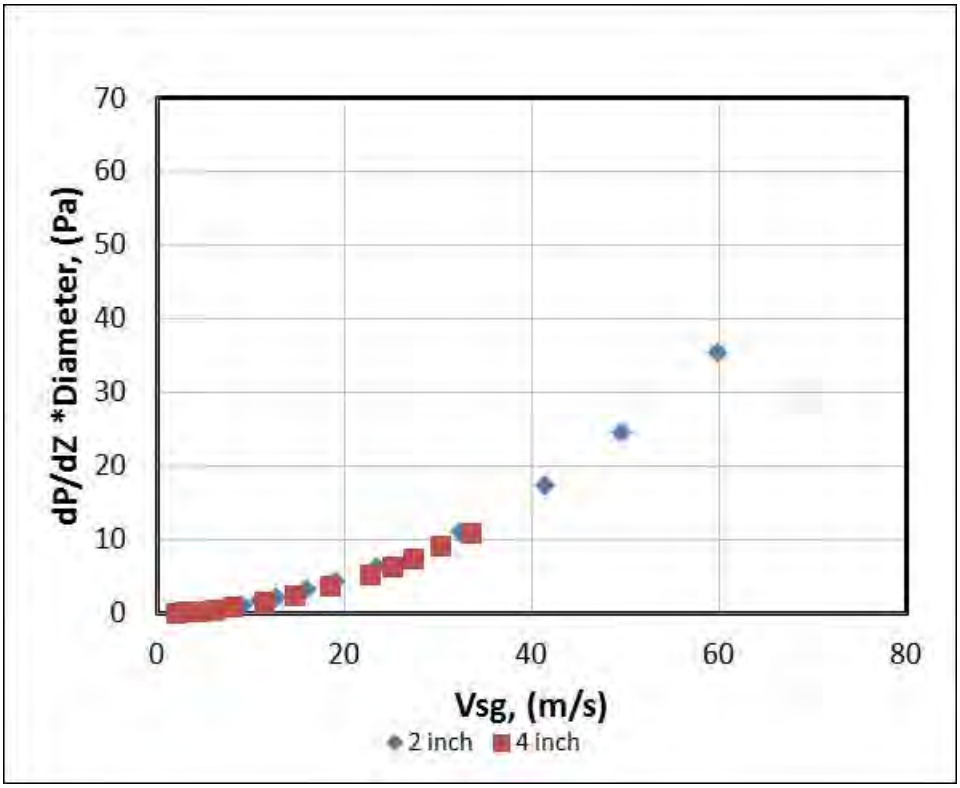

Figure 3.46: Theoretical Pressure Drop in 2 and 4-inch Pipes

In Figure 3.45, we observe that by multiplying the pressure gradient from experiment by the pipe diameter, we were able to collapse the pressure drop values for 2-inch and 4-inch diameter pipes. Same trend was observed in Figure 3.46 where the theoretically measured pressure drop values have been multiplied by the pipe diameter. Hence, despite the deviation in the theoretical and measured pressure gradient in Figures 3.43 and 3.44, the characteristics of the experimental and theoretical pressure drop values are similar.

In section 2 of this report, we showed the results for air-water flow. To summarize what we have already discussed in the section, the liquid film reversal was evident when the residual pressure drop becomes zero (the difference between total pressure drop and gravitational pressure drop). As the gas velocity is lowered further, the residual pressure drop becomes negative indicating film reversal. We want to apply the same methodology for foam flow to detect liquid loading.

In the still frames shown in Figures 3.47(a) and 3.48(b), we show the film characteristic in 2-inch pipe for a data point in intermittent flow. The position of a gas bubble in the film has been tracked and found to move downward with increase in time. This is for air-water flow.

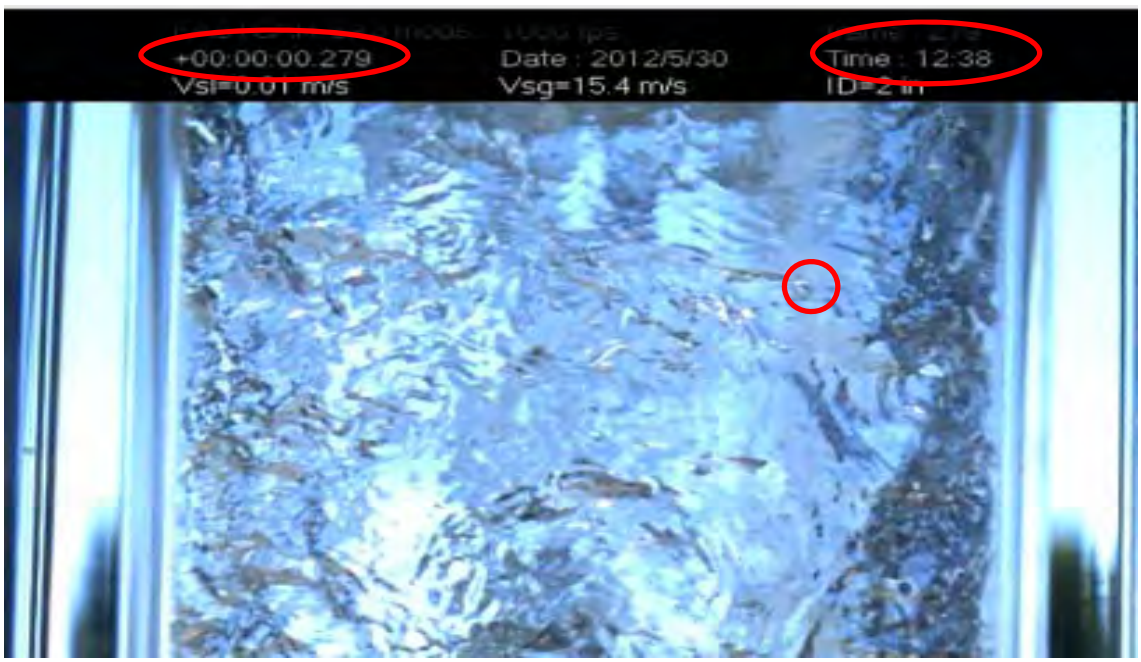

Figure 3.47(a): Still Frame of Air-Water Flow in 2-inch ID at $v_{Sg} = 15.4\ m/s$ and $v_{SL} = 0.01\ m/s$ (Skopich, 2012)

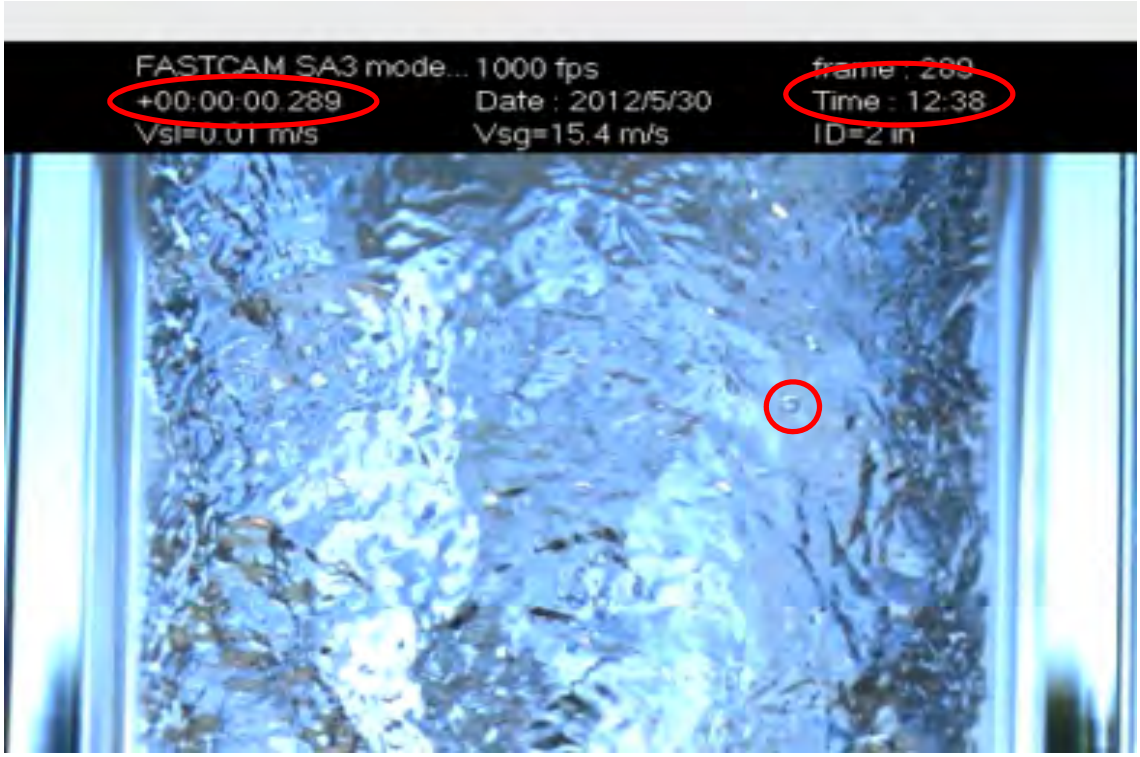

Figure 3.47(b): Still Frame of Air-Water Flow in 2-inch ID at $v_{Sg} = 15.4\ m/s$ and $v_{SL} = 0.01\ m/s$ (Skopich, 2012)

In the still frames shown in Figures 3.48(a) and 3.48(b), we show the film characteristic in 2-inch pipe for data a point in annular flow. The position of a gas bubble in the film has been tracked and found to move upward with increase in time.

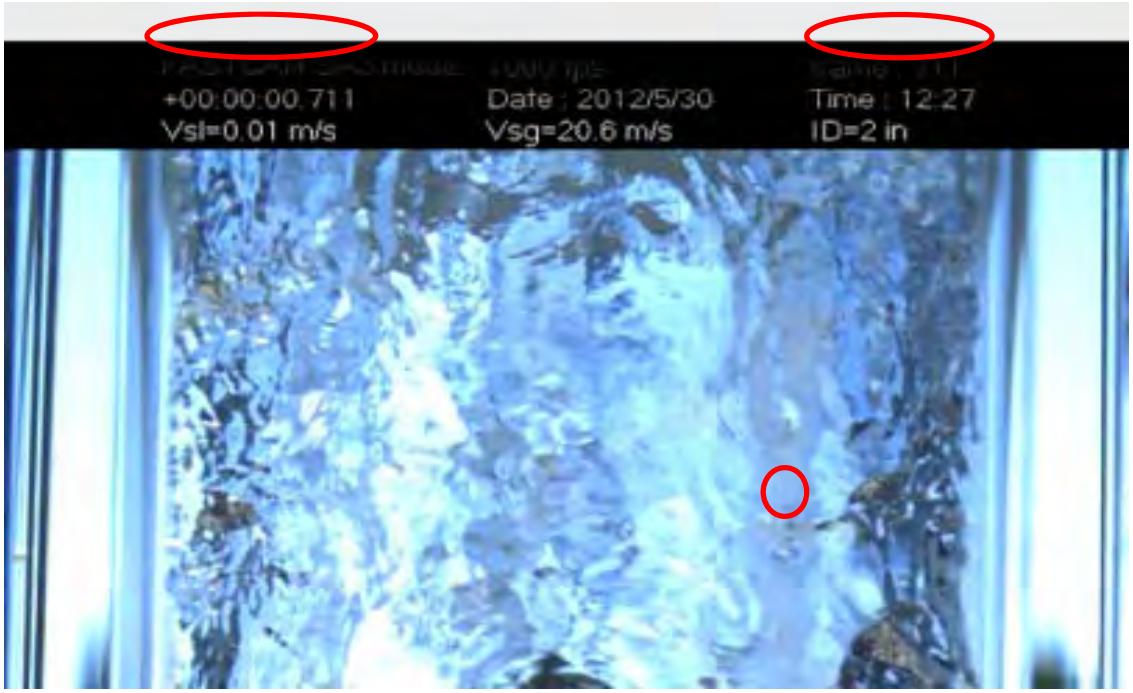

Figure 3.48(a): Still Frame of Air-Water Flow in 2-inch ID at $v_{Sg} = 20.6\ m/s$ and $v_{SL} = 0.01\ m/s$ (Skopich, 2012)

Figure 3.48(b): Still Frame of Air-Water Flow in 2-inch ID at $v_{Sg} = 20.6\ m/s$ and $v_{SL} = 0.01\ m/s$ (Skopich, 2012)

By comparing the film characteristics in Figures 3.47 and 3.48, we also observe that the film in Figure 3.48 is lot thinner than the film in Figure 3.47.

We apply the same principles to demonstrate the pressure gradient in 2-inch pipe under foam flow. Next we comment on the film direction in 2-inch pipe and then we look into the structure of the film with increasing superficial gas velocity. Aforementioned sequence was also followed in discussing the results of foam flow experiments conducted with 4-inch pipe.

For experiments conducted under air-water foam flow, we present observations made based on the direction of film flow in 2-inch pipe. In Figure 3.49, we show a plot of pressure gradient versus superficial gas velocity for Anionic surfactant at 1600 ppm in 2-inch pipe at a superficial liquid velocity v_{SL}, of 0.01 m/s.

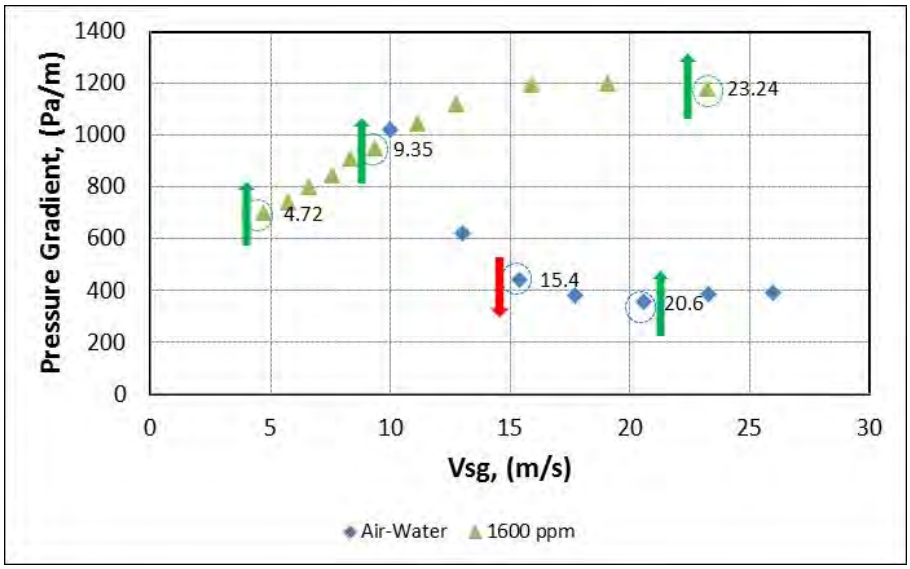

Figure 3.49: Pressure Gradient in Anionic Foamer at 1600 ppm in 2-inch Pipe at $v_{SL} = 0.01\ m/s$

In Figure 3.49, from film flow observation using high speed camera videos, the direction of the film is upward for all the ranges of superficial gas velocities investigated under foam flow. In Figure 3.49, we also plotted the pressure gradient results for air-water two phase flow at a superficial liquid velocity of 0.01 m/s in 2-inch pipe from experiments conducted by Skopich (2012). At a superficial gas velocity of 15.4 m/s, we observed that the film direction in air-water flow is downward while it is upward for Anionic surfactant at 1600 ppm for the whole range of superficial gas velocity tested. Application of foam flow at this concentration is able to delay transition to intermittent flow to superficial velocities below 4.72 m/s.

In Figure 3.49, the pressure gradient under foam flow did not display any minimum. However, as shown later in the next section, depending on the surfactant, concentration, superficial gas velocity and pipe diameter, the minimum on the pressure gradient curve is also displayed under foam flow.

In Figures 3.50 to 3.52, for Anionic surfactant at a superficial liquid velocity of 0.01 m/s and concentration of 1600 ppm in 2-inch pipe, we present still frames showing the evolution of the structure of the foam film under annular flow with increase in superficial gas velocity v_{Sg}. Images presented correspond to experiments conducted at superficial gas velocities of 4.72 m/s, 9.35 m/s and 23.54 m/s respectively. These are the circled data points in Figure 3.49.

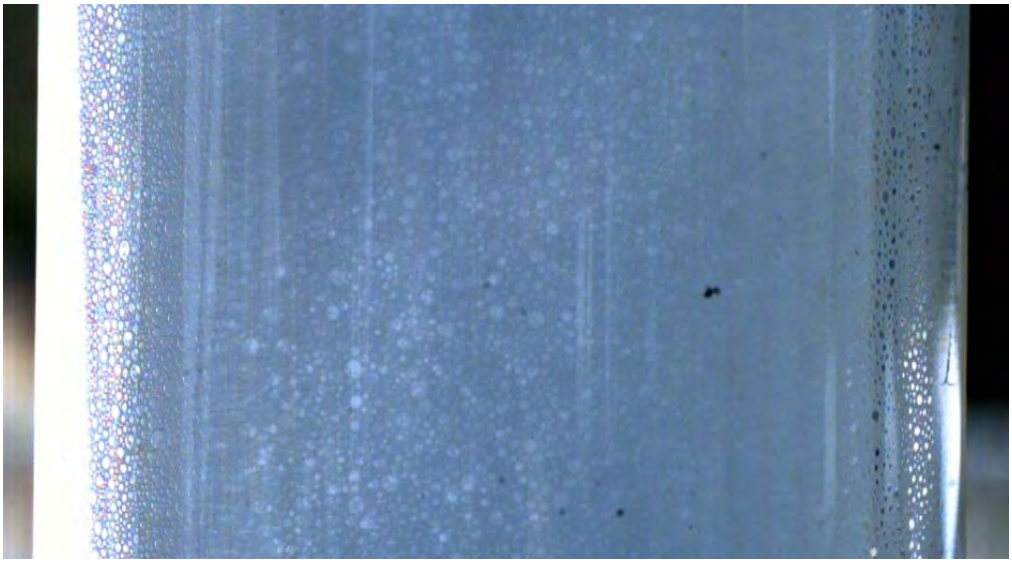

Figure 3.50: Foam Film Structure: Anionic Foamer in 2-inch Pipe at 1600 ppm, $v_{Sl} = 0.01\ m/s$, $v_{Sg} = 4.72\ m/s$

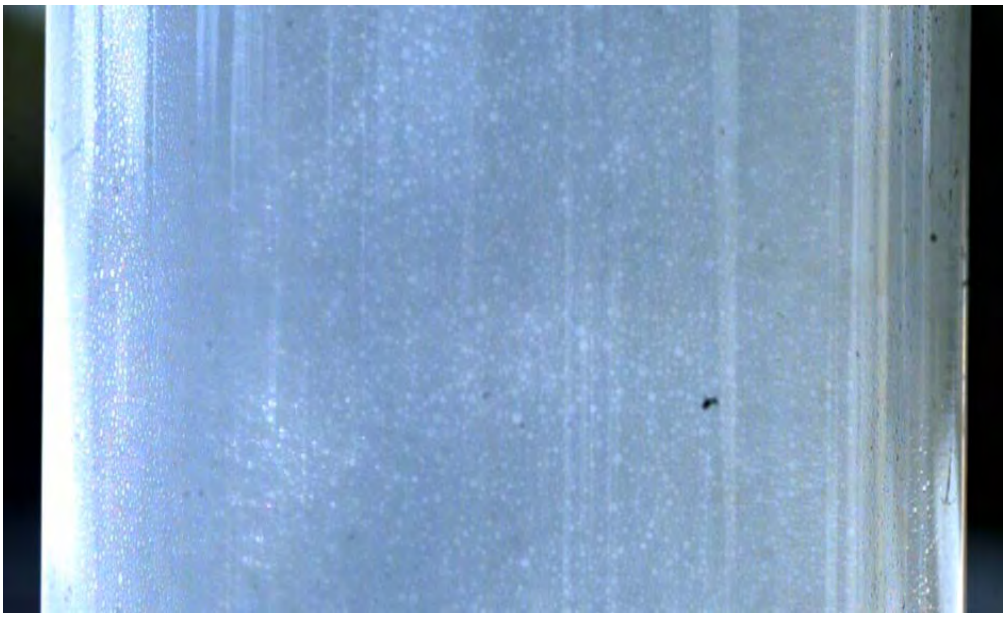

Figure 3.51: Foam Film Structure: Anionic Foamer in 2-inch Pipe at 1600 ppm, $v_{Sl} = 0.01\ m/s$, $v_{Sg} = 9.35\ m/s$

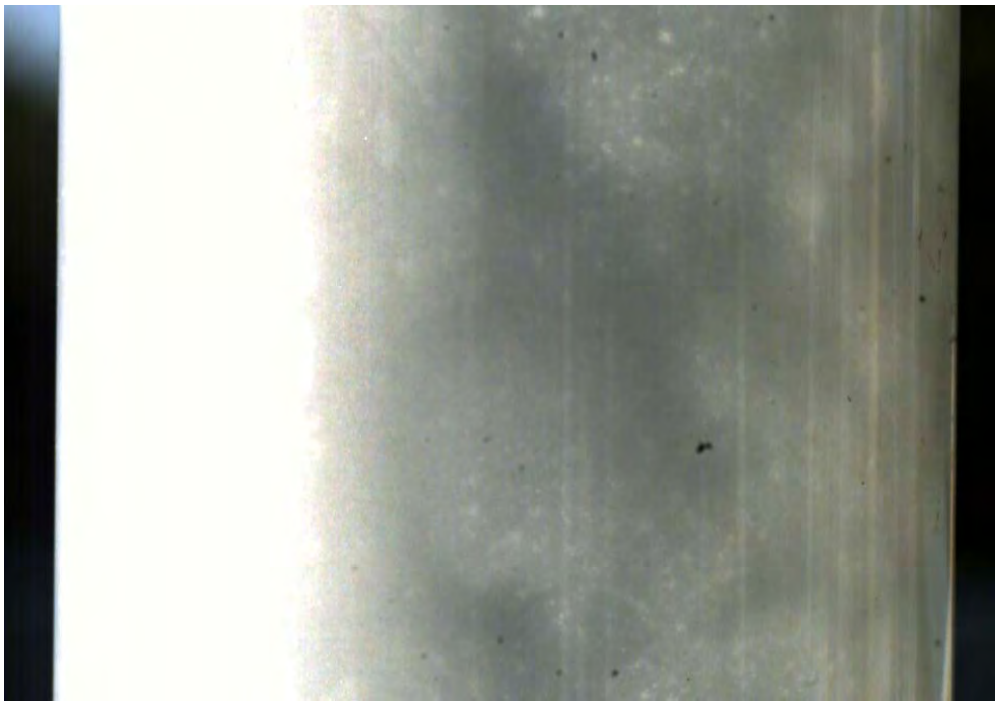

Figure 3.52: Foam Film Structure: Anionic Foamer in 2-inch Pipe at 1600 ppm, $v_{Sl} = 0.01\ m/s, v_{Sg} = 23.54\ m/s$

In Figure 3.50, under annular flow, the foam film consists of bubbles. These bubbles are brought to the pipe wall by the foam bulk travelling upward. The bubbles are being brought forth to the pipe wall and instantaneously swept off the pipe wall as the foam bulk passes by. While the bubble size decreases with increase in superficial gas velocity, aforementioned observation corresponds to the events seen in the foam film of data points in the superficial gas velocity range of 4.72 m/s to 8.33 m/s in Figure 3.49. These are points corresponding to increasing pressure gradient as the superficial gas velocity increases.

In Figure 3.51, the foam film consists of tinnier gas bubbles as compared to those observed in Figure 3.50. These bubbles move upwards as the bulk of the foam moves upwards. However, when the bulk of the foam is gone, we observe that the bubbles tend to stay back on the wall of the pipe. They are again swept off by the next foam bulk moving upwards. The cycle is then repeated again. The high speed camera video also shows that the film exhibit a tendency to be rumpled together hence forming intermittent wave like structure which breaks off as they form. These observations correspond to the events seen in the foam film of data points in the superficial gas velocity range of 9.35 to 15.88 m/s in Figure 3.49. These are points corresponding to increasing pressure gradient as the superficial gas velocity increases from 9.35 m/s at 950 Pa/m to 15.88 m/s at 1196 Pa/m.

In Figure 3.52, the foam film consists of very tiny gas bubbles. The overall structure of the gas bubbles in the foam film has a creamy look than those observed

in Figures 3.50 and 3.51. Here, the film exhibits three events, these are explained next. One, no upward bulk flow of foam is observed; all foam flows on the pipe wall. Two, a part of the foam film is consigned to the wall due to the shearing action and high slippage of the gas in the core; this foam film forms a foam substrate on the pipe wall and does not move with the flow of foam in the film. Three, clearly visible creased roll waves of foam film flows over the foam substrate sticking to the pipe wall as explained in the two above. These observations correspond to the events seen in the foam film of data points in the superficial gas velocities greater than 15.88 m/s up to 23.54 m/s. These are points corresponding to superficial gas velocities greater than 15.88 m/s. In this region, in Figure 3.49, we observed that the pressure gradient decreases from 1196 at a superficial gas velocity v_{SG}, of 15.88 m/s to 1180 Pa/m at a v_{Sg} of 23.54 m/s.

Next, we present observations made based on direction of the film flow in 4-inch pipe. In Figure 3.53, we show a plot of pressure gradient versus superficial gas velocity for Anionic surfactant at 1600 ppm in 4-inch pipe at a superficial liquid velocity v_{SL}, of 0.01 m/s.

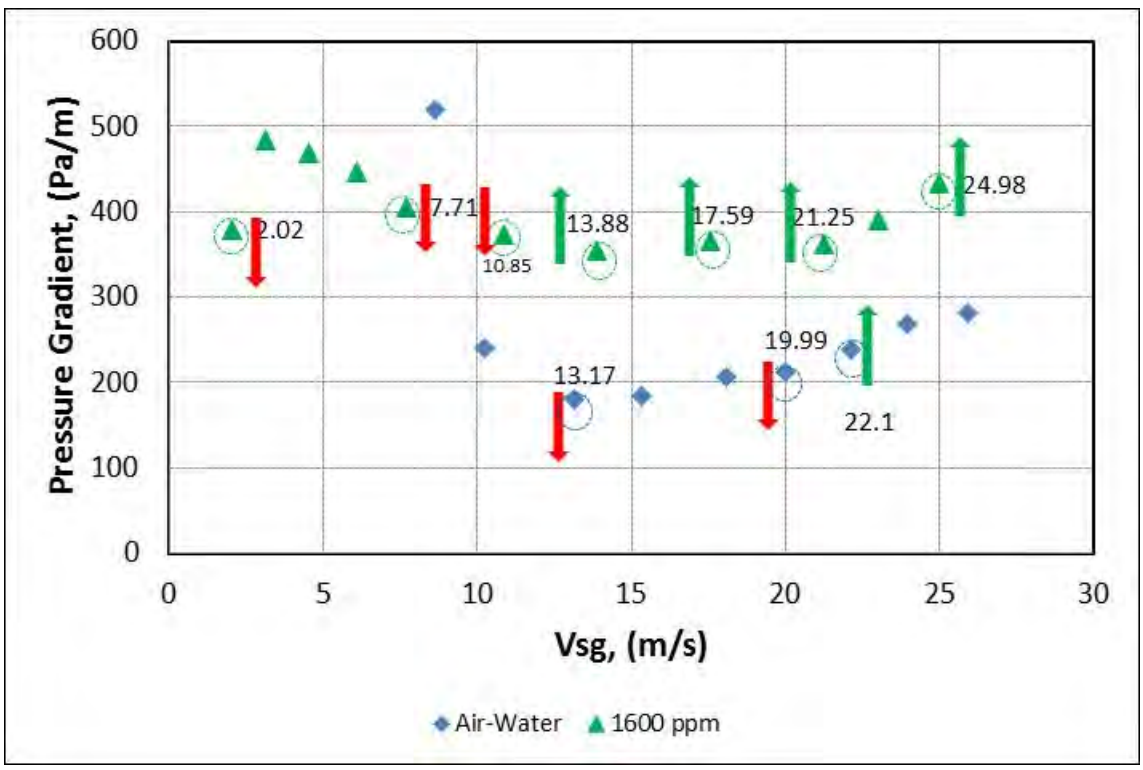

Figure 3.53: Pressure Gradient in Anionic Foamer at 1600 ppm in 4-inch Pipe at $v_{SL} = 0.01\ m/s$

In Figure 3.53, from film flow observation under foam flow with high speed camera videos, the direction of the foam film is upward from a superficial gas velocity of 24.98 m/s to 13.88 m/s. At a superficial gas velocity of 10.85 m/s, the foam film switches direction and begins to flow downward despite the fact that the bulk of foam

flow is upward. In Figure 3.53, we also plotted the pressure gradient results for air-water two phase flow at a superficial liquid velocity of 0.01 m/s in 4-inch pipe from experiments conducted by Skopich (2012). For air-water flow, at a superficial gas velocity of 19.99 m/s, we observed that the film direction is downward while it is upward at a superficial gas velocity of 13.88 m/s under foam flow. This shows the benefit of using foam to delay the onset of transition from annular flow to intermittent flow.

In Figure 3.53, the pressure gradient under foam flow displayed a minimum for this surfactant at 1600 ppm in 4-inch pipe. By comparing the foam flow results in 2-inch pipe (Figure 3.49) to that of 4-inch pipe (Figure 3.53), it is evident that the absence of a minimum on the pressure gradient curve of the 2-inch data shows that surfactant benefit is bigger in 2-inch pipe than 4-inch pipe.

In the still frames shown in Figures 3.54(a) and 3.54(b), we show the foam film characteristic in 4-inch pipe at a superficial gas velocity of 10.85 m/s. The position of a gas bubble in the film has been tracked and found to move downward with increase in time. Thus, the data point lies in the intermittent flow regime.

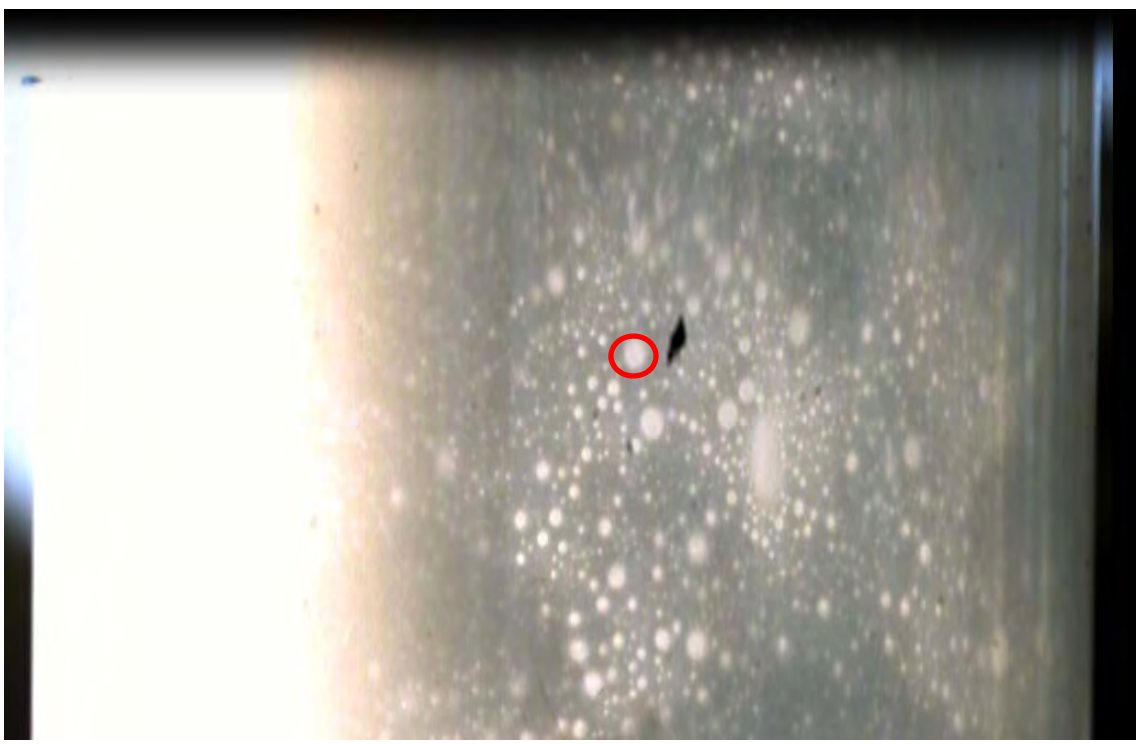

Figure 3.54(a): Still Frame of Foam Flow in 4-inch ID at $v_{Sg} = 10.85\ m/s$ and $v_{SL} = 0.01\ m/s$

Figure 3.54(b): Still Frame of Foam Flow in 4-inch ID at $v_{Sg} = 10.85\ m/s$ and $v_{SL} = 0.01\ m/s$

In Figures 3.55 to 3.57, for Anionic surfactant at a superficial liquid velocity of 0.01 m/s and concentration of 1600 ppm in 4-inch pipe, we present still frames showing that no stagnant foam film was found on the pipe at very high superficial gas velocities. Images presented correspond to experiments conducted at superficial gas velocities of 17.39 m/s, 21.29 m/s and 24.98 m/s respectively as shown in Figure 3.53.

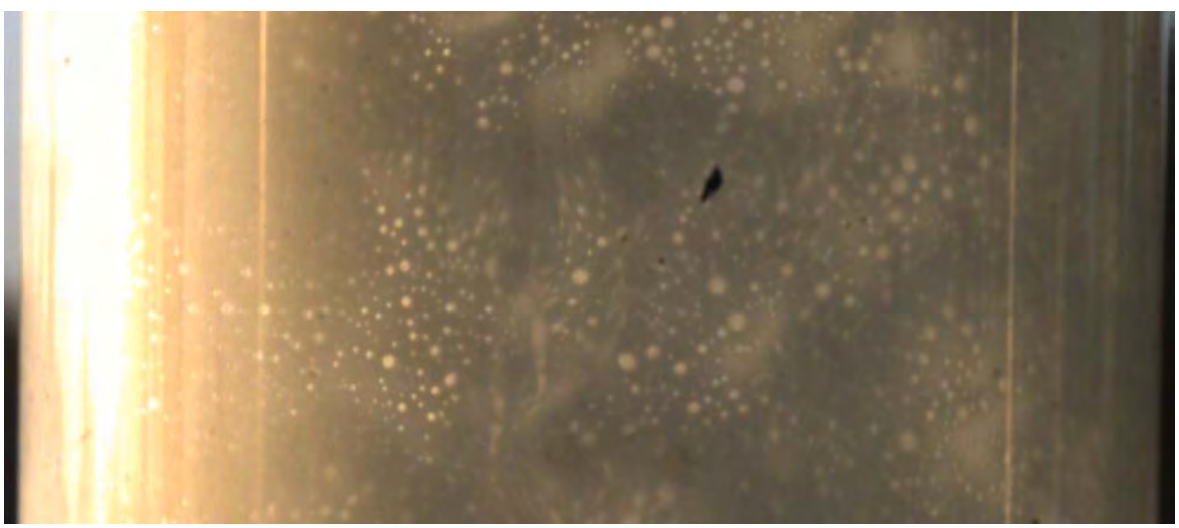

Figure 3.55: Foam Film Structure: Anionic Foamer in 4-inch Pipe at 1600 ppm, $v_{Sl} = 0.01\ m/s, v_{Sg} = 17.59\ m/s$

Figure 3.56: Foam Film Structure: Anionic Foamer in 4-inch Pipe at 1,600 ppm, $v_{Sl} = 0.01\ m/s, v_{Sg} = 21.25\ m/s$

Figure 3.57: Foam Film Structure: Anionic Foamer in 4-inch Pipe at 1,600 ppm, $v_{Sl} = 0.01\ m/s, v_{Sg} = 24.98\ m/s$

From Figures 3.55 to 3.57, the quantity of gas bubbles in the foam film decreased. The roll waves of foam seen in Figure 3.52 for 2-inch pipe can be observed in Figure 3.57 but these are very thin and not as conspicuous as seen in Figure 3.52.

In Figures 3.58 and 3.59, we present the pressure gradient and liquid holdup for Anionic surfactant in 2-inch pipe at a superficial liquid velocity of 0.01 m/s.

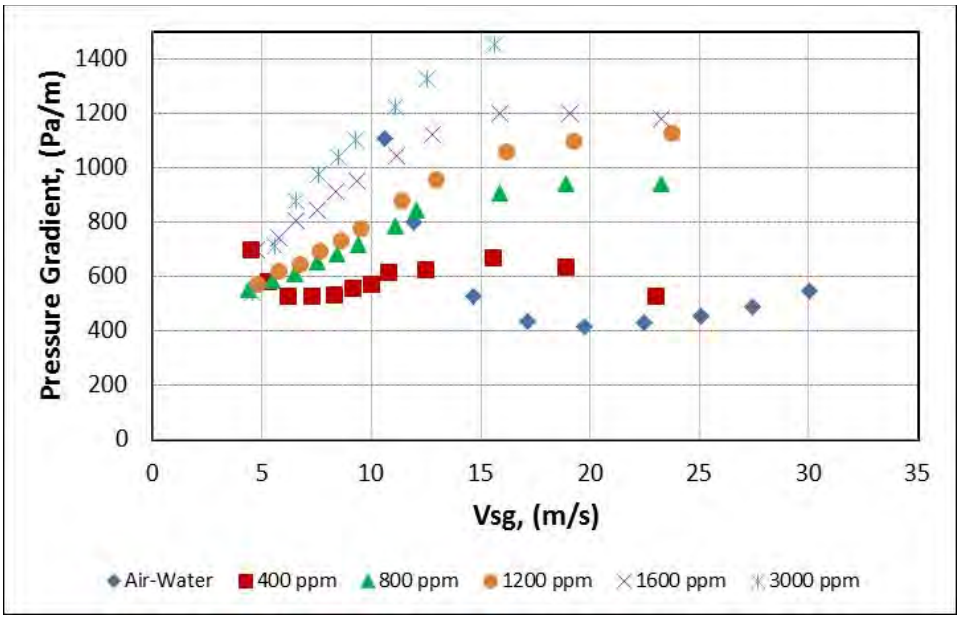

Figure 3.58: Pressure Gradient for Anionic Foamer [v_{SL}= 0.01 m/s, 2-in pipe]

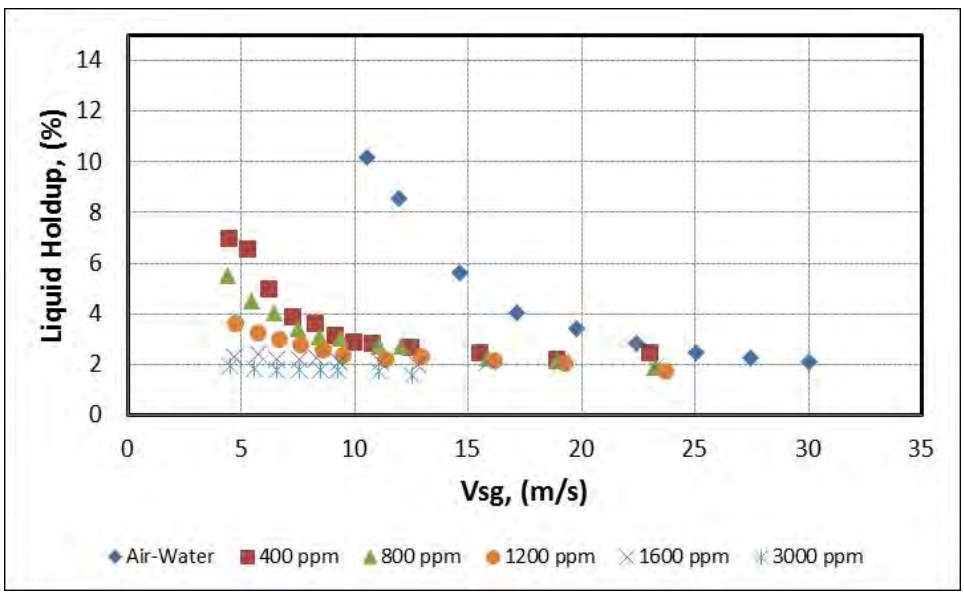

Figure 3.59: Liquid Holdup for Anionic Foamer [v_{SL}= 0.01 m/s, 2-in pipe]

Plots for the pressure gradient and liquid holdup for Anionic surfactant in 2-inch pipe at a superficial liquid velocity of 0.03 m/s can be found in Ajani (2014). In Figure 3.58, for superficial gas velocity $v_{SG} < 10m/s$, foam decreases the pressure gradient when compared to the air-water case for all concentrations considered. In Figure 3.59, for superficial gas velocity $v_{SG} < 10m/s$, foam decreases the liquid holdup when compared to the air-water case for all concentrations considered.

For superficial gas velocity $v_{SG}, < 10m/s$, from Figure 3.59, we observed that the decrease in the liquid holdup is the main reason for the decrease observed in the pressure gradient in Figure 3.58. In Figure 3.58, for superficial gas velocity $v_{SG}, >$

$10m/s$, foam increases the pressure drop compared to the air-water case. From the high speed video observation of the foam film structure (Figures 3.51 to 3.52), foam increases the waviness of the liquid film at high superficial gas velocities in 2-inch pipe. Consequently, the friction is increased and this causes an increase in the pressure drop. In Figure 3.58, at 400 ppm, the pressure gradient attained a peak value at a superficial gas velocity of 16 m/s and it falls afterwards. At 800 ppm, 1200 ppm and 1600 ppm, the pressure gradient also attained a peak value at a superficial gas velocity of 16 m/s but instead of falling as observed for 400 ppm, it remains relatively steady with increase in superficial gas velocity. At 3000 ppm, the pressure gradient shows a tendency to increase with increasing superficial gas velocity. While it is evident that surfactant concentration has a strong effect on pressure drop, aforementioned trends are evidently due to the fact that surfactant application will not be required for a gas well operating at a superficial gas velocity greater than 17 m/s.

In Figures 3.60 and 3.61, we present the pressure gradient and liquid holdup for Anionic surfactant in 4-inch pipe at a superficial liquid velocity of 0.01 m/s.

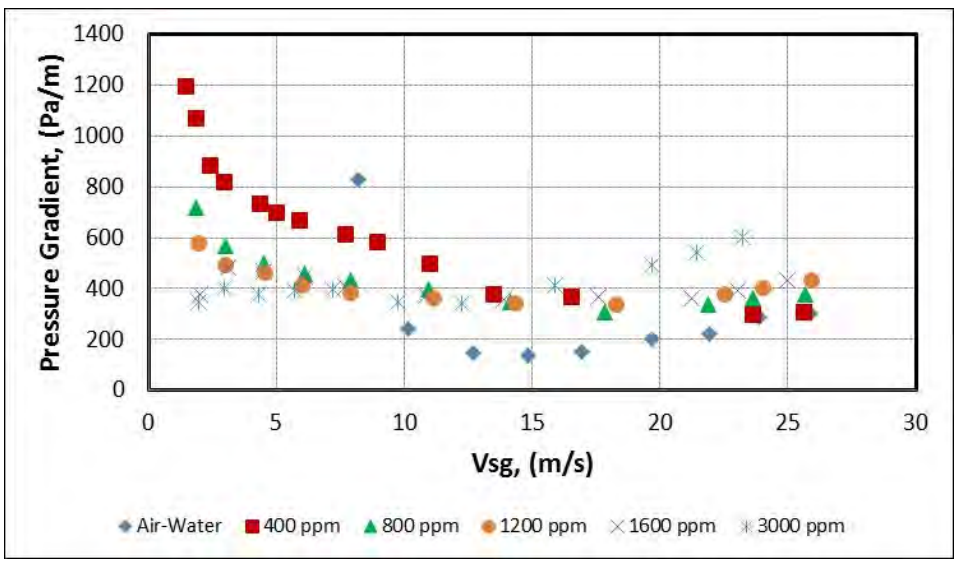

Figure 3.60: Pressure Gradient for Anionic Foamer [v_{SL}= 0.01 m/s, 4-in pipe]

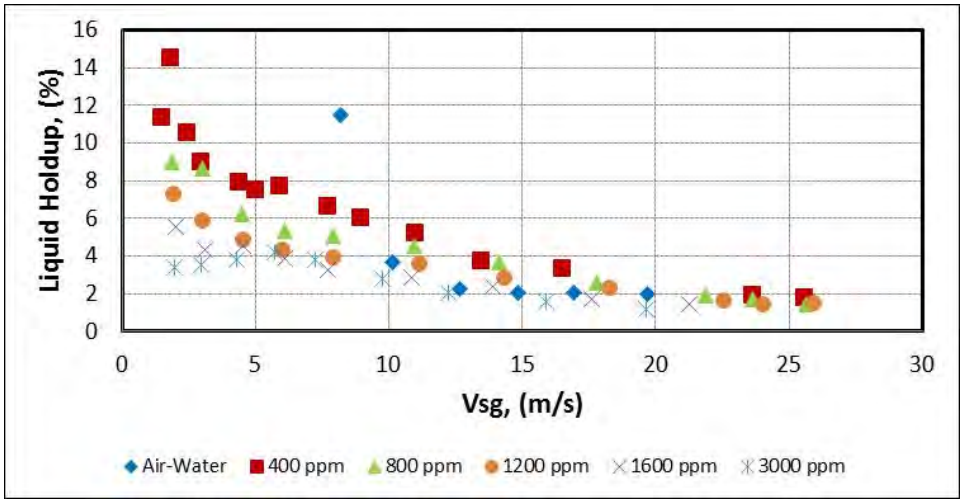

Figure 3.61: Liquid Holdup for Anionic Foamer [v_{SL}= 0.01 m/s, 4-in pipe]

In Figure 3.60, for v_{SG} < 10 m/s, foam decreases the pressure gradient. Figure 3.61 shows that foam flow causes lower liquid holdup as compared to the air-water case; hence the reason for the lower pressure gradient seen in Figure 3.60 for v_{SG} < 10 m/s.

In Figure 3.60, for v_{SG} > 10 m/s, foam flow causes a higher pressure gradient but not as high as seen in the 2-inch pipe for this range of superficial gas velocity. A probable reason for this may be due to the fact that the foam film structure seen in 4-inch pipe (Figures 3.55 to 3.57) exhibit roll waves with very little gas bubble trapped in them as compared to the case of 2-inch pipe (Figures 3.51 to 3.52). These roll waves are also very thin when compared to those observed in 2-inch pipe at high superficial gas velocity.

Furthermore, in contrast to the liquid holdup observation in 2-in pipe for v_{SG} > 10 m/s, in Figure 3.61, foam flow does not reduce the liquid holdup in 4-in pipe; rather, it causes liquid accumulation in the pipe. This effect is even more evident at a superficial liquid velocity of 0.03 m/s (Ajani, 2014). All concentrations tested exhibited a minimum on the pressure gradient plot; as seen in the high speed video (Figure 3.53), this shows that a substantial part of the flow in the intermittent regime. Therefore, in Figure 3.60, a second probable reason for the high pressure gradient seen beyond a superficial gas velocity of 10 m/s is due to the gravitational pressure drop gained due to increasing liquid. To offset this effect, as seen in Figure 3.61, a very high concentration of the surfactant will be required to drive the liquid holdup in 4-inch pipe below that seen in air-water two phase flow for the same pipe. This was achieved at 3000 ppm in Figure 3.61. The observations noted for Anionic surfactant as detailed above are similar to those observed in other foamers tested: Amphoteric I, Amphoteric II, Sulphonate and Cationic surfactants. The results for other surfactants can be found in Ajani (2014).

A comparison is made between the percent mass of liquid unloaded at half-life concentration (bench top facility) and the pressure gradient observed for each surfactant at the half-life concentration in the large scale facility. In Figures 3.31 and 3,32, we showed the percent mass of liquid unloaded at 0.50 LPM and 0.75 LPM with concentrations at highest half-life values.

As explained before, Anionic and Sulphonate foamers can be sparged at a lower rate while Amphoteric I, Amphoteric II and Cationic Surfactants can all be sparged at a higher rate. In Figures 3.31 and 3.32, for the unloading test conducted at 0.50 LPM and 0.75 LPM, it was observed that the low rate foamers (Anionic and Sulphonate) unloaded the highest percent mass of liquid. In Figure 3.32, it was observed that the Cationic Surfactant (a high rate foamer) unloaded comparative percent mass of liquid as the Anionic and Sulphonate foamers after running the test for about 15 minutes.

In Figures 3.62 and 3.63, we show the pressure gradients versus superficial gas velocities in 2-inch pipe and at superficial liquid velocities of 0.01 and 0.03 m/s for Anionic, Amphoteric I and Amphoteric II at the half-life concentration of each surfactant. The pressure gradients of the Sulphonate and Cationic surfactants are shown at 1200 ppm and 2400 ppm as against 1000 ppm and 3000 ppm half-life concentrations. This was because the large scale test was conducted at approximately their half-life concentrations.

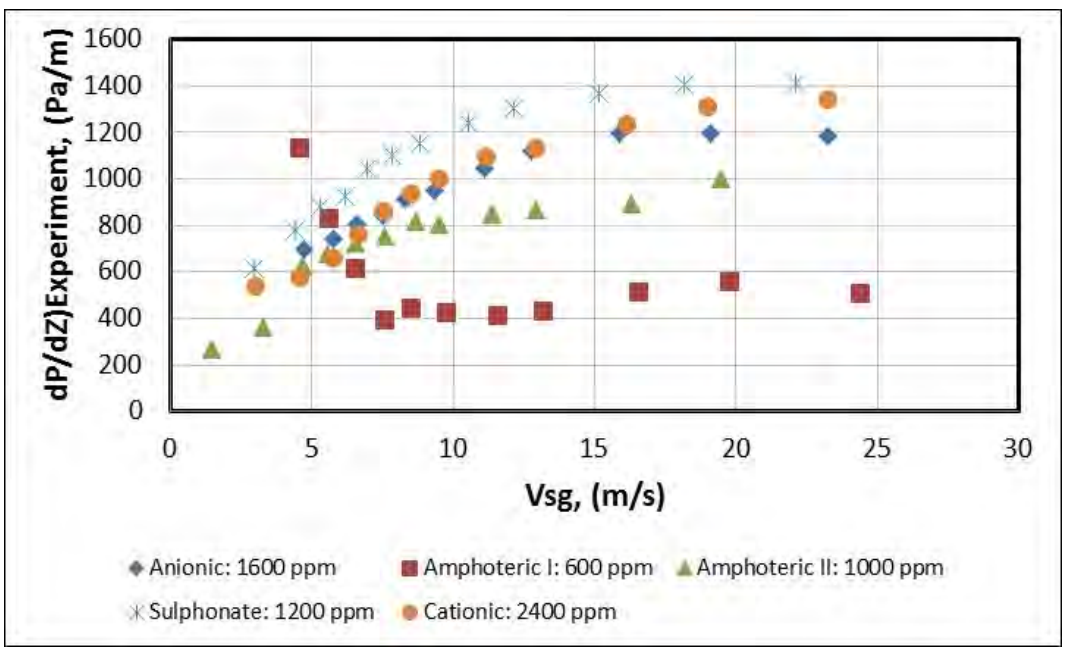

Figure 3.62: Pressure Gradients at Half-life Concentrations: 2-inch Pipe, $v_{SL} = 0.01\ m/s$

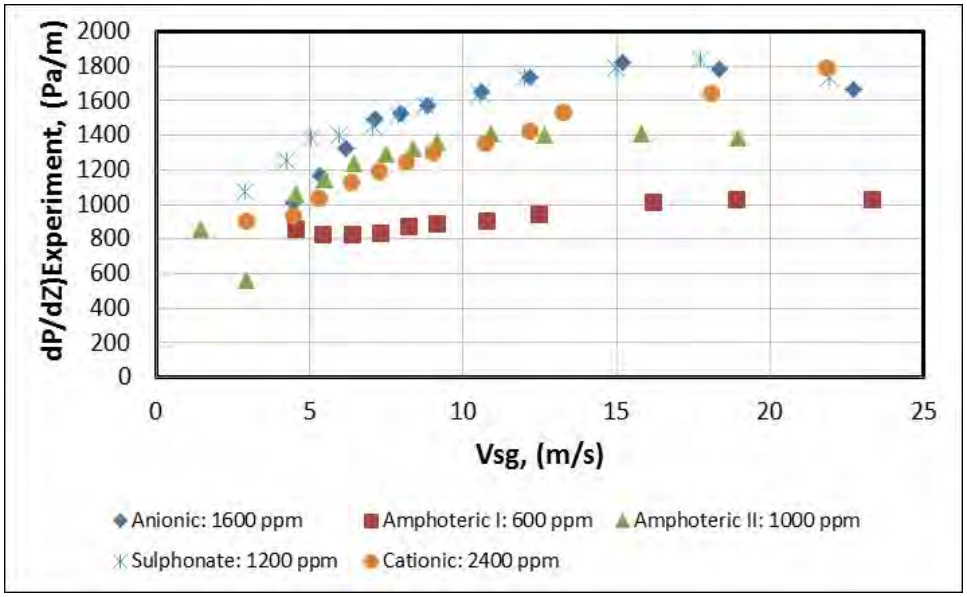

Figure 3.63: Pressure Gradients at Half-life Concentrations: 2-inch Pipe, $v_{SL} = 0.03\ m/s$

Comparing Figure 3.32 with Figure 3.63, it was observed that the low rate foamers (Anionic and Sulphonate) exhibited a higher pressure gradient than the high rate foamers (Amphoteric I, Amphoteric II and Cationic Surfactants) for the range of superficial gas velocities tested. The Cationic surfactant which exhibited a comparative percent mass of liquid unloaded as the low rate foamers in Figure 3.32 also exhibited a comparatively high pressure gradient as the low rate foamers in Figures 3.62. In Figures 3.62 and 3.63, Amphoteric I and Amphoteric II (high rate foamers) exhibited a low pressure gradient as compared to the low rate foamers and Cationic surfactant. In Figures 3.64 and 3.65, we observe similar observation in 4-inch pipe at superficial liquid velocities of 0.01 and 0.03 m/s and superficial gas velocities greater than 20 m/s. The increase in pressure gradient exhibited by the low rate foamers and the Cationic surfactant is not as prominent as seen in the two-inch pipe.

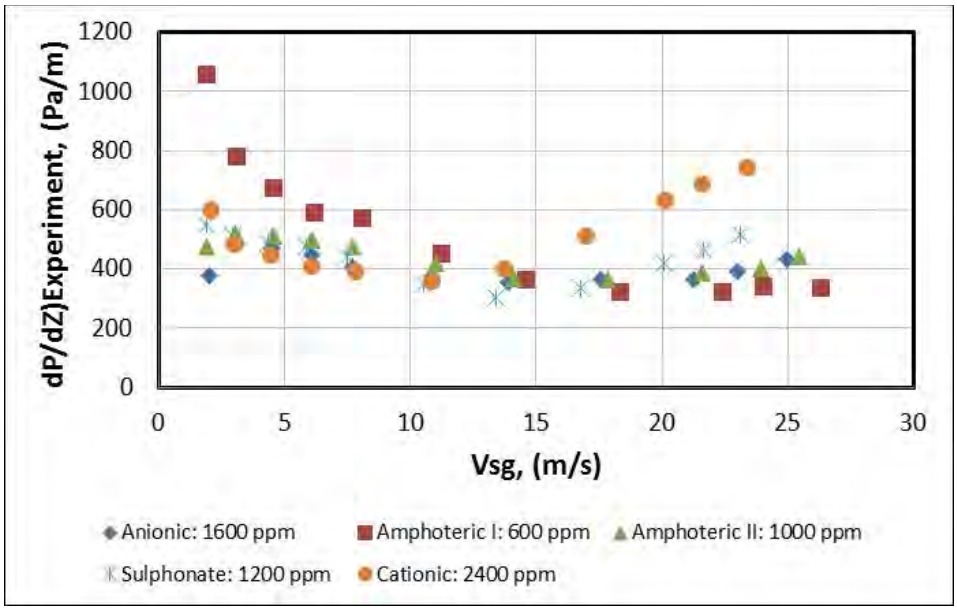

Figure 3.64: Pressure Gradients at Half-life Concentrations: 4-inch Pipe, $v_{SL} = 0.01\ m/s$

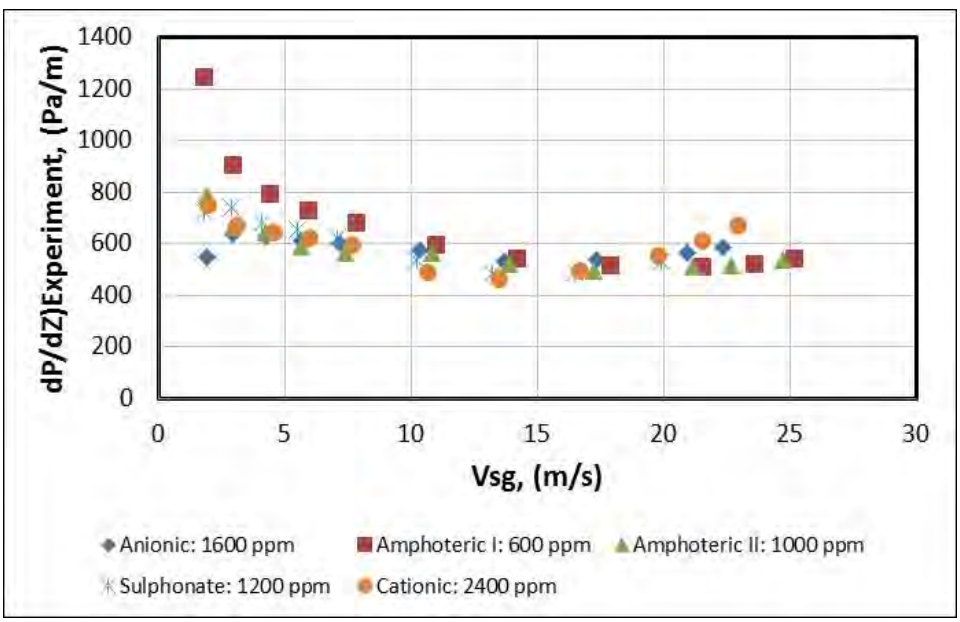

Figure 3.65: Pressure Gradients at Half-life Concentrations: 4-inch Pipe, $v_{SL} = 0.03\ m/s$

In summary, the high rate foamers (Amphoteric I and Amphoteric II) with lower half-life values and lower percent mass of liquid unloaded in the bench top tests gave lower pressure drop values in the large scale test. The low rate foamers (Anionic and Sulphonate foamers) gave a high pressure loss in the large scale test. The cationic surfactant is found to behave as a partial low rate foamer. The low rate foamers forms more bulky foam and are able to retain more liquid and transport more liquid with time. Hence, they have higher half-life and percent mass of liquid

unloaded values. These are good indices for surfactant selection in the bench top tests. However, the bulky and sticky foam formed creates a high shear effect; this is the reason for the high pressure loss seen in the large scale facility. From a practical standpoint, in selecting a product for field usage; ease of foaming, high half-life and high percent mass of liquid unloaded in different media at different temperatures are good indicators. However, attention must be paid to what pressure gradient value the operator is willing to accommodate by selecting surfactants with the lowest ease of foaming, highest half-life and highest percent mass of liquid unloaded.

The effect of pipe diameter on liquid holdup in air-water foam flow is demonstrated using only Anionic Surfactant. For illustration purposes, we have selected concentrations around the critical micelle's concentration; these are 800 ppm and 1200 ppm at a constant superficial liquid velocity of 0.01 m/s.

In Figures 3.66 and 3.67, at a constant superficial liquid velocity of 0.01 m/s, it was observed that the liquid holdup in 4-in pipe is greater than the liquid holdup in 2-in pipe. An opposite trend was observed for air-water liquid holdup in 2-in and 4-in pipes made on these plots.

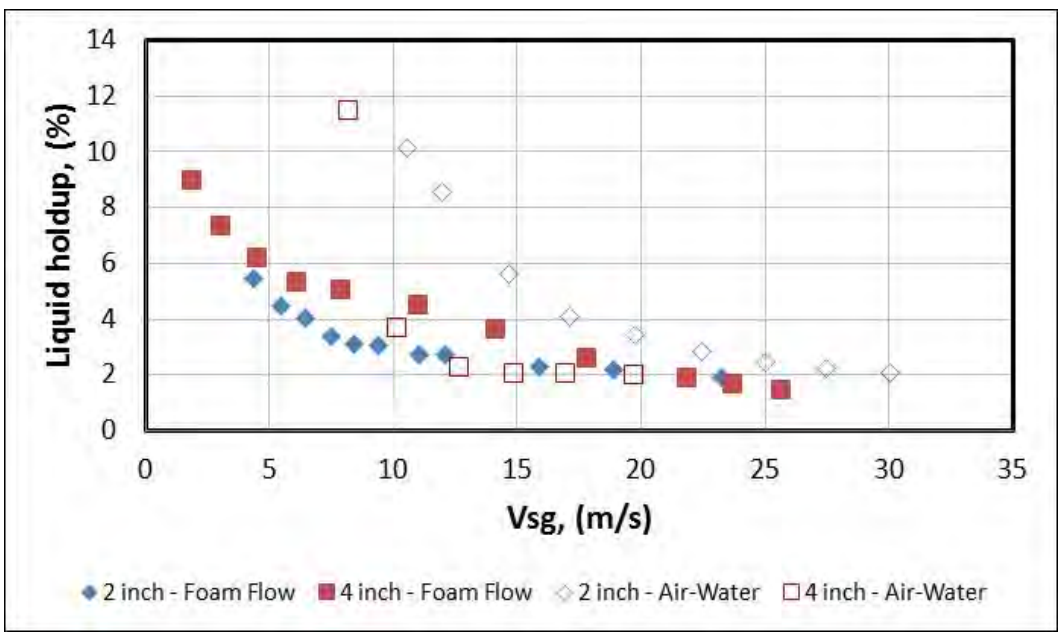

Figure 3.66: Liquid Holdup for Anionic Surfactant [800 ppm, $\boldsymbol{v_{SL} = 0.01\ m/s}$] vs. Liquid Holdup in Air-Water Flow

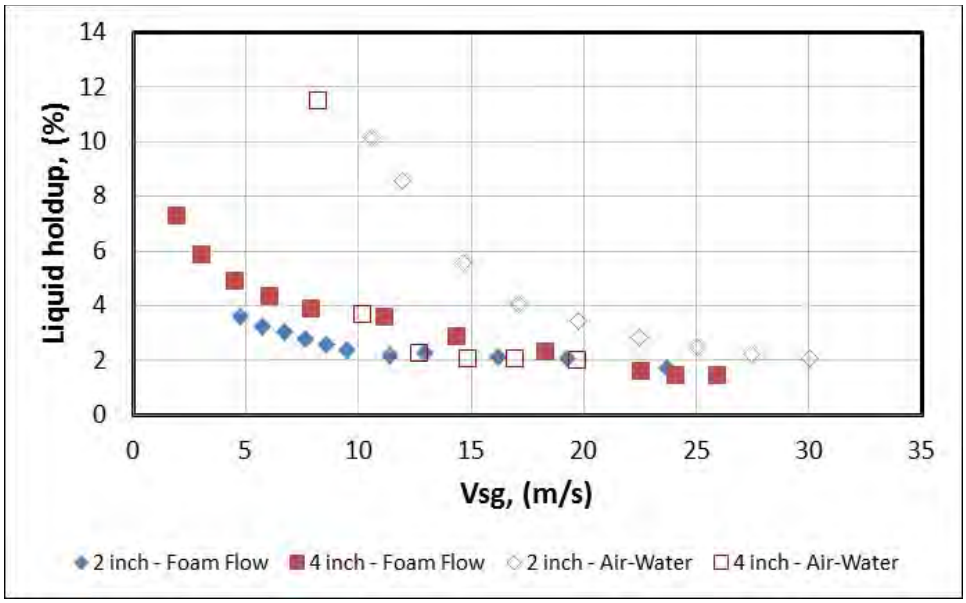

Figure 3.67: Liquid Holdup for Anionic Surfactant [1200 ppm, $\boldsymbol{v_{SL} = 0.01\ m/s}$] vs. Holdup in Air-water Flow

The contrary trend of liquid holdup seen in foam flow from that of air-water flow show that the flow dynamics under foam flow is not the same as that of air-water flow. Since the liquid holdup for 2-inch pipe is persistently lower than those observed in 4-inch pipe, then foam flow is more effective at unloading liquid from smaller diameter pipes. The film thickness is related to liquid holdup. As the liquid holdup increases, we expect that film thickness will increase. With higher liquid holdup, the film thickness for 4-inch pipe is significantly greater than 2-inch pipe. This explains the success of the application of velocity/capillary strings in enhancing production from wells with liquid loading problems.

Next, we present results from the second batch of data collected on the large scale facility. The curves are not continuous in some of the plots to be presented below. This is because there are times the liquid interface being monitored enters into pressure transducer clamps or pipe joints. There are also cases where we have very dense foam thereby making it practically impossible to monitor the height of the liquid draining from the trapped foam up to five minutes after trapping the pipe section.

Here, we conducted foam flow experiments with Anionic, Amphoteric I and Sulphonate foamers at 1000 ppm, 600 ppm and 800 ppm respectively. Aforementioned concentrations are optimum concentrations for these foamers based on bench top tests. In Figures 3.68 and 3.69, we show the liquid holdup with time using the liquid draining from the trapped foam in the 2 and 4-inch pipes. The experiments were conducted at an approximate superficial gas velocity of 4.50 m/s and a superficial liquid velocity of 0.01 m/s and 0.03 m/s respectively.

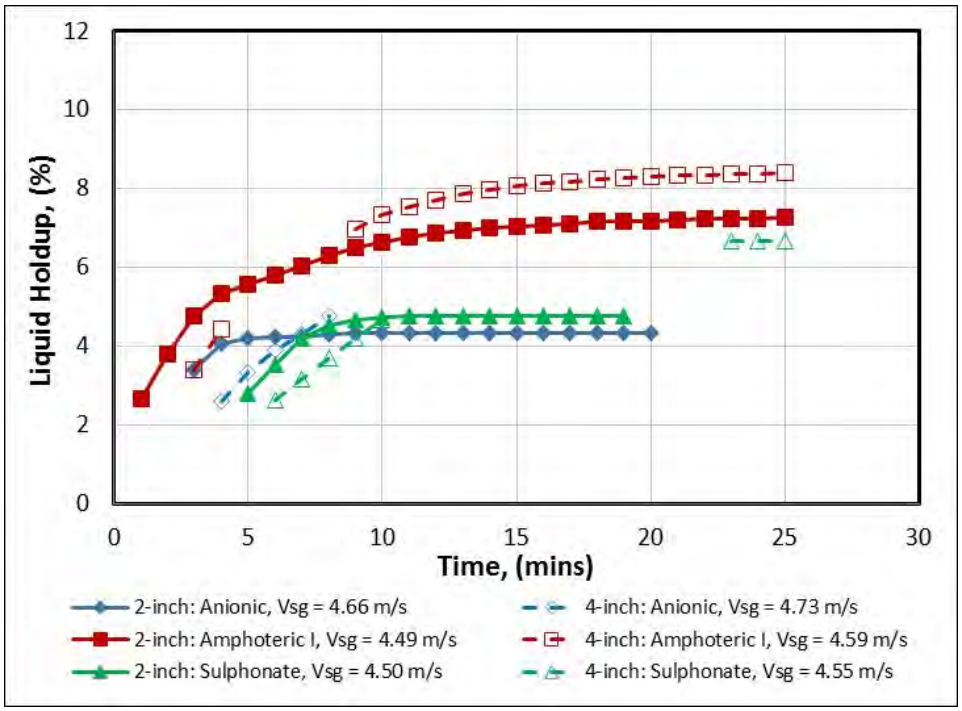

Figure 3.68: Liquid Holdup with Time for Anionic (1000 ppm), Amphoteric I (600 ppm) and Sulphonate (800 ppm) Foamers at $v_{SG} = 4.50\ m/s$ and $v_{SL} = 0.01\ m/s$

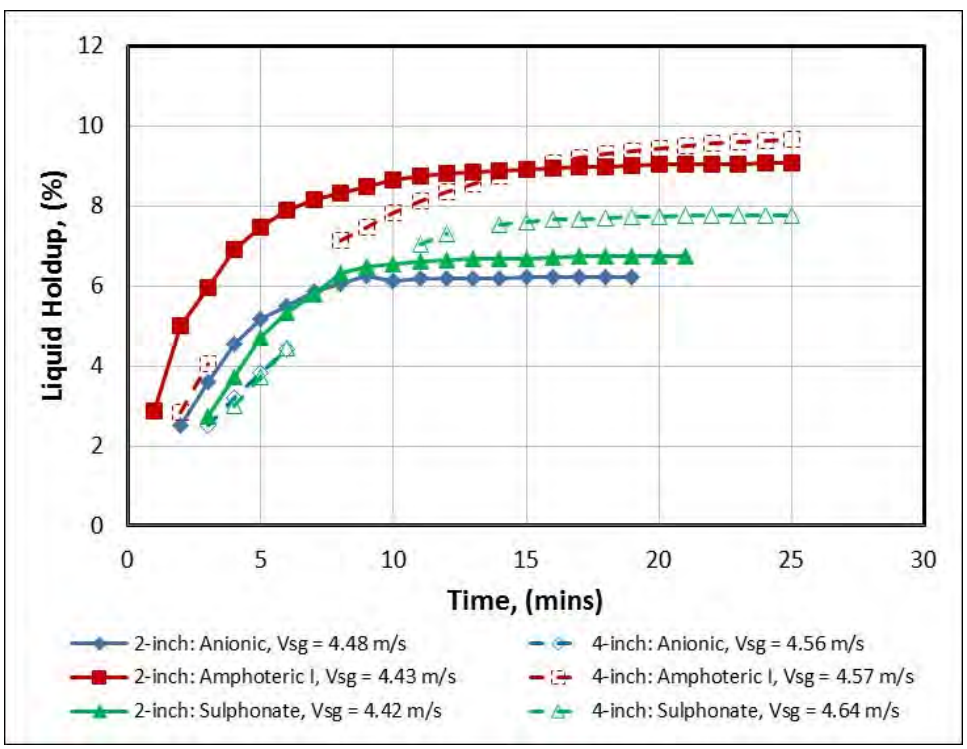

Figure 3.69: Liquid Holdup with Time for Anionic (1,000 ppm), Amphoteric I (600 ppm) and Sulphonate (800 ppm) Foamers at $v_{SG} = 4.50\ m/s$ and $v_{SL} = 0.03\ m/s$

In these figures, we observe that liquid drains faster from 2-inch pipe than 4-inch pipe.

Here, foam flow experiments was conducted on the Anionic, Amphoteric I, Sulphonate and Cationic foamers at 1,000 ppm, 600 ppm, 800 ppm and 1,200 ppm respectively. These concentrations are optimum concentrations for the foamers based on bench top tests. In Figures 3.70 to 3.71, we show the initial fraction of gas trapped in foam at the instant of shutting the quick closing values. These values were typically obtained within fifteen to forty seconds. The experiments were conducted in 2-inch and 4-inch pipes at a superficial liquid velocity of 0.01 m/s and 0.03 m/s and superficial gas velocity range from annular to intermittent flow.

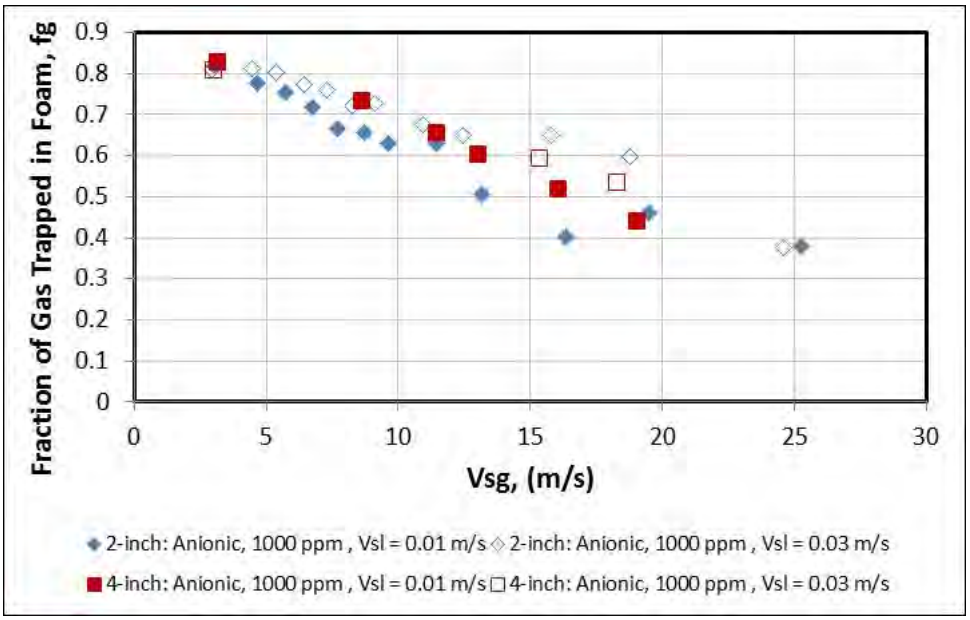

Figure 3.70: Fraction of Gas Trapped in Foam: Anionic Surfactant at 1,000 ppm

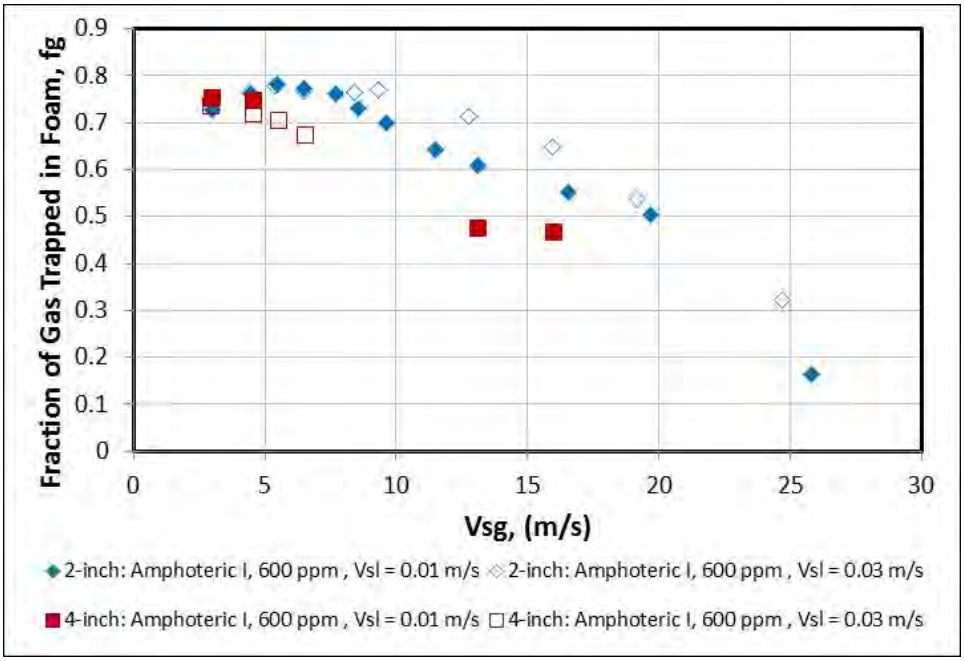

Figure 3.71: Fraction of Gas Trapped in Foam: Amphoteric I Surfactant at 600 ppm

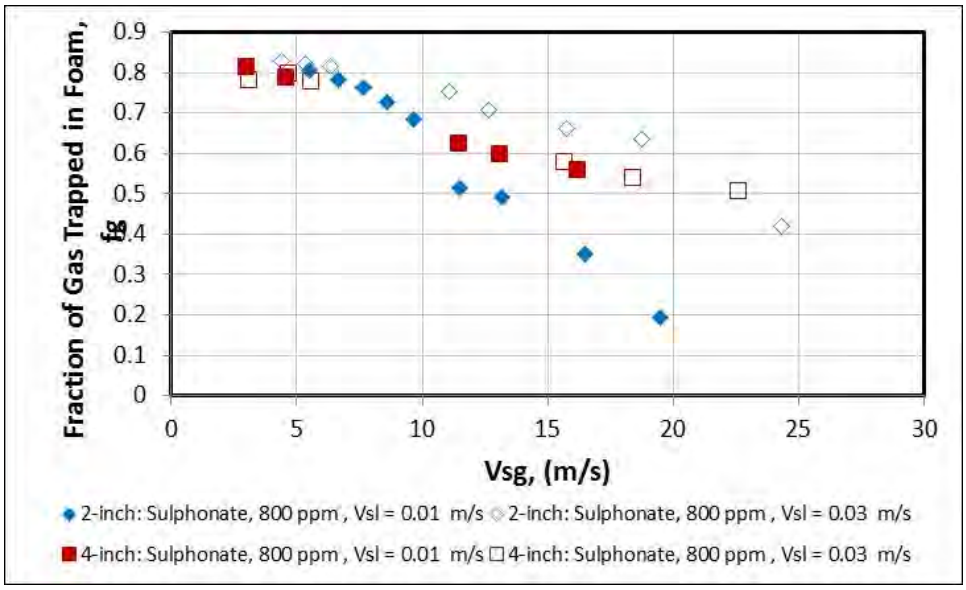

Figure 3.72: Fraction of Gas Trapped in Foam: Sulphonate Foamer at 800 ppm

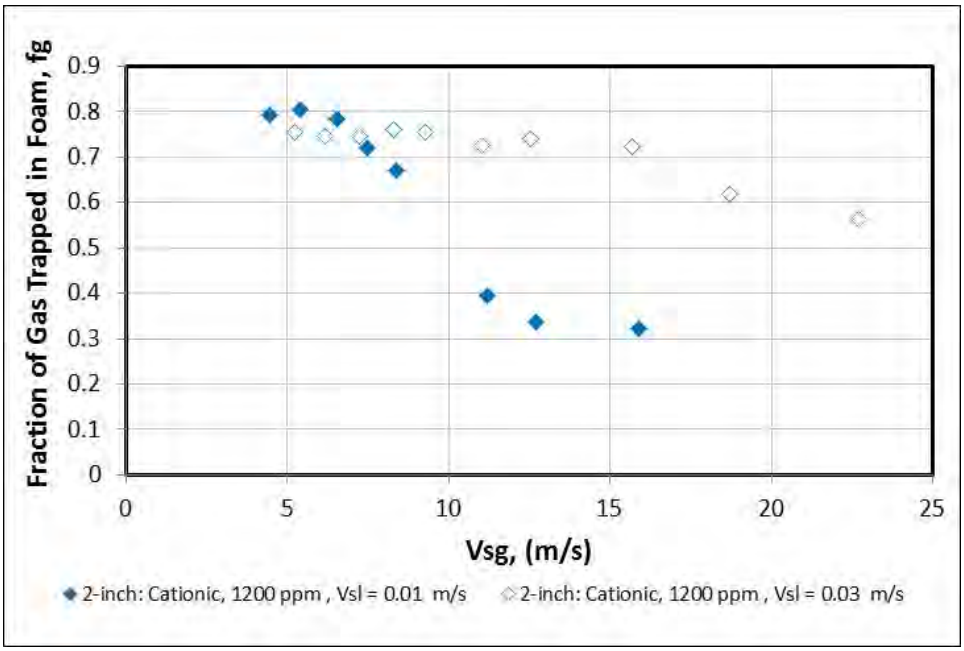

Figure 3.73: Fraction of Gas Trapped in Foam: Cationic Surfactant at 1200 ppm

Except in Sulphonate and Cationic surfactants at a superficial liquid velocity of 0.01 m/s, we observe that the fraction of gas trapped in the foam generally decreases with increase in superficial gas velocity regardless of pipe diameter and superficial liquid velocity. In Figures 3.74 and 3.75, we show the effect of increasing concentration on Sulphonate and Cationic Surfactants respectively.

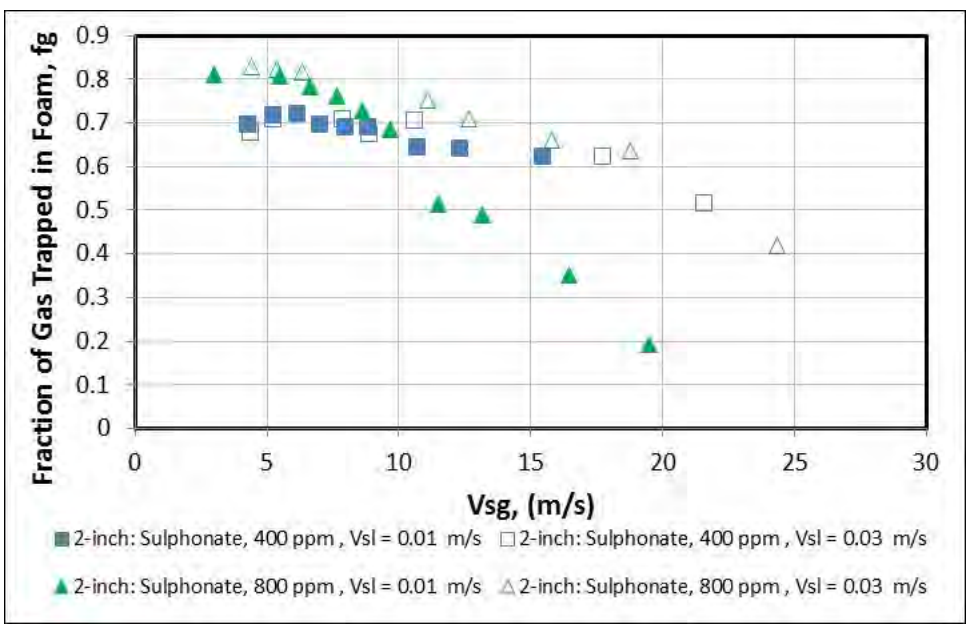

Figure 3.74: Fraction of Gas Trapped in Foam: Sulphonate Foamer at 400 and 800 ppm

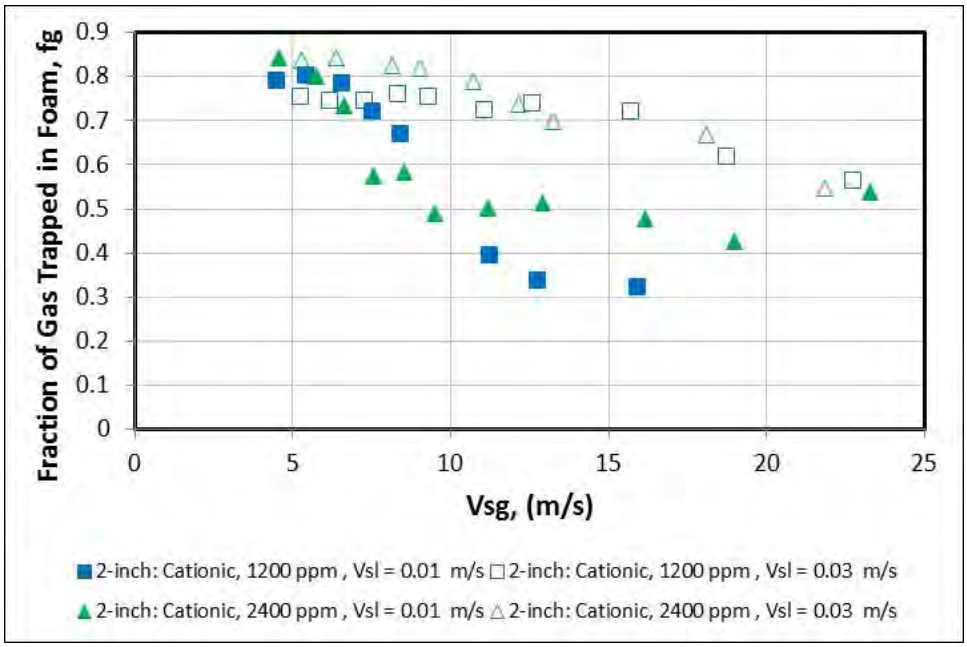

Figure 3.75: Fraction of Gas Trapped in Foam: Cationic Surfactant at 1,200 and 2,400 ppm

In Figures 3.74 and 3.75, the fraction of gas trapped in foam at a superficial liquid velocity of 0.03 m/s is higher than that trapped in the foam at a superficial liquid velocity of 0.01 m/s. In Figure 3.76, we show the trend of the fraction of gas trapped in foam for the surfactants tested.

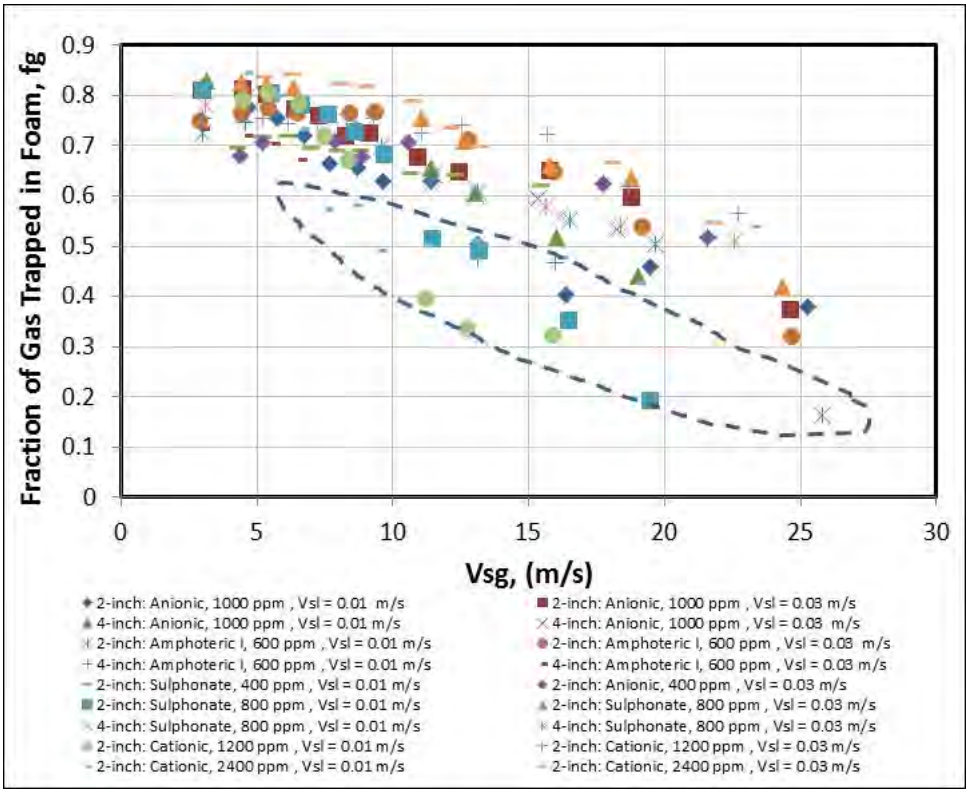

Figure 3.76: Fraction of Gas Trapped in Foam for Anionic, Amphoteric I, Sulphonate and Cationic Surfactants at Optimum Concentration in 2 and 4-inch Pipes

In Figure 3.76, except for the few data points circled in the dotted ellipse, the fraction of gas trapped in the foam decreases as the superficial gas velocity increases regardless of the foamer or pipe diameter. The fraction of gas trapped in the foam could be correlated with other experimental variables for modeling purposes.

In Figures 3.77 to 3.79, we show the foam holdup in the pipe at the instant of shutting the quick closing values. These values were typically obtained within fifteen to forty seconds. The experiments were conducted in 2-inch and 4-inch pipes at a superficial liquid velocity of 0.01 m/s and 0.03 m/s and superficial gas velocity range from annular to intermittent flow.

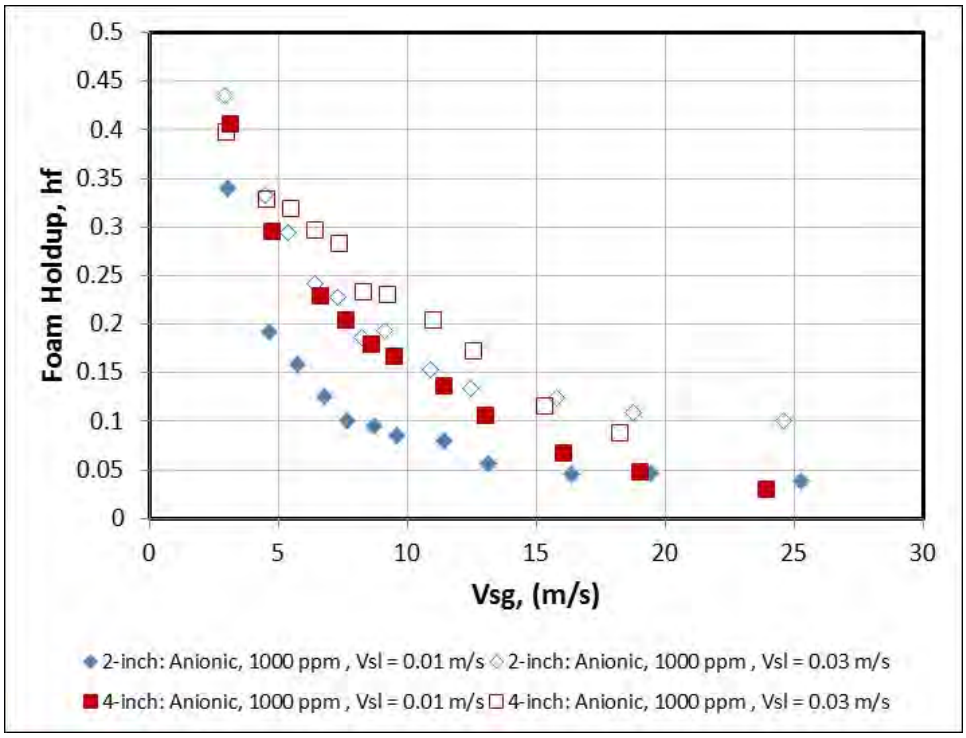

Figure 3.77: Foam Holdup: Anionic Surfactant at 1000 ppm ($v_{SL} = 0.01\ and\ 0.03\ m/s$)

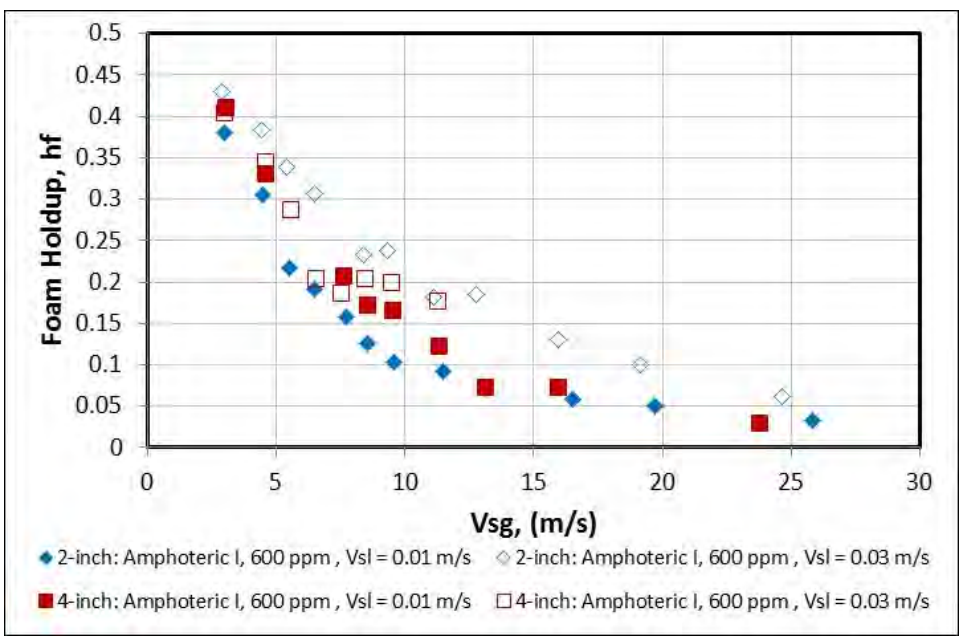

Figure 3.78: Foam Holdup: Amphoteric I at 800 ppm ($v_{SL} = 0.01\ and\ 0.03\ m/s$)

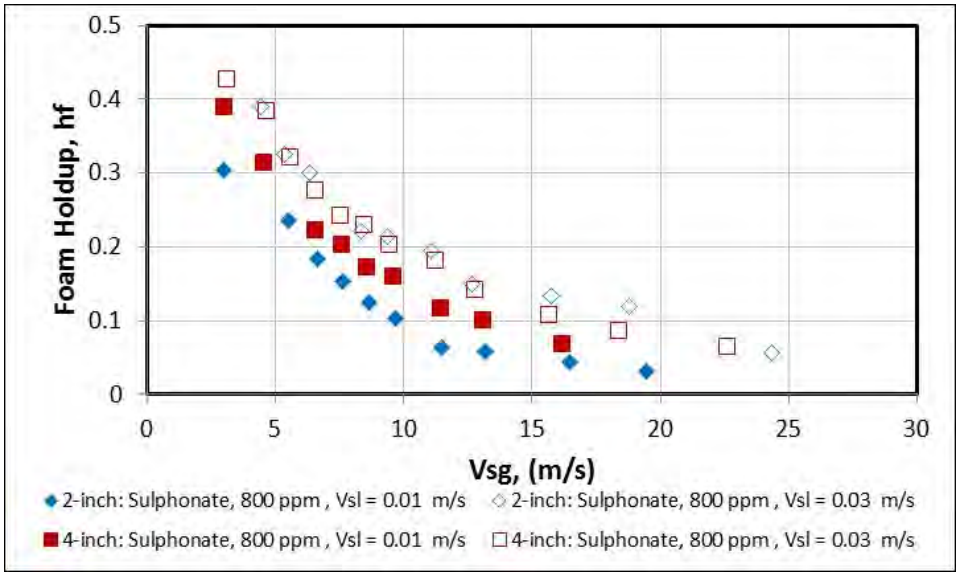

Figure 3.79: Foam Holdup: Sulphonate Foamer at 800 ppm
($v_{SL} = 0.01\ and\ 0.03\ m/s$)

In Figures 3.77 to 3.79, foam holdup in 2-inch pipe at a superficial liquid velocity of 0.03 m/s is greater than that at a superficial liquid velocity of 0.01 m/s. Foam holdup in 4-inch pipe is greater than that in 2-inch pipe at superficial liquid velocity of 0.01 m/s. Except in Amphoteric I (Figure 3.78), foam holdup in 4-inch pipe at a superficial liquid velocity of 0.03 m/s is greater than that at a superficial liquid velocity of 0.01 m/s.

In Figure 3.80, the foam holdup for Anionic, Amphoteric I, Sulphonate and Cationic surfactants are plotted at superficial liquid velocities of 0.01 and 0.03 m/s. Except for Cationic whose data is only available for 2-inch, the foam holdup of other foamers have been plotted for 2 and 4-inch pipes.

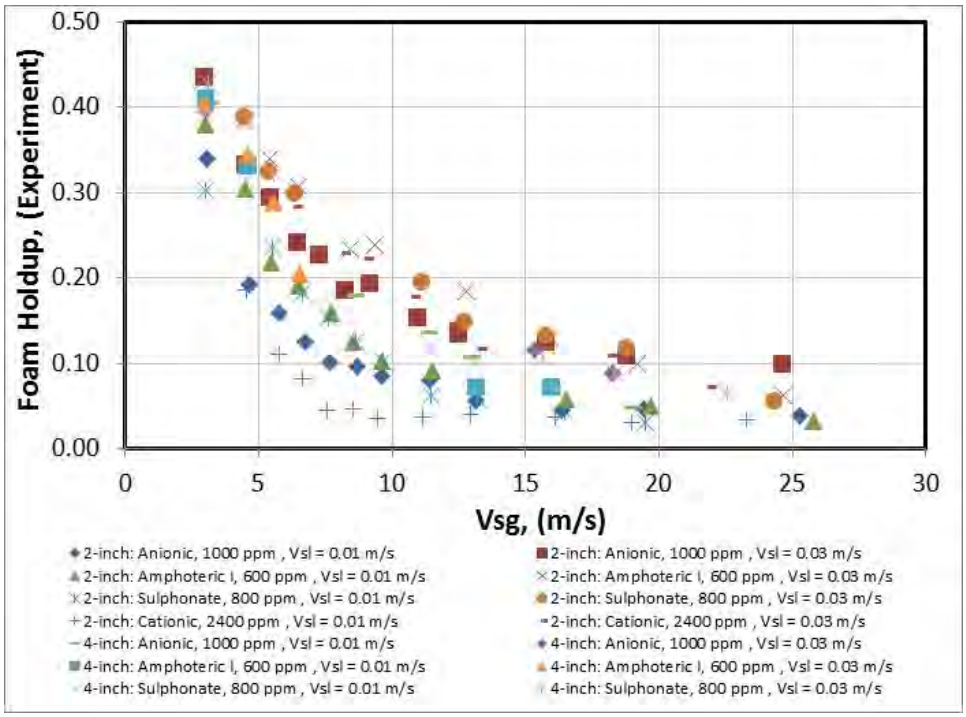

Figure 3.80: Foam Holdup in Anionic, Amphoteric I and Sulphonate Foamers in 2 and 4-inch Pipes ($v_{SL} = 0.01\ and\ 0.03\ m/s$)

In Figure 3.80, the foam holdup exhibited a general trend of decrease with increasing superficial gas velocity. No clear distinction can be observed among the four surfactants tested. Hence, the foam holdup can be correlated with other experimental variables for modeling purposes.

Modeling of Foam Data

In modeling the foam data based on the experimental results, we wanted to satisfy two objectives. One objective is to predict the liquid loading for foam flow. That is, what is the gas velocity at which liquid loading occurs if we use foam. The second objective is to predict the pressure drop under foam flow conditions. We discuss both these subjects in separate sub-sections.

Liquid Loading Under Foam Flow Conditions

As a way of background, we have already discussed the prediction of liquid loading for air-water flow in a previous section. As discussed, we observed that when the liquid film reversal occurs on the surface of the pipe (i.e., the liquid film starts falling downwards instead of being carried upwards by high gas velocity), it is considered an inception of liquid loading. The physical observation of liquid film falling downwards also coincides with the residual pressure gradient reaching a zero value. That is, when the pressure drop is independently measured and we subtract the gravitational pressure drop from it, we observe that the residual value reaches zero when the liquid film starts falling downwards. This is consistent with

the physical reality that the sign of frictional loss would change when liquid falls downwards.

We applied the same principle also for foam flow. That is, we measured the pressure drop using differential pressure transducer; we measured the liquid holdup using the quick closing valves and then we calculated the residual pressure drop.

In evaluating air-water flow and behavior under liquid loading conditions, we observed that the transition from annular to intermittent flow is not very sensitive to the superficial liquid velocity. Hence, in reporting the superficial gas velocity at which transition occurs, we use an average value of the superficial gas velocities at the transition point for experiments conducted at superficial liquid velocities of 0.01 and 0.03 m/s.

Figures 3.81 to 3.84 show the total pressure gradient and residual pressure gradient plots for air-water-foam flow experiments conducted with Anionic surfactant in 2-inch and 4-inch pipes at superficial liquid velocities of 0.01 and 0.03 m/s respectively. The point at which the residual pressure gradient goes to zero has been indicated on each plot.

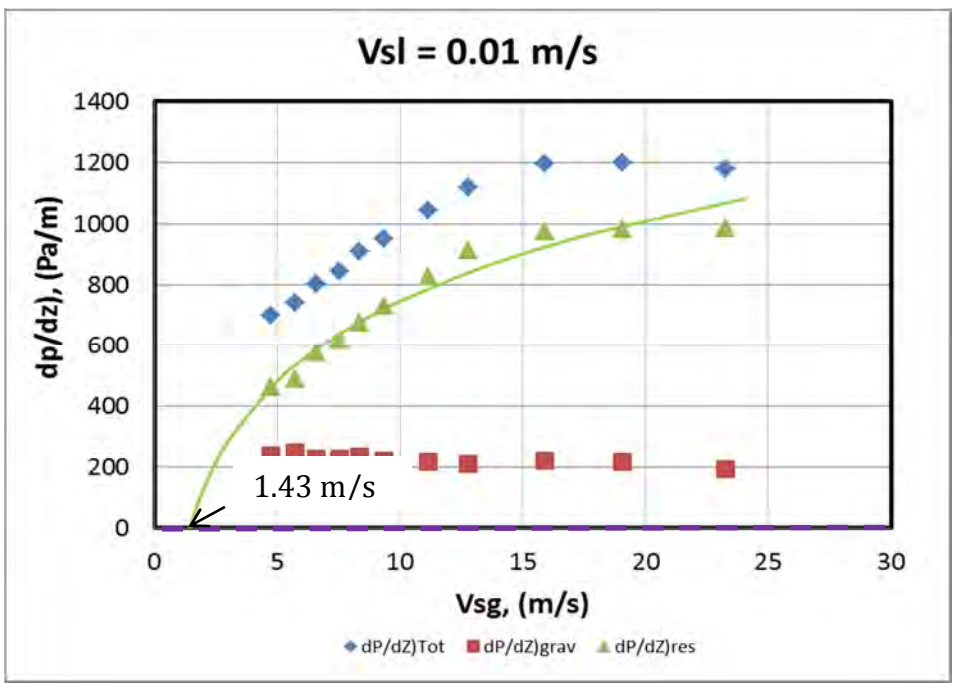

Figure 3.81: Pressure Gradient and Residual Pressure Gradient: Anionic Surfactant, 1600 ppm, 2-inch Pipe, $v_{SL} = 0.01\ m/s$

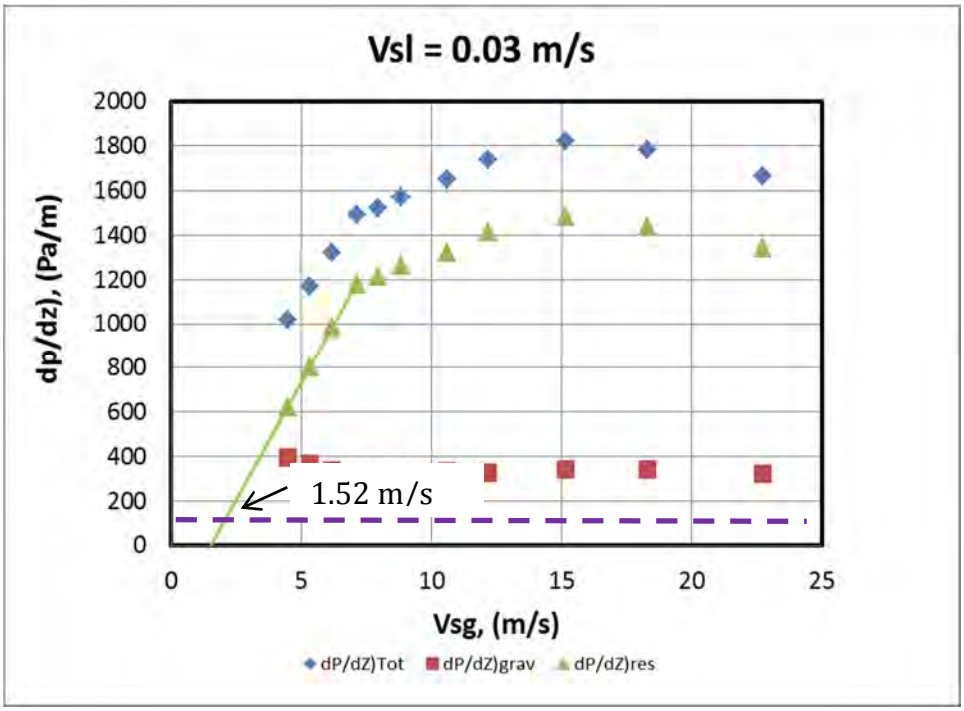

Figure 3.82: Pressure Gradient and Residual Pressure Gradient: Anionic Surfactant, 1600 ppm, 2-inch Pipe, $v_{SL} = 0.03\ m/s$

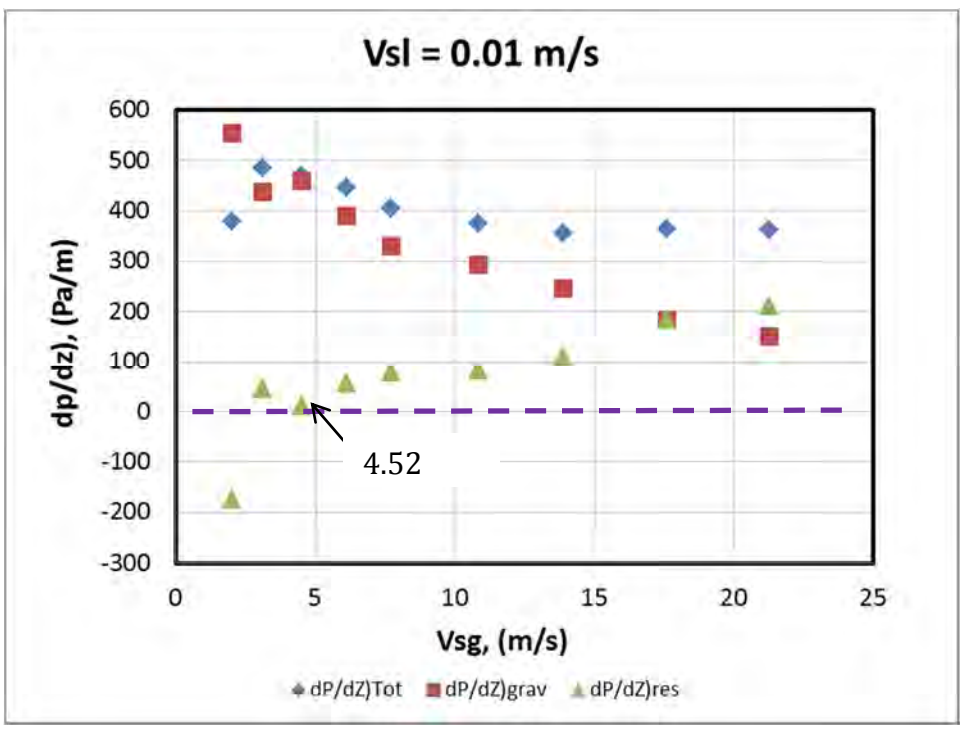

Figure 3.83: Pressure Gradient and Residual Pressure Gradient: Anionic Surfactant, 1600 ppm, 4-inch Pipe, $v_{SL} = 0.01\ m/s$

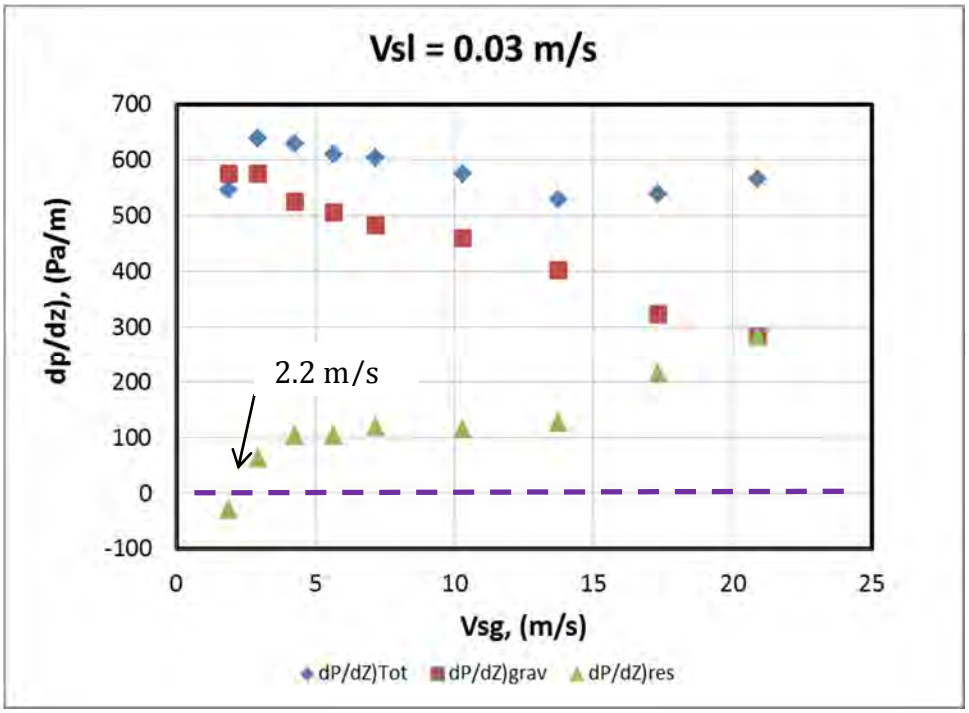

Figure 3.84: Pressure Gradient and Residual Pressure Gradient: Anionic Surfactant, 1600 ppm, 4-inch Pipe, $v_{SL} = 0.03\ m/s$

In Figures 3.81 and 3.82, the residual pressure gradient goes to zero at 1.4 m/s and 1.5 m/s respectively; these points were obtained by extrapolating the curve to reach the x-axis. The average critical velocity corresponding to addition of 1600 ppm of the Anionic surfactant in a 2-in pipe at superficial liquid velocities of 0.01 and 0.03 m/s is the average of these values, which is 1.45 m /s. From Figures 3.83 and 3.84, the residual pressure gradient goes to zero at 4 m/s and 2 m/s respectively. The average critical velocity corresponding to addition of 1600 ppm of the Anionic surfactant in a 4-in pipe at superficial liquid velocities of 0.01 and 0.03 m/s is the average of these values, which is 3 m /s.

The procedure outlined in the last paragraph was used to collate the average critical velocities corresponding to addition of each concentration of the five surfactants tested in the large scale facility. The average critical velocities obtained for the air-water flow case was also collated. Figures 3.85 to 3.89 show plots of average critical velocities at the point the residual pressure gradient goes to zero versus increasing concentration of each surfactant in 2-in and 4-in pipes. The critical velocities for air-water flow have also been superimposed on these plots at zero concentration. The details of the raw data based on which these plots are created can be found in Ajani (2014).

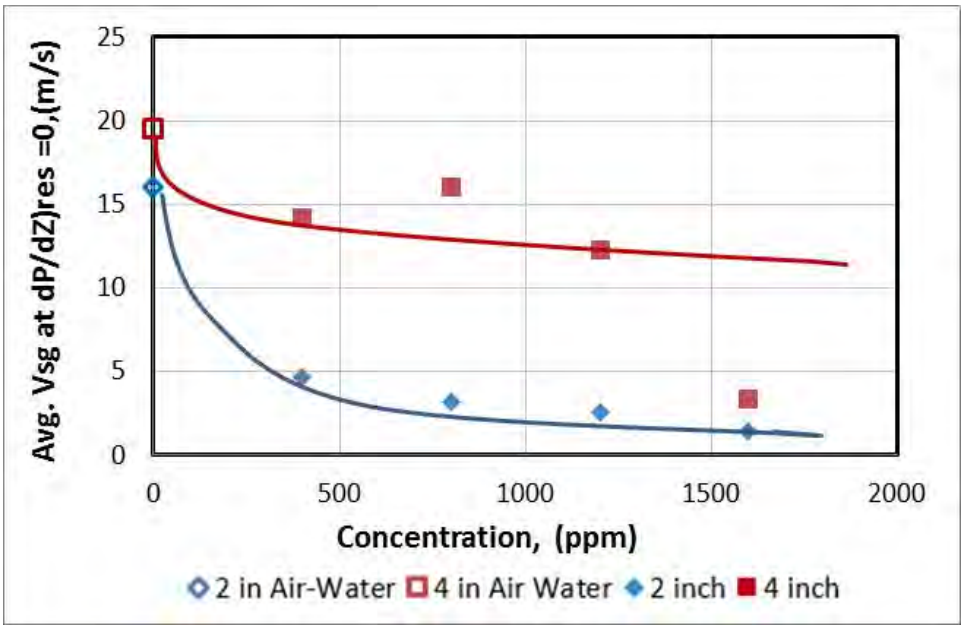

Figure 3.85: Average Critical Velocity Anionic Surfactant in 2 and 4-inch Pipes

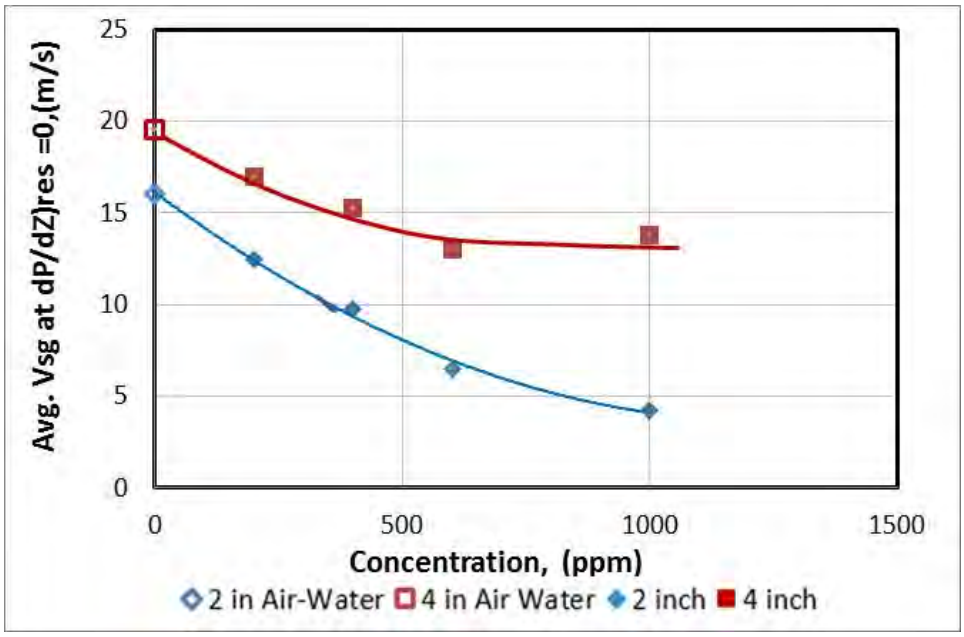

Figure 3.86: Average Critical Velocity Amphoteric I Surfactant in 2 and 4-inch Pipes

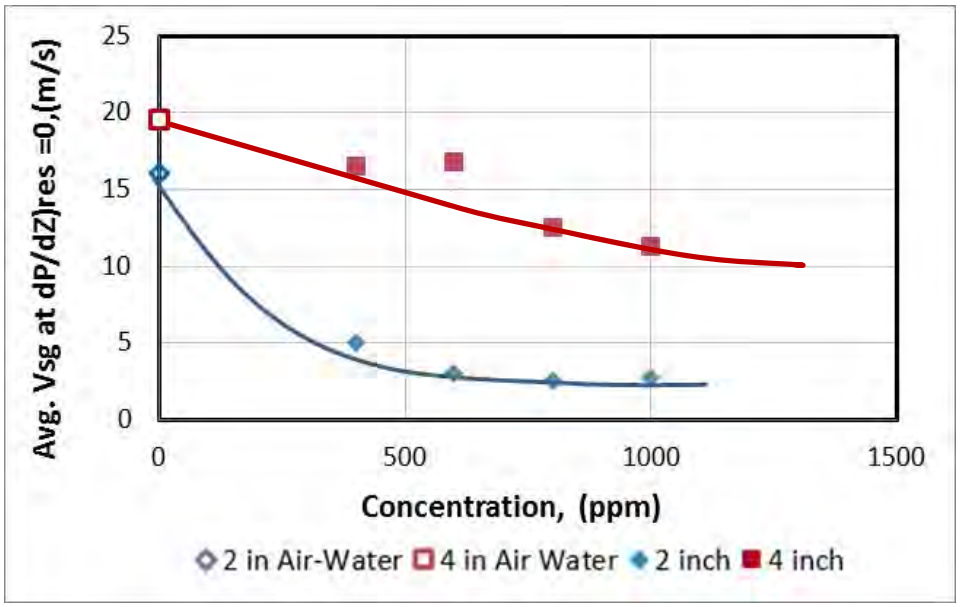

Figure 3.87: Average Critical Velocity Amphoteric II Surfactant in 2 and 4-inch Pipes

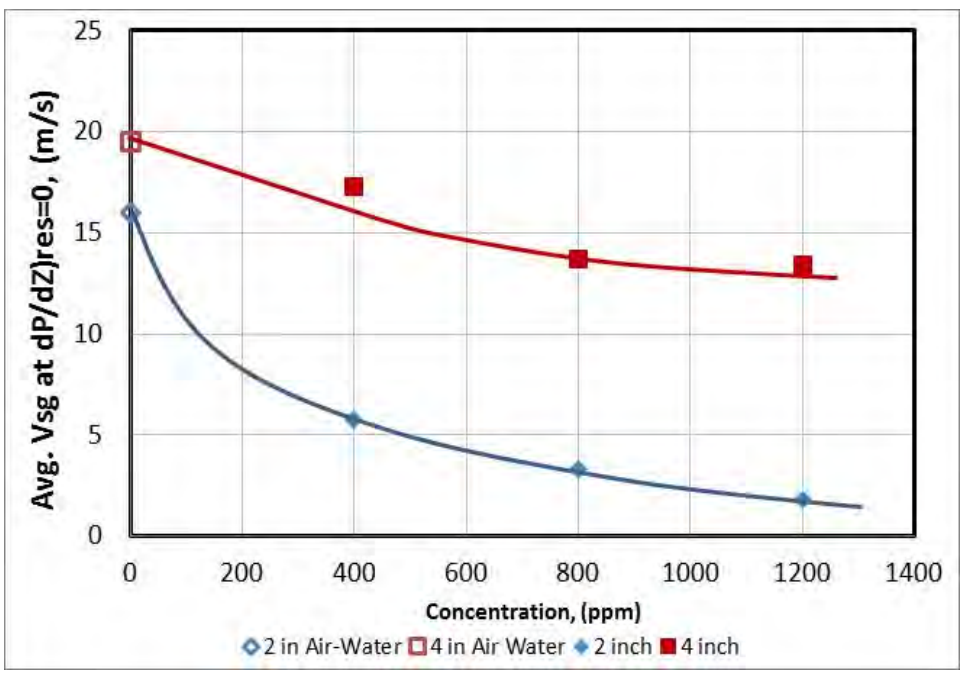

Figure 3.88: Average Critical Velocity Sulphonate Foamer in 2 and 4-inch Pipes

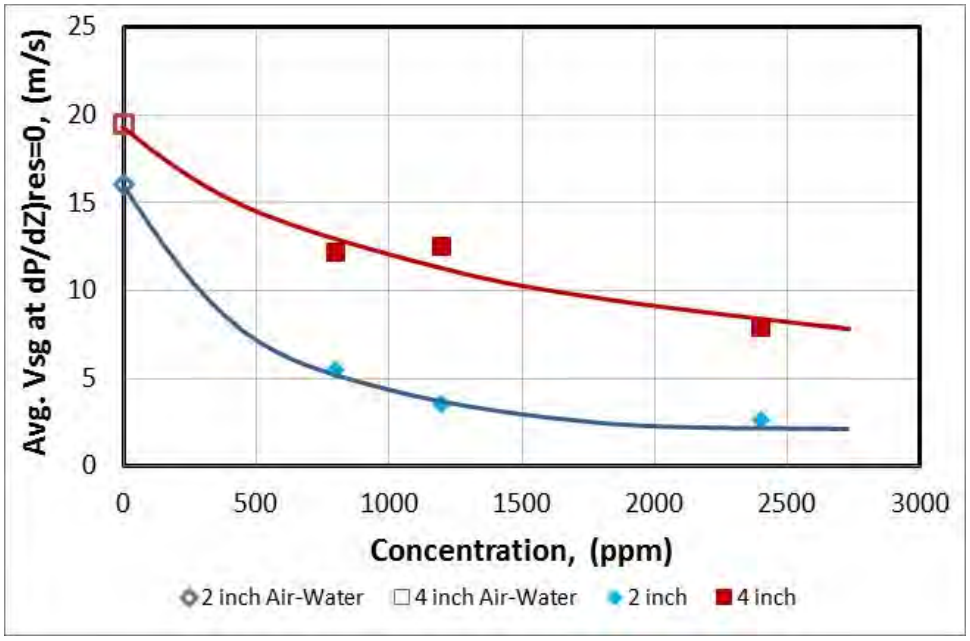

Figure 3.89: Average Critical Velocity Cationic Surfactant in 2 and 4-inch Pipes

Figures 3.85 to 3.89 show that for 2-in pipe, addition of surfactant reduces the average critical velocity from 16 m/s (for air-water flow case) to as low as 1.45 m/s for Anionic surfactant at 1600 ppm. From Figures 3.85 to 3.89, we observed that addition of surfactant also reduces the average critical velocity for 4-in pipe from 20 m/s (for air-water case) to a range of approximately 11 to 17 m/s.

However, for Anionic surfactant in 4-inch pipe (Figure 3.85), we observed that addition of 1600 ppm of the surfactant cause a reduction of the critical velocity from 20 m/s to 3 m/s. This does not match physical observation regarding liquid reversal at that concentration. In addition, in Figures 3.86 to 3.89, addition of surfactant in 4-inch pipe rarely reduces the critical velocity beyond 11 m/s. Consequently, it is worthwhile investigating this critical velocity further.

In high speed video for anionic surfactant, the film was flowing upward at a superficial gas velocity of 13.88 m/s and film reversal occurred at 10.785 m/s. However, as indicated in Figure 3.85, we expect the residual pressure gradient becomes zero at 4.52 m/s. This critical velocity is different from that predicted by the high speed camera video.

However, a careful view of Figure 3.85 reveals that the point at which the film reversal occurs matches the point at which the residual pressure gradient begins to rise. Hence, for 4-inch pipes, Figure 3.85 shows that while it is possible for the residual pressure gradient to be greater than zero, it is more appropriate to define the inception of liquid loading as the point at which the residual pressure gradient starts increasing. This corresponds to a superficial gas velocity of approximately 11 m/s in Figure 3.85.

Based on the results above, one can observe that surfactants are much more effective for smaller diameter pipes than larger diameter pipes. The reduction in liquid loading gas velocity is significant for 2' diameter pipe; whereas, for 4" pipe, the effect is small.

Foam Flow Modeling

Our goal is to be able to predict the behavior of foam flow based on the information gathered from small scale set up, as well as the data we have collected in our large scale Facility. The reason for such relationship is the fact that many chemical companies simply do not have the ability to collect the foam data in large scale facility. To be able to correlate the small scale data to large scale can help predict the performance of foam flow at field conditions.

We start with the foam flow modeling by assuming foam flow behavior similar to annular flow for gas-liquid flow. The annular transition model below is a modification of the Barnea (1986a) transition criterion. The schematic of foam flow structure under annular flow is shown in Figure 3.90.

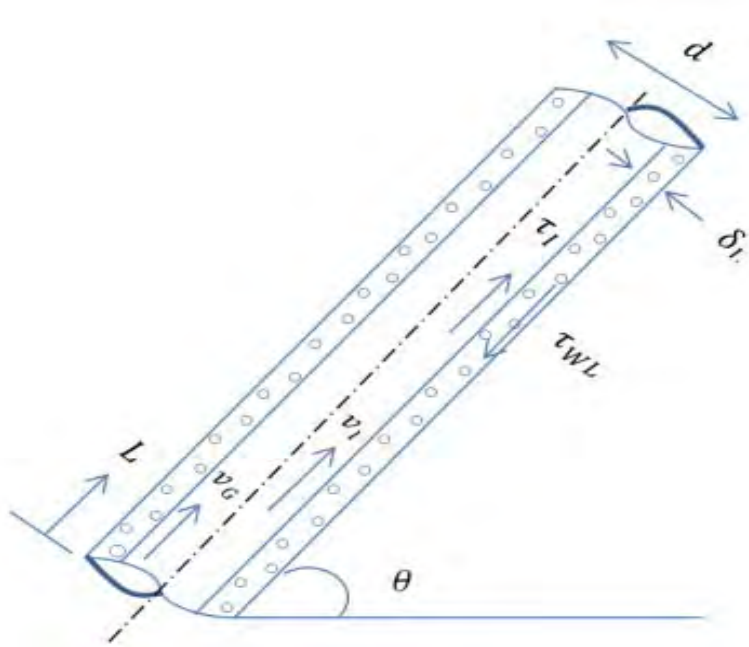

Figure 3.90: Schematic of Air-Water-Foam Flow Structure in Annular Flow

The above schematic is based on the experimental evidence and observations. When we shut-in the foam flow, we observed that there is free gas at the top of foam representing core gas, and the foam from the foam film on the pipe wall falls below the free gas. We assumed that foam is incompressible, the gas flows alone in the gas core (no liquid entrainment) and gas bubbles are trapped in the foam film. Hence, the liquid film is treated as a mixture of liquid and gas bubbles.

The starting point for the foam transition model is the force balance on the foam film as

$$-\left(\frac{dP}{dL}\right)_F + \tau_I \frac{S_I}{A_F} - \tau_{WF} \frac{S_F}{A_F} - \rho_F g Sin\theta = 0\,. \tag{3.9}$$

Similarly, a force balance over the core gives

$$-\left(\frac{dP}{dL}\right)_c - \tau_I \frac{S_I}{A_c} - \rho_c g Sin\theta = 0\,. \tag{3.10}$$

For fully developed flow, the pressure gradients in the foam film and gas core are equal. Hence we can eliminate the pressure gradient from Equations (3.9) and (3.10) to have the combined momentum equation below.

$$-\tau_{wF} \frac{S_F}{A_F} + \tau_I S_I \left(\frac{1}{A_F} + \frac{1}{A_C}\right) - (\rho_F - \rho_C) g Sin\theta = 0. \tag{3.11}$$

The geometrical variables in Equation (3.11) are given as follows:

$$S_F = \pi d, \tag{3.12}$$

$$S_I = \pi(d - 2\delta_F), \tag{3.13}$$

$$A_F = \pi\delta_F(d - \delta_F), \tag{3.14}$$

$$A_C = \frac{\pi}{4}(d - 2\delta_F)^2, \tag{3.15}$$

The foam film wall shear stress τ_{wF} is given by

$$\tau_{wF} = f_F \frac{\rho_F {v_F}^2}{2}, \tag{3.16}$$

where

$$f_F = C_F \left(\frac{d_F v_F \rho_F}{\mu_F}\right)^{-n_F}. \tag{3.17}$$

For foam flow, the six variables on the right side of Equation (3.17) are defined as follows:

The hydraulic diameter of the foam film is given by

$$d_F = 4\frac{\delta_F}{d} d \left(1 - \frac{\delta_F}{d}\right). \tag{3.18}$$

The velocity of the foam film is obtained by writing a mass balance over the foam film. We can write the mass balance on liquid as

$$v_{SL}\frac{\pi}{4}d^2 = q_L = v_F\pi\delta(d-\delta)\left(1-f_g\right).$$

Solving for v_F we obtain

$$v_F = \frac{d^2}{4\delta_F(d-\delta_F)}\left(\frac{v_{SL}}{1-f_g}\right). \tag{3.19}$$

The density of foam is written based on average two phase densities using the fraction of gas trapped in the foam film. We assume that there is no slippage in the foam film under annular flow. This is given by

$$\rho_F = \rho_g f_g + \rho_L\left(1-f_g\right). \tag{3.20}$$

The viscosity of foam is adopted from the work of Hatschek (1911) which was later modified by Mitchell (1970) based on foam flow experimental data. Mitchell (1970) related Foam viscosity to foam quality. For foam with qualities greater than 0.74 and up to 0.98, which are those seen in our experiment, the effective absolute viscosity of the foam was approximated by

$$\mu_F = \frac{\mu_L}{1-f_g^n}, \tag{3.21}$$

where "n" is an exponent that depends on the type of foam being used and can vary from 0.33 to 0.49 (Lyons and Plisga, 2005). Mitchell (1970) reported that higher values of "n" are more associated with stiff foam. For our model, we have used the upper bound of "n" (0.49) based on preliminary results from transition boundary.
Next, from Equation (3.17), we need to find the constant C_F and exponent n_F under foam flow. Based on 300 data points relating to various foaming systems, different pipe diameters, different foam structures and flow regimes, Deshpande et al. (2000) presented the friction factor equation below under foam flow.

$$f_F = \frac{18.36}{Re^{0.97}}, \tag{3.22}$$

where
C_F = *18.36,*
n_F =*0.97 and*
$$R_e = \frac{\rho_F v_F d}{\mu_F}. \tag{3.23}$$

Substituting the geometrical relationships and the foam film shear stress expression into Equation (3.11) and solving for the interfacial shear stress we have
$\tau_I = g(\rho_F - \rho_G)dsin\theta\left(\widetilde{\delta_F} - \widetilde{\delta_F}^{\,2}\right)\left(1-2\widetilde{\delta_F}\right) +$

$$\frac{1}{32}C_F\rho_F\left(\frac{\rho_F d}{\mu_F}\right)^{-n_f}\left(\frac{v_{SL}}{1-f_g}\right)^{2-n_f}\left[\frac{(1-2\widetilde{\delta_F})}{(\widetilde{\delta_F}-\widetilde{\delta_F}^{\,2})^2}\right] \tag{3.24}$$

where

$\widetilde{\delta_F} = \frac{\delta_F}{d}$,

Equation (3.24) relates the required interfacial shear stress to maintain annular flow structure, τ_I, to the dimensionless foam film thickness, $\widetilde{\delta_F}$, for a given superficial liquid velocity, v_{SL}.

For air-water flow, Barnea (1986a) plotted the required interfacial shear stress to maintain annular flow as a function of $\widetilde{\delta_L}$ at different superficial liquid velocities. The curves obtained displayed a minimum value which corresponds to the critical film thickness at the transition from annular to intermittent flow. The minima points are associated with the change of velocity profile in the liquid film. This approach was extended to foam flow. The critical foam film thickness at the minimum point was obtained by differentiating Equation (3.24) with respect to $\widetilde{\delta_F}$ and equating it to zero. The differentiated equation is as

$$g(\rho_F-\rho_G)d\sin\theta\left[\left(1-2\widetilde{\delta_F}\right)^2-2\left(\widetilde{\delta_F}-\widetilde{\delta_F}^{\,2}\right)\right]-$$
$$\frac{1}{16}C_F\rho_F\left(\frac{\rho_F d}{\mu_F}\right)^{-n_f}\left(\frac{v_{SL}}{1-fg}\right)^{2-n_f}\left[\frac{(\widetilde{\delta_F}-\widetilde{\delta_F}^{\,2})+(1-2\widetilde{\delta_F})^2}{(\widetilde{\delta_F}-\widetilde{\delta_F}^{\,2})^3}\right]=0. \tag{3.25}$$

Barnea (1986a) explained that transition from annular flow to slug flow occurs when the liquid blocks the gas core, promoting slugging. The blockage can occur as a result of two mechanisms: instability of annular flow configuration and spontaneous blockage of the core by wave growth on the liquid film (Shoham (2006)). For foam flow, only the instability criterion will be used to determine the dimensionless film thickness at the minimum point. This is because the second criterion is usually associated with very high liquid flow rate (Luo (2013)). Foam flow is not often applicable for gas well under very high liquid flow rate.

For the instability criterion, Equation (3.25) is iterated for the value of dimensionless foam film thickness $\widetilde{\delta_F}$ until it converges to zero. Obtained $\widetilde{\delta_F}$ is the dimensionless foam film thickness at the minimum point or at the boundary, $\widetilde{\delta_{F,MIN}}$ for a given value of superficial liquid velocity, v_{SL}.

Next, we solve for the critical velocity at the transition boundary. For a given superficial liquid velocity, we solve for the velocity of the foam (Equation (3.19)) so we can obtain the foam Reynolds number (Equation (3.23)). Consequently, we can use Deshpande's friction factor (Equation (3.22)) to obtain the constants C_F and exponent n_F under foam flow. Equation (3.23) is only applicable to laminar flow which is the flow regime observed in the foam film for all our experiments.

The supplied interfacial shear stress is provided by the gas-phase. This is given as

$$\tau_I = \frac{1}{2} f_I \rho_G v_G^2. \tag{3.26}$$

Equation (3.26) requires the velocity of the gas phase, v_G, and the interfacial friction factor, f_I, under foam flow.

The velocity of the gas under foam flow is obtained by writing a mass balance over the gas phase. The volumetric flowrate of gas in the core q_{gc}, is given as

$$q_{gc} = q_{g(Total)} - q_g \; in \; foam. \tag{3.27}$$

By definition, the volumetric flowrate of gas in the foam film is given as

$$q_g \; in \; foam = \frac{f_g}{1-f_g} q_L. \tag{3.28}$$

By substituting Equation (3.28) into (3.27), we have

$$q_{gc} = q_{g(Total)} - \frac{f_g}{1-f_g} q_L. \tag{3.29}$$

Dividing both sides by A_c we obtain

$$v_c = \frac{q_{gc}}{A_c} = \frac{A_p}{A_c}\left[v_{SG} - \frac{f_g}{1-f_g} v_{SL}\right] \quad . \tag{3.30}$$

By substituting the respective areas of the pipe and core into Equation (3.30), simplifying and expressing resulting equation in terms of dimensionless foam film thickness, we have

$$v_C = \frac{1}{\left(1-2\widetilde{\delta_F}\right)^2}\left[v_{SG} - \left(\frac{f_g}{1-f_g}\right) v_{SL}\right]. \tag{3.31}$$

Above is the expression for the velocity of gas in the core. It is used in place of gas velocity in Equation (3.26).

To find the interfacial friction factor, f_I, first we find an expression for the interfacial shear stress from the force balance written over the gas core (Equation (3.10)) as

$$\tau_I = \frac{A_C}{S_I}\left[\left(\frac{\Delta P}{\Delta L}\right)_{Experiment} - \rho_G g Sin\theta\right]. \tag{3.32}$$

Equation (3.32) requires pressure gradient, perimeter of the interface and area of the core. The pressure gradient was obtained directly from experiment. The area of the core, A_C, (Equation (3.15)) and perimeter of the interface, S_I, (Equation (3.13)) require knowledge of the foam film thickness. The expression for the foam film thickness was obtained from mass balance over the foam film. This expression is a function of the fraction of gas trapped in the foam film and liquid holdup: these are parameters measured directly from experiment. This is given as

$$\delta_F = \frac{d}{2}\left[1 - \sqrt{1 - \frac{H_L}{1-fg}}\right]. \tag{3.33}$$

For experimental data points in annular flow, Equation (3.33) was used in Equations (3.13) and (3.15) to find perimeter of the interface, S_I and area of the gas core A_c. These are used alongside the pressure gradient value from experiment in Equation (3.32) to find the interfacial shear stress. Consequently, the interfacial friction factor, f_I, was found from the equation

$$f_I = \frac{2\tau_I}{\rho_C(v_C - v_F)^2}. \tag{3.34}$$

From gas-liquid experimental observations we know that a correlation exists between the interfacial friction factor computed from Equation (3.34) and the gas Reynolds number and core Reynolds number. The core Reynolds number is given as

$$Re_C = \frac{\rho_C v_C d_C}{\mu_C}. \tag{3.35}$$

From the observed correlation, two different equations for interfacial friction factor were developed using foam flow experimental data in annular flow. The equations are based on an observation in annular flow that interfacial friction factor is a function of both gas friction factor and the film thickness. The correlations are as

$$f_I[II] = C_F\left[\frac{\rho_G v_{SG} d}{\mu_G}\right]^{-m_f}\left[1 + a\left(\frac{\delta_F}{d}\right)\right], \tag{3.36}$$

$$f_I[III] = C_F\left[\frac{\rho_G v_{SG} d}{\mu_G}\right]^{-m_f}. \tag{3.37}$$

The constants in each of the correlations above are provided later.

The flow geometry under air-water-foam flow is as presented in Figure 3.90. Hence, the liquid film is treated as a mixture of liquid and gas bubbles.

- For air-water two phase flow under annular flow regime, Alves et al. (1991) solved Equation (3.11) for liquid film thickness. This is substituted into either Equation (3.9) or (3.10) to obtain the pressure gradient. We slightly modified Alves et al. (1991) equation as follows: Based on high speed camera video

observations at high superficial gas velocities, we assumed no liquid droplet is entrained in the gas core, therefore $f_e = 0$.

- The foam film friction factor f_F, is adopted from the work of Deshpande et al. (2000) as given by Equation (3.22). The foam viscosity μ_F, is adopted from the work of Mitchell (1970) as given by Equation (3.21). The friction factor and viscosity correlations used have become necessary since they were not measured in our study and there are no better correlations to predict them under foam flow.
- Based on experimental data, correlations have been developed for interfacial friction factor under foam flow. These are given by Equations (3.36) to (3.37).

For a given concentration of surfactant, the pressure gradient under foam flow was predicted using correlations developed for the following variables: liquid holdup, H_L, foam holdup, h_f, fraction of gas trapped in foam film, f_g, and either of the two correlations developed for interfacial friction factor, f_I. Details of the development and performance of each of these correlations are shown below.

Following are the steps used in our model to predict pressure gradient under air-water foam flow after establishing that annular flow exists:

- For a given surfactant and concentration, determine the unloading potential, $\left.\frac{vlr_{SS}}{vsg_{SS}}\right]_{6.2\ mm/s}$.
  A detailed development of this variable is given below. This is an input variable from the Bench top unloading test.
- Using the unloading potential, calculate the gas holdup as
  $$H_g = \frac{v_{SG}}{v_{SG}+v_{SL}+a\left[\frac{v_{SL}}{\left.\frac{vlr_{SS}}{vsg_{SS}}\right]_{0.75\ LPM}}\right]^{n1} v_{SG}{}^{1-n1}}. \quad (3.38)$$
  The liquid holdup is calculated from
  $$H_L = 1 - h_g. \quad (3.39)$$
- The foam holdup is calculated using the correlation
  $$h_F = aH_L + b\left(\frac{v_{SL}}{v_{SG}}\right). \quad (3.40)$$
- The fraction of gas in foam film is calculated from the correlation:
  $$f_g = a\left(\frac{v_{SG}}{h_F}\right) + b\left(\frac{v_{SL}}{h_F}\right) + c. \quad (3.41)$$
- The foam density is calculated using Equation (3.20).
- The film thickness is calculated using Equation (3.33).
- Calculate the hydraulic diameter of the gas core using
  $$d_C = (d - 2\delta_L). \quad (3.42)$$
- Calculate the interfacial perimeter and area of the gas core using Equations (3.13) and (3.15).
- Calculate the core and film velocities using Equations (3.31) and (3.19).
- Calculate the interfacial friction factor using either Equation (3.36) or (3.37).

- Calculate the interfacial shear stress by rearranging Equation (3.34).
- Finally, back calculate the pressure gradient by re-arranging the force balance over the gas core in Equation (3.10).

In the procedure discussed above, we discussed the unloading potential. This allows us to tie what we observe in small scale experiment with what we observe in large scale experiment. Figures 3.91 to 3.92 show the percent mass of liquid unloaded with time for Anionic and Amphoteric I surfactants at different concentrations.

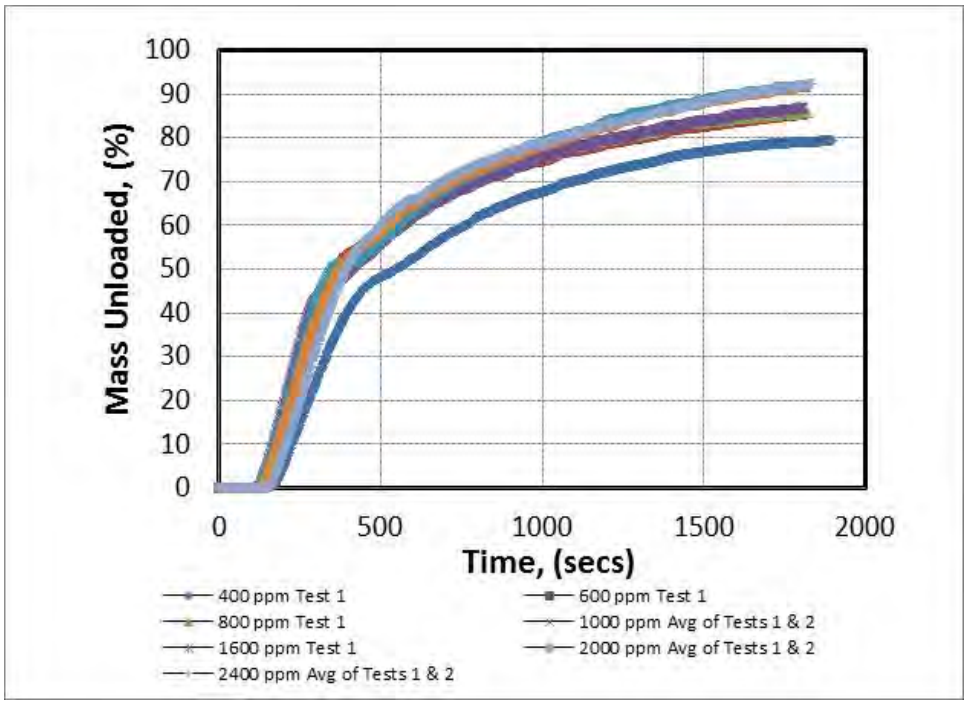

Figure 3.91: Percent Mass of Liquid Unloaded with Time (Anionic Surfactant)

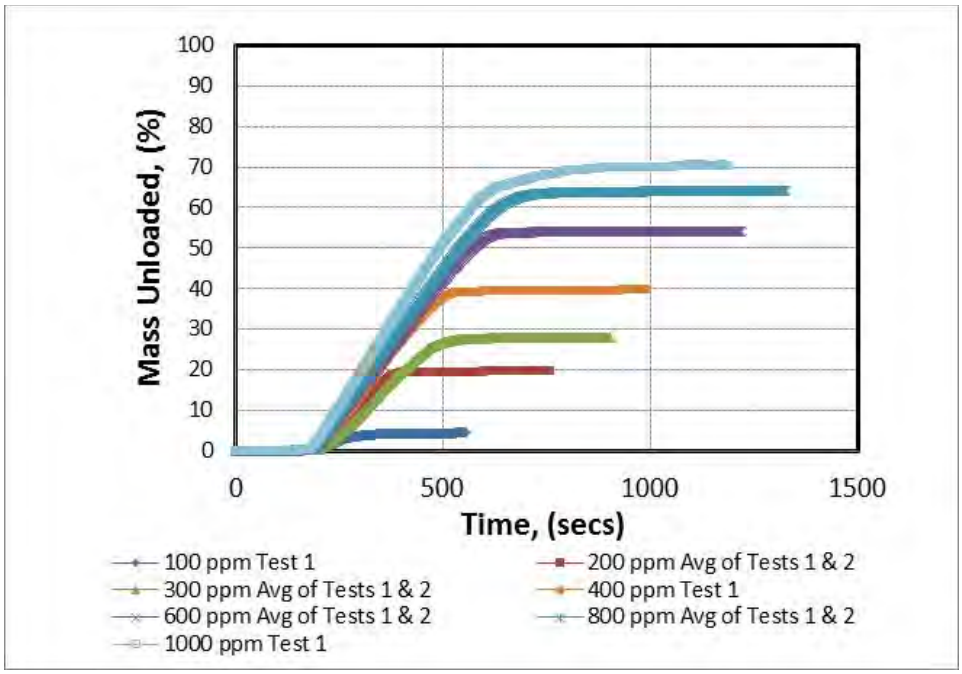

Figure 3.92: Percent Mass of Liquid Unloaded with Time (Amphoteric I Surfactant)

The data for Amphoteric II, Sulphonate and Cationic surfactants can be found in Ajani (2014). It can be seen that as the concentration increases, the amount of unloaded liquid increases until we reach certain critical concentration. Once a critical concentration is reached, additional increase does not further increase the unloaded liquid. We assume that the efficacy of unloading can directly change the liquid holdup. As foam is better able to lift the liquid, the liquid holdup in large scale facility would become smaller.

Figure 3.93 shows the liquid holdup versus superficial gas velocity from the large scale test for Anionic surfactant at a superficial liquid velocity of 0.01 m/s in 2-inch pipe. Based on the information in the foregoing paragraph, Figure 3.93 shows that an increase in concentration of the foamer increases the transport capability of the flow and this in turn decreases the liquid holdup observed in the trap section for the large scale test.

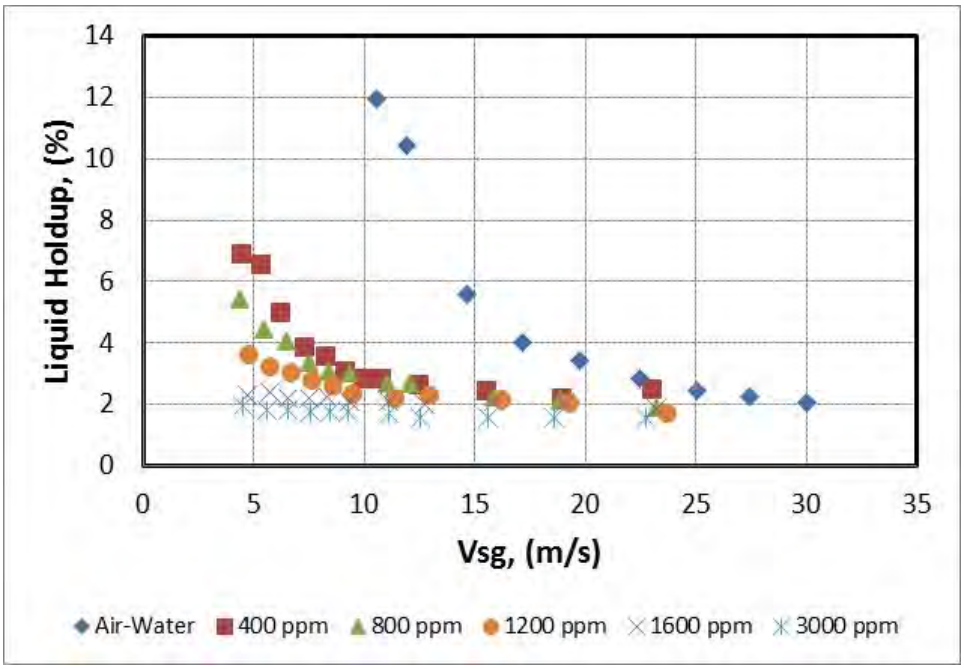

Figure 3.93: Anionic Surfactant, 2-inch pipe, $v_{Sl} = 0.01\ m/s$: Decrease in Liquid Holdup with Increase in Surfactant Concentration

Next, we seek to relate the unloading capability of the foamers seen in the bench top facility to that seen in the large scale facility by defining an expression that will capture a characteristic of the bench top experiment and use same to predict the liquid holdup in the large scale facility. Unloading test conducted using Amphoteric I at 600 ppm will be used to illustrate this concept.

Since the density of the surfactant solutions is approximately equal to one, a one to one relationship exists between mass of liquid unloaded and the volume of liquid unloaded.

In Figure 3.94, we show the volume of liquid unloaded with time for Amphoteric I surfactant at 600 ppm in the unloading test. The volumetric rate of liquid carryover $\dot{q}$, (mL/sec) is obtained from the slope of the linear part of the unloading plot as illustrated in Figure (3.94).

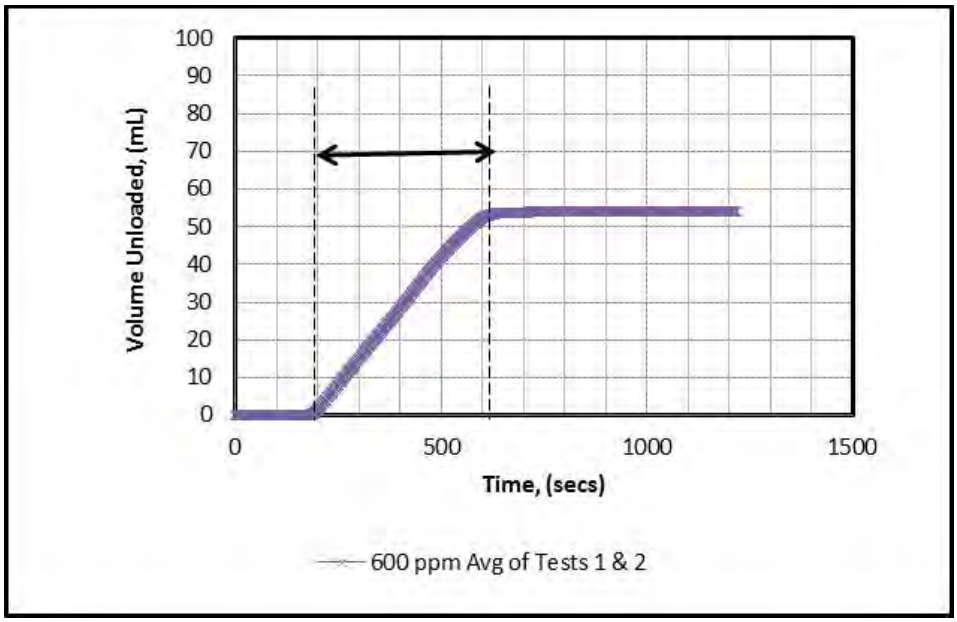

Figure 3.94: Volumetric Rate of Liquid Removal (Amphoteric I at 600 ppm)

Next, the incremental unloading benefit associated with using a higher concentration of each foamer is calculated from the rate of liquid transport as

$$v_{lr\ ss} = \frac{\dot{q}}{A_{p\ ss}}, (m/s), \tag{3.43}$$

where $A_{p\ ss}$ is the area of pipe used for the unloading test, (m^2).

Furthermore, the rate of liquid carryover was divided by the superficial gas velocity used in conducting the unloading experiment. This yields a dimensionless parameter called the unloading potential , $\left(\frac{vlr_{ss}}{v_{sg\ ss}}\right)$. The reason for using gas velocity in the definition of unloading potential is because of our observation that the gas velocity does impact the amount of liquid unloaded in the system. Figures 3.95 and 3.96 show the unloading potential as a function of concentration for the surfactants tested at a sparge rate of 4.1 mm/s and 6.2 mm/s respectively. Although the trend for various chemicals is the same for two different gas velocities, the effect of gas velocities on unloading is different for different chemicals. Hence the values on y axis do change depending on superficial gas velocity. We developed hold up correlation for the two possible gas velocities.

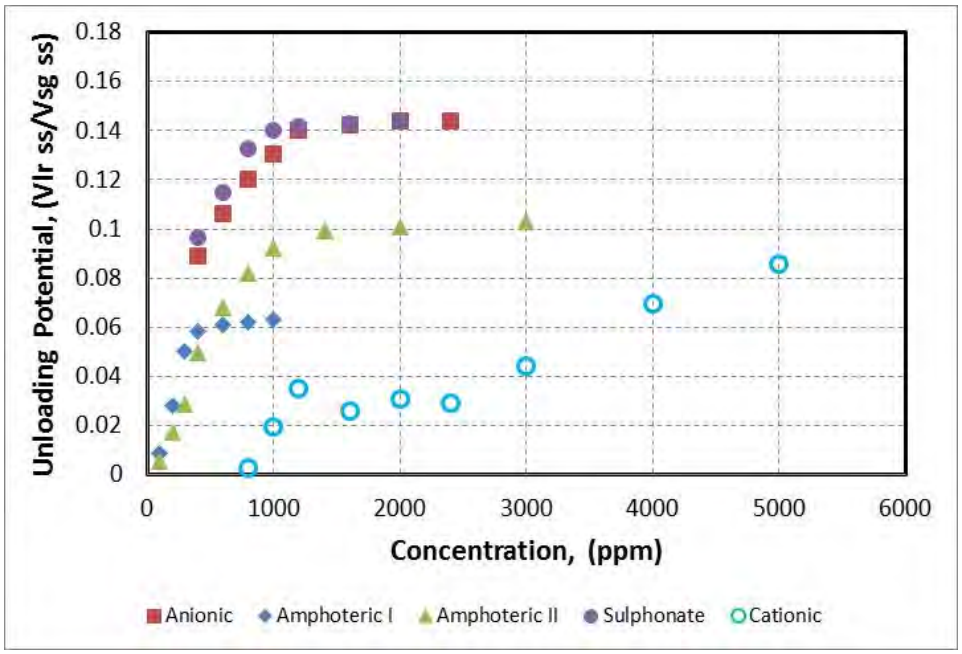

Figure 3.95: Unloading Potential at 4.1 mm/s

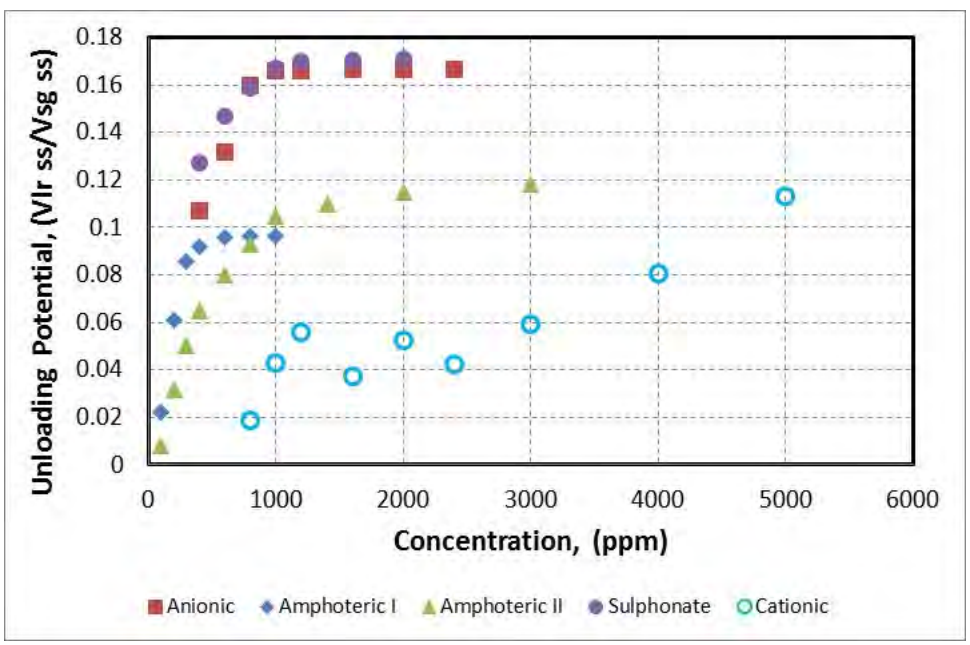

Figure 3.96: Unloading Potential at 6.2 mm/s

The Unloading potential defined from liquid carryover experiment was used to develop a correlation for liquid holdup under foam flow as discussed below.

The liquid holdup correlation was developed using experimental data points collected at and around the optimum concentration of each surfactant as reported in the work of Ajani (2014). These are as outlined below:

- Anionic surfactant: 800 ppm, 1000 ppm and 1200 ppm
- Amphoteric I surfactant: 600 ppm and 1000 ppm
- Amphoteric II surfactant: 800 ppm and 1000 ppm
- Sulphonate Foamer: 800 ppm and 1200 ppm
- Cationic Surfactant: 1200 ppm and 2400 ppm

A correlation for gas holdup was developed using the unloading potential of each surfactant with the superficial liquid and gas velocities used in the large scale experiments conducted at the concentrations listed above. This correlation is given as

$$H_G = \frac{v_{SG}}{(v_{SL}+v_{SG})+a\left[\frac{v_{SL}}{\frac{v_{lr\,ss}}{v_{sg\,ss}}}\right]^{n1} v_{SG}^{1-n1}}. \tag{3.38}$$

Consequently, the liquid holdup is calculated as

$$H_L = 1 - H_G, \tag{3.39}$$

where $\frac{v_{lr\,ss}}{v_{sg\,ss}}$ is the unloading potential. The constants "*a*" and "*n1*" in Equation (3.38) are as given in Table 3.8. These constants are dependent on the gas sparge rate used in conducting the Bench top experiment.

Table 3.8: Constants in Gas Void Fraction (Equation 3.38)

Constants in Equation (33)	**Small Scale Gas Sparge Rate**	
	4.1 mm/s	**6.2 mm/s**
a	0.16	0.18
n1	0.37	0.37

Figures 3.97 and 3.98 show the predicted versus measured liquid holdup for different surfactants. The sum of the squared errors for the predictions in these Figures is 0.017 for both velocities. Figures 3.97 and 3.98 are liquid holdup predicted with a sparge rate of 4.1 mm/s and 6.2 mm/s respectively from the Bench top test.

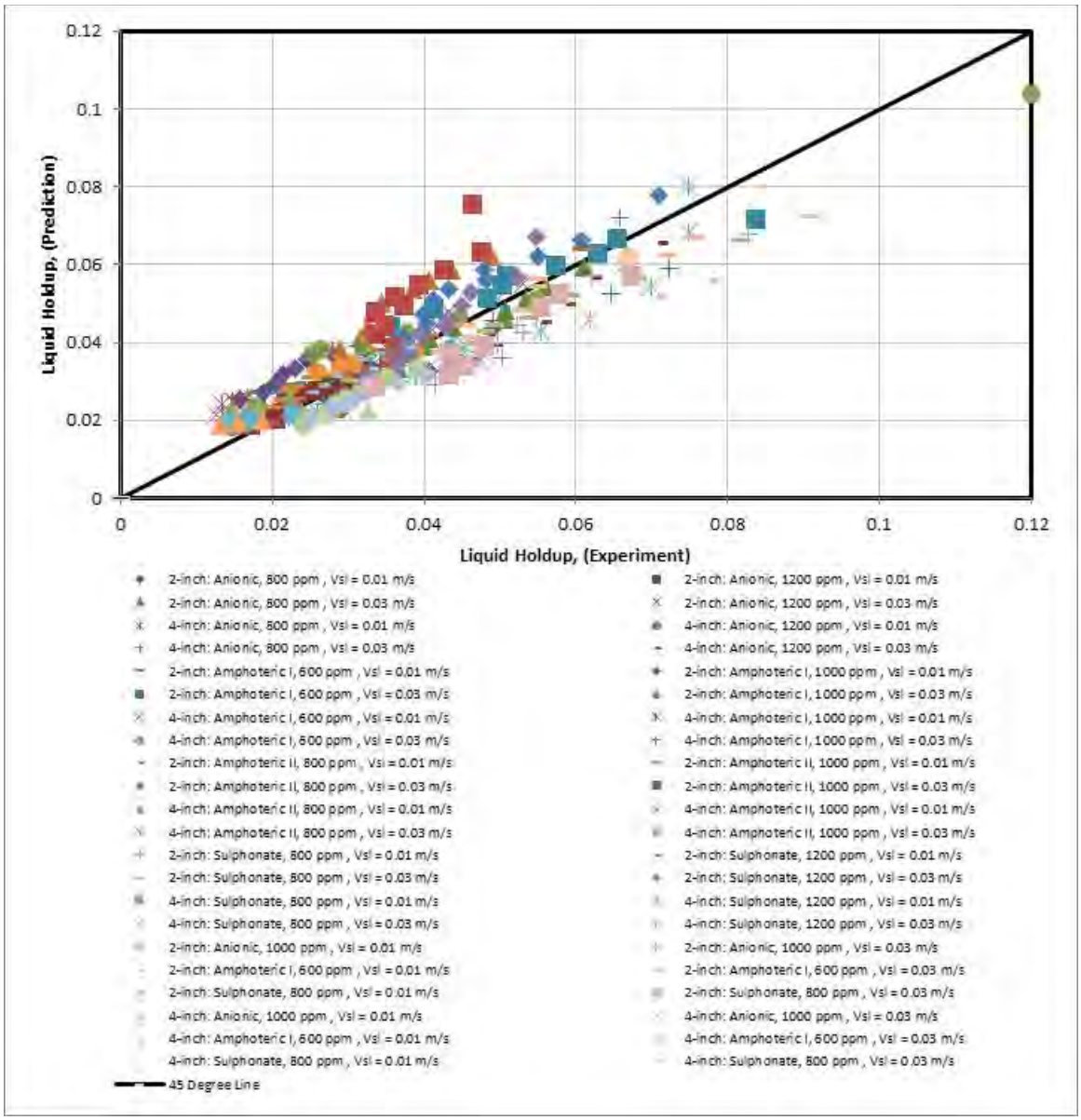

Figure 3.97: Predicted Versus Measured Liquid Holdup for Four Surfactants at Unloading Test at 4.1 mm/s (No Cationic)

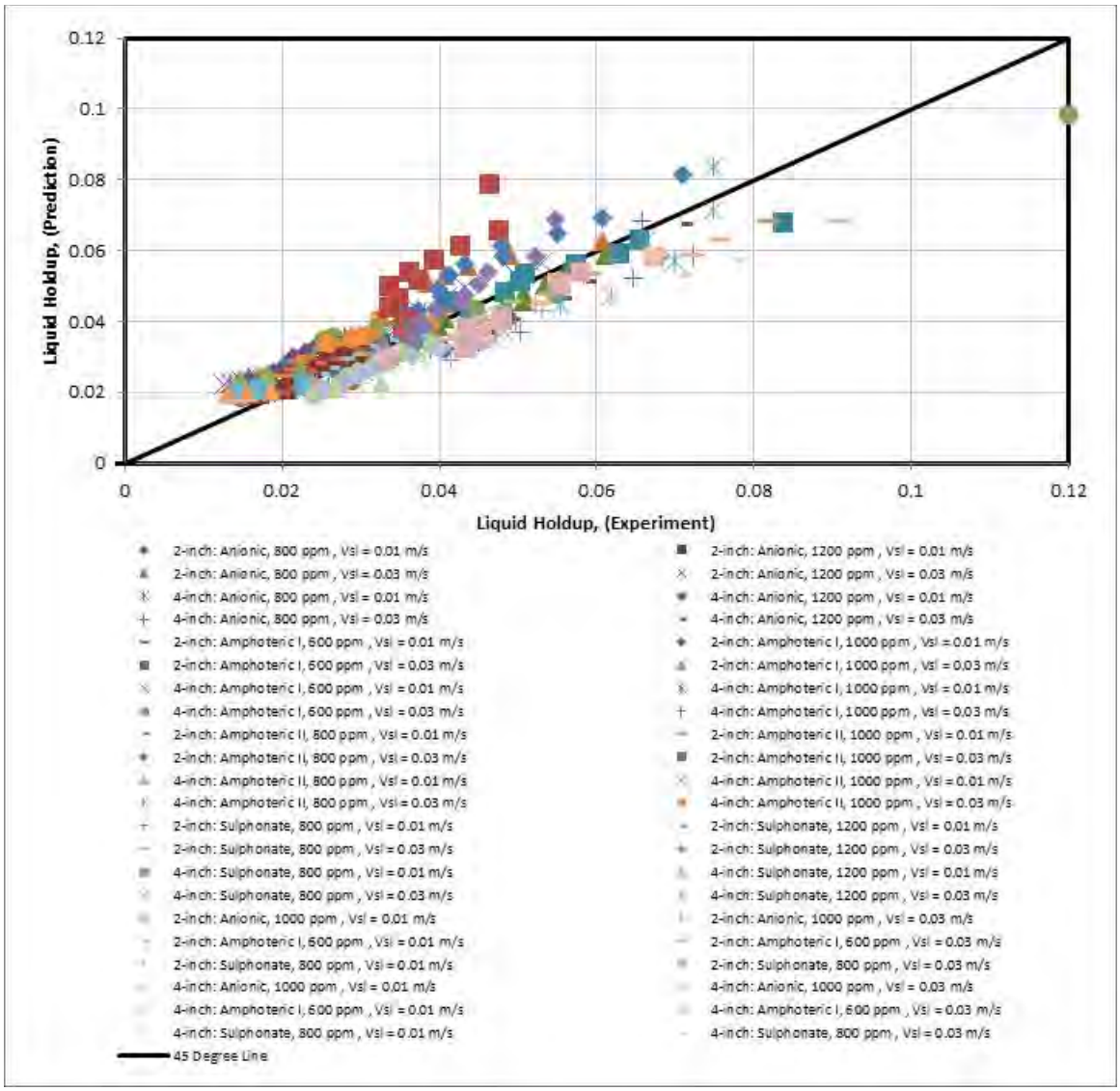

Figure 3.98: Predicted versus Measured Liquid Holdup for Four Surfactants at Unloading Test at 6.2 mm/s (No Cationic)

High speed camera videos of the large scale experiments revealed that there are data points in annular and intermittent flow regimes. The liquid holdup correlations have been developed using all data points observed in these flow regimes for the concentration of surfactants tested.

In the large scale experiment, the liquid holdup and pressure gradient data were collected for every experimental data point. The following additional foam variables were collected on a limited scale due to the time required to collect the data:

- Foam holdup
- Fraction of gas trapped in foam

The transition criterion under foam flow differentiates data points in annular flow from those in intermittent flow. However, the transition criterion to be developed is also required to sort out experimental data points so only data points in annular flow are used to develop correlations. Therefore, a preliminary criterion is required to identify data points for foam holdup and fraction of gas in foam in annular flow. As discussed in previous sub-section, we used the residual pressure gradient approach to distinguish between annular flow and intermittent flow. That is, when residual pressure gradient is greater than zero, we assume the data point to be in annular flow and when the residual pressure gradient is less than zero, we assumed the data point to be in intermittent flow.

Figure 3.99 shows a plot of the data set collected for foam holdup versus superficial gas velocity. Figure 3.100 shows the relationship observed between the foam holdup and liquid holdup. Both these graphs are intuitively consistent. As gas velocity increases, more of the gas will flow in core, hence reducing the foam holdup. Also, as the liquid hold increases, the foam volume will also increase.

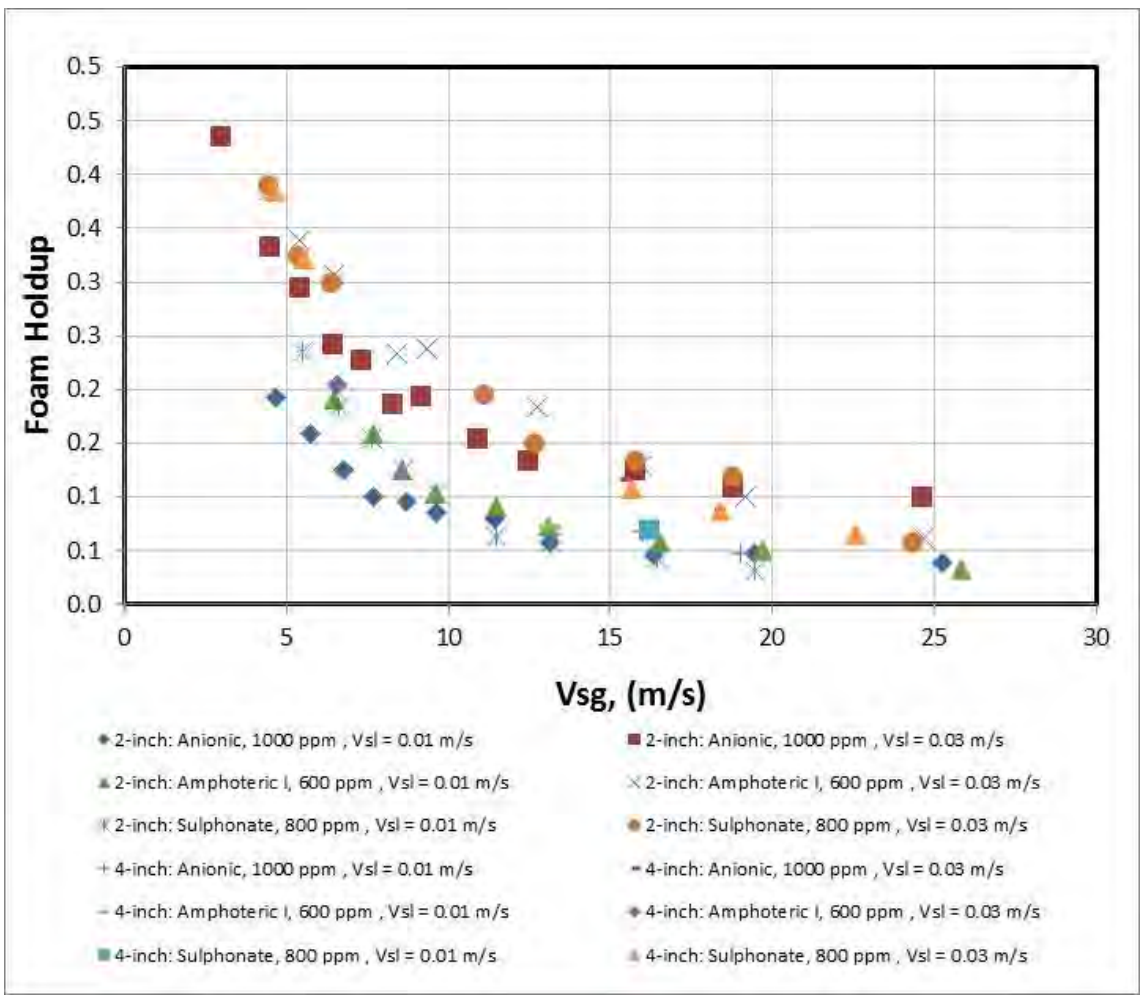

Figure 3.99: Foam Holdup versus Superficial Gas Velocity (No Cationic)

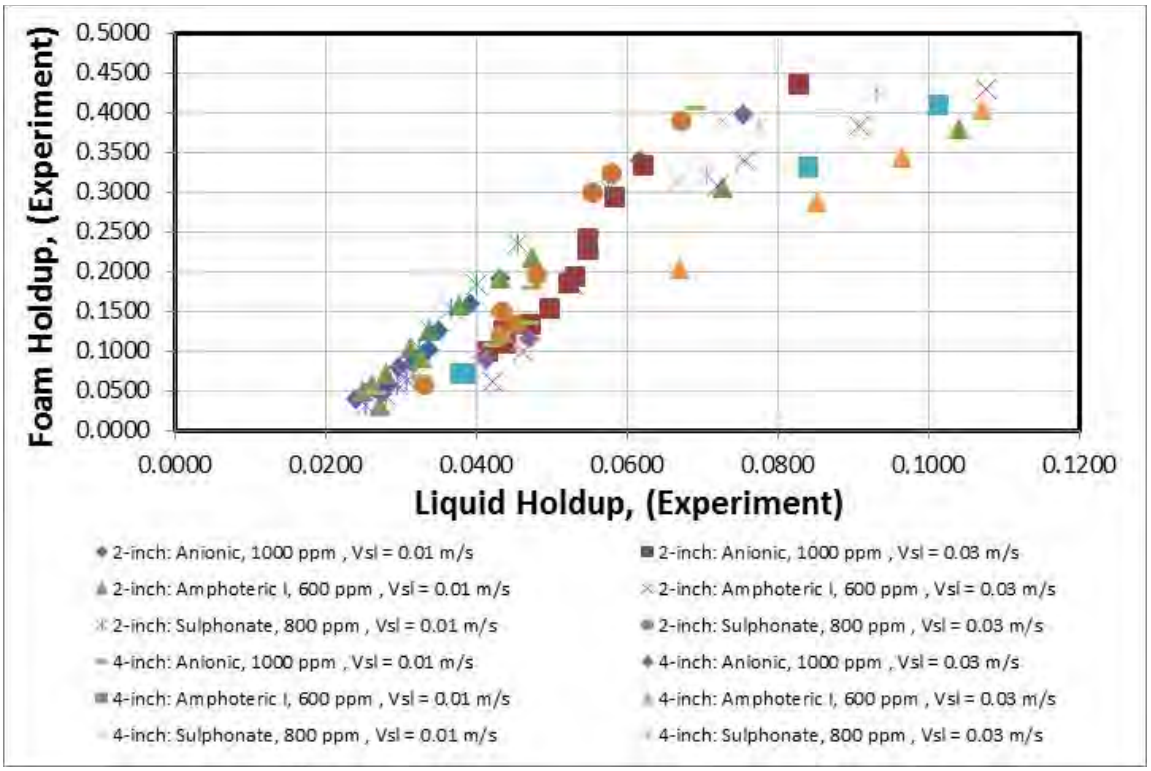

Figure 3.100: Foam Holdup versus Liquid Holdup (No Cationic)

Based on the observations in Figures 3.99 and 3.100, the following equation was used to correlate the foam holdup to liquid holdup, superficial gas and liquid velocities.

$$h_F = aH_L + b\left(\frac{v_{SL}}{v_{SG}}\right), \tag{3.40}$$

where $a = 1.60$ and, $b = 36.12$.

The foam holdup correlation has been developed for data points adjudged by the residual pressure approach to be in annular flow. Since the foam holdup correlation is directly related to the liquid holdup, a good prediction of the liquid holdup is required to get a good prediction of the foam holdup. The measured liquid holdup has been used directly in developing the foam holdup correlation.

Figure 3.101 shows the predicted foam holdup versus the foam holdup measured from experiment.

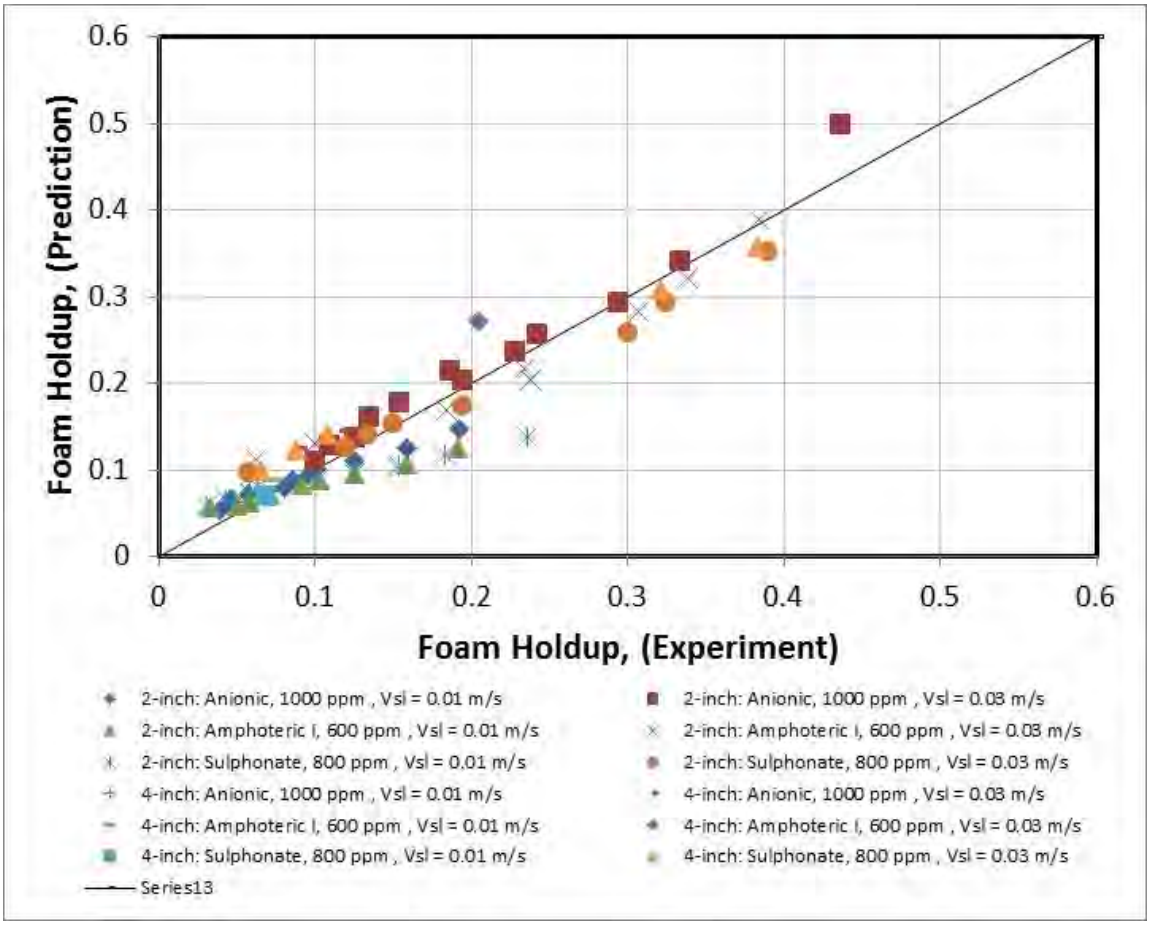

Figure 3.101: Predicted Foam Holdup versus Experimental Foam Holdup

Figure 3.102 shows the measured fraction of gas trapped in foam versus the superficial gas velocity. At a first glance, the relationship may appear counterintuitive; however, it can be explained by the fact that as the gas velocity decreases, the ability to shear the foam decreases, thus, the foam becomes more stable and traps more gas at lower gas velocities. At higher gas velocities, the foam in the film is constantly sheared by high gas velocity thus releasing the gas from the foam into the core. This is also seen in the high speed videos. At low gas velocities, the foam is stable on the wall with lots of small gas bubbles trapped in the liquid. At high gas velocities, one can observe the roll waves constantly disrupting the steady state foam flow and breaking it apart.

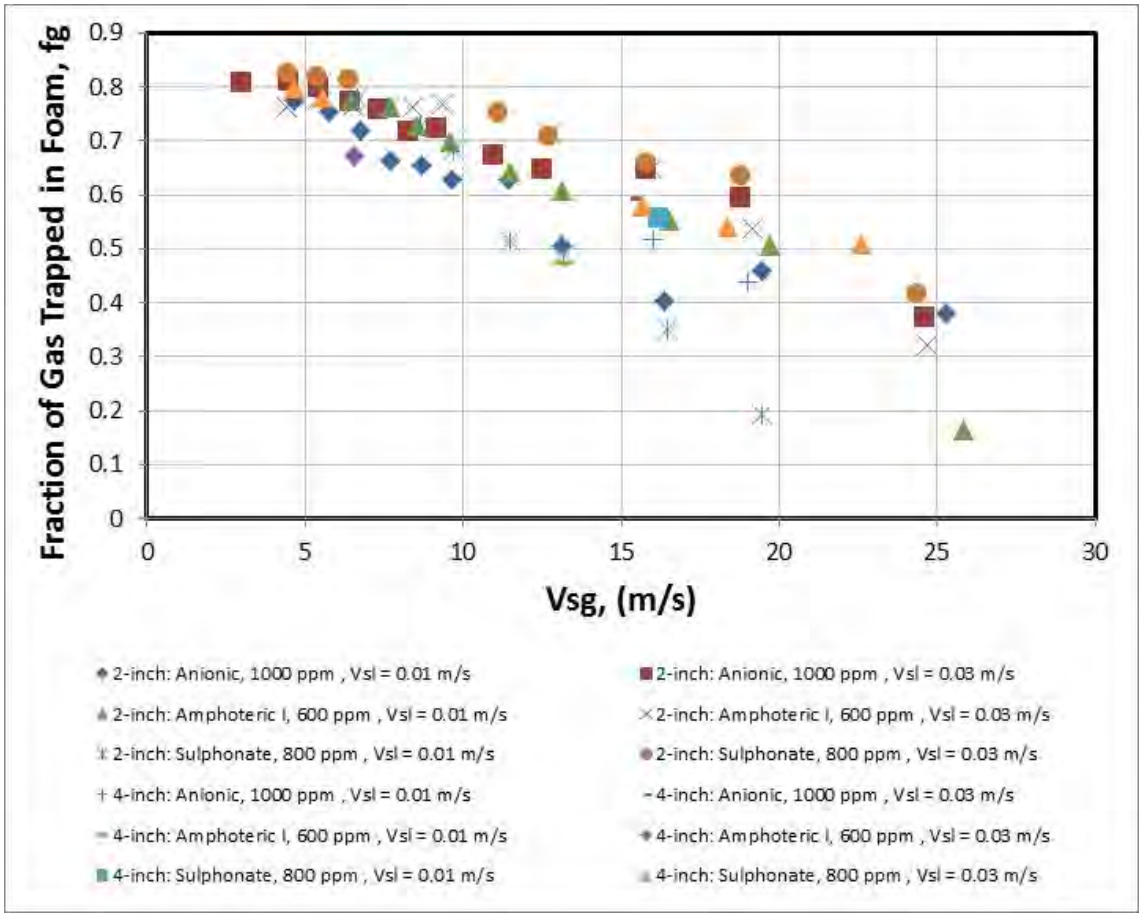

Figure 3.102: Fraction of Gas Trapped in Foam

The correlation below was used to predict the trend of the fraction of gas trapped in foam for data points adjudged to be in annular flow using the residual pressure gradient approach.

$$f_g = a\left(\frac{v_{SG}}{h_F}\right) + b\left(\frac{v_{SL}}{h_F}\right) + c, \tag{3.41}$$

where

$a = -0.00076$
$b = -0.28$
$c = 0.80$

The sum of squared errors between the predicted and measured fraction of gas trapped in foam is 0.18. Figure 3.102 shows the predicted fraction of gas in foam versus that measured directly from experiment.

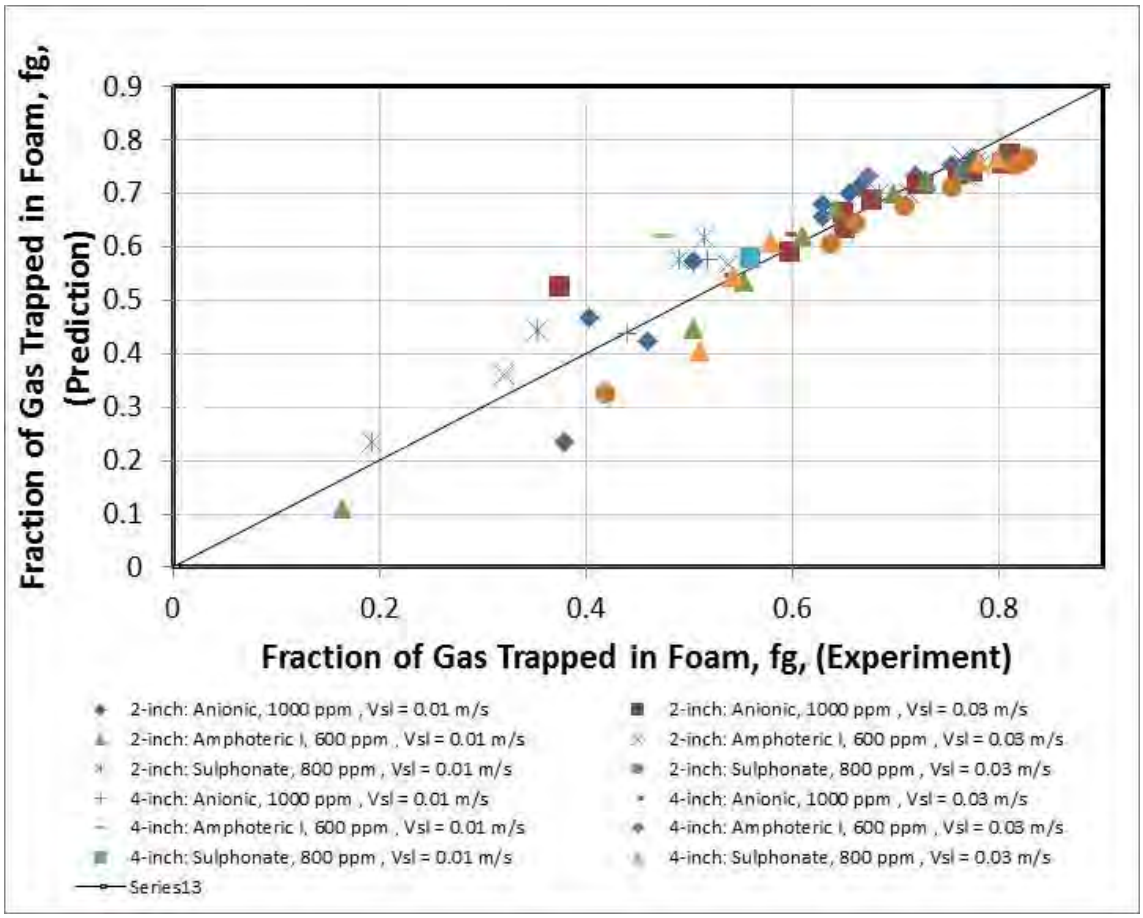

Figure 3.103: Predicted versus Measured Fraction of Gas Trapped in Foam

The interfacial friction factor under foam flow was obtained as defined by Equation (3.34) using experimental data. Figure 3.104 shows a plot of the interfacial friction factor versus superficial gas Reynolds number.

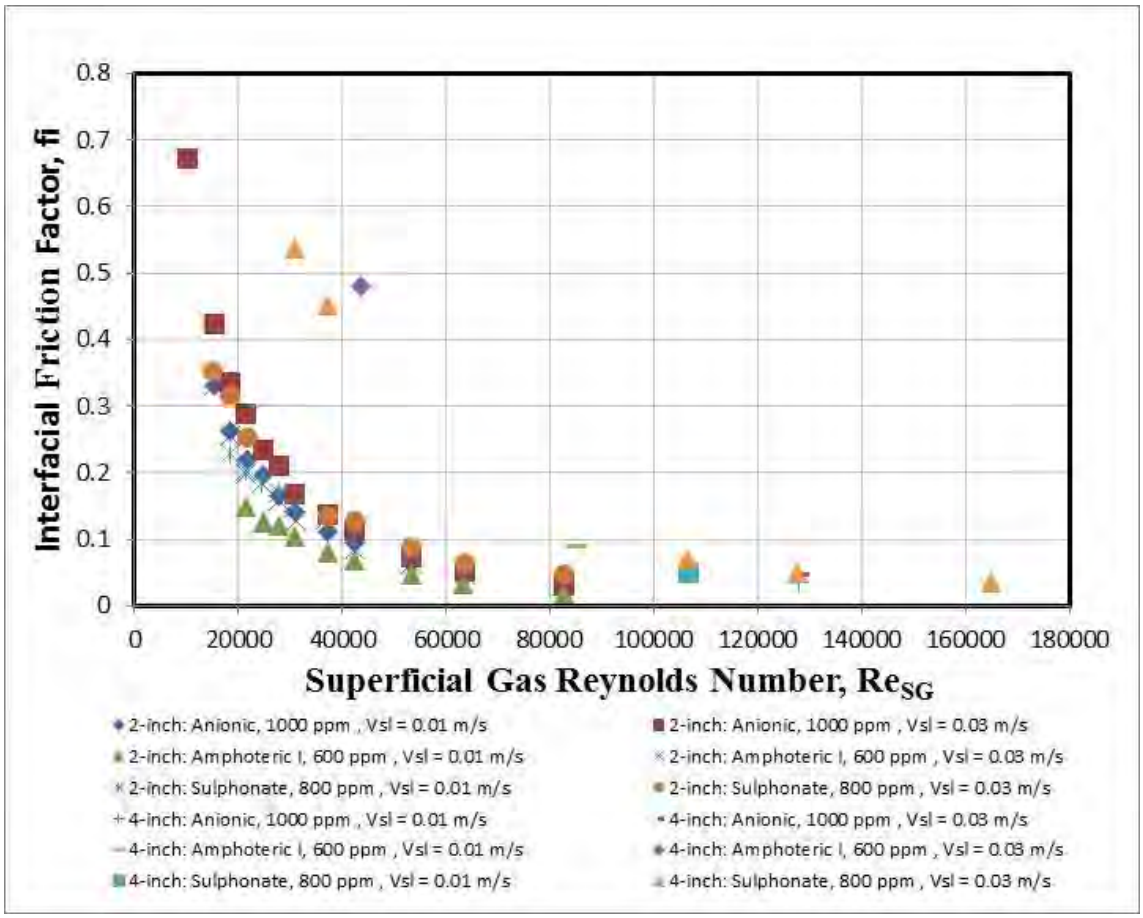

Figure 3.104: Interfacial Friction Factor versus Superficial Gas Reynolds Number

Equations (3.36) to (3.37) are used to correlate the interfacial friction factor to superficial gas Reynolds number and core Reynolds number for data points in annular flow. These equations are given as

$$f_I[II] = C_F \left[\frac{\rho_G v_{SG} d}{\mu_G}\right]^{-m_f} \left[1 + a\left(\frac{\delta_F}{d}\right)\right], \tag{3.36}$$

$$f_I[III] = C_F \left[\frac{\rho_G v_{SG} d}{\mu_G}\right]^{-m_f}. \tag{3.37}$$

Equations (3.36) and (3.37) have similar level of accuracy. The constants in these equations are as tabulated:

Table 3.9: Constants in Correlations for Predicting Interfacial Friction Factor

fi	C_F	m_f	a
Equation (31)	0.88	0.31	80.51
Equation (32)	24051.47	1.15	-

Figures 3.105 and 3.106 show the predicted versus calculated interfacial friction factor from experimental data points in annular flow.

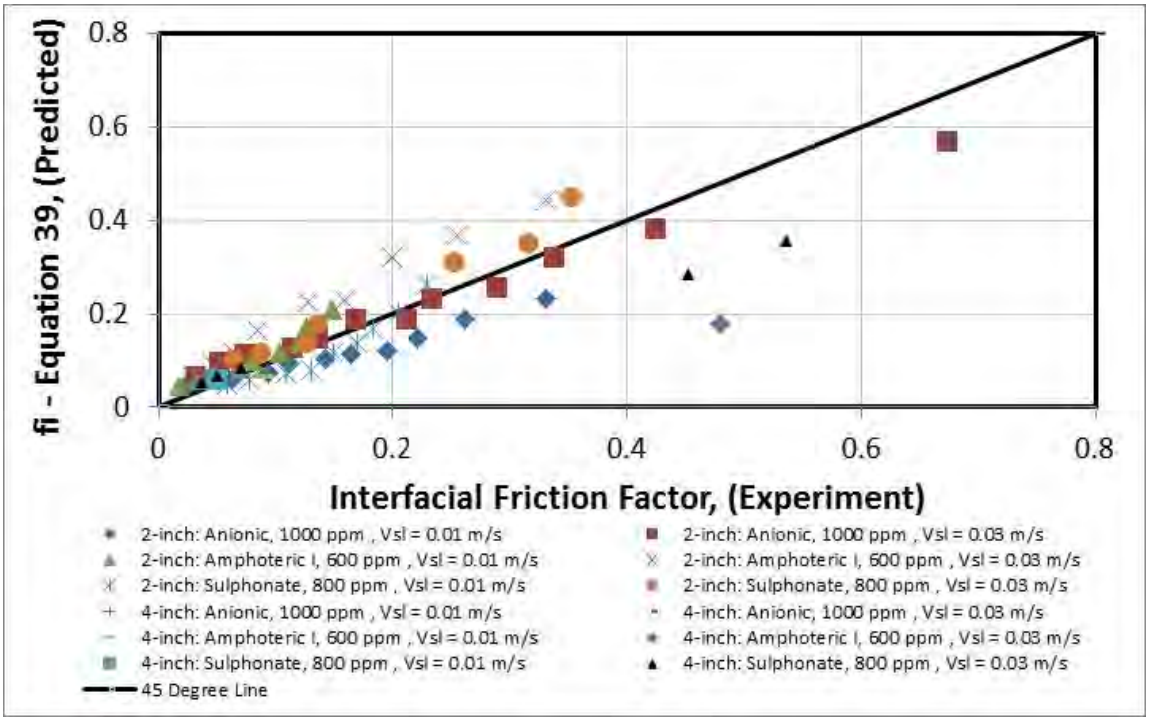

Figure 3.105: Predicted Interfacial Friction Factor (Equation 3.36) versus Interfacial Friction Factor Calculated from Experiment

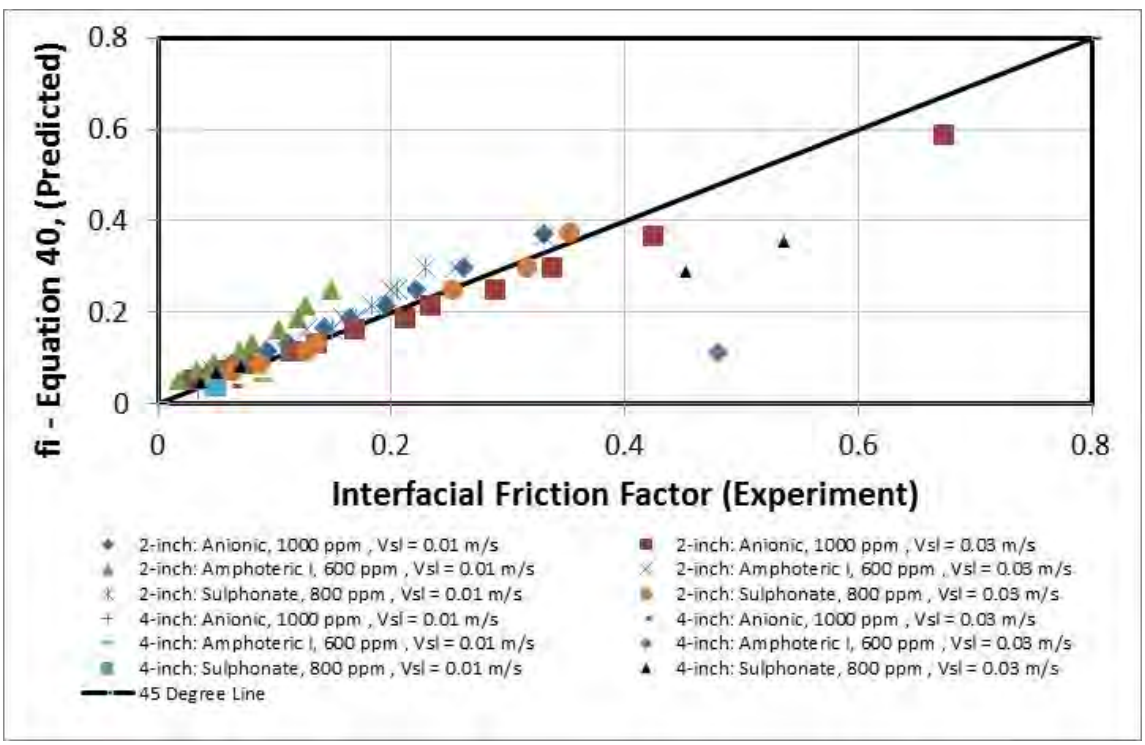

Figure 3.106: Predicted Interfacial Friction Factor (Equation 3.32) versus Interfacial Friction Factor Calculated from Experiment

These correlations are used to both predict the transition boundary between annular and intermittent flow as well as to predict the pressure drop under foam flow conditions.

The transition boundary results for foam flow are illustrated using experimental data points for Anionic surfactants in 2-inch and 4-inch pipes, at 800 ppm and a superficial liquid velocity of 0.01 m/s. The liquid holdup was predicted using constants from liquid carryover tests conducted at 6.2 mm/s (in Table 3.8). Figures 3.97 and 3.98 show that predicted liquid holdup at 4.1 mm/s and 6.2 mm/s are very similar. The different superficial gas velocities investigated are as illustrated in Figures 3.107 to 3.108. These Figures show the comparison of transition boundary based on air-water flow versus foam flow. We used the two interfacial friction factor equations presented above to determine the transition boundary. The transition boundary – as would be expected – is shifted to the left when foam is used. The solid green circular frames in Figures 3.107 and 3.108 represent the actual data point.

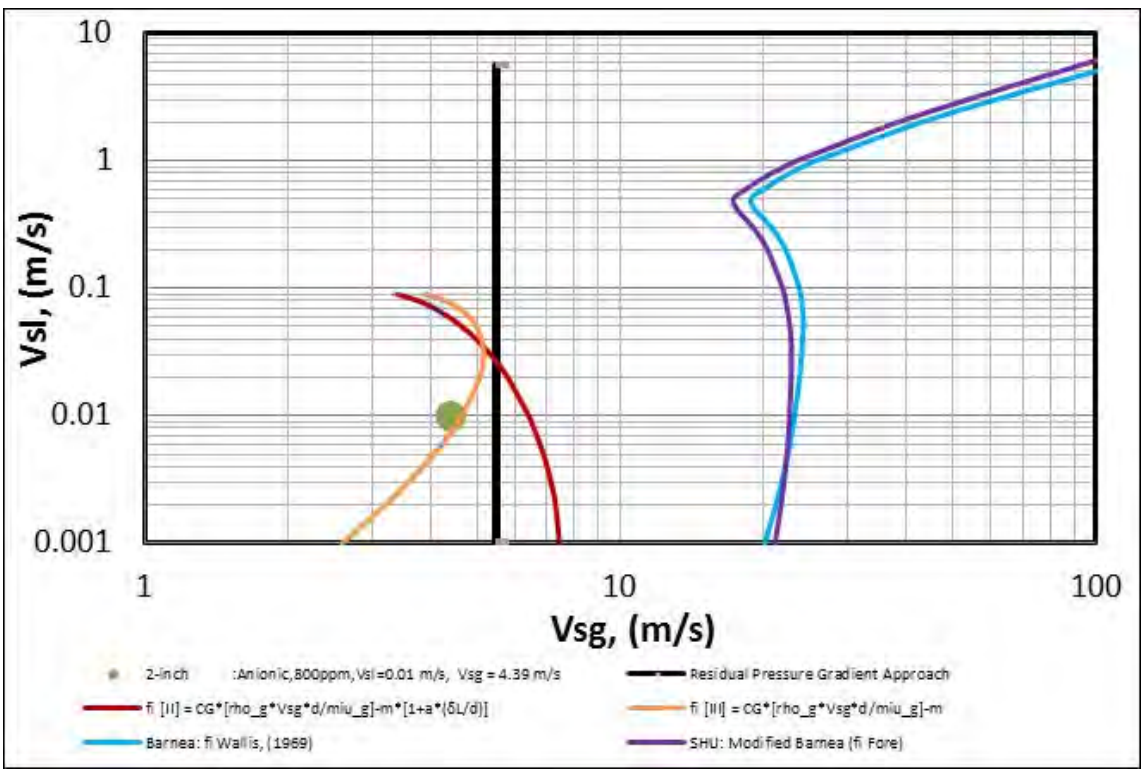

Figure 3.107: Transition Boundary Plot: Anionic Surfactant, 800 ppm, 2-inch Pipe, $v_{Sl} = 0.01\ m/s$ and $v_{Sg} = 4.39\ m/s$

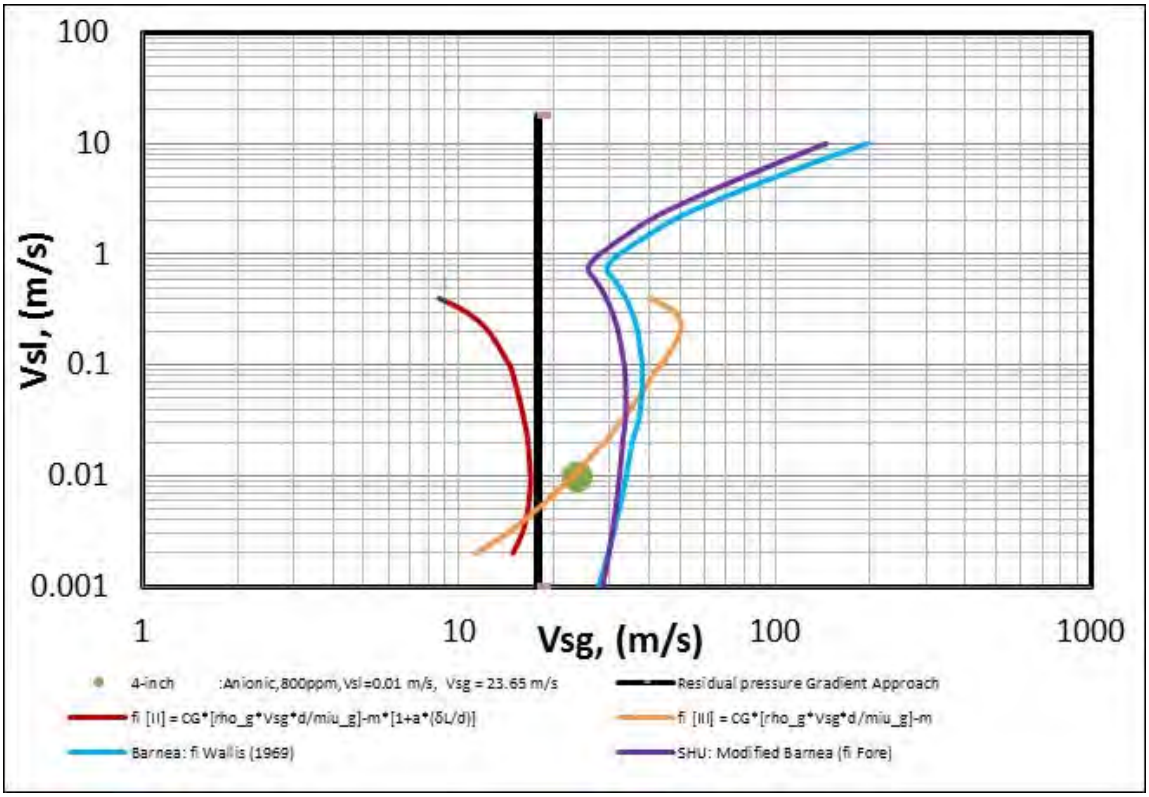

Figure 3.108: Transition Boundary Plot: Anionic Surfactant, 800 ppm, 4-inch Pipe, $v_{Sl} = 0.01\ m/s$ and $v_{Sg} = 23.65\ m/s$

In Figures 3.107 and 3.108, in addition to the transition boundary curves defined by using the foam flow interfacial friction factors in Equations (3.36) and (3.37), the following transition boundary criteria for air-water flow have also been indicated on each of the plots:

- Barnea(1986a) transition criterion (solid light blue curve)
- Luo(2013) modification to Barnea (1986a) transition criterion (solid purple curve)
- Luo(2013) residual pressure gradient approach (solid black line)

The air-water transition boundary criteria have been included on these plots so as to show how closely or otherwise they predict the transition boundary for foam flow.

In Figure 3.107, judging by the residual pressure gradient approach, a data point on the right of the black dotted vertical line is in annular flow while that on the left is in intermittent flow. Therefore the data point being investigated (solid green circular frame) is in intermittent flow since it falls on the left of the black dotted vertical line. The foam flow transition maps generated with the two correlations for interfacial friction factor predicted the flow regime of the data point being

investigated correctly. The Barnea (1986a) and Luo (2013) transition criteria for air-water flow predicted correctly as well but they are very conservative.

In Figure 3.108, judging by the residual pressure gradient approach, the data point being investigated (green dot) is in annular flow since it falls on the right of the black dotted vertical line. The foam flow transition maps generated with the two correlations for interfacial friction factor predicted the flow regime of the data point being investigated correctly. The Barnea (1986a) and Luo (2013) transition criteria for air-water flow predicted the data point as being in intermittent flow; which is not correct.

Overall, the foam flow transition boundary maps are less conservative when compared to the Luo (2013) residual pressure gradient approach. This reflects the foam's ability to postpone the liquid loading. The reason for this is the ability of liquid film to trap the gas. This results in reduced gravitational gradient in the film. In addition, the interfacial friction factor is greater than air-water flow. This also helps in postponing the transition further.

Based on the observation of the direction of the foam film in the work of Ajani (2014), for 2-inch pipe, the foam film was observed to be flowing upward at a superficial gas velocity of 4.72 m/s. For 4-inch pipe, the direction of the foam film was observed to be reversed from upwards to downwards at a superficial gas velocity of 13.88 m/s. These observed velocities are critical velocities. They were observed for experiments conducted at the optimum concentration of the surfactants. We observed that the critical velocities do not change significantly after the optimum concentration. Therefore, annular flow was observed under foam flow at 4.72 m/s and 13.88 m/s in 2-inch and 4-inch pipes respectively. The observed critical velocities in 2-inch and 4-inch pipes are used as a benchmark to sort experimental data points into loaded (superficial gas velocity lower than or equal to benchmark superficial gas velocity) and unloaded (superficial gas velocity greater than benchmark superficial gas velocity).

Figures 3.109 to 3.110 show two important pieces of information. These are explained next.

One, based on the benchmarking explained above, the transparent blue and red circular frames represent observed 2-inch pipe foam flow data points in intermittent and annular flow respectively. In addition, the solid blue and red circular frames represent observed 4-inch pipe foam flow data points in intermittent and annular flow respectively. Therefore, the blue frames represent data points observed to be in intermittent flow and the red frames represent data points observed to be in annular flow.

Two, the observed foam flow superficial gas velocities are plotted against the predicted critical superficial gas velocities obtained by using the interfacial friction factors defined in Equations (3.36) and (3.37) in the foam transition boundary

model. If data points fall above the 45 degree line, they should represent loaded wells (critical velocity is greater than observed gas velocity). If data points fall below the 45 degree line, they should represent unloaded wells (annular flow). Correct prediction of our correlation means, the unloaded and loaded data points based on experimental observations match our correlation. That is, all the blue points should be above the 45 degree line and all the red points should be below the 45 degree line.

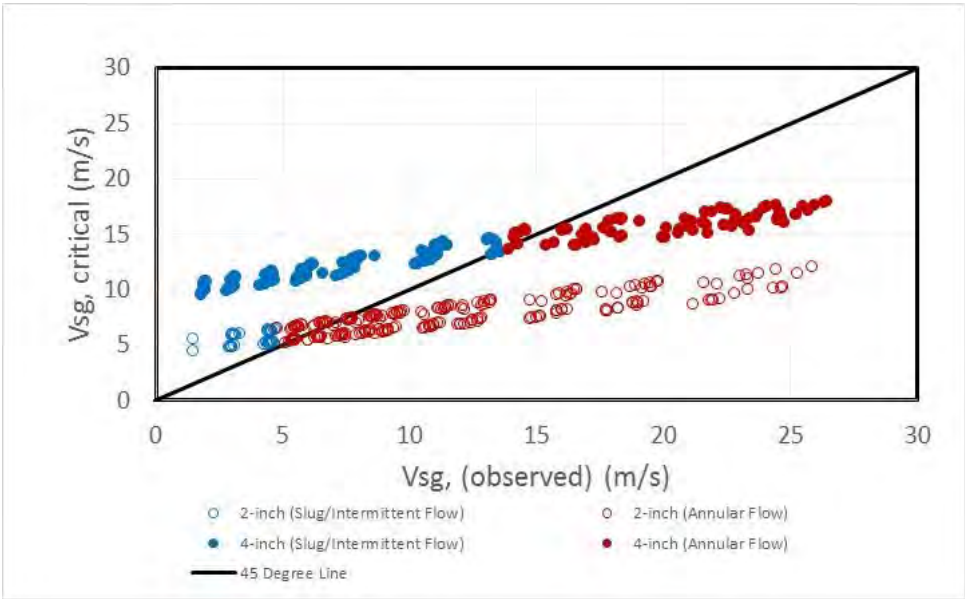

Figure 3.109: Predicted versus Observed Critical Velocity Obtained using the Interfacial Friction Factor Given by Equation (3.36)

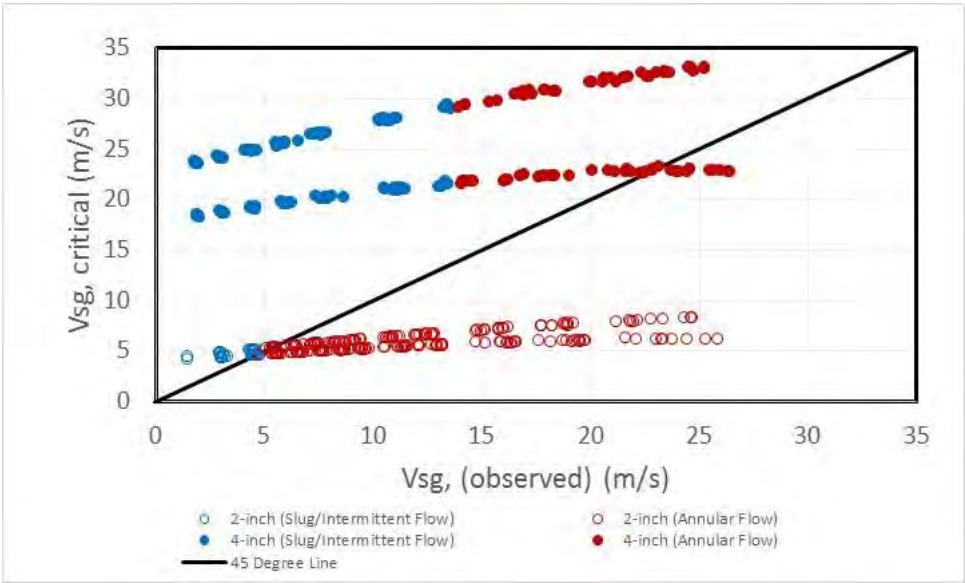

Figure 3.110: Predicted versus Observed Critical Velocity Obtained using the Interfacial Friction Factor Given by Equation (3.32)

A comparison of predicted critical velocities and experimentally observed critical velocities in Figures 3.109 and 3.110 reveal the following.

In Figure 3.109, for both 2-inch and 4-inch pipes, the transition boundaries obtained by using the interfacial friction factor defined in Equation (3.36) gave a reasonable match with experimental observations. For the two pipe diameters, the model predicted data points around the transition boundary to be in intermittent flow while they were observed to be in annular flow. This imperfection in the model is more predominant in the 2-inch pipe than in 4-inch pipe.

In Figure 3.110, for 2-inch pipe, the transition boundary obtained by using the interfacial friction factor defined in Equation (3.37) gave a better match between model predictions and experimentally observed critical velocity. However, for 4-inch pipe, the transition boundary obtained by using the interfacial friction factor defined in Equation (3.37) gave a poor match between model predictions and experimentally observed critical velocity. For 4-inch pipe, a greater proportion of the data points observed to be in annular flow were predicted to be in intermittent flow.

Below we present the results of pressure drop prediction for data points in annular flow using the interfacial friction factor correlations in Equations (3.36) and (3.37). The predicted versus observed pressure gradients are as shown in Figures 3.111 and 3.112.

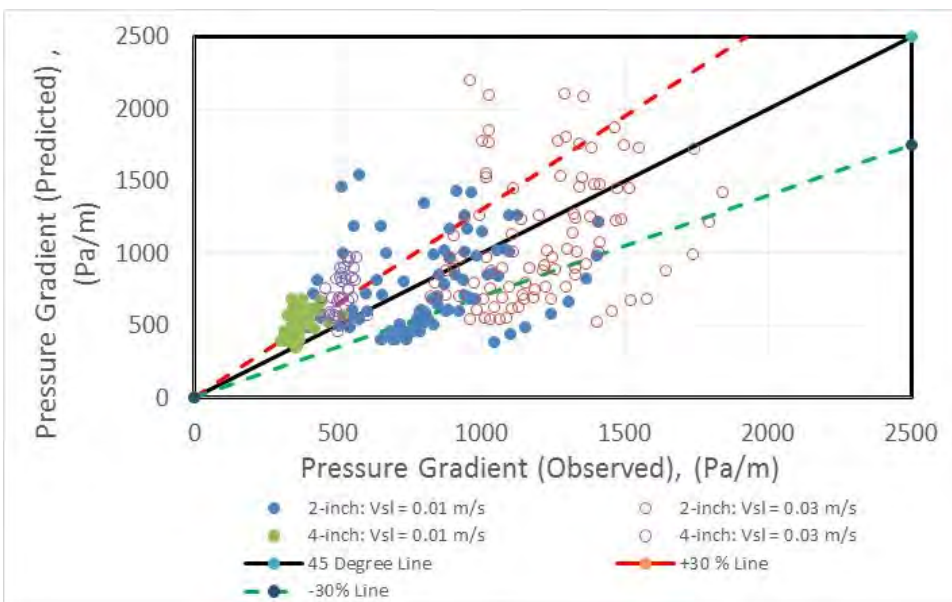

Figure 3.111: Predicted versus Observed Pressure Gradient Obtained using the Interfacial Friction Factor Given by Equation (3.36)

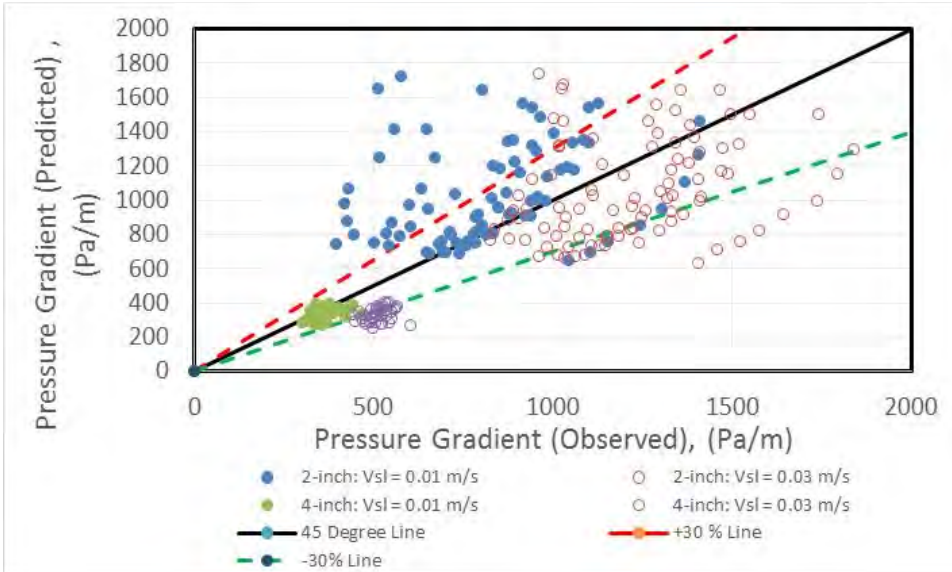

Figure 3.112: Predicted versus Observed Pressure Gradient Obtained using the Interfacial Friction Factor Given by Equation (3.37)

Majority of the results in Figure 3.111 show clear trends off the 45 degree line. The predicted data points show a tendency to curve upwards as they approach the 45 degree diagonal line. From inspection, the data points curving upwards are those corresponding to superficial gas velocities greater than 16 m/s in 2-inch pipe. The predictions in Figure 3.112 show a more representative match with experimental data than that in Figure 3.111. However, these predictions have a wide spread around the 45 degree diagonal line. We provide some reasons below for the differences in predicted versus observed data.

One, it may not be appropriate to lump different surfactants together and predict their pressure gradient with a common correlation. However, this lumping makes the correlation practical. Second and more important, there may be errors associated with underlying assumption in liquid holdup correlations. This is explained next.

Figure 3.113 shows the measured pressure gradient versus superficial gas velocity for Sulphonate foamer in 2-inch pipe at a superficial liquid velocity of 0.01 m/s. The pressure gradient in this Figure shows an increasing trend with increase in concentration of the foamer. The premise of our liquid holdup model development stems from Figure 3.114 where we identified that increase in the concentration of the surfactant causes increase in the transport capacity of the foamer. As a result, more liquid is removed from the tubing as the concentration of the surfactant increases. This results in lowering of the holdup. However, as can be seen in Figure 3.114, the change in hold up is quite small once the concentration reaches a critical value. This is also consistent with our observation in bench top test (Figure 3.115) where we see that for most surfactants, once we reach critical concentration, the unloading capacity reaches a stable value. Unfortunately, this is not true for

pressure drop calculations. As seen in Figure 3.113, the pressure drop keeps on increasing as concentration increases, even beyond critical concentration. We cannot capture this behavior because of our reliance on small scale data.

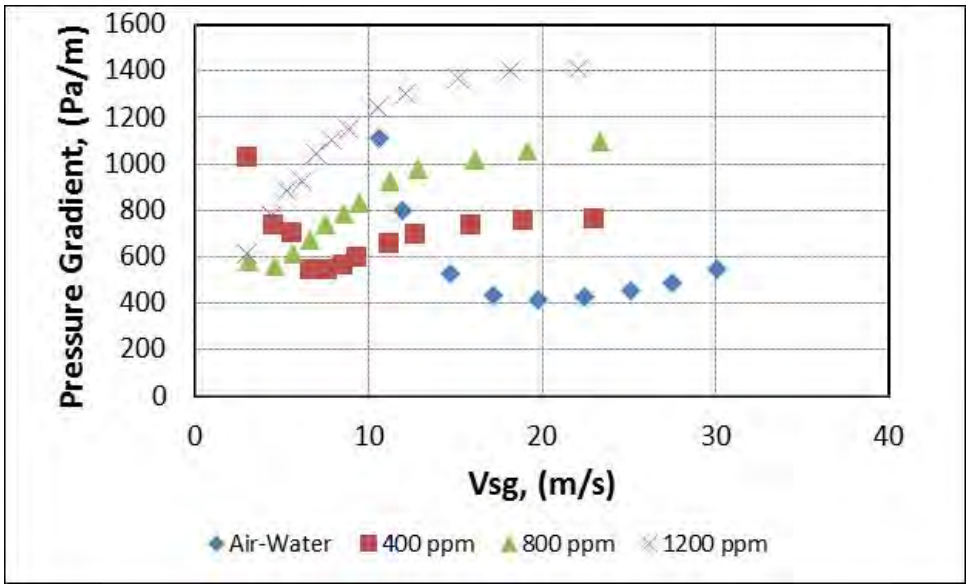

Figure 3.113: Pressure Gradient for Sulphonate Foamer [v_{SL}= 0.01 m/s, 2-in pipe]

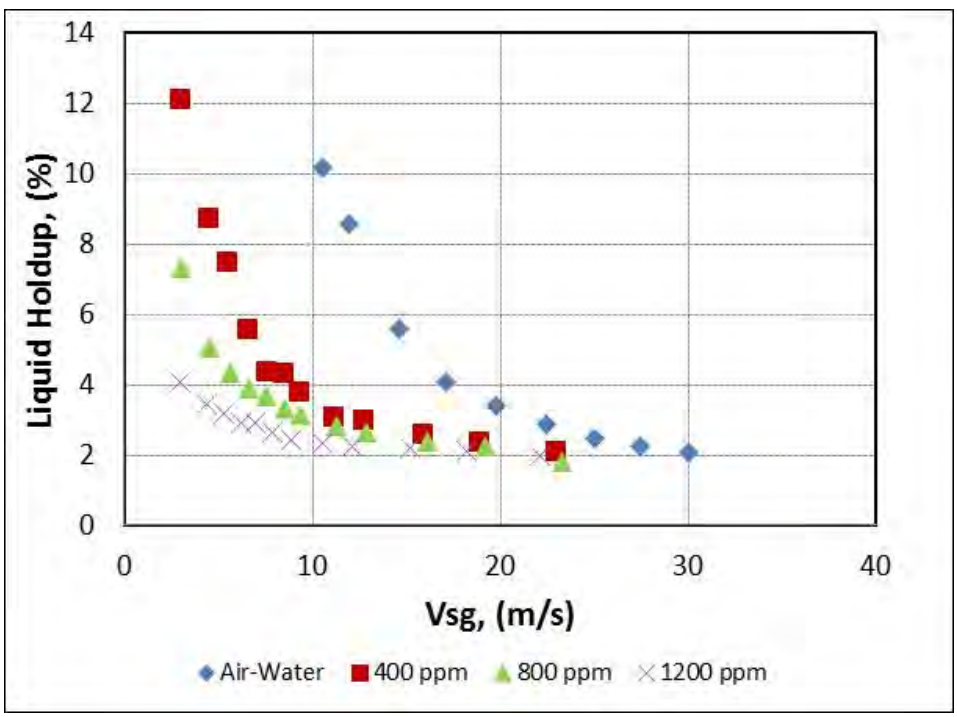

Figure 3.114: Liquid Holdup for Sulphonate Foamer [v_{SL}= 0.01 m/s, 2-in pipe]

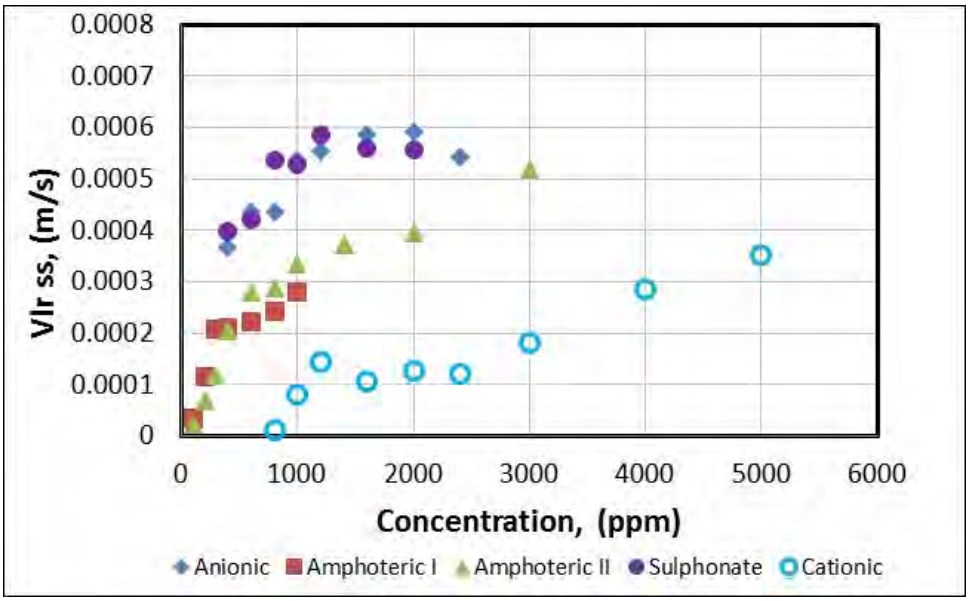

Figure 3.115: Rate of Liquid Transport
(For Unloading Tests Conducted at 4.1 mm/s)

Therefore, to improve the prediction of the pressure gradients in Figures 3.111 and 3.112, a parameter that will properly capture the effect of concentration on pressure drop seen in large scale facility needs to be defined. Unfortunately, if we make the correlation too specific to a particular surfactant as well as the concentration, the generality of the correlation is lost and we may not be able to use the correlation where limited data are available. Although there is a clear room for improvement in calculating the pressure drop, our correlation is better than the use of standard gas–liquid correlations such as Gray correlation (1978) which can significantly under-predict the frictional pressure drop and significantly over-predict gravitational pressure drop for foam flow conditions.

Figure 3.113 shows the pressure gradient predicted using Gray correlation (1978) for foam flow experimental data points in annular flow (data points with solid and transparent red circular frames in Figure 3.109).

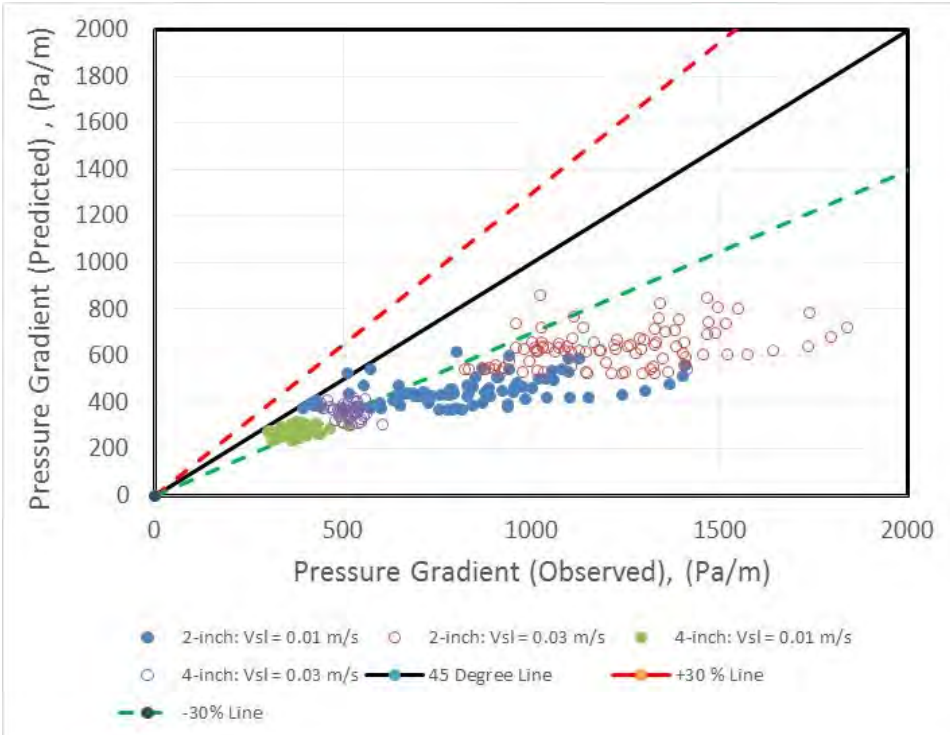

Figure 3.116: Predicted Pressure Gradient (Gray Correlation (1978)) versus Observed Pressure Gradient

Figure 3.116 shows that the Gray correlation (1978) significantly under-predicts foam flow pressure drop in annular flow. As shown in Figures 3.111 and 3.112, our correlations and model are better able to predict the pressure gradient under foam flow within 30 % error with 90 % confidence. Although not shown here, we have compared our results with limited field data and the results are similar.

Impact to Producers

The purpose of this work is to help both large as well as independent producers who produce significant amount of gas from both conventional as well as unconventional formations. Large number of gas wells eventually start liquid loading. This is because as the production rate declines, every well produces some amount of water from the formation. In addition, some wells produce condensate as well. When the gas rate is low enough so that the well loses its ability to carry the liquid to the surface, the liquid loading starts. In our study we provide a new tool to predict when the liquid loading is initiated in a gas well so that appropriate action can be taken to prevent it. The proposed correlation for predicting liquid loading is a significant improvement over currently available correlations. It can account for the diameter of the tubing, it can account for inclination of the well as well as it can account for the amount of liquid present in a gas well. We have compared the proposed correlation with the available literature data and have demonstrated that it is a better predictor of liquid loading compared to other literature correlations.

The second and the most important benefit to the producers is a detailed investigation of surfactants on liquid loading. As the wells start loading, one of the most commonly used techniques to prevent liquid loading is the use of surfactant or foam to carry the liquid to the surface. However, until this investigation, there is no correlation available to correctly predict the surfactant and its impact on the liquid loading. The current investigation accomplishes several tasks which can be of significant benefit to the operators. These include

- What is the type of surfactant which can be used to unload a well?
- What is the optimum concentration of surfactant which should be used to unload a well?
- What would happen to liquid loading when surfactant is added? At what point the benefit of surfactant will diminish and the well will start loading?
- What is the pressure drop under foam flow conditions?

These questions are answered in the current investigation. They will provide practical tools to make a better decision regarding the type of surfactant as well as its benefits on liquid loading.

Technology Transfer Efforts

In transferring the technology to the beneficial users, we approached it in several different ways. The first effort involved asking some companies to join a joint industry project so that the project can be supported by both operating and service companies. We were successful in securing the membership of six companies: these included: Marathon, Chevron, Shell, ConocoPhillips, Nalco and Multi-Chem. Four of these companies are operating companies and two of the companies were service companies which supplied chemicals to the operators. We met with all the six member companies twice a year and made presentations to them regarding the progress of the project. In addition, we also provided computer programs which can be used to predict the liquid loading behavior as well as predict the foam flow behavior. In addition, we collected significant field data from the operators. We gathered liquid loading as well as foam flow data from Chevron, ConocoPhillips and Shell which we used to validate our correlations. In addition, to ensure that the chemicals we use are indeed used by the operators, we collected samples of the chemicals from the service companies and used them in our experiment. The variety of chemicals selected in our analysis cover a broad range of chemicals typically used in the industry. The operating ranges we considered in our experimental set up are consistent with what operators told us about their parameters.

In addition to presenting the work to the member companies, we also published papers in respected journals as well as made presentation in SPE conferences. We provided seminars to oil companies as well as made presentations to various universities explaining the technology we have developed.

Conclusions

The following conclusions can be drawn based on the work we have done in this project.

Liquid Loading

1. We examined various definitions of liquid loading and proposed that the most appropriate definition is to assume that the liquid loading starts when the liquid film reversal starts.
2. Using experimental data, we showed that depending on the definition of liquid loading, different values of gas velocities can be determined as transition velocities at which liquid loading starts. Interestingly, using the traditional definition of liquid loading, the liquid loading starts earlier in the smaller tubing size. In contrast, using film reversal model, the liquid loading starts earlier in larger tubing.
3. We developed a relatively simple method of determining the transition point based on a film reversal model. Since it is difficult to experimentally observe the film reversal, we use frictional gradient calculation to determine the transition point. We observe that frictional gradient becomes negative when the film reversal starts. We are not aware of any literature which states this observation.
4. We improved Barnea's model, which is based on film reversal, and developed a new correlation to calculate liquid loading gas velocity. The new model accounts for the following: (i) variable liquid film thickness due to changes in inclination angle; (ii) fraction of liquid entrained in gas core; and (iii) interfacial friction factor between the liquid film and gas core. The new improved model includes the ability to predict transition point for inclined pipes as well as annular flows.
5. We compared the model with large amount of field data. We consistently observed that the new model is better able to predict the transition point compared to all the available literature correlations.
6. A user friendly program is developed to predict the liquid loading.

Foam Flow

We collected experimental data in both small scale and large scale facilities. We studied five different surfactants in both of the facilities and utilized the small scale facility data to predict the pressure drop in large scale facility. The following conclusions can be drawn based on the study:

1. The presence of foam results in lowering the critical gas velocity at which liquid loading occurs. This effect is observed in both 2" and 4" pipes.
2. Foam flow causes the liquid loading to be postponed because of two reasons: it creates a stable liquid mixture which is lighter (mixture of gas and liquid) which is easy to carry upwards. Second, the frictional losses are higher in the presence of foam due to higher foam viscosity and, in some instances, the formation of foam substrate on the wall of the pipe.

3. We can predict the inception of liquid loading in the foam flow by observing the velocity at which residual pressure gradient (difference between gravitational and total pressure gradient) reaches zero. This observation is consistent with air-water flow.
4. The effect of foam for 2" pipe is significantly different than 4" pipe. The reduction in gas velocity at which liquid loading occurs is significantly lower in 2" pipe compared to 4" pipe. This is a result of subtle variations in the foam behavior in those two pipes.
5. Although the concentration of surfactant has an impact on the critical gas velocity at which liquid loading occurs, the benefit of adding surfactant is diminished as the concentration increases. At the same time, the pressure drop increases rapidly at higher concentrations. Therefore, it is prudent to find a concentration of surfactant at which relative increase in surfactant does not further reduce the critical gas velocity significantly. This concentration can be significantly lower than critical micellar concentration. This not only will reduce the cost of surfactant but also reduce the frictional losses in the tubing.
6. We investigated five different surfactants covering a broad range of surfactants. Although the individual results vary, the overall trend for all the surfactants is the same. This indicates that the recommendations can be applied to any surfactants.
7. Significant amount of both small scale and large scale data on foam unloading potential, liquid holdup, foam holdup, foam quality and pressure gradient are collected on five different surfactants.
8. Using only small scale data – unloading capacity of foam – a correlation for liquid holdup was developed which reasonably predicts the liquid holdup in large scale facility. This is extremely useful since very few chemical vendors have the ability to collect the data in large scale facility.
9. A new mechanistic model was developed to describe foam flow in vertical pipes. The model is a modification of Barnea (1986a) model. Instead of assuming liquid film, the model assumes foam film is attached to the wall and gas moving in the core. Various input parameters required for the model are developed based on experimental data. These include foam fraction in vertical section, gas fraction in the foam and liquid holdup.
10. A new correlation for interfacial friction factor was developed. Two alternatives are presented in this study – both predicting the experimental data with equal accuracy.
11. A transition criterion was developed to predict the transition from annular to intermittent flow for foam flow. The criterion was validated by comparing the experimental data with predictions.
12. The pressure drop under annular flow conditions is compared with the prediction from the model. The pressure drop prediction is accurate within 30 % for 90 % of the data. The reason for lack of accuracy is the transition from small scale facility to large scale data by assuming that the foam quality is the same and small scale represents what is happening in large scale. The foam quality in large scale facility can vary and is a function of various ways gas and liquid can be mixed. It is impossible to correctly predict the foam quality based

on what we observe in small scale facility. However, the strength of the correlation is that it is able to use small scale data to predict the pressure drop in large scale facility. The correlation is the only correlation available in the literature for foam flow pressure drop prediction. It is a significant improvement over conventional correlations such as Gray's correlation (1978) which significantly under predict pressure drop.

Recommendations

We have collected significant amount of data on foam flow. We have advanced the prior work and have provided tools which be used by operators to understand the behavior of the foam on liquid loading. Several questions though still remain to be answered. We recommend that our present work can be extended to study the following additional topics:

1. We were never able to create the quality of foam which is consistent in both the small scale and large scale facilities. It would be good if one can come up with a procedure to consistently create the foam quality which can be reproduced in both small scale and large scale facilities.
2. We did not investigate the effect of pressure and temperature on the foam flow in large scale facilities
3. We did not consider the impact of condensates on foam flow behavior
4. Although we collected limited amount of field data under foam flow conditions, it would be useful to gather more foam flow data to test the correlation
5. Our current pressure drop correlation has significant error in prediction. This correlation needs to be improved by properly accounting for various foams and their qualities.

BIBLIOGRAPHY

[1] Ajani, A.A.: "Experimental Study and Modeling of effect of Surfactants on Liquid Loading in Vertical Pipes," PhD dissertation, University of Tulsa (2014).

[2] Alves et al.: "Modeling Annular Flow Behavior for Gas Wells", SPE 20384-PA, SPE Production Engineering Journal, Volume 6, Issue 4, pp. 435-440, (1991).

[3] Arashiro, E.Y. and Demarquette, N.R.: "Use of Pendant Drop method to measure Interfacial Tension between Molten Polymers" Material Research, Vol. 2, No. 1, 23-32, 1999.

[4] Bashforth, S. and Addams, J.C.: "An Attempt to test the Theory of Capillary Action", Cambridge University Press and Deighton, Bell and Co, London, 1982.

[5] Barigou, M. and Davidson, J.F.,: "Pressure Drop and Liquid Entrainment in a Foam Flowing in a Vertical Pipe", IChemE Research Event, Second European Conference for Young Researchers in Chemical Engineering, pages 952-954, 2-3 April, 1996

[6] Barnea, D., 1986a. Transition from annular flow and from dispersed bubble flow – unified models for the whole range of pipe inclinations. *Int. J. Multiphase Flow* 12, 733-744.

[7] Barnea, D., 1986b. A unified model for predicting flow – pattern transitions for the whole range of pipe inclinations. *Int. J. Multiphase Flow* 13, 1-12.
[8] Belfroid, S.P.C., Schiferli, W., Alberts, G.J.B., Veeken, C.A.M., Biezen, E., 2008. Prediction onset and dynamic behaviour of liquid loading gas wells. SPE 115567, SPE Annual Technical Conference and Exhibition held in Denver, Colorado, USA, 21-24 September 2008.
[9] Christiansen, R.L.,: "A New Look at Foam for Unloading Gas Wells", Penn-State Sub-Contract No. 2772-CSM-DOE-2098, DOE Award Number DE-FC26-00NT42098, June, 2006
[10] Chupin, G., Hu, B., Haugset, T., Sagen, J., & Claudel, M. (2007, November). Integrated Wellbore/Reservoir Model Predicts Flow Transients in Liquid-Loaded Gas Wells. In *SPE Annual Technical Conference and Exhibition*
[11] Coleman, S. B., Clay, H. B., McCurdy, D. G., Norris, H. Lee III, 1991a. A New look at predicting gas-well load-up. *J. Pet Tech* 43(3), 329-333.
[12] Coleman, S. B., Clay, H. B., McCurdy, D. G., Norris, H. Lee III, 1991b. Understanding gas-well load-up behavior. *J. Pet Tech* 43(3), 334-338.
[13] Deshpande, N.S. and Barigou, M.: "The Flow of Gas Liquid Foams in Vertical Pipes", Chem. Engg. Science 55, pp. 4297-4309 (2000)
[14] Dousi, N., Veeken, C., & Currie, P. K. (2006). Numerical and Analytical Modelling of the Gas Well Liquid Loading Process. *SPE Production & Operations*, *21*(4), 475-482.
[15] Duggan, J. (1961). Estimating flow rates required to keep gas wells unloaded. *Journal of Petroleum Technology*, *13*(12), 1173-1176.
[16] Fore, L. B., Beus, S. G., & Bauer, R. C. (2000). Interfacial friction in gas–liquid annular flow: analogies to full and transition roughness. *International journal of multiphase flow*, *26*(11), 1755-1769.
[17] Gray, American Petroleum Institute , API Manual 14B, "Subsurface Controlled Subsurface Safety valve Sizing Computer program", Appendix B, Second Edition, January (1978).
[18] Guo, B., Ghalambor, A., & Xu, C. (2006). A Systematic approach to predicting liquid loading in gas wells. *SPE Production & Operations*, *21*(1), 81-88.
[19] Hatchek, E.: "Die Viskosite der Dispersoide", Kolloid-Z, pp. 34-39 (1911)
[20] Heuvei , S.O. and Adelizzi, C., "Gas Well Deliquification by Chemical Foam": www.alrdc.com/workshops/2013-2013
[21] Liu, L., Li, X., Tong, L. and Liu, Y.: "Effect of Surfactant Additive on Vertical Two Phase Flow", Journal of Petroleum Science and Engineering, 115 (2014) 1-10
[22] Lyons, W.C. and Plisga, G.J.: "Standard handbook of petroleum and natural gas Engineering", ISBN 978-0-7506-7785-1 (2005)
[23] Luo, S.: "Inception of Liquid Loading and Possible Solutions", PhD Dissertation, University of Tulsa, Tulsa, OK (2013).
[24] Mitchell, B.J.: "Viscosity of Foam", PhD Dissertation, Petroleum Engineering Department, University of Oklahoma, Norman, (1970)
[25] Saleh, S., Al-Jamae'y, M.: "Foam-Assisted Liquid Lifting in Low Pressure Gas Wells", SPE 37425, SPE Production Operations Symposium, Oklahoma City, Oklahoma, 9-11 March 1997

[26] Schinagl et al.: "Highly Successful Batch Application of Surfactant in North Sea Gas Wells", SPE 108380, Offshore Europe 2007, Aberdeen, Scotland, U.K., 4-7 September, 2007
[27] Shoham, O.: "Mechanistic Modeling of Gas-Liquid Two-Phase Flow in Pipes", ISBN 978-1-55563-107-9 (2006).
[28] Siddiqui, S., Yang, J.: "Successful Application of Foam for Lifting Liquids from Low-Pressure Gas Wells", SPE-52122-MS, 1999 Mid-Continent Operations Symposium. Oklahoma City, Oklahoma, 28-31 March
[29] Skopich, A. (2012): " Experimental Study of Surfactant Effect on Liquid Loading in 2-in and 4-in Diameter Vertical Pipes", M.S. Thesis, U of Tulsa, Tulsa, OK
[30] Solesa, M., Sevic, S.: "Production Optimization Challenges of Gas Wells with Liquid Loading Problem Using Foaming Agents", SPE 101276, 2006 Russian Oil and Gas Technical Conference and Exhibition, Moscow, Russia, 3-6 October 2006
[31] Sutton, R., Cox, S., Lea, J., & Rowlan, O. L. (2010). Guidelines for the proper application of critical velocity calculations. *SPE Production & Operations*, *25*(2), 182-194.
[32] Turner, R. G., Hubbard, M. G., & Dukler, A. E. (1969). Analysis and prediction of minimum flow rate for the continuous removal of liquids from gas wells. *Journal of Petroleum Technology*, *21*(11), 1475-1482.
[33] Van Nimwegen, A.T., Portela, L.M. and Henkes, R.A.W.M.,: "A first Look at the Hydrodynamics of Air-Water-Foam Flow for Gas Well Deliquification", Multiphase Technology, pp. 367-378, 2012
[34] Van Nimwegen, A.T., Portela, L.M. and Henkes, R.A.W.M.: "The Effect of Surfactants on Vertical Air/Water Flow for Prevention of Liquid Loading", SPE 164095, SPE International Symposium on Oilfield Chemistry. The Woodlands, Texas, USA, 8-10 April 2013.
[35] Van Nimwegen, A.T., Portela, L.M. and Henkes, R.A.W.M.: "The Effect of Surfactants on Air-Water Annular and Churn Flow in Vertical Pipes. Part 2: Liquid Holdup and pressure Gradient Dynamics", International Journal of Multiphase Flow (2014), http://dx.doi.org/10.1016/j.ijmultiphaseflow.2014.03.007
[36] Van't Westende, J. M. C., Kemp, H. K., Belt, R. J., Portela, L. M., Mudde, R. F., & Oliemans, R. V. A. (2007). On the role of droplets in cocurrent annular and churn-annular pipe flow. *International journal of multiphase flow*, *33*(6), 595-615.
[37] Van't Westende, J. M. C. (2008). Droplets in annular-dispersed gas-liquid pipe-flows. PhD thesis, Delft Technical University, Delft, The Netherlands
[38] Veeken, K., Hu, B., Schiferli, W., 2010. Gas well liquid loading field data analysis and multiphase flow modeling. *SPE Production & Operations* August 2010.
[39] Wallis, G. B. (1969). *One-dimensional two-phase flow* (Vol. 1). New York: McGraw-Hill.
[40] Waltrich, P.J., Falcone, G., Barbosa, J.R., 2011. Performance of vertical transient two-phase flow models applied to liquid loading in gas wells. SPE

147128, SPE Annual Technical Conference and Exhibition held in Denver, Colorado, USA, 30 October – 2 November 2011.

[41] Willis et al.,: "Chemical Foamers for Gas Well Deliquification", SPE 115633, SPE Asia Pacific Oil & Gas Conference and Exhibition, Perth, Australia, 20-22 October 2008

[42] Xu, R. and Yang, L.: "A New Binary Surfactant Mixture Improved Foam Performance in Gas Well Production" SPE 29004, SPE International Symposium in Oilfield Chemistry, San Antonio, Texas, USA, 14-17 February, 1995.

[43] Yang, J., Jovancicevic, V. and Ramachandran, S.: "Foam for Gas Well Deliquification", Colloids and Surfaces A: Physicochem. Eng. Aspects 309 (2007) 177-181

[44] Yuan, G., 2011. Liquid loading problems of natural gas wells. M.S. Thesis, U of Tulsa, Tulsa, OK.

[45] Zhou, J.: "Flow Patterns in Vertical Air/Water Flow with and without Surfactant", Master's Thesis, Chemical Engineering Department, University of Dayton, Dayton , Ohio, USA, 2013

LIST OF ACRONYMS AND ABBREVIATIONS

a, b, c, n1 = Constants , (-)
d = Pipe diameter, (m)
g = Accelaration due to gravity, (m/s^2)
L = Pipe length, (m)
n = Exponent in foam viscosity, (-)

A_C/A_G = Area of core/Area of gas in core, (m^2)
A_F = Area of foam film, (m^2)
A_p = Area of pipe, (m^2)
C_F = Coefficient in foam friction factor or in interfacial friction factor, (-)
d_F = Hydraulic diameter of foam film, (m)
d_C = Hydraulic diameter of the core, (m)
f_g = Fraction of gas trapped in foam, (-)
f_I = Interfacial friction factor, (-)
f_F = Foam friction factor
h_F = Foam holdup, (-)
h_g = gas void fraction, (-)
H_L = Liquid holdup, (-)
m_F = Exponent in interfacial frcition factor, (-)
n_F = Exponent in foam friction factor, (-)
q_F = Volumetric flowrate of foam film, (m^3/s)
q_g = Volumetric flowrate of gas, (m^3/s)
q_{gc} = Volumetric flowrate of gas in the core, (m^3/s)
$q_g\ in\ foam$ = Volumetric flowrate of gas in foam, (m^3/s)
$q_{g(Total)}$ = Total volumetric flowrate of gas, (m^3/s)

q_L = Volumetric flowrate of liquid, (m^3/s)
Re = Reynolds number, (-)
S_I = Perimeter of Interface, (m)
S_F = Perimeter of Foam Film, (m)

μ_C/μ_G = Core or Gas viscosity, (Kg/m.s)
μ_F = Foam viscosity, (Kg/m.s)
μ_L = Liquid viscosity, (Kg/m.s)
v_F = Velocity of foam film, (m/s)
v_C/v_G = Core or Gas velocity, (m/s)
τ_I = Interfacial shear stress, (Pa)
τ_{wF} = Foam film wall shear stress, (Pa)
δ_F = Foam film thickness, (m)
θ = Pipe inclination angle, (degrees)
ρ_F = Foam density, (Kg/m^3)
ρ_C/ρ_G = Core or Gas density, (Kg/m^3)
ρ_L = Liquid density, (Kg/m^3)
ρ_F = Foam density, (Kg/m^3)
v_{SL} = Superficial liquid velocity, (m/s)
v_{Sg} = Superficial gas velocity, (m/s)
$\widetilde{\delta_F}$ = Dimensionless foam film thickness, (-)
$\widetilde{\delta_{F,min}}$ = Dimensionless critical foam film thickness at the minimum point, (-)
π = pie (3.142)

APPENDICES

Appendix A - Available Field Data for Liquid Loading Prediction

Table A.1: Turner's Field Data and Calculation Results

Wellhead Pressure (psi)	Tubing Diameter (inch)	Gas Rate (mscf/d)	Liquid Rate (bbl/d)	Current Gas Velocity (m/s)	Turner's Equation (w/c) (m/s)	Turner's Equation (w) (m/s)	Zhang et al. Model (m/s)	Barnea's Model (m/s)	New Model (m/s)
Unloading Wells									
3434	1.995	2926	37.4	1.89	0.91	1.36	2.00	2.52	1.81
3660	1.995	3726	36.8	2.30	0.88	1.32	1.96	2.38	1.71
3472	1.995	2572	106.9	1.65	0.91	1.35	2.13	2.23	1.61
3092	2.441	3351	117.6	1.57	0.97	1.44	2.37	2.81	1.97
3455	1.995	2769	104.3	1.78	0.91	1.36	2.14	2.21	1.60
3615	2.441	3890	68.3	1.62	0.89	1.32	2.13	2.71	1.89
3025	2.441	3517	54.8	1.67	0.98	1.46	2.30	3.08	2.16
7405	2.441	6946	10.8	2.02	0.56	0.87	1.31	1.80	1.24
2226	1.995	1959	17.9	1.86	1.17	1.72	2.40	3.23	2.44
2169	1.684	7504	2.5	10.26	1.18	1.74	2.28	2.93	2.27
1520	3.958	4150	13.1	1.52	1.43	2.10	3.74	5.65	4.09
1117	3.309	5513	10.3	4.11	1.68	2.46	4.08	6.05	4.49
1913	3.309	9897	24.8	4.01	1.27	1.86	3.19	4.92	3.39
1953	3.309	9289	31.8	3.68	1.25	1.84	3.16	4.84	3.32
2256	2.684	9747	15.1	5.04	1.16	1.71	2.72	3.93	2.77
2223	2.684	9860	3.7	5.17	1.17	1.72	2.67	3.82	2.81
2003	2.684	11767	3.7	6.89	1.23	1.82	2.82	4.06	2.98
1600	1.684	6423	26.7	12.26	1.39	2.04	2.98	3.03	2.32
1835	1.995	8672	28.2	10.11	1.90	1.90	2.91	3.22	2.38
2421	1.995	6654	28.2	5.80	1.64	1.64	2.49	2.89	2.11
2705	1.995	5136	28.2	4.03	1.55	1.55	2.31	2.81	2.04
2884	1.995	3917	28.2	2.91	1.50	1.50	2.19	2.77	2.01
5056	1.995	3376	8.9	1.73	1.10	1.10	1.53	2.04	1.49
4931	1.995	4830	8.9	2.50	1.11	1.11	1.57	2.08	1.51
4786	1.995	6221	8.9	3.27	1.13	1.13	1.61	2.12	1.53
4575	1.995	7792	8.9	4.19	1.16	1.16	1.66	2.17	1.56
1902	1.995	1138	30.9	1.28	1.27	1.87	2.61	3.50	2.66
1737	1.995	1712	0.9	2.12	1.33	1.96	2.67	3.17	2.61
1480	1.995	2473	0.9	3.67	1.45	2.13	2.90	3.52	2.88
1246	1.995	2965	0.9	5.36	1.59	2.33	3.16	3.87	3.18
1895	1.995	1797	54.1	2.02	1.27	1.87	2.70	3.48	2.58
1861	1.995	2502	54.1	2.87	1.28	1.89	2.72	3.43	2.54
1784	1.995	3460	54.1	4.16	1.31	1.93	2.90	3.39	2.51
1680	1.995	4439	54.1	5.71	1.36	1.99	3.04	3.37	2.51
2814	1.75	1596	4.3	1.57	1.52	1.52	1.99	2.55	1.98
2582	1.75	2423	4.3	2.58	1.59	1.59	2.09	2.70	2.09
2104	1.75	3598	4.3	4.70	1.77	1.77	2.33	3.03	2.35
1575	1.75	4410	4.3	7.93	2.06	2.06	2.71	3.52	2.75
2783	1.75	2939	3.4	2.92	1.03	1.53	2.01	2.60	2.00
2655	1.75	4140	3.4	4.30	1.06	1.57	2.07	2.68	2.06
2406	1.75	5820	3.4	6.63	1.12	1.65	2.19	2.85	2.18
2205	1.75	6871	3.4	8.55	1.17	1.73	2.30	2.98	2.29
2574	1.75	1943	4.7	2.08	1.59	1.59	2.09	2.70	2.09
2224	1.75	2910	4.7	3.59	1.72	1.72	2.27	2.94	2.28
1839	1.75	3742	4.7	5.66	1.90	1.90	2.51	3.25	2.53
1509	1.75	4485	4.7	8.47	2.11	2.11	2.78	3.60	2.82
2611	1.995	3436	5.5	2.79	1.07	1.58	2.19	2.94	2.22
2527	1.995	4471	5.5	3.74	1.09	1.61	2.24	3.01	2.27
2556	1.995	1550	7.7	1.28	1.08	1.60	2.20	2.93	2.24

2415	1.995	1804	7.7	1.58	1.12	1.65	2.27	3.03	2.31
2149	1.995	2385	7.7	2.35	1.19	1.75	2.42	3.25	2.48
1765	1.995	2949	7.7	3.59	1.32	1.94	2.69	3.60	2.77
2862	2.599	3024	5	1.33	1.01	1.50	2.29	3.17	2.36
Loading Wells									
725	2.441	775	6	1.72	2.10	3.07	4.45	5.60	4.63
400	1.995	417	18	2.63	4.15	4.15	5.47	6.95	5.89
108	2.041	568	22	13.20	8.01	8.01	10.02	12.95	11.52
540	1.995	712	21	3.26	3.56	3.56	4.77	6.23	5.12
450	1.995	442	11.3	2.46	2.68	3.91	5.17	6.45	5.49
3607	1.995	1525	37.4	0.95	0.89	1.33	1.89	2.51	1.82
3340	2.992	2611	130.8	0.77	0.93	1.38	2.35	3.34	2.26
3540	2.441	1814	113.5	0.77	0.90	1.34	2.13	2.81	1.96
3525	1.995	1792	106.9	1.14	0.90	1.34	2.05	2.35	1.69
3338	2.441	2261	117.6	1.00	0.93	1.38	2.22	2.84	1.98
3665	2.441	2542	68.3	1.05	0.88	1.31	2.07	2.79	1.94
3212	2.441	2547	54.8	1.16	0.95	1.41	2.20	3.04	2.13
8215	2.441	3472	10.8	0.98	0.51	0.82	1.20	1.64	1.15
2182	1.684	5501	2.5	7.47	1.18	1.74	2.26	2.90	2.26
1590	3.958	3009	13.1	1.05	1.40	2.05	3.65	5.41	3.94
1245	3.309	4441	10.3	2.92	1.59	2.33	3.86	5.69	4.22
1184	3.309	4843	10.3	3.38	1.63	2.39	3.96	5.85	4.34
1958	3.309	8185	24.8	3.23	1.25	1.84	3.14	4.87	3.36
2040	3.309	6702	31.8	2.53	1.22	1.80	3.07	4.77	3.28
2284	2.684	7109	15.1	3.63	1.15	1.70	2.68	3.91	2.78
2352	2.684	6361	3.7	3.15	1.13	1.67	2.58	3.65	2.70
2042	1.684	4124	26.7	6.01	1.22	1.80	2.54	2.85	2.16
2823	2.599	3863	5	1.72	1.02	1.52	2.31	3.24	2.39
760	2.441	1247	91.2	2.63	3.00	3.00	4.48	6.26	4.74
704	2.441	1313	72.4	3.01	3.12	3.12	4.62	6.50	4.95
822	2.441	1356	53	2.62	2.88	2.88	4.27	6.03	4.60
1102	2.441	1365	49.9	1.90	2.48	2.48	3.71	5.25	3.95
552	2.441	1607	47.4	4.80	3.53	3.53	5.17	7.26	5.64
315	7.386	5740	10	3.39	3.21	4.68	9.93	14.45	11.13
422	7.386	3890	10	1.69	2.77	4.04	8.70	12.13	9.32
459	7.386	2780	10	1.11	2.66	3.87	8.37	11.24	8.70
484	7.386	1638	10	0.62	2.58	3.77	8.17	10.29	8.09
500	2.599	400	14	1.17	2.54	3.71	5.43	6.90	5.76
500	1.677	800	5	5.63	3.71	3.71	4.61	5.61	4.81
660	3.901	4300	3.5	4.14	3.22	3.22	5.56	7.57	5.96
280	2.599	500	28	2.70	4.97	4.97	7.13	9.52	7.98
210	3.901	470	24	1.52	5.74	5.74	9.41	12.41	10.49

Table A.2: Coleman's Field Data and Calculation Results

Wellhead Pressure (psi)	Tubing Diameter (inch)	Gas Rate (mscf/d)	Liquid Rate (bbl/d)	Current Gas Velocity (m/s)	Turner's Equation (m/s)	Zhang et al. Model (m/s)	Barnea's Model (m/s)	New Model (m/s)
275	2.441	726	2	4.53	5.01	6.99	7.92	7.14
205	2.441	660	2.9	5.58	5.81	7.99	9.26	8.40
212	2.441	585	9.6	4.77	5.71	7.87	9.93	8.69
150	2.441	468	9.6	5.44	6.80	9.19	11.42	10.23
185	2.441	573	10.6	5.38	6.12	8.37	10.61	9.33
145	2.441	593	7.1	7.14	6.91	9.33	11.54	10.38
145	2.441	617	7.1	7.43	6.91	9.32	11.57	10.39
70	2.441	250	11.2	6.30	9.96	12.78	15.47	14.60
140	2.441	607	9.9	7.58	7.03	9.47	12.02	10.71
138	2.441	600	9.9	7.60	7.09	9.54	12.09	10.78
130	2.441	635	1.3	8.55	7.30	9.78	10.48	10.02
125	2.441	583	7	8.17	7.45	9.96	12.30	11.16
165	2.441	649	8.2	6.85	6.48	8.81	11.07	9.82
395	2.441	647	0	2.76	4.18	5.91	5.36	5.05
255	2.441	612	0	4.13	5.21	7.23	6.53	6.30
355	2.441	952	22.6	4.55	4.41	6.23	8.48	6.97
105	2.441	430	6.5	7.19	8.13	10.74	12.91	11.95
99	2.441	396	0	7.03	8.37	11.01	9.99	10.10
70	2.441	164	3.3	4.13	9.96	12.77	13.21	13.22
43	2.441	329	0	13.55	12.71	15.67	14.50	15.24
52	2.441	267	0	9.08	11.55	14.47	13.32	13.88
352	2.441	640	0	3.08	4.43	6.24	5.65	5.36
225	2.441	615	0	4.72	5.54	7.65	6.91	6.71
495	2.441	1072	0	3.60	3.73	5.32	4.83	4.51
94	2.441	748	0	13.99	8.59	11.25	10.23	10.36
65	2.441	276	15.7	7.50	10.33	13.20	16.55	15.45
59	2.441	500	5.6	14.98	10.85	13.74	16.70	15.88
50	2.441	366	3.6	12.95	11.78	14.72	16.82	16.54
39	2.441	324	8.3	14.72	13.34	16.34	20.01	19.42
97	2.441	90	12.7	1.63	8.46	11.10	12.34	11.83
60	2.441	220	21.5	6.48	10.76	13.65	17.26	16.12
90	2.441	355	21.5	6.94	8.78	11.49	14.88	13.44
50	2.441	338	18.4	11.96	11.78	14.74	19.08	17.82
60	2.441	401	12.8	11.81	10.76	13.65	17.36	16.18
80	2.441	450	12.8	9.91	9.31	12.09	15.39	14.10
107	2.441	471	19.9	7.73	8.05	10.66	13.94	12.42
135	2.441	372	5.9	4.82	7.16	9.62	11.31	10.42
131	2.441	518	4.1	6.92	7.27	9.75	11.43	10.56
130	2.441	330	10	4.44	7.30	9.78	11.89	10.84
82	2.441	511	0	10.98	9.20	11.93	10.87	11.08
90	2.441	558	0	10.91	8.78	11.46	10.43	10.58
100	2.441	493	3.3	8.66	8.33	10.96	12.59	11.90
183	2.441	627	8.9	5.95	6.15	8.41	10.61	9.35
120	2.441	518	5.3	7.56	7.60	10.14	12.14	11.18
47	2.441	358	1	13.48	12.15	15.11	15.06	15.58
315	2.441	885	0	4.79	4.68	6.57	5.94	5.66
165	2.441	712	7.5	7.51	6.48	8.81	11.08	9.82
75	2.441	408	9.5	9.59	9.62	12.42	15.39	14.33
380	2.441	666	2.3	2.96	4.26	6.02	6.87	6.09

155	2.441	648	8.3	7.29	6.68	9.05	11.40	10.14
145	2.441	564	8.3	6.79	6.91	9.33	11.63	10.42
235	2.441	781	4.5	5.73	5.42	7.51	9.16	8.09
225	2.441	755	4.5	5.79	5.54	7.66	9.32	8.26
165	2.441	620	6.3	6.54	6.48	8.80	10.83	9.70
49	2.441	430	4.9	15.53	11.90	14.86	17.71	17.15
59	2.441	397	15.1	11.89	10.85	13.75	17.68	16.41

Table A.3: Veeken's Field Data and Calculation Results

Wellhead Pressure (psi)	Tubing Diameter (inch)	Gas Rate (mscf/d)	Current Gas Velocity (m/s)	Turner's Equation (m/s)	Zhang et al. Model (m/s)	Barnea's Model (m/s)	New Model (m/s)
58	4.41	1306.5	12.34	8.33	16.82	21.01	25.34
58	4.95	1589.0	11.91	8.33	17.53	22.04	26.19
79.75	2.81	741.5	12.51	7.09	12.42	15.01	20.12
87	2.87	918.1	13.60	6.78	12.13	14.95	18.89
87	2.99	918.1	12.53	6.78	12.54	15.65	14.35
87	2.99	918.1	12.53	6.78	12.25	15.06	19.57
79.75	2.87	847.4	13.71	7.09	12.73	15.72	17.77
87	3.96	1765.5	13.74	6.78	13.43	17.14	22.84
87	4.89	2153.9	10.99	6.78	14.65	18.84	22.54
87	4.89	2401.1	12.26	6.78	14.79	19.37	21.08
87	4.89	2507.0	12.80	6.78	14.71	19.26	22.29
87	4.89	3072.0	15.68	6.78	14.40	19.03	25.34
87	2.99	918.1	12.53	6.78	12.14	14.83	20.60
87	1.75	388.4	15.48	6.78	10.23	11.84	14.56
87	4.89	1942.1	9.91	6.78	14.58	18.51	22.88
87	4.89	2224.5	11.35	6.78	14.78	19.17	21.21
87	4.89	2507.0	12.80	6.78	14.37	18.56	25.14
87	4.89	2612.9	13.34	6.78	13.38	16.72	22.90
87	4.89	2224.5	11.35	6.78	14.73	19.08	21.77
101.5	3.96	1871.4	12.47	6.27	11.91	14.79	20.66
217.5	4.41	3531.0	10.54	4.44	9.94	13.05	12.93
348	4.28	4237.2	8.33	3.38	7.50	10.19	12.40
217.5	6.09	7768.2	12.16	4.52	11.28	15.26	15.65
667	4.41	4590.3	4.33	2.41	5.62	7.89	8.22
1189	4.41	7062.0	3.66	1.73	4.10	6.24	6.28
217.5	4.28	3884.1	12.24	4.39	9.58	12.74	14.65
1174.5	6.09	10946.1	3.01	1.80	4.66	6.94	7.87
1421	4.28	7062.0	3.73	1.65	3.95	5.84	4.28
1232.5	4.28	7062.0	4.31	1.78	4.27	6.25	4.62
725	4.28	6002.7	6.28	2.50	5.88	7.92	6.05
1232.5	4.28	6355.8	3.88	1.78	4.27	6.20	4.60
667	6.09	18714.3	9.48	2.57	6.83	10.01	9.09
493	6.09	13770.9	9.51	2.99	7.84	11.20	10.39
739.5	6.09	14477.1	6.59	2.41	5.98	8.43	9.83
565.5	6.09	13064.7	7.84	2.79	6.87	9.46	11.19

391.5	6.09	10946.1	9.57	3.39	8.21	11.01	13.30
319	6.09	12358.5	13.30	3.58	8.63	12.21	14.91
667	4.28	5296.5	5.38	2.42	4.40	5.57	7.12
478.5	4.28	4590.3	6.56	2.91	5.25	6.42	8.35
319	4.28	4943.4	10.69	3.52	6.27	7.76	10.31
174	4.41	6002.7	21.83	4.75	9.67	13.17	17.54
282.75	4.41	4766.9	10.62	3.73	8.07	10.97	14.16
522	4.41	4943.4	5.91	2.66	6.03	8.55	10.65
348	4.41	4060.7	7.36	3.28	7.31	10.11	12.88
304.5	4.41	3884.1	8.07	3.53	7.82	10.70	13.73
261	4.41	3354.5	8.15	3.80	8.35	11.33	14.66
290	4.41	3531.0	7.71	3.75	8.25	10.85	13.96
365.4	6.09	8297.9	7.47	3.36	8.11	11.00	13.36
174	6.18	7062.0	13.16	4.93	12.22	16.77	17.41
174	6.09	7768.2	14.91	5.02	12.15	16.44	19.39
638	4.41	5649.6	5.33	2.40	5.46	7.89	9.71
652.5	4.41	5120.0	4.72	2.45	5.70	8.02	8.50
355.25	4.41	4237.2	8.21	3.49	7.95	10.48	11.12
391.5	4.28	6708.9	12.67	3.34	7.45	10.10	11.78
522	4.28	5296.5	7.46	2.85	6.43	8.70	10.01
362.5	4.28	4590.3	9.37	3.43	7.64	10.15	11.92
1261.5	4.28	7062.0	4.01	1.69	3.83	5.71	6.82
275.5	4.41	6002.7	14.15	4.00	8.78	11.66	14.78
275.5	4.41	2824.8	6.53	3.59	7.91	10.83	13.99
362.5	4.28	5649.6	10.74	3.39	6.85	8.92	11.53
391.5	4.67	2966.0	3.93	3.18	5.95	7.13	9.24
435	2.88	2048.0	6.40	3.07	5.35	6.49	8.87
449.5	4.28	4449.1	6.08	2.89	5.14	6.48	8.47
336.4	3.92	2860.1	6.28	3.41	6.29	7.79	10.36
449.5	4.41	3990.0	5.13	2.98	6.22	8.10	10.30
1609.5	6.18	19950.2	3.56	1.43	3.76	6.34	7.04
1319.5	6.09	26023.5	5.58	1.62	4.40	7.47	6.51

Table A.4: Chevron Data and Calculation Results

Wellhead Pressure (psi)	Tubing Diameter (inch)	Gas Rate (mscf/d)	Liquid Rate (bbl/d)	Current Gas Velocity (m/s)	Turner's Equation (m/s)	Zhang et al. Model (m/s)	Barnea's Model (m/s)	New Model (m/s)
50	1.995	84.86	2.27	4.48	12.21	13.43	16.45	15.86
45	1.995	602.85	5.47	35.37	12.87	14.08	18.21	17.18
127	1.995	290.16	6.00	5.96	7.65	9.00	11.52	10.37
48	1.995	126.28	6.72	6.94	12.46	13.70	17.89	16.74
77	1.995	167.11	4.12	5.7	9.83	11.19	14.10	13.12
50	1.995	117.52	2.48	6.2	12.21	13.43	16.55	15.92
78	1.995	95.44	2.52	3.22	9.77	11.11	13.59	12.82
117	1.995	227.83	4.25	5.09	7.97	9.32	11.72	10.69
37	1.995	95.67	1.98	6.83	14.19	15.23	18.63	18.26
55	1.995	66.30	5.33	3.18	11.64	12.93	16.63	15.58
77	1.995	151.14	3.64	5.16	9.83	11.18	14.00	13.07
52	1.995	56.87	0.99	2.88	11.97	13.20	15.15	14.99
23	1.995	79.17	1.36	9.12	18.00	18.51	22.36	22.59
105	1.995	354.75	7.24	8.85	8.42	9.79	12.66	11.44
78	1.995	263.89	8.79	8.89	9.77	11.15	14.59	13.29
75	1.995	444.93	5.62	15.6	9.96	11.32	14.52	13.41
74	1.995	233.97	6.40	8.31	10.03	11.39	14.71	13.54
75	1.995	90.18	0.99	3.16	9.96	11.30	12.86	12.54
75	1.995	232.61	2.99	8.15	9.96	11.31	13.99	13.15
100	1.995	73.70	7.47	1.93	8.63	10.00	12.96	11.73
122	1.995	190.56	4.98	4.08	7.81	9.16	11.61	10.52
56	1.995	142.15	1.95	6.69	11.53	12.80	15.47	14.92
97	1.995	145.43	1.58	3.93	8.76	10.11	11.92	11.30
68	1.995	228.11	3.42	8.83	10.46	11.80	14.74	13.86
75	1.995	309.37	6.55	10.84	9.96	11.33	14.64	13.46
75	1.995	135.75	2.77	4.76	9.96	11.30	13.92	13.12
23	1.995	213.15	2.05	24.54	18.00	18.53	23.07	22.99
65	1.995	228.05	3.55	9.24	10.70	12.02	15.08	14.19
128	1.995	133.21	2.76	2.72	7.62	8.95	10.96	10.08
80	1.995	116.94	4.03	3.84	9.65	11.01	13.85	12.87
65	1.995	99.58	1.36	4.03	10.70	12.01	14.07	13.65
30	1.995	180.06	1.83	15.88	15.76	16.63	20.33	20.14
61	1.995	131.11	1.12	5.66	11.05	12.34	14.25	13.96
115	1.995	163.24	5.19	3.71	8.04	9.40	11.95	10.85
128	2.441	467.44	4.07	6.37	7.62	9.64	12.17	11.02
34	2.441	193.37	4.44	10.04	14.81	16.94	22.12	21.24
54	2.441	139.89	5.62	4.56	11.74	13.99	18.31	17.10
56	2.441	265.25	2.65	8.34	11.53	13.76	17.02	16.25
25	2.441	106.79	3.05	7.55	17.27	19.20	24.65	24.26
47	2.441	154.78	1.67	5.81	12.59	14.81	17.68	17.29
95	2.441	190.82	2.86	3.52	8.85	10.98	13.53	12.57
39	2.441	96.72	4.35	4.38	13.82	16.02	20.78	19.84
141	2.441	101.04	1.16	1.25	7.26	9.23	10.46	9.84
120	2.441	414.99	4.72	6.04	7.87	9.91	12.66	11.45
35	2.441	421.80	2.14	21.28	14.59	16.74	20.61	20.24
265	2.441	772.93	4.45	4.99	5.29	6.95	8.84	7.70
87	2.441	565.61	13.47	11.4	9.25	11.43	15.61	13.90
65	2.441	109.78	2.35	2.97	10.70	12.92	15.76	15.01
66	2.441	240.25	4.95	6.4	10.62	12.85	16.59	15.41
69	2.441	139.71	2.70	3.56	10.39	12.59	15.53	14.68

75	2.441	132.18	2.69	3.09	9.96	12.15	14.96	14.09
71	2.441	200.27	3.84	4.96	10.24	12.45	15.76	14.71
33	2.441	153.48	9.50	8.22	15.03	17.18	23.58	22.14
76	2.441	174.54	10.90	4.03	9.90	12.10	16.39	14.77
75	2.441	117.07	1.73	2.74	9.96	12.14	14.40	13.77
7	2.441	83.83	2.99	21.23	32.64	31.88	43.35	44.62
121	2.441	326.94	4.48	4.71	7.84	9.88	12.57	11.38
128	2.441	68.80	0.91	0.94	7.62	9.63	10.66	10.16
1180	2.441	1118.18	12.21	1.43	2.48	3.43	4.74	3.71
198	2.441	126.89	1.01	1.11	6.12	7.93	8.86	8.23
187	2.441	433.24	4.12	4.01	6.30	8.15	10.28	9.13
140	2.441	287.75	5.82	3.58	7.29	9.27	11.99	10.70
60	2.441	72.05	8.19	2.11	11.14	13.38	17.90	16.45
71	2.441	299.89	8.55	7.42	10.24	12.45	16.65	15.17
61	2.441	162.12	3.59	4.68	11.05	13.28	16.78	15.81
48	2.441	166.20	3.59	6.1	12.46	14.69	18.67	17.78
52	2.441	53.41	1.22	1.81	11.97	14.18	16.41	16.16
96	2.441	499.28	4.56	9.11	8.80	10.93	13.96	12.77
89	2.441	415.95	15.76	8.19	9.14	11.32	15.57	13.80
72	2.441	252.55	6.38	6.16	10.17	12.38	16.24	14.91
92	2.441	133.38	4.07	2.54	8.99	11.13	14.10	12.98
133	2.441	86.64	1.69	1.13	7.48	9.48	11.12	10.35
76	2.441	245.76	2.57	5.68	9.90	12.09	14.81	13.96
38	2.441	317.06	6.78	14.73	14.00	16.19	21.68	20.44
214	2.441	356.14	29.87	2.87	5.89	7.68	10.80	9.04
140	2.441	397.41	5.06	4.94	7.29	9.26	11.88	10.64
1300	2.441	1657.45	14.29	1.9	2.36	3.27	4.56	3.54
25	2.441	221.66	3.45	15.68	17.27	19.22	24.89	24.40
35	2.441	125.12	4.12	6.31	14.59	16.74	21.72	20.88
45	2.441	110.22	0.63	4.32	12.87	15.06	16.35	16.60
200	2.441	405.31	5.41	3.5	6.09	7.90	10.17	8.93
75	2.441	233.98	2.40	5.48	9.96	12.15	14.81	14.01

Table A.5: ConocoPhillips Data and Calculation Results

Wellhead Pressure (psi)	Tubing Diameter (inch)	Gas Rate (mscf/d)	Liquid Rate (bbl/d)	Current Gas Velocity (m/s)	Turner's Equation (m/s)	Zhang et al. Model (m/s)	Barnea's Model (m/s)	New Model (m/s)
Unloading Wells								
163	1.995	600	0	8.83	6.70	7.75	9.17	8.60
145	1.995	700	6	11.58	7.11	8.20	10.85	9.71
250	1.995	710	2.5	6.81	5.40	6.40	8.06	7.21
210	1.995	950	10	10.85	5.90	6.96	9.42	8.18
90	1.995	650	2	17.33	9.03	10.08	12.54	11.84
95	1.995	700	4	17.68	8.78	9.87	12.82	11.83
110	1.995	720	1	15.70	8.16	9.23	10.85	10.39
160	1.995	850	0.1	12.75	6.76	7.81	9.25	8.68
195	1.995	500	2	6.15	6.12	7.17	8.87	8.08
128	1.995	720	0.6	13.50	7.57	8.63	9.68	9.37
150	1.995	700	0.1	11.20	6.99	8.04	9.52	8.96
170	1.995	400	2	5.65	6.56	7.62	9.43	8.65
210	1.995	950	3	10.85	5.90	6.93	8.82	7.91
Loading Wells								
50	2.441	450	5	14.42	12.12	13.97	18.79	17.67
80	1.751	250	5	9.73	9.57	10.17	13.20	12.22
90	1.751	250	5	8.65	9.03	9.65	12.52	11.54
55	1.995	220	5	9.60	11.55	12.51	16.57	15.55
60	1.995	190	5	7.60	11.06	12.05	15.94	14.90
82	1.995	400	5	11.70	9.46	10.53	13.87	12.80
52	1.995	300	5	13.84	11.88	12.81	16.99	15.98
170	1.995	580	5	8.19	6.56	7.63	10.01	8.93
190	1.995	500	3	6.31	6.20	7.25	9.23	8.32
160	1.995	570	2	8.55	6.76	7.83	9.69	8.92
215	1.995	550	0.1	6.14	5.83	6.84	8.10	7.49
130	1.995	400	1.5	7.38	7.51	8.58	10.41	9.76
130	1.995	380	0.5	7.01	7.51	8.58	9.45	9.20
102	1.995	400	0.1	9.41	8.48	9.53	8.81	9.20
100	1.995	300	3	7.20	8.56	9.65	12.30	11.42
205	1.906	500	0.15	6.41	5.97	6.88	6.70	6.67
235	2.375	380	1	2.74	5.58	7.02	8.13	7.50
170	1.995	720	0.1	10.16	6.56	7.61	9.00	8.42
170	1.995	440	0.5	6.21	6.56	7.61	8.38	8.05
72	1.995	300	0.1	10.00	10.09	11.09	10.28	10.93
160	1.995	520	6	7.80	6.76	7.85	10.39	9.25
130	1.995	500	3	9.23	7.51	8.59	10.94	10.04
140	1.995	480	0.08	8.23	7.23	8.22	7.43	7.72
180	1.995	500	0.1	6.66	6.38	7.42	8.77	8.18
175	1.995	600	2	8.23	6.47	7.52	9.31	8.53
195	1.995	600	2	7.38	6.12	7.17	8.87	8.08
130	1.995	390	0.1	7.20	7.51	8.57	7.90	8.16
130	1.995	450	0.1	8.31	7.51	8.57	7.90	8.16
170	1.995	450	0.2	6.35	6.56	7.61	7.61	7.56
150	1.995	400	2	6.40	6.99	8.05	9.98	9.21
145	1.995	550	2.5	9.10	7.11	8.19	10.29	9.45
160	1.995	500	1	7.50	6.76	7.82	9.18	8.63
170	1.995	400	1.5	5.65	6.56	7.61	9.23	8.54

155	1.995	510	1.1	7.89	6.87	7.94	9.38	8.81
90	1.995	280	0.5	7.46	9.03	10.08	11.14	11.03
130	1.995	450	0.5	8.31	7.51	8.57	9.45	9.20
140	1.995	520	0.1	8.91	7.23	8.29	9.82	9.27
148	1.995	520	0.1	8.43	7.03	8.09	9.58	9.02
165	1.995	630	1.4	9.16	6.66	7.72	9.30	8.65
155	1.995	500	0.5	7.74	6.87	7.93	8.73	8.43
125	1.995	440	0.25	8.45	7.66	8.73	8.95	8.95
120	1.867	450	0.09	10.27	7.81	8.67	7.99	8.32
120	1.995	400	0.75	8.00	7.81	8.88	10.17	9.80
183	1.995	750	0.1	9.83	6.32	7.36	8.71	8.12
140	1.995	480	1.5	8.23	7.23	8.31	10.07	9.41
165	1.995	590	3	8.58	6.66	7.72	9.83	8.92
160	1.995	600	2.5	9.00	6.76	7.83	9.85	9.00
110	1.867	490	0.1	12.20	8.16	9.00	10.58	10.14
115	1.995	480	0.1	10.01	7.98	9.05	10.72	10.21